COMposite superstructures for large PASsenger Ships (COMPASS)

Technical Report

Date : September 2016
Project name : COMPASS – COMposite superstructures for large PASsenger Ships

Author : Vasileios Karatzas

DTU Mechanical Engineering
Department of Mechanical Engineering

DTU Civil Engineering
Department of Civil Engineering

Content

DTU Mechanical Engineering
Department of Mechanical Engineering

DTU Civil Engineering
Department of Civil Engineering

Preface

This document presents the major findings of the COMPASS project. COMPASS focused on the design of superstructures made out of composite materials for large Passenger ships.

The project was funded by the Danish Maritime Fund (Den Maritime Fond) and the Maritime Reconversion Fund (Den Maritime Omstillingspulje). The project was carried out in a partnership between Danish Institute of Fire and security Technology (DBI) and the Technical University of Denmark (DTU), Department of Civil Engineering and Department of Mechanical Engineering.

The scope of the COMPASS project was to demonstrate how an existing passenger ferry may be refurbished substituting parts of the existing superstructure with polymer composite materials. Emphasis has been given in the potential effects on the ships performance and the behaviour of the selected composite materials at elevated temperatures in the event of fire.

Key words: *Superstructure, passenger ship conversion, FRP composite, fire tests, structural integrity*

Acknowledgements

The Project Partners would like to express their gratitude to DIAB, Morgan Thermal Ceramics and Hoffmann Engineering for sponsoring materials for the conduction of the experiments. Additionally, the project partners would like to thank Scandlines for providing documentation for the RoPax vessel PRINSESSE BENEDIKTE.

1 Introduction

Fibre Reinforced Polymer composite materials (FRP) are increasingly being implemented in a wide variety of industrial applications where metallic materials were predominantly considered as the only viable option. This is due to the attributes they exhibit, such as the high specific strength/stiffness ratio, their durability and their resistance to corrosion to name a few. Moreover, recent technological advancements have led to the industrialization of composite materials reducing their cost.

In the marine industry composite materials have been mainly used for small crafts and military vessels as the use of composite materials on SOLAS ships had been restricted until 2002 when the so-called Rule 17 was introduced in the SOLAS convention. This regulation enabled the use of combustible composite materials provided that the same level of safety as for the metallic design could be demonstrated.

This regulation has allowed for alternative designs which can increase the efficiency of ships and after its introduction has sparked the interest of regulatory bodies, ship stakeholders and researchers on quantifying the benefits of implementing composite materials. Simultaneously, significant effort has been invested on defining an accepted approach for the implementation of regulation 17 paving the way for the use of composites also onboard SOLAS vessels. Despite the benefits that the implementation of composite materials represent, to this day, this regulation has been rarely used in practice as both the technical aspects and the appropriate regulatory approval related to the implementation of composites have proven to be complex, time-consuming and therefore not appealing to the ship stakeholders. One notable case where the rule 17 has been implemented is the bulk carrier *Nordic Oshima* of which the hatch covers have been made of composite materials and approved by the flag state.

Several research projects have been realized dealing with the use of composites on SOLAS vessels, however it is only a handful of them that have been focusing on addressing the performance of composite materials in the case of fire, which is widely considered as the Achilles' heel of fibre reinforced composite materials.

2 Background

In general two different approaches can be identified regarding the implementation of Rule 17. The first one is referred to as the prescriptive approach. This approach consists of staying as close as possible to the prescriptive regulations by making conservative equivalences in terms of passive protection compared to an equivalent prescriptive (steel) design and does not consider if the prescriptive design provides a balanced safety level. As there is no quantified absolute safety level associated with the prescriptive rules in SOLAS the resulting safety level may not be appropriate (too conservative or even too low) for a given novel ship design. The second approach involves the realization of fire engineering analysis so as to achieve a level of fire risk that is sufficient and acceptable for the composite design at stake.

Each approach presents different advantages and disadvantages as the prescriptive approach is easier to be implemented but predominantly results in overly conservative and therefore unfavourable solutions. On the other hand, a risk based fire engineering approach results in a more optimized and scientifically proven approach. However, the performance of such analysis tends to be overly complicated, time consuming and has not yet become common practice in the shipbuilding field, despite the fact that it has been used for more than a decade in the built environment on land and even for offshore structures. However, steps have been taken towards the implementation of a risk based approach. A brief description of some key research projects related to the implementation of rule 17 is presented in this passage.

SAFEDOOR (2005-2009) developed a risk-based regulatory framework for the maritime industry and addressed the complexity of a full comprehensive system, while *SURSHIP-FIRE (2006-2010)* dealt with the survivability of ships in case of fire. These projects have not addressed directly the use of composite materials; however they are representatives of a risk assessment approach to assess safety and could potentially be used for the assessment of composite structures on board SOLAS vessels.

The *Eco-Island Ferry (2010-2015)* project made an evaluation of alternative design and arrangements for a small ro-ro ship built in fibre reinforced composites in load bearing structures using fire engineering analysis. A base design was considered by simply replacing the steel structure with an equivalent one made of composite materials. Results indicated that the selected base design was shown to pose a risk more than four times as high as the prescriptive design, however a performance criterion with a safety factor of 50 % provided three acceptable trial alternative designs.

A similar approach to the one followed in the Eco-Island Ferry project was followed in *BESST (2015).* In particular an engineering analysis in accordance with SOLAS chapter II-2 regulation 17 was performed for the Panamax cruise vessel the Norwegian Future. The five upper decks were redesigned in FRP composite. A prerequisite was that thermal insulation was added to all interior surfaces in order to achieve 60 minutes of fire protection. Fire scenarios where differences in fire safety would be significant were identified and studied. In the quantitative assessment a number of identified potential fire hazards were managed independently whilst others were incorporated in fire scenarios involving representative space groups.

E-LASS, Lightweight Construction Applications at Sea (2009), investigated technically and economically four different vessels in which appropriate parts had been re-designed using lightweight materials. The target was to be able, after finalisation of the project, to provide practical solutions for how to actually build a lightweight ship using either aluminium or fibre reinforced polymer (FRP) composite as construction materials. Constraints were that the weight reduction should be at least 30 % where new materials were used and that the total cost should be at least 25 % lower based on a life cycle cost analysis (LCCA).

LASS-C (2011) has focused on bringing a large cruise vessel, with an FRP composite superstructure, through the whole design and approval process demonstrating how an equivalent level of fire safety will be obtained in line with SOLAS II-2/17. Fire and risk analysis as well as analysis considering costs and environmental effects (LCC/LCA) have been further studied.

FIRE-RESIST (2011-2015) addressed issues related to the performance of composites at elevated temperatures such as the degradation of the mechanical properties and the generation of smoke and toxic by-products. This was achieved through the development of material technologies and improved simulation capabilities.

These projects reflect the increasing interest for the introduction of composites on board SOLAS vessels and that significant research is being performed towards that direction.

3 The COMPASS project

3.1 Scope

The COMPASS project is a demonstration project in which part of the superstructure of the RoPax Ship PRINSESSE BENEDIKTE was redesigned out of composite materials. The benefits of a light superstructure become more prominent in large passenger ships, as the superstructures constitute a significant percentage of the Lightship; additionally, depending on the size of the ship, the superstructure may tower several decks above the weather deck, affecting the stability of the ship. The project's main aims can be summarized as follows:

a) to quantify the potential benefits from implementing composite superstructures in large passenger ships

b) to demonstrate how Rule 17 could be applied in praxis.

c) to investigate the load bearing capacity of structural elements beyond 60 minutes fire exposure, which is the threshold prescribed by the regulations.

d) To suggest a new approach for the design and analysis of composite structures prior to proceeding to full scale testing.

3.2 Technical Approach

A brief outline on the work performed to address the aforementioned issues is presented here. More information concerning the technical approach can be found at the respective annexes.

The superstructure was redesigned using glass fibres in an epoxy matrix and a PET core provided by DIAB. The design was performed according to the rules and regulations prescribed by DNV-GL. It should be outlined that it was decided to keep the same general arrangement for the new composite superstructure and the composite design is not optimized with respect to the vessel's life cycle.

To address the first aim, structural analysis was performed for the original steel design and its composite counterpart using the finite element method (**Annex A**). Comparing the two designs revealed that the composite superstructure performs satisfactorily when subjected to the loads prescribed by the regulations. In the following, having designed the composite superstructure, weight, stability and resistance calculations were performed for the vessel and compared to the relevant ones for the original steel design. Moreover, a rough estimation of the fuel oil consumption reduction was performed. These calculations are presented in **Annex B**.

Additionally, a steel-to-composite joint was designed. A numerical investigation was performed for the proposed design studying what would be the temperature distribution in the joint due to heat conduction from the steel part in the event of a fire in the steel deck below (**Annex C**).

The demonstration of how Rule 17 could be applied was achieved by following the prescriptive approach. Having redesigned the superstructure, bulkhead structures made of steel, aluminium and composite materials were tested according to the FTP code to demonstrate that the A-60 and FRD-60 requirements could be met, fulfilling the prescriptive requirements.

In order to investigate what is the remaining load bearing capacity of these structural elements beyond the 60 minutes threshold prescribed by the FTP code, the bulkheads were tested well beyond 60 minutes opting to identify when ultimate failure would occur. Moreover, additional tests were performed, similar in principle to the ones prescribed by the FTP code with a different imposed fire curve and increased mechanical loading. (**Annex D**).

Having performed the full scale tests, a new simplified approach was sought for the design and analysis of structural components made of composites. The suggested approach is intended to act as an intermediate test to help designers investigate alternative configurations for composite structural elements, aiming to assist in the design of structural elements. The simplified approach consists of performing mid-scale tests under combined thermal and mechanical loading using heat flux to achieve the same temperature gradient as in the full scale tests.

The approach can be discretized in the following steps:

a) Performance of material characterisation tests at different temperatures for the selected materials to investigate the dependence of the mechanical properties to the temperature (**Annex E**).

b) Experimentally measuring the reaction to fire of the selected materials (**Annex F**).

c) Performance of small scale furnace tests with the ISO curve for the back calculation of the temperature gradient in the specimen employing numerical methods (**Annex G**).

d) Performance of combined thermal and mechanical loading using the heat flux and analysis (**Annex H**)

3.3 Conclusions and major findings

Starting with aim a) (Section 1.2.1) results indicated that the Lightship weight was reduced around 5 % compared to the existing steel design. This reduction in combination with the position of the centre of Gravity of the superstructure resulted in significantly increased stability for the examined loading cases were examined i.e. the full load departure one and the average operating condition. The latter was based on data provided by Scandlines.

Contrarily, the reduction of the Lightship's weight did not significantly affect the resistance of the vessel. Consequently, the reduction of the fuel oil consumption amounted to about 1.4 % of the initial annual estimation. This marginal reduction is attributed to the fact that the new design was not optimized with respect to the vessel's life circle. Additionally, it highlights that designing the composite superstructure to accommodate more passengers might represent a more beneficial approach compared to keeping the same design as it was decided in this project. Last but not least it should be underlined that Prinsesse Benedikte served as a study case and in reality a retrofitting/conversion on a ship is performed to address a well-defined problem such as the increase of stability and the increase of payload.

As mentioned, the prescriptive approach was followed for the implementation of Rule 17. The performed full scale tests on metallic and composite bulkheads demonstrated that the composite design met the 60 minutes requirement. What was most interesting though, was the behaviour of the tested bulkheads beyond the 60 minutes threshold. This investigation was sparked by the fact that there have been several documented accidents where an uncontrolled fire has been burning for hours and due to weather conditions the passengers and the crew cannot evacuate the vessel. The performance of a composite superstructure under such situations represents a major concern.

Testing revealed that there is an important difference between the metallic structural components and the composite ones. In the case of the metallic components the governing factor is the containment of fire, meaning that the structural element will not collapse when the fire exceeds 60 minutes rather than allow for the spread of fire in the adjusting spaces. Contrarily, the elevated temperatures that develop in the fire exposed side of the composite structure after the 60 minutes are not reflected at the unexposed side of the bulkhead, as the composite structure acts as an insulator. However, the elevated temperature, in combination with the applied loading leads to the loss of the load bearing capacity of the bulkhead relatively shortly after 60 minutes due to the degradation of the mechanical properties.

The fact that metallic constructions can retain their load bearing capacity even in cases where an uncontrolled fire has been ongoing for several hours is referred to as "implicit robustness" and is not directly addressed by the regulations. Trying to impose the prescriptive requirements on composite structures leaves a gap between the two designs. The composite case can be designed to sustain 60 minutes of fire according to FTP regulations, but as there is no explicit requirements for the load bearing capacity after that would potentially lead to the structural collapse of the element. Therefore, either a new set of requirements should be defined for the FRP structures to account for the load bearing capacity beyond 60 minutes, or an alternative holistic risk based approach should be sought to account for an acceptable level of safety to account for such events.

At the end of the project, emphasis has been placed on developing an approach that would facilitate the design and analysis of composite structures. The approach consisted of the correlation of the experimentally measured material properties of the composite to the integrity of structural components under combined thermal and mechanical loading. To this end, a novel approach has been developed serving as an intermediate step. This approach allowed for the performance of different loading scenarios under simpler testing conditions compared to the full scale tests.

Additional testing is required, however, to allow the direct connection of the mid-scale test series to the large-scale ones. Despite that fact, significant insight has been gained on the evolution of damage, the failure mechanisms and the governing parameters for sandwich structures subjected to combined thermal and mechanical loading.

4 List of annexes

Annex A: Structural analysis of the Superstructure

Annex B: Effects on the ship

Annex C: Thermal numerical modelling of joints at steel/FRP interface

Annex D: Large-scale bulkhead fire tests – summary report

Annex E: Material characterisation tests at elevated temperatures

Annex F: Reaction to fire of composite sandwich-materials

Annex G: Fire Resistance for small scale composite specimen

Annex H: Mid-scale tests under combined thermal and mechanical loading (H-TRIS tests)

Annex A: Structural analysis of the Superstructure

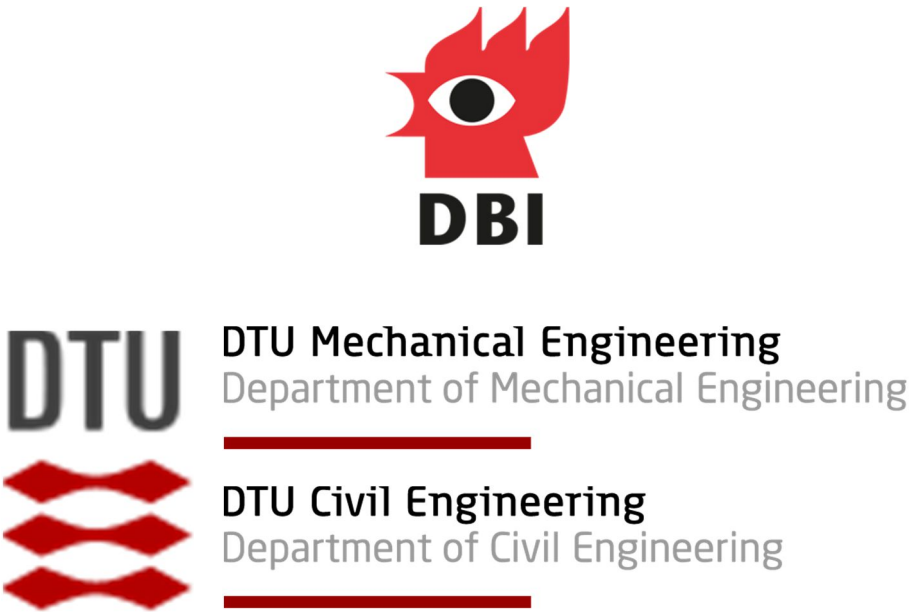

Date : January 2016
Project name : COMPASS – Composite superstructures for large PASSenger ships

Author : Vasileios Karatzas

Content

1 Introduction

The interaction of the superstructure with the hull of the ship is quite complex. In ships with long continuous superstructures the superstructures unavoidably carry stresses transmitted from the hull girder. Therefore these structures are made effective with adequate scantlings. In smaller ships however it is common to design the superstructure in such a way so as not to contribute to the longitudinal strength of the ship. This can be achieved by different means. One of them, which can be found in older ships, is by fitting expansion joints (Figure 1) in suitable positions rendering in this way the structure ineffective from a load carrying perspective. Other methods include the use of lower modulus materials, such as aluminium, as the lower modulus of elasticity results in lower stresses in the structure compared to the steel case, [1] or geometrically designing the superstructure in such a way so that the stress transmission is minimized [2]. As one might suspect, the hull-superstructure-interaction has long been of concern to naval architects which had to rely on basic understanding of how topological features affect this interaction and on experience for the design. It wasn't until the development of the finite element method that such an adequate analysis became possible. With the use of 3D finite element modelling the analyst is able to model the whole ship and study the interaction between the hull and the rest of the structure. However this task can prove to be tedious and overly time consuming. In addition detailed structural drawings along with the necessary documentation are needed for the whole ship and the analyst has to find a middle ground between the detailed design and ease of modelling which requires experience and good understanding of the ship structure. As the modelling of the whole ship was demanding a lot of resources a different way was sought in the project, namely via the regulation requirements.

Figure 1: Expansion Joint

1.1 Case study

The ship which was the study case is a double-ended RoPax ferry named PRINSESSE BENEDIKTE and is operated by Scandlines. The main characteristics of the vessel are listed in Table 1. The upper decks of the superstructure, i.e. the wheelhouse and passenger decks, were selected for retrofitting. which lie above 17.7 m measuring from the baseline (Figure 2). The deck positioned at 17.7m was made out of steel for both the existing and the retrofitted case.

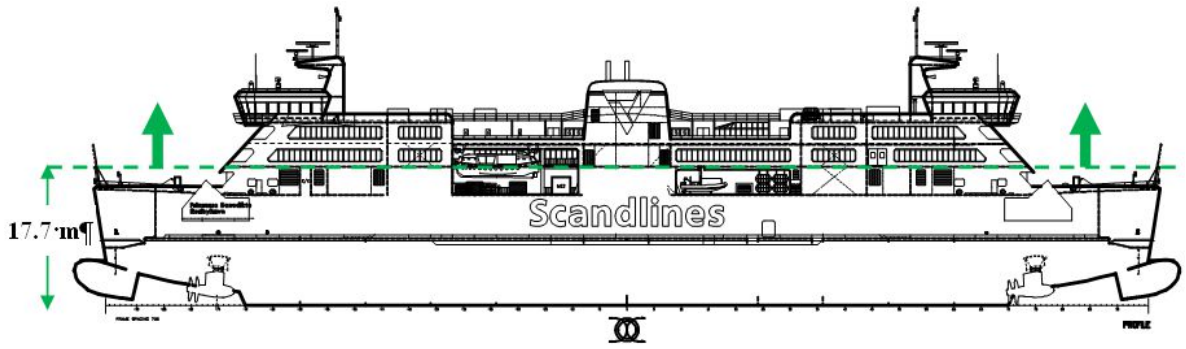

Figure 2: Part of the superstructure for retrofitting

In this work, it was decided to keep the same general arrangement of the superstructure, given that the original requirements and constraints were unknown.

Materials properties and arrangement

Glass fibres impregnated in Prime 20LV epoxy resin were selected for the sandwich faces. The core was Divinycell P100 provided by DIAB which exhibits good fire, toxicity and smoke properties and high temperature performance. Typical marine grade steel was used in the case of the steel with Young's modulus equal to 203 GPa and Yield Strength equal to 235 MPa. DNV's rules were used for the design of the composite superstructure. In particular, the scantling calculations were performed following DNV's Rules for Classification of High Speed, Light Craft and Naval Surface Craft [3,5] while the design loads were calculated according to DNV's Rules for Classifications of Ships [4,5]. The sandwich panel ply sequence along with the material properties of the selected laminae are listed in Tables 1 and 2.

Table 1: Material Properties

Lamina Material Properties

Material Properties	Type of material	Fibre direction	Fibre volume fraction	Cured ply thickness	Cured ply weight	Longitudinal tensile modulus	Transverse tensile modulus	Longitudinal compressive modulus	Transverse compressive modulus	In-Plane Shear Modulus	Longitudinal Interlaminar shear modulus	Longitudinal tensile strain	Transverse tensile strain	Longitudinal compressive strain	Transverse compressive strain
				[mm]	[g/m²]	[MPa]	[MPa]	[MPa]	[MPa]	[MPa]	[MPa]	[%]	[%]	[%]	[%]
UE800	Unidirectional E-glass	0°	0.48	0.641	1171	35910	8450	35910	8450	3190	3190	1.80%	0.45%	-1.25%	-1.50%
BE900	E-glass Stitched fabric	0°/90°	0.46	0.754	1364	21220	21220	21220	21220	3050	3050	1.50%	1.50%	-1.20%	-1.20%
WRE580	E-glass woven rovings	0°/90°	0.45	0.496	881	20380	20380	20380	20380	3278	2980	1.50%	1.50%	-1.25%	-1.25%
XE905	E-glass Stitched fabric	+/-45°	0.46	0.750	1364	9737	9737	9737	9737	9471	9471	1.50%	1.50%	-1.20%	-1.20%
UCHSC500	Unidirectional Carbon	0°	0.48	0.578704	835.213	112110	6350	107540	6350	3390	3390	1.00%	0.45%	-0.67%	-1.50%

Core Properties

Core Properties	Average density	Longitudinal Shear strength	Longitudinal Shear Modulus	Transverse Shear strength	Transverse Shear Modulus	Compressive Modulus
	[kg/m³]	[MPa]	[MPa]	[MPa]	[MPa]	[MPa]
P100	110	0.88	28	0.88	28	100

The lay-up sequence and orientation for each structural element is listed below

Table 2: Lay-up

Ply Number	Wheelhouse Deck 6 Material	Sun Deck 7 Material	Superstructure Material	Wheelhouse Panels Material	Structural Bulkheads Material
1	1 x WRE602 Ehfv @ 0°	1 x WRE602 Ehfv @ 0°	1 x WRE602 Ehfv @ 0°	1 x WRE602 Ehfv @ 0°	1 x XE905 Ehfv @ 0°
2	1 x XE905 Ehfv @ 0°	1 x XE905 Ehfv @ 0°	1 x XE905 Ehfv @ 0°	1 x XE905 Ehfv @ 0°	1 x XE450 Ehfv @ 45°
3	1 x XE450 Ehfv @ 45°	1 x XE905 Ehfv @ 45°	1 x XE450 Ehfv @ 45°	1 x XE450 Ehfv @ 45°	
4	1 x XE905 Ehfv @ 0°	1 x XE905 Ehfv @ 0°	1 x XE905 Ehfv @ 0°	1 x XE905 Ehfv @ 0°	
	DIAB P100/50mm	DIAB P100/50mm	DIAB P100/50mm	DIAB P100/40mm	DIAB P100/40mm
1	1 x XE905 Ehfv @ 0°	1 x XE905 Ehfv @ 0°	1 x XE905 Ehfv @ 0°	1 x XE905 Ehfv @ 0°	1 x XE905 Ehfv @ 45°
2	1 x XE450 Ehfv @ 45°	1 x XE905 Ehfv @ 45°	1 x XE450 Ehfv @ 45°	1 x XE450 Ehfv @ 45°	1 x XE905 Ehfv @ 0°
3	1 x XE905 Ehfv @ 0°	1 x XE905 Ehfv @ 0°	1 x XE905 Ehfv @ 0°		

Hull - superstructure interaction

In order to determine if the superstructure was considered as a longitudinal strength member, the moment of inertia of the midship section was calculated using the vessels steel drawings. The minimum required thickness values were calculated according to DNV rules, where these were not listed in the drawings. Only the elements between the base line and the main deck were considered initially (Figure 3). The calculated moment of inertia was subsequently compared to the minimum required value for the midship section of inertia prescribed in DNV's Rules for Ships.

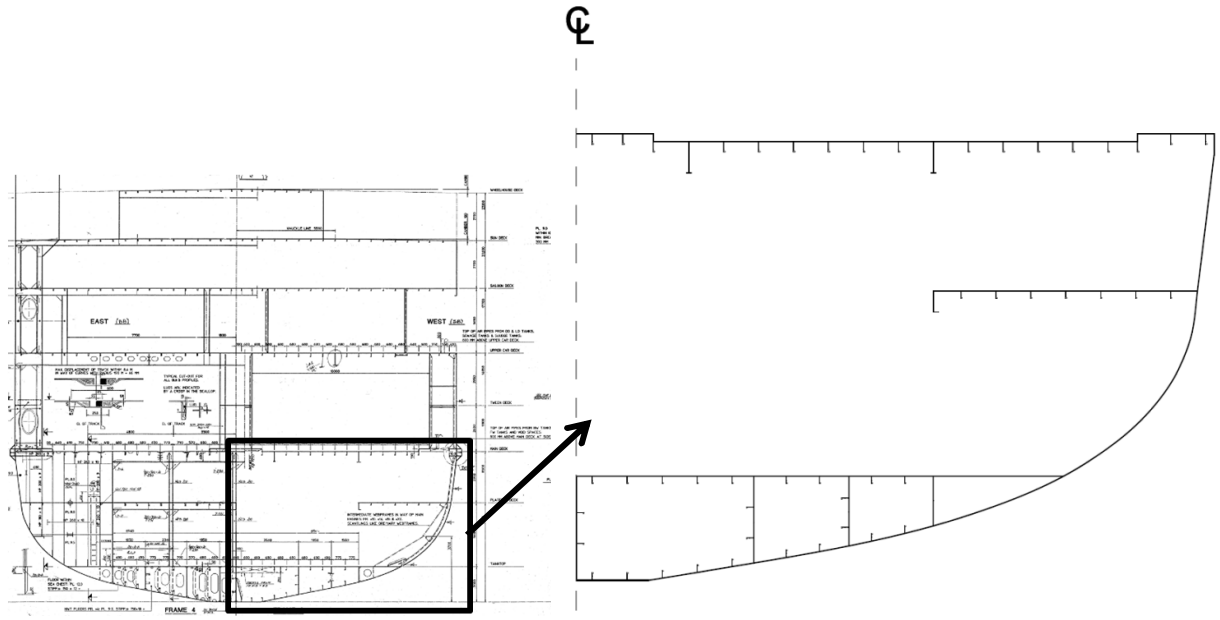

Figure 3: Elements considered for the calculation of the moment of inertia (up to the main deck)

The restriction service area of notation of PRINCESSE BENEDIKTE is not listed in the outline specifications or elsewhere in the ship's documentation. Depending on the service restriction notation reductions are allowed by the regulations in the midship and design bending moments. Therefore a R1 service area restriction by DNV rules was considered (Figure 4). The rationale was, that although the ship operates in a significantly lower range (the distance between Puttgarden and Rødby is around 12 nautical miles) it might be difficult to sell the ship afterwards if it is built for a R3 service area restriction. In reality, it might be that the ship has an R2 or R3 service area restriction. The service area of notation affects the required minimum moment of inertia of the vessel's cross section, lowering its value for more restricted areas. The difference between the moments of inertia is less than 5% which is reasonable considering that the minimum required values were considered for the calculation of the moment of inertia and that the real restriction service area is unknown (Table 4).

B 400 Service restrictions

401 The service area notation **R** followed by a number or a letter will be assigned to ships with certain modifications to arrangement, equipment or scantlings, in relation to ships built for unrestricted trade.

The service area restrictions, given in nautical miles and representing the maximum distance from nearest port or safe anchorage, are given in Table B1. For the various service area notations the restrictions are related to the zones, areas and seasonal periods as defined in the International Convention on Load Lines, 1966, Annex II.

The service area notation **RE** is limited to enclosed waters such as fjords, ports, rivers and lakes.

The service area restrictions as related to the assigned service area notation will be included in the "Appendix to the Class Certificate".

Table B1 Service area restrictions

Service area notations	*Seasonal zones (nautical miles)*		
	Winter	*Summer*	*Tropical*
R0	250	No restrictions	No restrictions
R1	100	200	300
R2	50	100	200
R3	20	50	100
R4	5	10	20
RE	Enclosed waters		

Figure 4: Service area restriction and notation according to DNV

The results indicate that the superstructure in the original design was not considered as a load bearing element of the vessel's structure. In other words, the superstructure is not effectively connected to the hull, which means that the hull girder loads are not transmitted from the latter to the former and only local acting loads should be considered in the design and analysis of the superstructure.

Table 4: Midship moments of inertia

Midship moment of Inertia *(up to main deck)*		
Calculated	[cm^4]	1.38e9
Minimum Required (according to DNV)	[cm^4]	1.44e9
Difference	[-]	4.58%

The alternative case was also studied, meaning, that the superstructure was considered to effectively contribute to the longitudinal strength. In this case the extent of the structure considered for the calculation of the moment of inertia was up to the car deck which is the last deck whose sides are the same with these of the hull (Figure 4). The moment of inertia was once again calculated using the vessel's steel drawings. Once again the minimum plate thicknesses as calculated by the DNV rules were considered for plating whose thickness was not listed in the steel drawings.

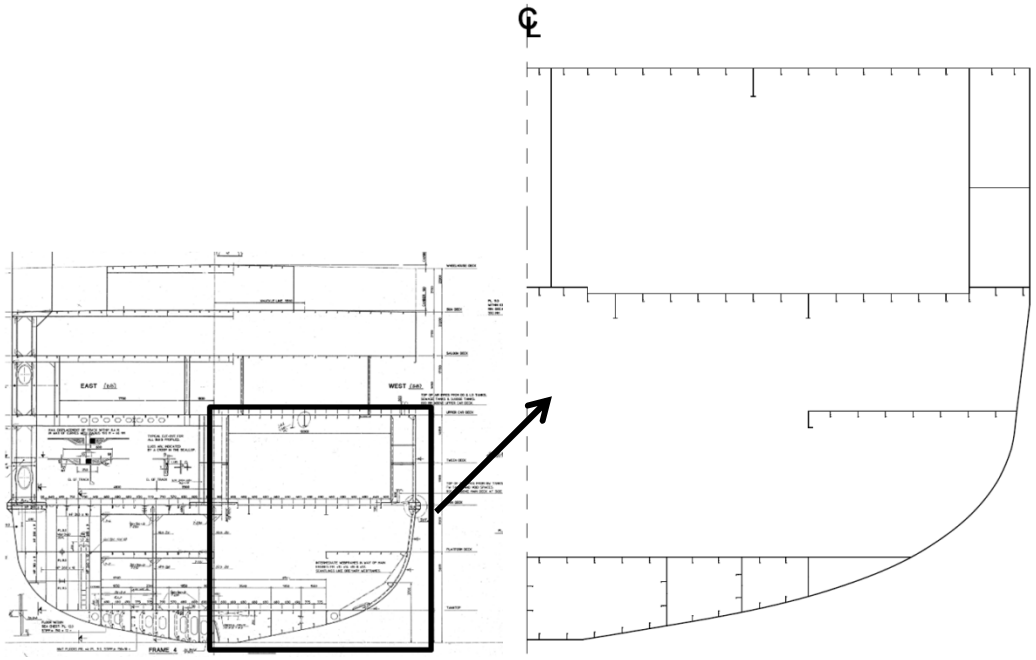

Figure 4: Elements considered for the calculation of the moment of inertia (up to the upper car deck)

Table 5: Midship moment of inertia up to the upper car deck

Midship moment of Inertia			
Calculated		[cm^4]	4.15e9

Calculation of Still Water and Wave Load Bending moments

Using the aforementioned moment of inertia in the regulation formulas the still water bending moment and wave load bending moment were calculated for both sagging and hogging conditions according to DNV's Rules for ships (Table 6). It should be pointed out that these values are the maximum design moments according to the regulations and not the ones that the ship is expected to encounter during its service. However it is common practice to use the design values for analyses when other data are not available as calculating the expected loading can be a challenging task.

Table 6: Calculated design Still water and Wave load bending moments

Still water moment calculation		
Mso		
Sagging	-270041.9842	kNm
	-270041984.2	kNmm
	-2.70042E+11	Nmm
Hogging	402008.2027	kNm
	402008202.7	kNmm
	4.02008E+11	Nmm

Wave load bending moment calculation		
Mwo		
Sagging	-474275.4175	kNm
	-474275417.5	kNmm
	-4.74275E+11	Nmm
Hogging	378093.6895	kNm
	378093689.5	kNmm
	3.78094E+11	Nmm

A simple estimate of the vertical deflection amidhips can be obtained assuming a prismatic hull with a constant bending moment which is the sum of the still water bending moment and the wave load moment for hogging and sagging respectively (Figure 5). With these assumptions we can employ the following formula:

$$\delta = R\left(1 - cos\frac{L}{2R}\right) \cong \frac{L^2}{8R} = \frac{L^2}{8}\kappa$$

Where L is the length of the ship, R is the radius of curvature and κ the curvature. Alternatively, using $M_s+M_w=EI_y\kappa$, the formula can be written as:

$$\delta = \frac{(M_s + M_w)L^2}{8EI_y}$$

$$\delta = R\left(1 - cos\frac{L}{2R}\right) \cong \frac{L^2}{8R} = \frac{L^2}{8}\kappa$$

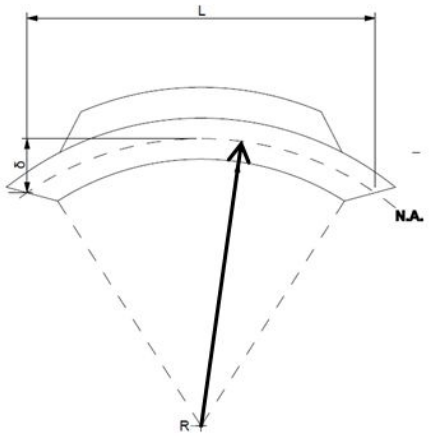

Figure 5: Hull Bending

Considering that the curvature is constant for the ship we can easily calculate the maximum deflection of the superstructure by substituting the superstructure's length in the previous formula [6]. Repeating these steps for both hogging and sagging conditions and superimposing the water bending moment to the wave load bending moment the deflections have been calculated (Figure 6).

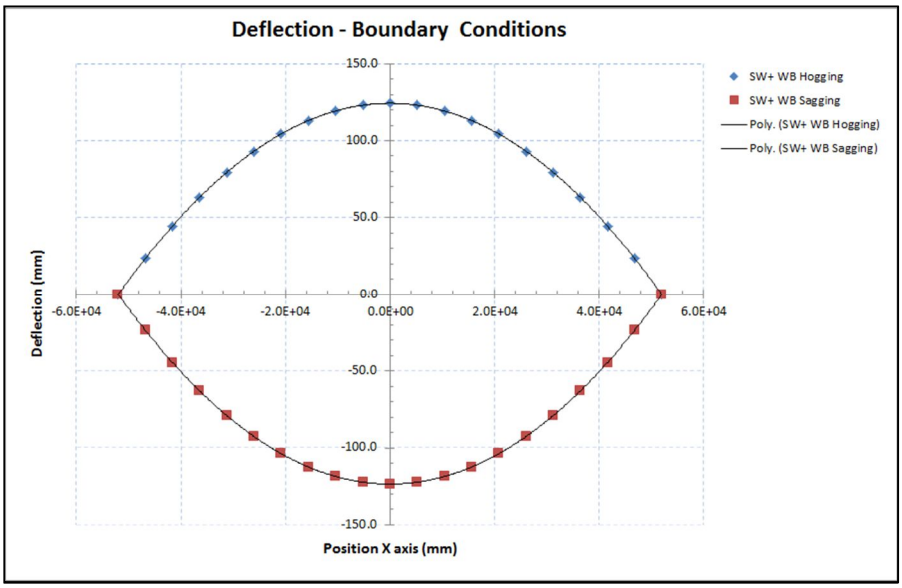

Figure 6: Superstructure deflections for Hogging and sagging

In this scenario it has been assumed that these deflections are directly acting on the bottom of the superstructure at the parts where structural continuity exists with the part below. In other words, the deflection variation along the superstructure length has been introduced as boundary conditions in the superstructure. This scenario represents the most conservative one as the superstructure is considered to be fully cooperative with the hull structure while at the same time the contribution of the structural elements of the superstructure to the midship section's moment of inertia has not been taken into consideration. The level of interaction varies in reality depending on the topological features of the superstructure an example is illustrated in Figure 7 below.

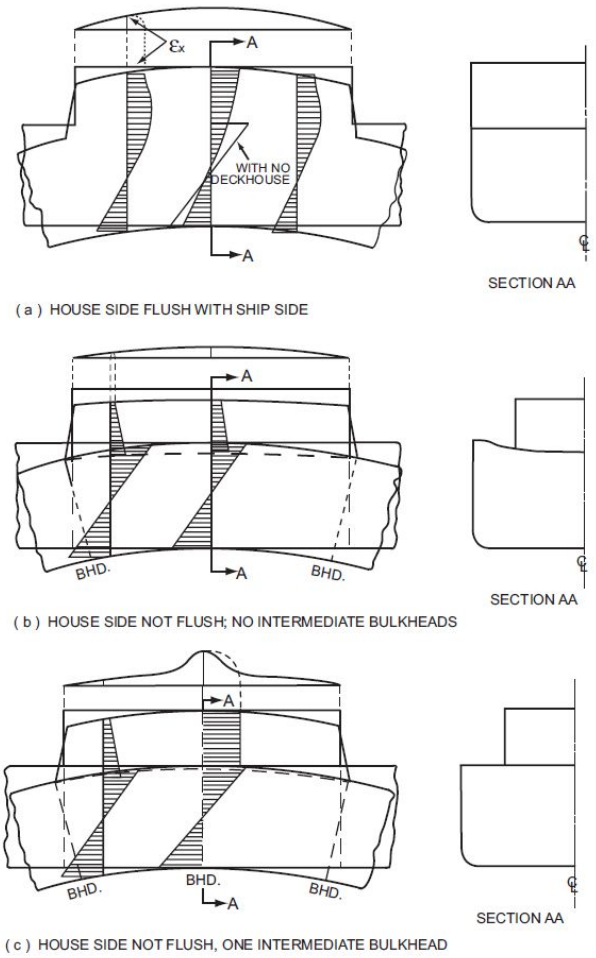

Figure 7: Interaction between Hull and superstructure [2]

2 Finite element modelling

2.1 Description of the finite element model

Simplifications to the real geometry were made to facilitate the creation of the finite element models. In addition the Mast and the funnel were not included as they are not considered as load bearing parts of the structure. The FE models were created using the commercial finite element program ABAQUS CAE. Conventional 4 node linear shell elements where used for the plating. Standard 2-node linear beam elements were used to model the supporting pillars between decks and the stiffeners in the transverse and longitudinal direction (Figure 8). For the composite case the ply lay-up and orientation were implemented using the composite layup feature and the composite stiffeners using the general meshed cross section feature [7]. The global element size was approximately 500mm. It must be noted at this point that the provided drawings were in some occasion conflicting and therefore there is an uncertainty factor introduced regardless of the simplification that were considered during modelling. The material properties and composite layup were in accordance to the ones described previously in this report.

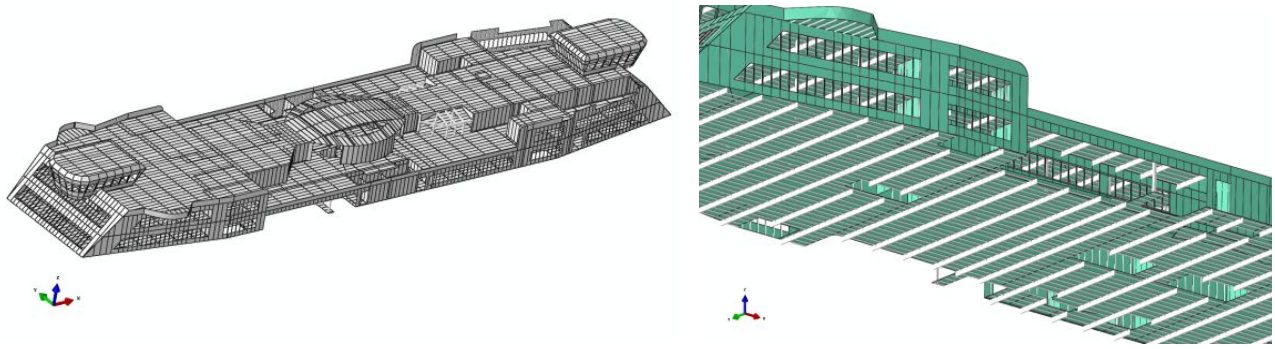

Figure 8: Superstructure FE model (left), steel decks' longitudinal and transverse stiffeners (right)

For the steel model all stiffeners and girders were modelled using the stringer options. For the composite model the stiffeners due to their shape and material composition the meshed cross section feature was used. More details about this feature can be found in the ABAQUS documentation. The geometrical and material details of the stiffeners are available in the general arrangement plan. All analyses were linear elastic ones.

2.2 Acting Loads and Boundary conditions

For the case where the superstructure is considered as non-contributing to the longitudinal strength only the local loads acting on the accommodation decks were considered. The loading was taken equal to the design load which is 0.35 t/m^2, when not directly calculated. For the alternative case, apart from the local load the calculated Hogging and Sagging displacements were imposed using the ABAQUS distributed analytical field option. The boundary conditions were imposed by considering the structural continuity of elements, such as bulkheads and pillars with the deck below the saloon deck (Figure 9). At this point it is reminded that the salon deck is identical and made out of steel for both the original and the retrofitted case.

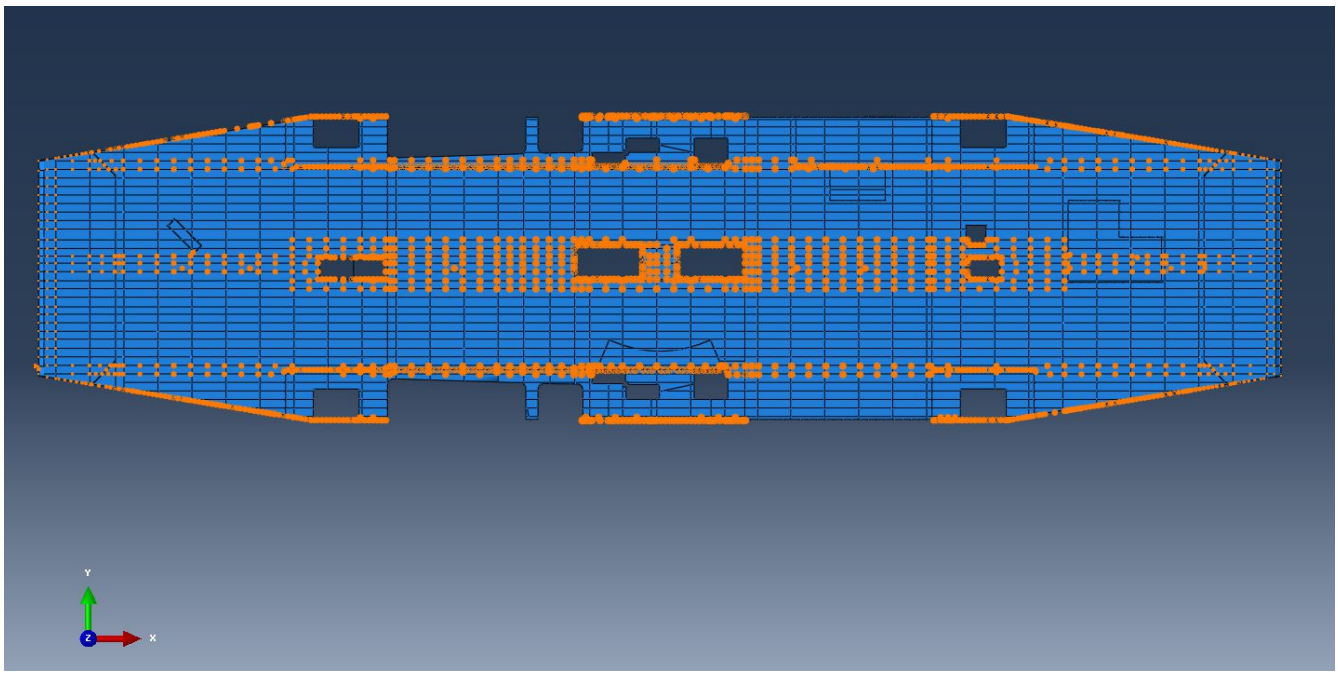

Figure 9: Regions of the steel saloon deck where the BCs are applied

The following cases (Table 7) based on the imposed boundary conditions were considered for each one of the two material configurations:

Table 7: Generated FE models

Material	**Applied boundary condition**		
Steel	Constrained	Hogging	Sagging
Composite	Constrained	Hogging	Sagging

2.3 Results & Discussion

For all cases the deflection was measured and compared. For the steel cases additionally the von Mises stress was plotted, while for the composite case the strain in the local coordinate system was deemed more suitable for the analysis of the results. As shell elements were used, which in the case of the composite structure consisted of multiple plies at different orientations, the figures of this report correspond to the minimum and maximum measured magnitudes regardless of the ply in which these are occuring through the shell thickness. (this feature is referred as envelope plot in ABAQUS). Due to the complexity and extent of the generated models representative results from the aforementioned load cases are presented in this report, namely the hogging cases and the non cooperating cases. The latter was selected to study the deflections caused solely by the acting local loads.

2.4 Steel and composite superstructures subjected to hogging

2.4.1 Steel Superstructure

As it can be seen in Figure 10 the global deflections acting on the superstructure follow the imposed boundary conditions starting from zero at the edge of the superstructure and reaching the maximum deflection at the middle of the superstructure's length.

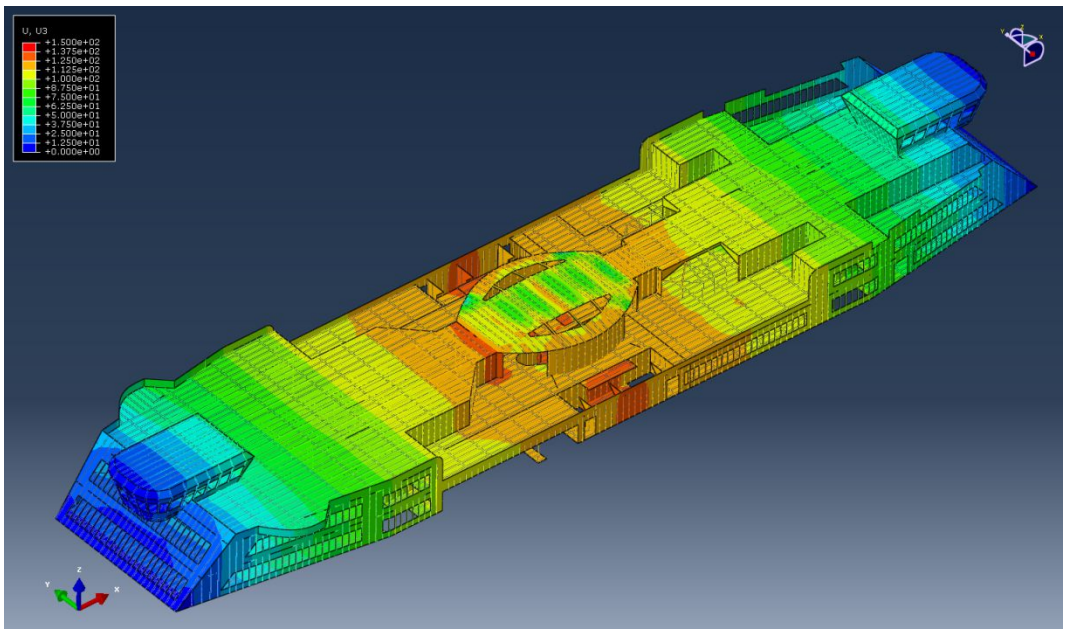

Figure 10: Displacement in the Z direction.

In Figures 11 to 13 the von Mises stress are plotted. The maximum stress value for the contour was chosen equal to 150 MPa. Results indicate that stress is generally considerably lower below 100 MPa despite the conservative approach that was considered for the hull superstructure interaction. The stress is higher at stress concentration points as expected and at the middle of the wheelhouse deck. The latter is attributed to the multiple openings at this area along with the fact that there is a large opening below.

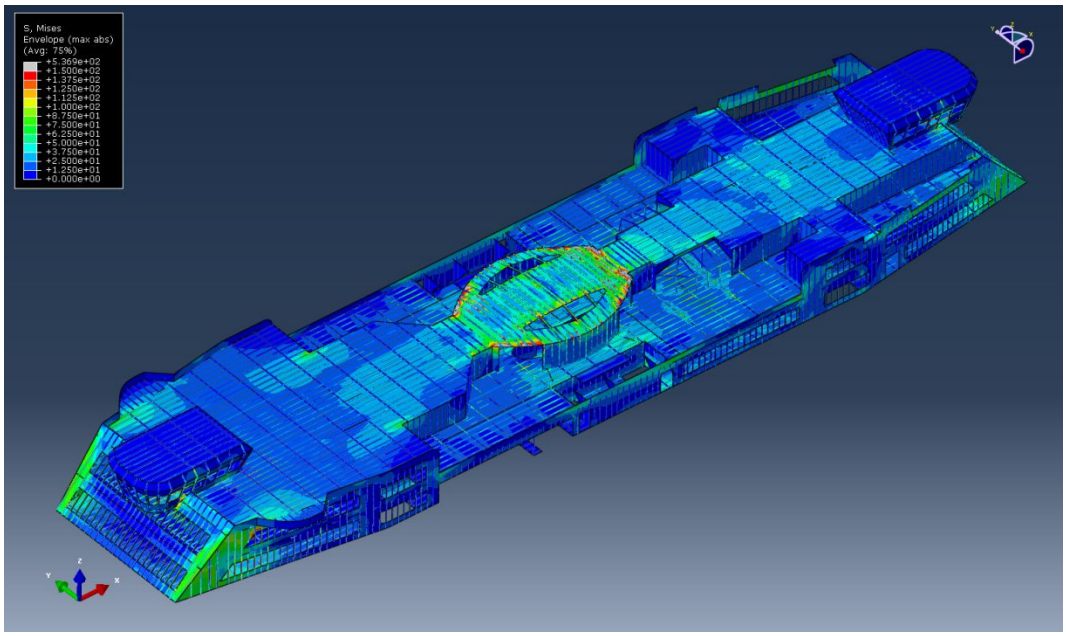

Figure 11: Von mises stress at the whole superstructure

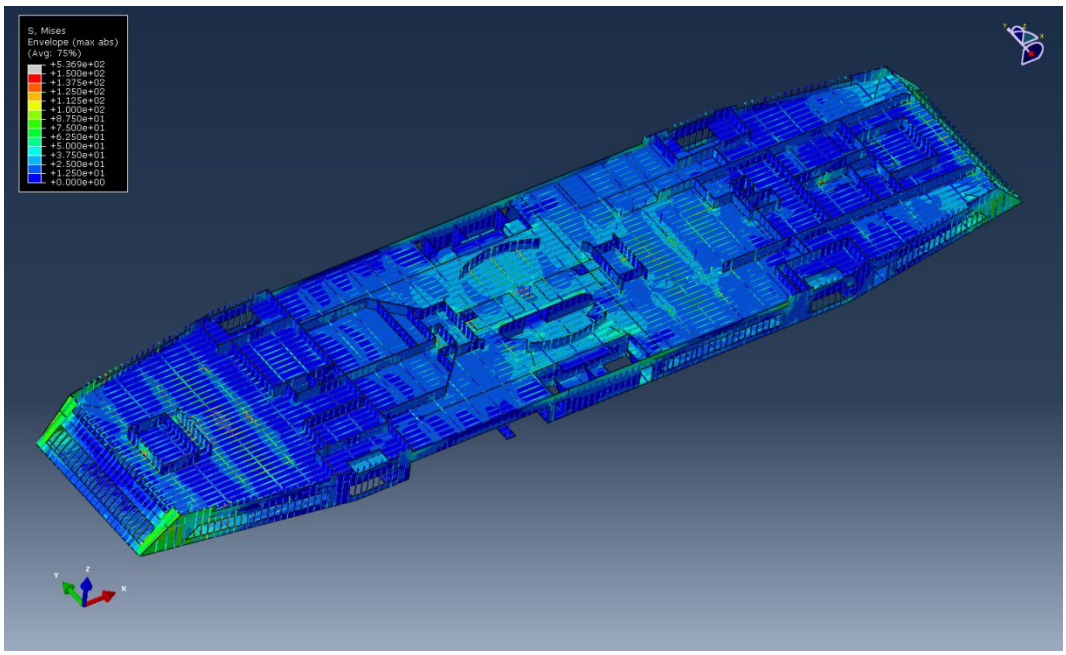

Figure 12: Von mises stress at the sun deck

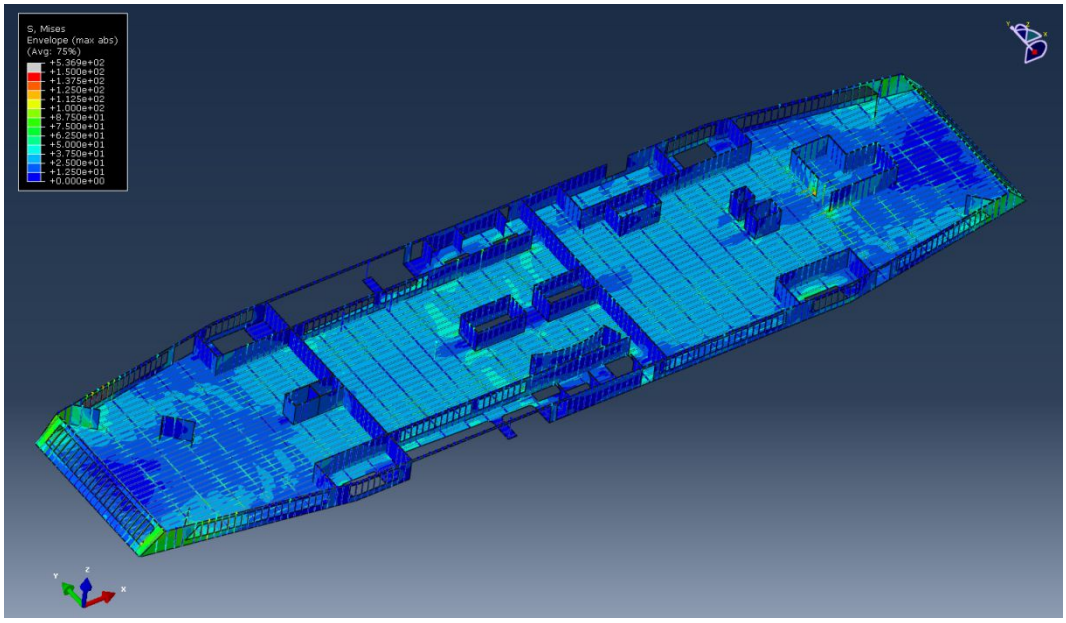

Figure 13: Von mises stress distribution at the saloon deck

2.4.2 Composite Superstructure

Given that the same deflections were applied in the composite superstructure the response of the structure is almost identical to the one exhibited by the steel superstructure (Figure 14). The maximum strain values before initiation of failure along with the relevant information for each sandwich structure are presented in detail at the Appendix.

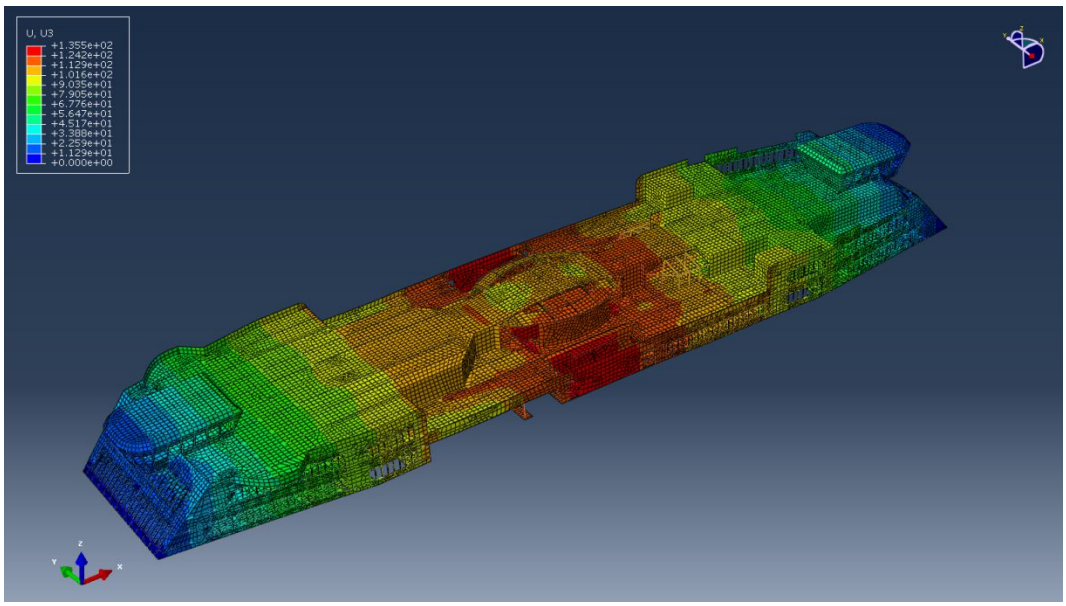

Figure 14: Displacement in the Z direction

The strain distribution in the local coordinate axis 1 and 2 are presented in Figures 15 to 18. At this point it is reminded that the saloon deck of the superstructure is made out of steel for both cases.

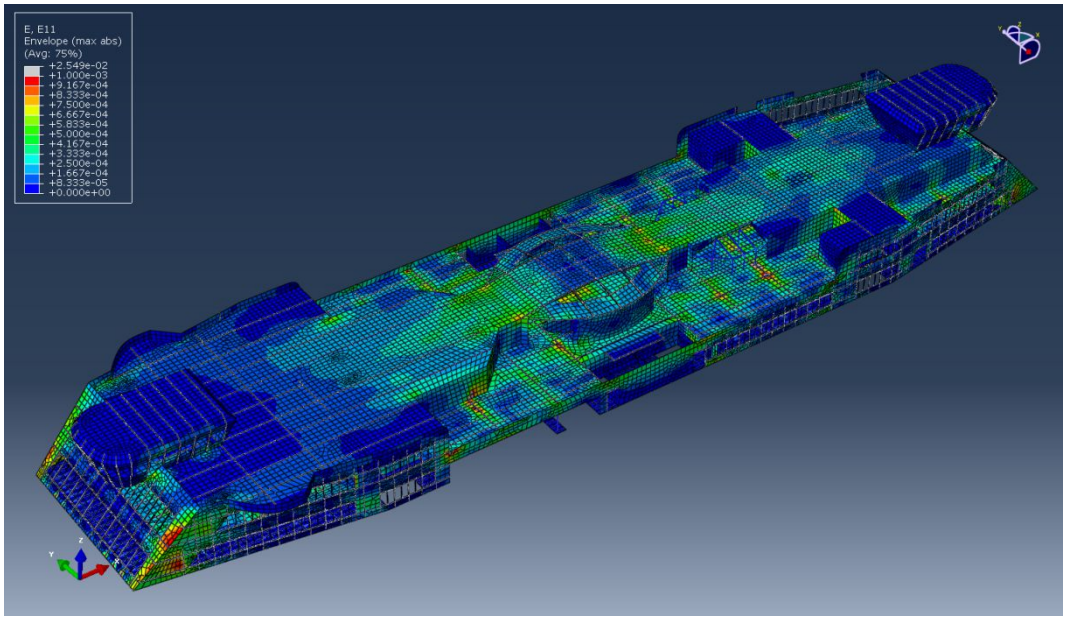

Figure 15: Envelop plot of E11 strains for the whole superstructure

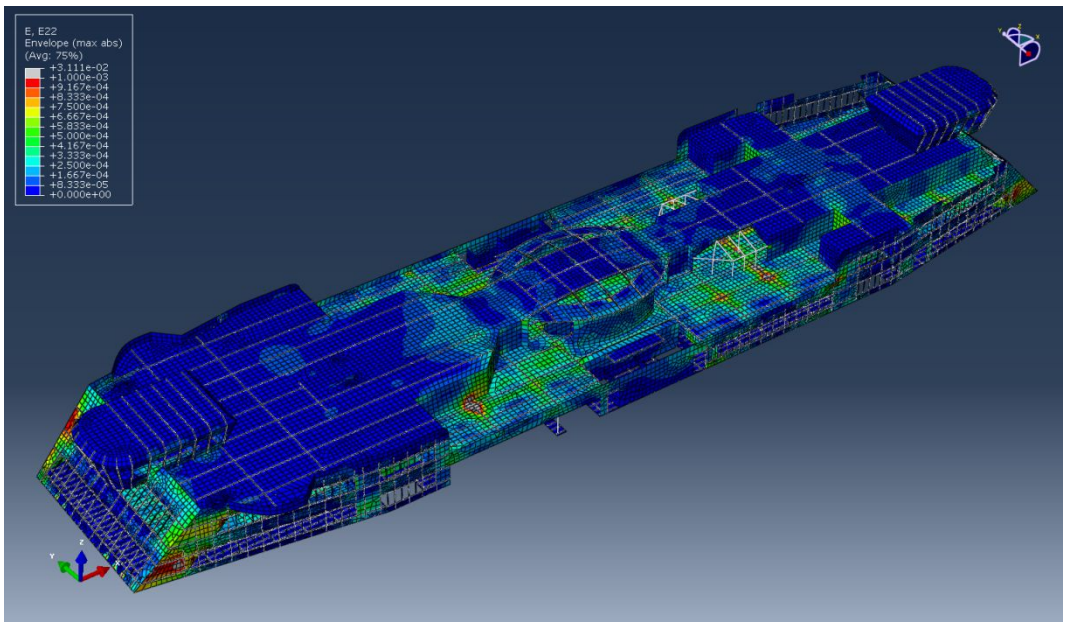

Figure 16: Envelop plot of E22 strains for the whole superstructure

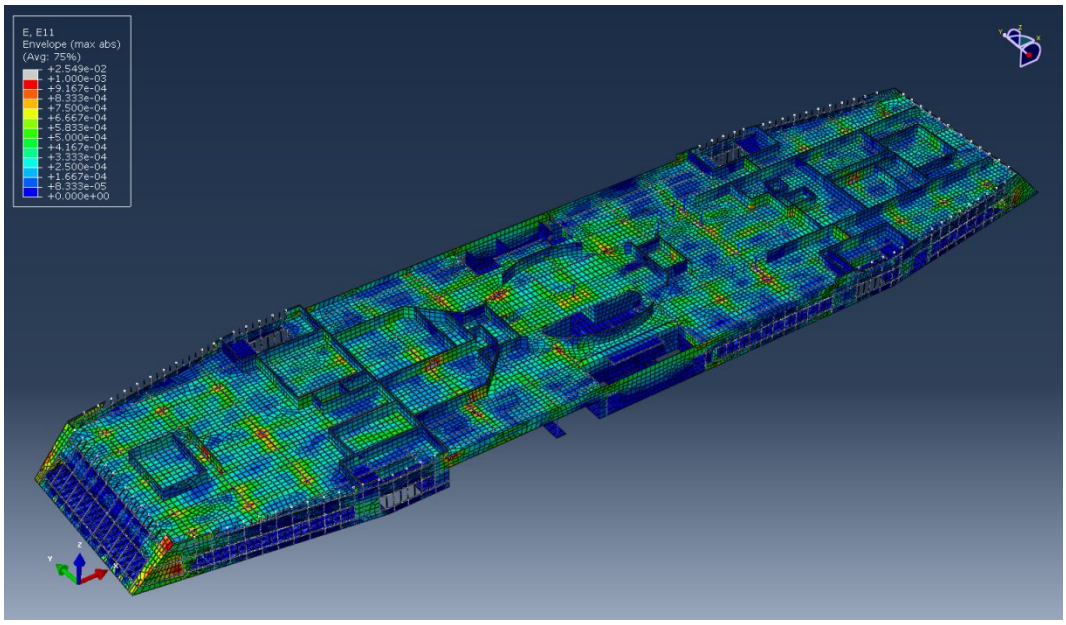

Figure 17: Envelop plot of E11 strains at the sun deck

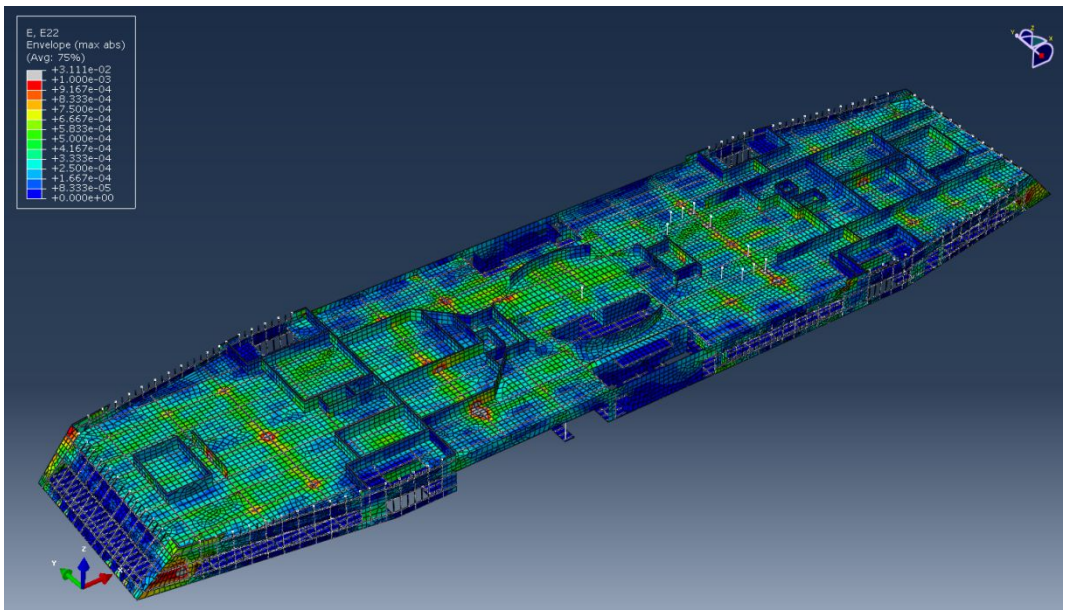

Figure 18: Envelop plot of E22 strains at the sun deck

For the composite case the strains were ranging from 0 to 0.1% for the major part of the superstructure. The maximum strains were exhibited at the face sheets. As in the steel structure at some points some mostly where pillars or sharp corners exist the strains are higher than the average. These strain concentrations were introduced to the analysis during the geometry simplification process. Submodelling introducing the precise geometry in combination with finer meshing is needed for the correct interpretation of stresses and strains at these points. However this was out of the scope of the present study.

2.5 Only local loads acting

For this case all degrees of freedom were constrained at the boundaries where structural continuity existed below the saloon deck. The imposed loading is 0.35 t/m^2 acting at the accommodation decks.

2.5.1 Steel Superstructure

The von Mises stress due to the local acting loads is below 50 MPa. Representative figures are presented in Figures 19 to 20

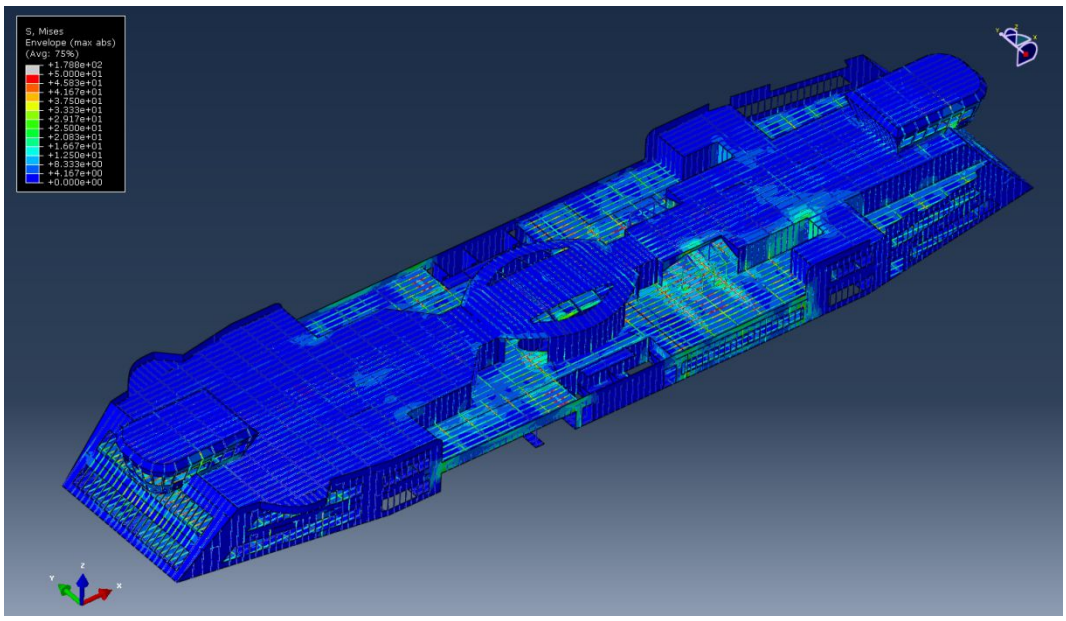

Figure 19: Von Mises stress

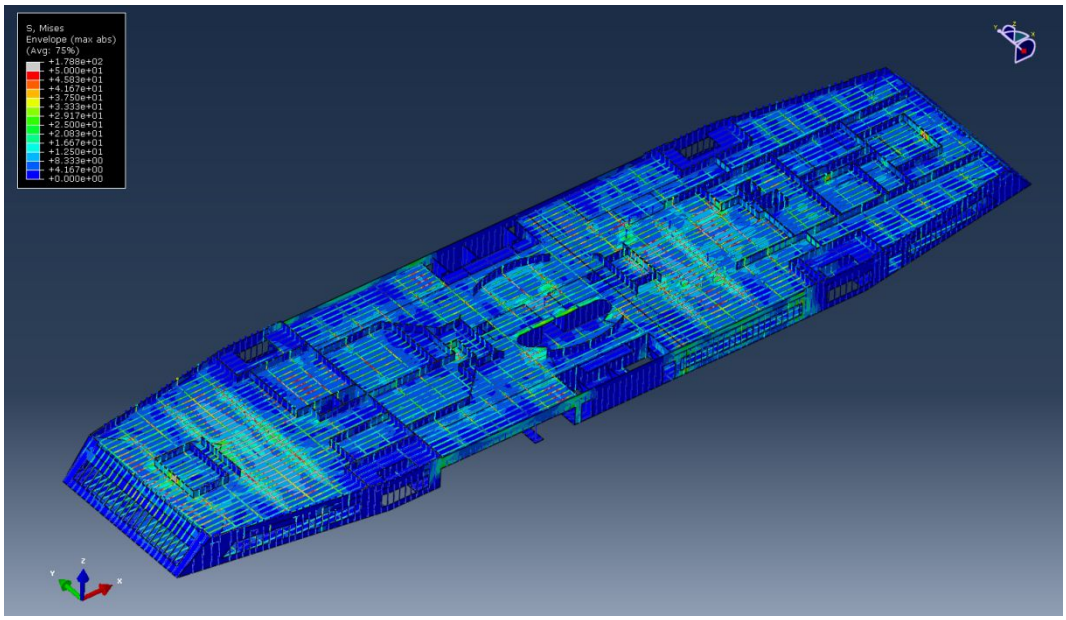

Figure 20: Von Mises stress at the sun deck

The deflections are presented in Figures 21 to 23. As it is depicted in the figures most of the superstructure does not deflect more than 10 mm. The maximum absolute deflection is around 16 mm and is localized at the fore end of the sun deck. This could be caused by the lack of supporting pillars as, as mentioned earlier, some of the details were not clearly depicted in the existing drawings.

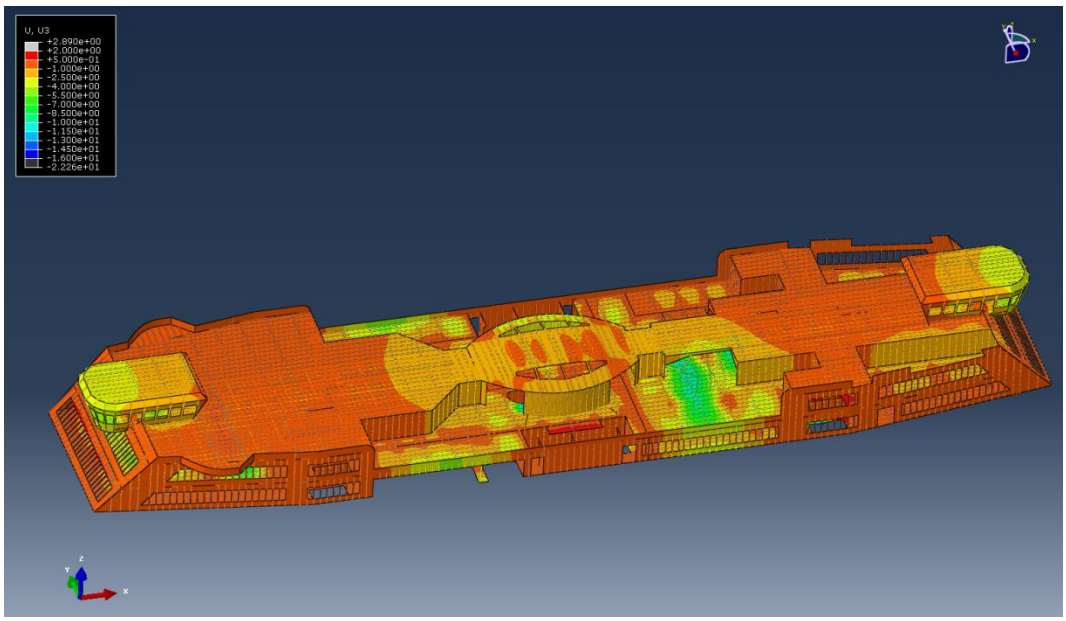

Figure 21: Displacement in the Z direction

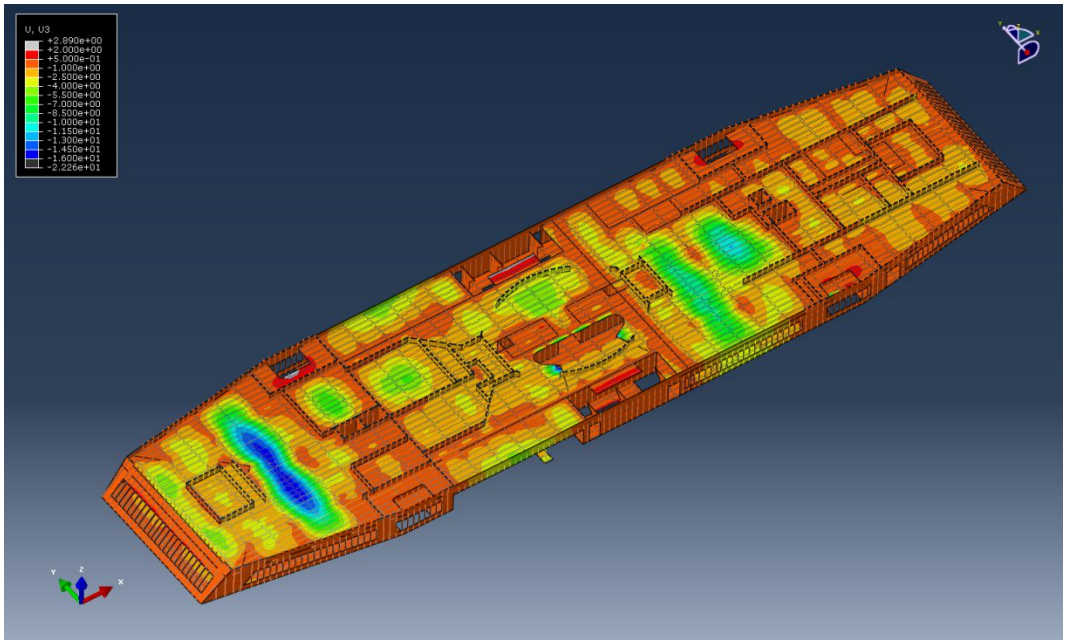

Figure 22: Displacement in the Z direction at the sun deck

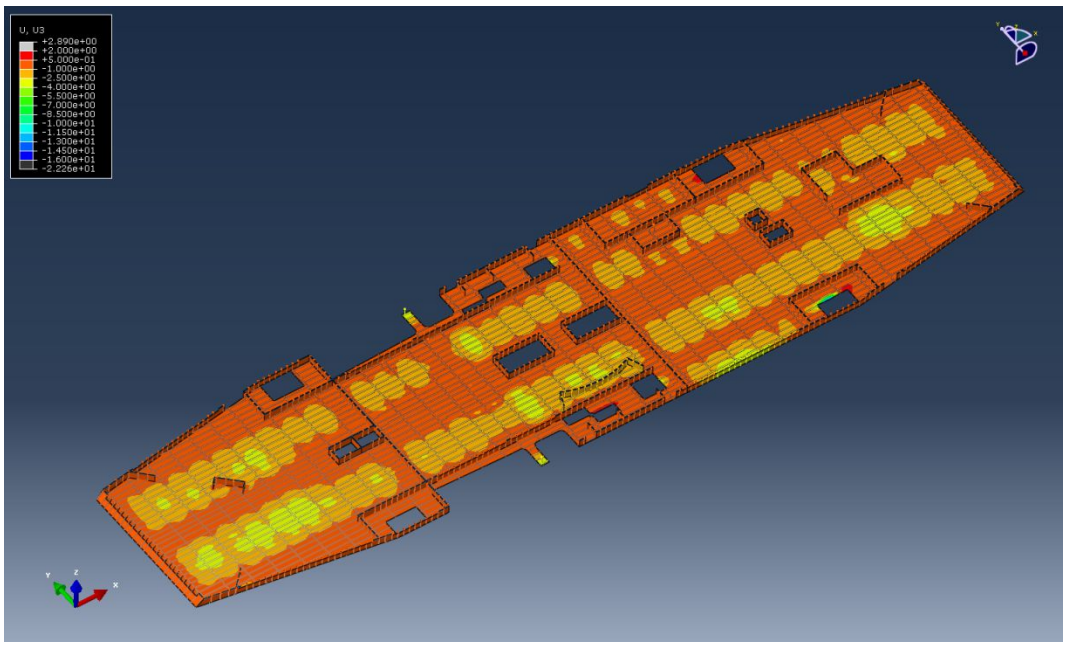

Figure 23: Displacement in the Z direction at the saloon deck

2.5.2 Composite Superstructure

Figures 24 to 25 depict the deflections of the composite superstructure. The deflections in the superstructure are slightly increased ranging up to 13 mm overall. The maximum deflections reach up to 30 mm at a few panels.

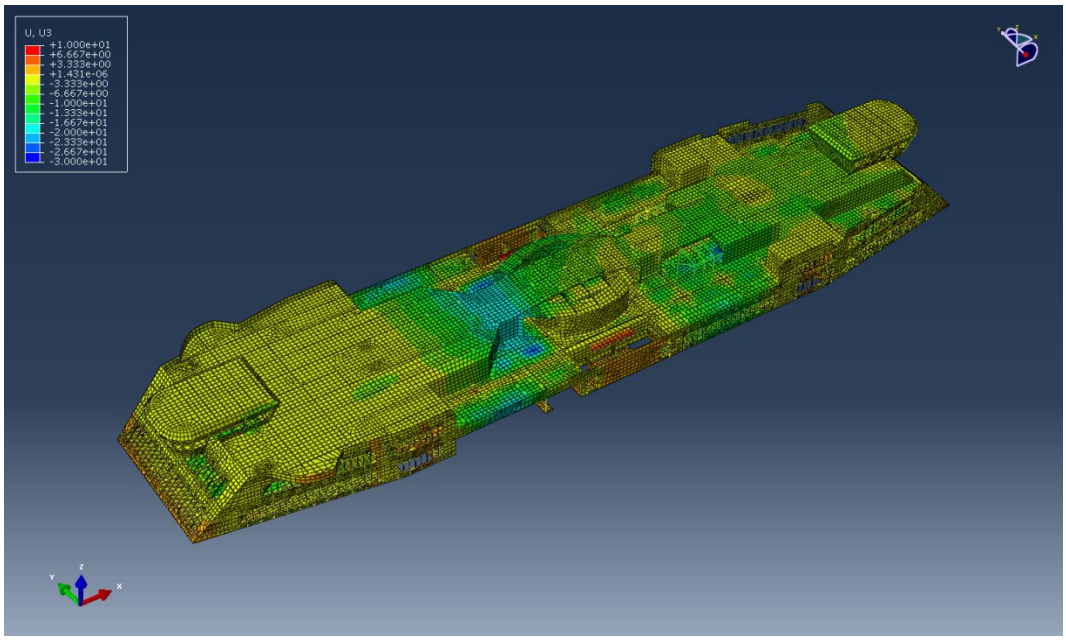

Figure 24: Displacement at the Z direction

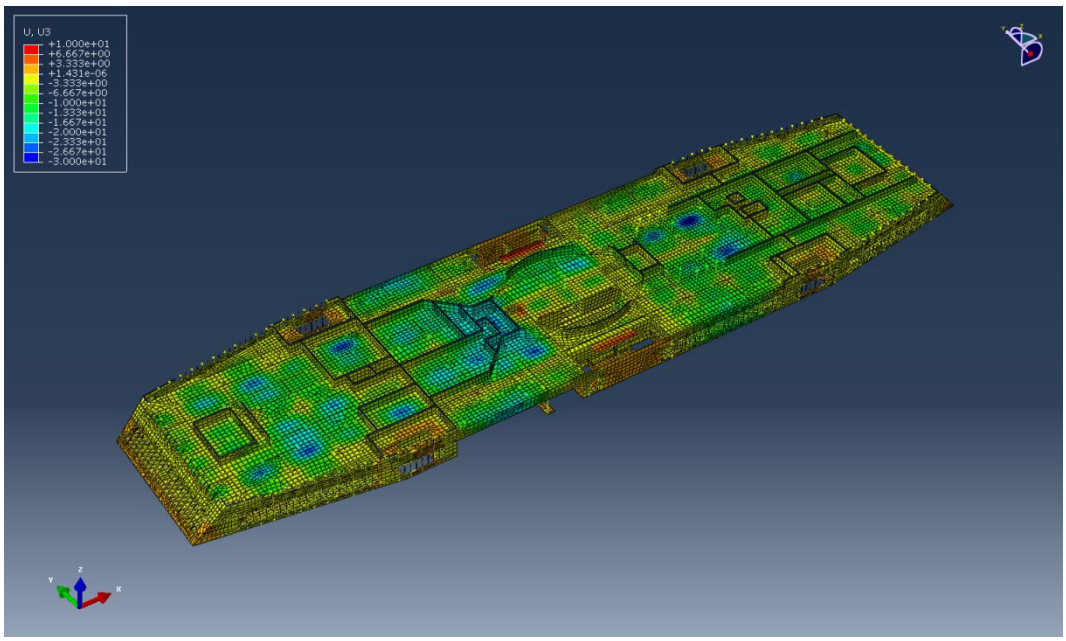

Figure 25: Displacement at the Z direction at the sun deck

The strains are depicted in Figures 26 to 30.

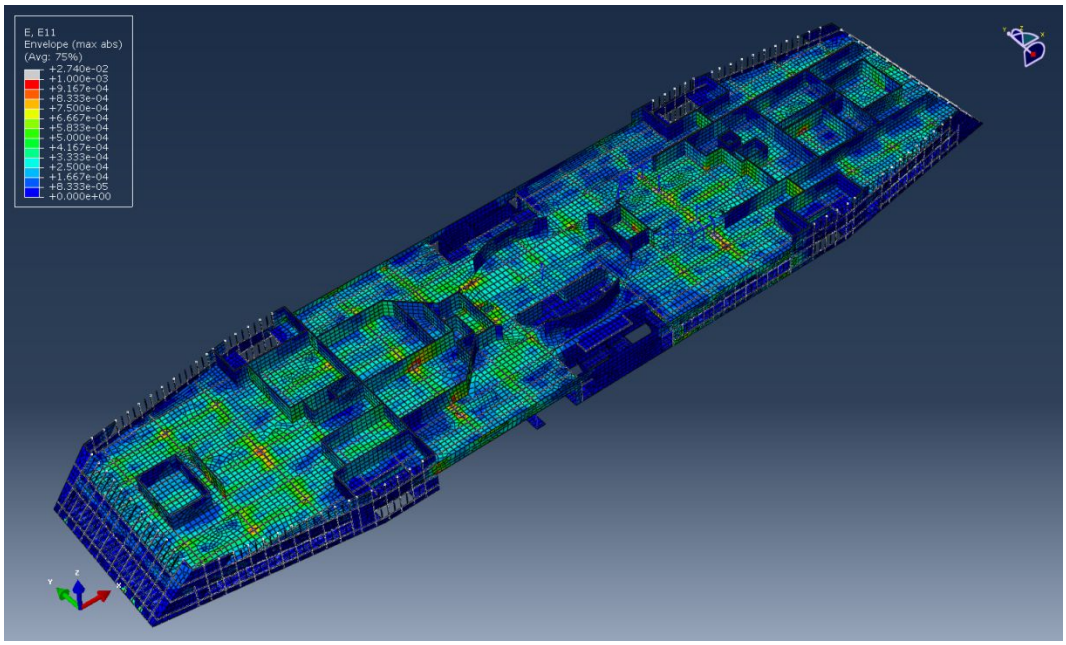

Figure 26: Envelop plot of E11 strains at the sun deck

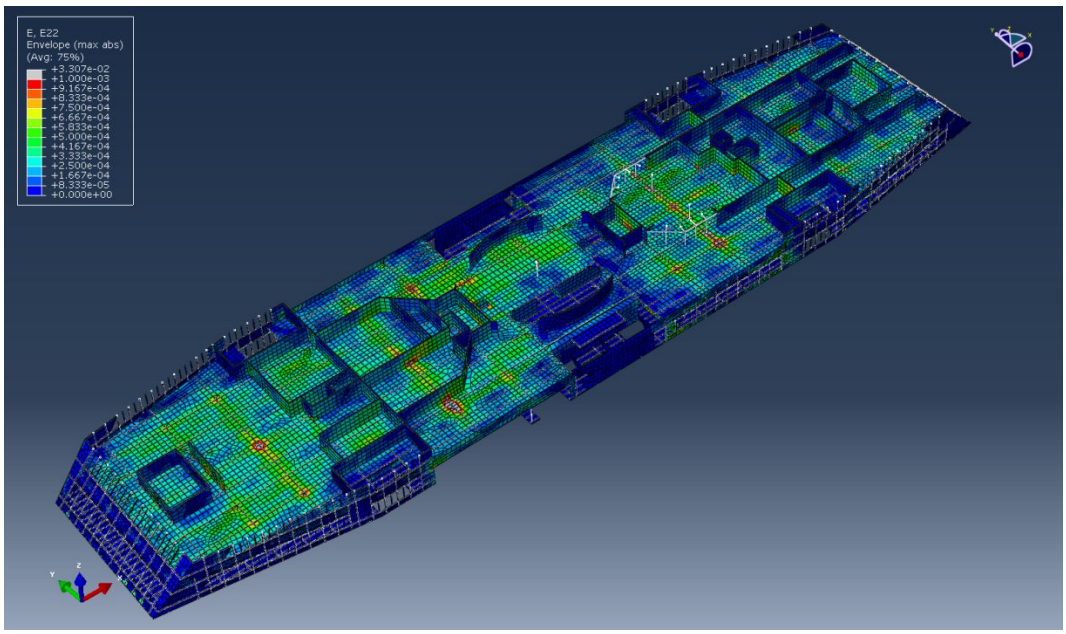

Figure 27: Envelop plot of E22 strains at the sun deck

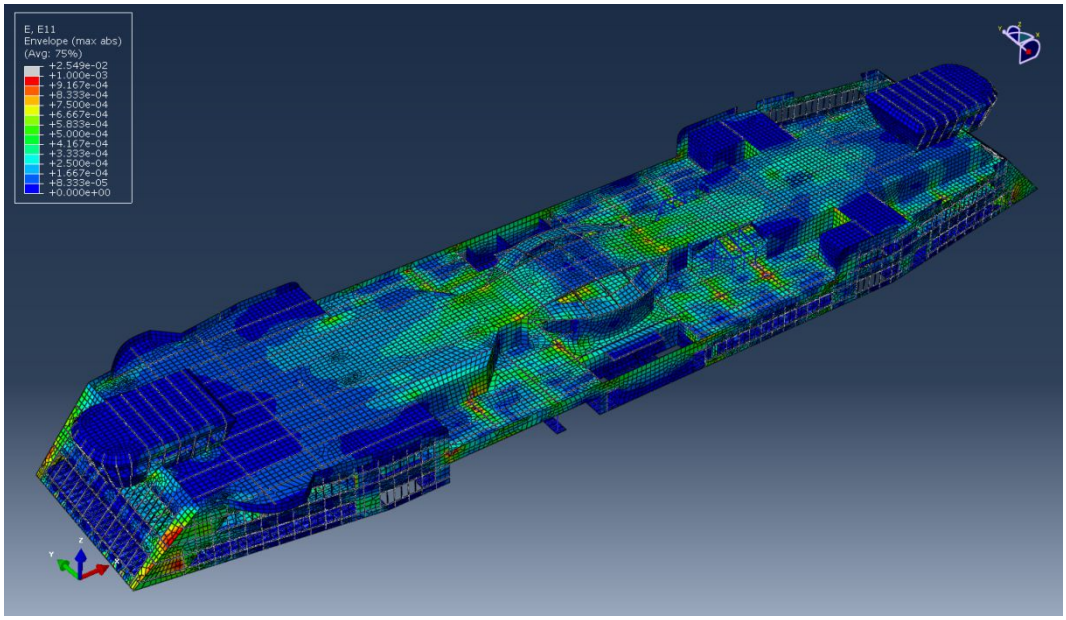

Figure 28: Envelop plot of E11 strains at the superstructure

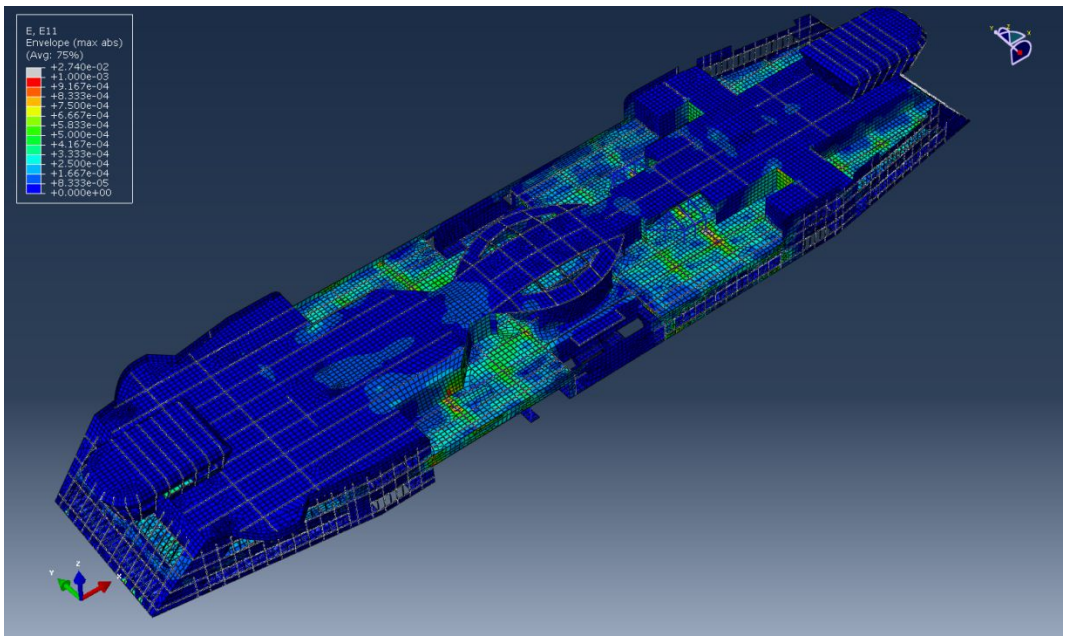

Figure 29: Envelop plot of E11 strains at the superstructure

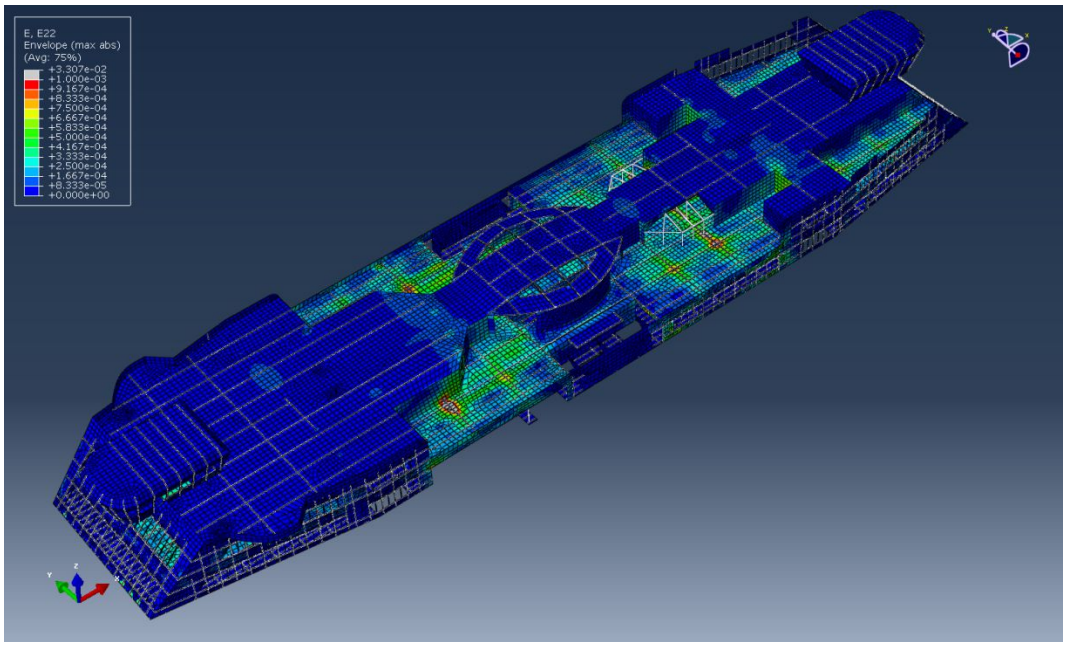

Figure 30: Envelop plot of E22 strains at the superstructure

An interesting observation for the composite superstructure can be made by comparing the structural response between the presented hogging case and the one where all the degrees of freedom are constrained. Due to the increased compliance compared to the steel case, the resulting strains at the superstructure are not significantly increased.

3 Conclusions

In this report the global structural response of a redesigned composite superstructure has been presented and compared to the global structural response of the existing steel superstructure considering the superstructure as a non-load bearing and load bearing part of the ship's structure respectively. Results indicate that the composite superstructure experienced significantly lower loading when subjected to the same loading conditions as the steel one, and that the global structural response of such a design does not represent an obstacle for the implementation of composites. Additionally the inherent versatility that characterizes composites along with their resistance to corrosion and fatigue can lead to more efficient vessels from a structural point of view. The main obstacles lie in the complexity associated with the regulatory approval and the lack of data from real applications on ships. However, classification societies are taking steps to gradually encompass composite materials in their regulations and to adopt a more standardized procedure for the evaluation and approval of composite designs. It is the authors' view that these developments, facilitating the design, acceptance and implementation of composites on SOLAS ships, will constitute composites an increasingly attractive alternative to metallic materials for secondary parts of ships

4 References

[1] D. J. Eyres, Ship Construction, 2012, Elsevier
[2] O. F. Hughes, J.k. Paik, Ship Structural Analysis, 2010, SNAME
[3] Det Norske Veritas, January 2014, 'DNV Rules for Classification of High Speed Light Craft and Naval Surface Craft'
[4] Det Norske Veritas, January 2014, 'DNV Rules for Classification of Ships'
[5] M. D. Jacobsen, N. Hjørnet, 2014, Private communication
[6] J.J. Jensen, 2001, 'Load and global response of ships', *Elsevier Ocean Engineering Series Volume 4, Pages 1-337*
[7] 'ABAQUS Analysis User's Manual', Version 6.14-2, 2014 Dassault Systèmes Simulia Corp. Providence: RI, USA

5 Appendix

Project: Kompas
Laminate: Structural bkh, P100

26-maj-15
09:06

LAYER		Panel	Zero Curv'e	Upper Skin	Lower Skin		ABD MATRIX		
1	1 x XE905 Ehfv @ 0°	IN-PLANE							
2	1 x XE905 Ehfv @ 45°	Longitudinal Modulus	1.250E+03	1.250E+03	1.648E+04	1.648E+04	[Mpa]		
3	40 mm P100	Transverse Modulus	1.250E+03	1.250E+03	1.648E+04	1.648E+04	[Mpa]	A 11 6.003E+04	[N/mm]
4	1 x XE905 Ehfv @ 45°	Poissons Ratio - Vxy	0.323	0.323	0.317	0.317		A 12 1.940E+04	
5	1 x XE905 Ehfv @ 0°	- Vyx	0.323	0.323	0.317	0.317		A 16 0.000E+00	
6		Shear Modulus	4.651E+02	4.651E+02	6.261E+03	6.261E+03	[Mpa]	A 22 6.003E+04	
7		FLEXURAL						A 26 0.000E+00	
8		Longitudinal Modulus	3.351E+03				[Mpa]	A 66 2.001E+04	
9		Transverse Modulus	3.351E+03				[Mpa]		
10		STIFFNESSES							
11		Longitudinal Stiffness - E * T	5.376E+04	5.376E+04	2.487E+04	2.487E+04	[N/mm]	B 11 -3.492E-10	[N]
12		Transverse Stiffness - E * T	5.376E+04	5.376E+04	2.487E+04	2.487E+04	[N/mm]	B 12 -2.474E-10	
13		Shear Stiffness - G * T	2.001E+04	2.001E+04	9.443E+03	9.443E+03	[N/mm]	B 16 0.000E+00	
14					Asymmetric Laminate			B 22 -3.492E-10	
15		Longitudinal Bending - EI	2.223E+07		4.058E+03	4.058E+03	[N mm^2/mm]	B 26 0.000E+00	
16		Transverse Bending - EI	2.223E+07		4.058E+03	4.058E+03	[N mm^2/mm]	B 66 -2.619E-10	
17		Torsional - GJ	8.136E+06		1.437E+03	1.437E+03	[N mm^2/mm]		
18		NEUTRAL AXIS			Asymmetric Laminate				
19		Longitudinal Bending	0.00	0.00	0.14	-0.14	[mm]	D 11 2.460E+07	[N.mm]
20		Transverse Bending	0.00	0.00	0.14	-0.14	[mm]	D 12 7.641E+06	
21		LAMINATE						D 16 0.000E+00	
22		Weight	9.85		2.73	2.73	[kg/m^2]	D 22 2.460E+07	
23		Core Thickness	40		0	0	[mm]	D 26 0.000E+00	
24		Total Thickness	43.02		1.51	1.51	[mm]	D 66 8.136E+06	
25									

	ALLOWABLE MOMENTS - CYLINDRICAL BENDING [N mm/mm width]							
	LONGITUDINAL MOMENT				TRANSVERSE MOMENT			
Compressive:	Top Skin		Bottom Skin		Top Skin		Bottom Skin	
	Moment	Ply	Moment	Ply	Moment	Ply	Moment	Ply
Longitudinal - Fibre Failure	13727	1	13727	5	28451	2	28451	4
- Microcrack	5147	5	5147	1	10669	4	10669	2
Transverse - Resin/Fibre Fail	28451	2	28451	4	13727	1	13727	5
- Resin/Microcrack	10669	4	10669	2	5147	5	5147	1
Resin Shear	17900	2	17900	2	17900	2	17900	2
Skin Wrinkling	9506		9506		9506		9506	

BENDING - PLY FAILURE SEQUENCE (CYLINDRICAL BENDING)

Failure Sequence	Failure Moment [N.mm/mm]	Ply Number	Ply	Failure Strain [%]	Failure Mode
LONGITUDINAL - Top Skin Compression					
	9506				Skin Wrinkling
1	5147	5	1 x XE905 Ehfv @ 0°	0.45	Longitudinal Microcrack
2	10669	4	1 x XE905 Ehfv @ 45°	0.45	Longitudinal Microcrack
3	10669	4	1 x XE905 Ehfv @ 45°	0.45	Transverse Resin/Microcrack
4	13727	1	1 x XE905 Ehfv @ 0°	-1.20	Longitudinal Fibre
5	17158	5	1 x XE905 Ehfv @ 0°	1.50	Longitudinal Fibre
6	17900	2	1 x XE905 Ehfv @ 45°	1.51	Resin Shear
LONGITUDINAL - Bottom Skin Compression					
	9506				Skin Wrinkling
1	5147	1	1 x XE905 Ehfv @ 0°	0.45	Longitudinal Microcrack
2	10669	2	1 x XE905 Ehfv @ 45°	0.45	Longitudinal Microcrack
3	10669	2	1 x XE905 Ehfv @ 45°	0.45	Transverse Resin/Microcrack
4	13727	5	1 x XE905 Ehfv @ 0°	-1.20	Longitudinal Fibre
5	17158	1	1 x XE905 Ehfv @ 0°	1.50	Longitudinal Fibre
6	17900	2	1 x XE905 Ehfv @ 45°	1.51	Resin Shear
TRANSVERSE - Top Skin Compression					
	9506				Skin Wrinkling
1	5147	5	1 x XE905 Ehfv @ 0°	0.45	Transverse Resin/Microcrack
2	10669	4	1 x XE905 Ehfv @ 45°	0.45	Transverse Resin/Microcrack
3	10669	4	1 x XE905 Ehfv @ 45°	0.45	Longitudinal Microcrack
4	13727	1	1 x XE905 Ehfv @ 0°	-1.20	Transverse Resin/Fibre
5	17158	5	1 x XE905 Ehfv @ 0°	1.50	Transverse Resin/Fibre
6	17900	2	1 x XE905 Ehfv @ 45°	1.51	Resin Shear
TRANSVERSE - Bottom Skin Compression					
	9506				Skin Wrinkling
1	5147	1	1 x XE905 Ehfv @ 0°	0.45	Transverse Resin/Microcrack
2	10669	2	1 x XE905 Ehfv @ 45°	0.45	Transverse Resin/Microcrack
3	10669	2	1 x XE905 Ehfv @ 45°	0.45	Longitudinal Microcrack
4	13727	5	1 x XE905 Ehfv @ 0°	-1.20	Transverse Resin/Fibre
5	17158	1	1 x XE905 Ehfv @ 0°	1.50	Transverse Resin/Fibre
6	17900	2	1 x XE905 Ehfv @ 45°	1.51	Resin Shear

Figure A1: Bulkhead panel calculations

Project: Kompas
Laminate: Sun Deck P100

26-maj-15
09:01

LAYER		Panel	Zero Curv'e	Upper Skin	Lower Skin		ABD MATRIX		
1	1 x WRE602 Ehfv @ 0°	IN-PLANE							
2	1 x XE905 Ehfv @ 0°	Longitudinal Modulus	1.766E+03	1.786E+03	1.868E+04	1.824E+04	[Mpa]		
3	1 x XE905 Ehfv @ 45°	Transverse Modulus	1.766E+03	1.786E+03	1.868E+04	1.824E+04	[Mpa]	A 11	1.043E+05 [N/mm]
4	1 x XE905 Ehfv @ 0°	Poissons Ratio - Vxy	0.243	0.240	0.220	0.244		A 12	2.507E+04
5	50 mm P100	- Vyx	0.243	0.240	0.220	0.244		A 16	0.000E+00
6	1 x XE905 Ehfv @ 0°	Shear Modulus	4.812E+02	4.828E+02	4.836E+03	5.190E+03	[Mpa]	A 22	1.043E+05
7	1 x XE905 Ehfv @ 45°	FLEXURAL						A 26	0.000E+00
8	1 x XE905 Ehfv @ 0°	Longitudinal Modulus	4.652E+03				[Mpa]	A 66	2.657E+04
9		Transverse Modulus	4.652E+03				[Mpa]		
10		STIFFNESSES							
11		Longitudinal Stiffness - E * T	9.721E+04	9.832E+04	5.188E+04	4.126E+04	[N/mm]	B 11	-2.660E+05 [N]
12		Transverse Stiffness - E * T	9.721E+04	9.832E+04	5.188E+04	4.126E+04	[N/mm]	B 12	-2.909E+04
13		Shear Stiffness - G * T	2.648E+04	2.657E+04	1.343E+04	1.174E+04	[N/mm]	B 16	0.000E+00
14					Asymmetric Laminate			B 22	-2.660E+05
15		Longitudinal Bending - EI	6.464E+07		3.654E+04	2.019E+04	[N mm^2/mm]	B 26	0.000E+00
16		Transverse Bending - EI	6.464E+07		3.654E+04	2.019E+04	[N mm^2/mm]	B 66	-3.958E+04
17		Torsional - GJ	1.753E+07		6.054E+03	3.173E+03	[N mm^2/mm]		
18		NEUTRAL AXIS			Asymmetric Laminate				
19		Longitudinal Bending	2.72	0.00	0.02	0.00	[mm]	D 11	6.911E+07 [N.mm]
20		Transverse Bending	2.72	0.00	0.02	0.00	[mm]	D 12	1.608E+07
21		LAMINATE						D 16	0.000E+00
22		Weight	14.60		5.01	4.09	[kg/m^2]	D 22	6.911E+07
23		Core Thickness	50		0	0	[mm]	D 26	0.000E+00
24		Total Thickness	55.04		2.78	2.26	[mm]	D 66	1.759E+07

Zero curvature for in-plane moduli, asymmetric laminate for bending

ALLOWABLE MOMENTS - CYLINDRICAL BENDING [N mm/mm width]

	LONGITUDINAL MOMENT				TRANSVERSE MOMENT			
Compressive:	Top Skin		Bottom Skin		Top Skin		Bottom Skin	
	Moment	Ply	Moment	Ply	Moment	Ply	Moment	Ply
Longitudinal - Fibre Failure	33692	2	27229	8	68507	3	56536	7
- Microcrack	10211	8	12373	1	21201	7	25690	3
Transverse - Resin/Fibre Fail	68507	3	56536	7	33692	2	27229	8
- Resin/Microcrack	21201	7	25690	3	10211	8	12373	1
Resin Shear	34723	7	34723	7	34723	7	34723	7
Skin Wrinkling	20626		20688		20626		20688	

BENDING - PLY FAILURE SEQUENCE (CYLINDRICAL BENDING)

Failure Sequence	Failure Moment [N.mm/mm]	Ply Number	Ply	Failure Strain [%]	Failure Mode
LONGITUDINAL - Top Skin Compression					
	20626				Skin Wrinkling
1	10211	8	1 x XE905 Ehfv @ 0°	0.45	Longitudinal Microcrack
2	10748	6	1 x XE905 Ehfv @ 0°	0.45	Longitudinal Microcrack
3	21201	7	1 x XE905 Ehfv @ 45°	0.45	Longitudinal Microcrack
4	21201	7	1 x XE905 Ehfv @ 45°	0.45	Transverse Resin/Microcrack
5	33692	2	1 x XE905 Ehfv @ 0°	-1.20	Longitudinal Fibre
6	34036	8	1 x XE905 Ehfv @ 0°	1.50	Longitudinal Fibre
LONGITUDINAL - Bottom Skin Compression					
	20688				Skin Wrinkling
1	12373	1	1 x WRE602 Ehfv @ 0°	0.45	Longitudinal Microcrack
2	12634	2	1 x XE905 Ehfv @ 0°	0.45	Longitudinal Microcrack
3	13468	4	1 x XE905 Ehfv @ 0°	0.45	Longitudinal Microcrack
4	25690	3	1 x XE905 Ehfv @ 45°	0.45	Longitudinal Microcrack
5	25690	3	1 x XE905 Ehfv @ 45°	0.45	Transverse Resin/Microcrack
6	27229	8	1 x XE905 Ehfv @ 0°	-1.20	Longitudinal Fibre
TRANSVERSE - Top Skin Compression					
	20626				Skin Wrinkling
1	10211	8	1 x XE905 Ehfv @ 0°	0.45	Transverse Resin/Microcrack
2	10748	6	1 x XE905 Ehfv @ 0°	0.45	Transverse Resin/Microcrack
3	21201	7	1 x XE905 Ehfv @ 45°	0.45	Transverse Resin/Microcrack
4	21201	7	1 x XE905 Ehfv @ 45°	0.45	Longitudinal Microcrack
5	33692	2	1 x XE905 Ehfv @ 0°	-1.20	Transverse Resin/Fibre
6	34036	8	1 x XE905 Ehfv @ 0°	1.50	Transverse Resin/Fibre
TRANSVERSE - Bottom Skin Compression					
	20688				Skin Wrinkling
1	12373	1	1 x WRE602 Ehfv @ 0°	0.45	Transverse Resin/Microcrack
2	12634	2	1 x XE905 Ehfv @ 0°	0.45	Transverse Resin/Microcrack
3	13468	4	1 x XE905 Ehfv @ 0°	0.45	Transverse Resin/Microcrack
4	25690	3	1 x XE905 Ehfv @ 45°	0.45	Transverse Resin/Microcrack
5	25690	3	1 x XE905 Ehfv @ 45°	0.45	Longitudinal Microcrack
6	27229	8	1 x XE905 Ehfv @ 0°	-1.20	Transverse Resin/Fibre

Figure A2: Sun Deck calculations

Project: Kompas
Laminate: Superstructure P100

26-maj-15
09:04

LAYER		Panel	Zero Curv'e	Upper Skin	Lower Skin		ABD MATRIX		
1	1 x WRE602 Ehfv @ 0°	IN-PLANE							
2	1 x XE905 Ehfv @ 0°	Longitudinal Modulus	1.963E+03	1.990E+03	1.974E+04	1.954E+04	[Mpa]		
3	1 x XE450 Ehfv @ 45°	Transverse Modulus	1.963E+03	1.990E+03	1.974E+04	1.954E+04	[Mpa]	A 11	9.148E+04 [N/mm]
4	1 x XE905 Ehfv @ 0°	Poissons Ratio - Vxy	0.195	0.193	0.175	0.190		A 12	1.763E+04
5	40 mm P100	- Vyx	0.195	0.193	0.175	0.190		A 16	0.000E+00
6	1 x XE905 Ehfv @ 0°	Shear Modulus	4.257E+02	4.287E+02	4.087E+03	4.309E+03	[Mpa]	A 22	9.148E+04
7	1 x XE450 Ehfv @ 45°	FLEXURAL						A 26	0.000E+00
8	1 x XE905 Ehfv @ 0°	Longitudinal Modulus	5.156E+03				[Mpa]	A 66	1.898E+04
9		Transverse Modulus	5.156E+03				[Mpa]		
10		STIFFNESSES							
11		Longitudinal Stiffness - E * T	8.690E+04	8.808E+04	4.719E+04	3.667E+04	[N/mm]	B 11	-2.120E+05 [N]
12		Transverse Stiffness - E * T	8.690E+04	8.808E+04	4.719E+04	3.667E+04	[N/mm]	B 12	-2.405E+04
13		Shear Stiffness - G * T	1.885E+04	1.898E+04	9.772E+03	8.085E+03	[N/mm]	B 16	0.000E+00
14					Asymmetric Laminate			B 22	-2.120E+05
15		Longitudinal Bending - EI	3.727E+07		2.353E+04	1.165E+04	[N mm^2/mm]	B 26	0.000E+00
16		Transverse Bending - EI	3.727E+07		2.353E+04	1.165E+04	[N mm^2/mm]	B 66	-3.245E+04
17		Torsional - GJ	7.995E+06		3.737E+03	1.705E+03	[N mm^2/mm]		
18		NEUTRAL AXIS			Asymmetric Laminate				
19		Longitudinal Bending	2.39	0.00	0.01	0.00	[mm]	D 11	3.911E+07 [N.mm]
20		Transverse Bending	2.39	0.00	0.01	0.00	[mm]	D 12	7.206E+06
21		LAMINATE						D 16	0.000E+00
22		Weight	12.20		4.36	3.44	[kg/m^2]	D 22	3.911E+07
23		Core Thickness	40		0	0	[mm]	D 26	0.000E+00
24		Total Thickness	44.27		2.39	1.88	[mm]	D 66	8.050E+06

ALLOWABLE MOMENTS - CYLINDRICAL BENDING [N mm/mm width]

	LONGITUDINAL MOMENT				TRANSVERSE MOMENT			
Compressive:	Top Skin		Bottom Skin		Top Skin		Bottom Skin	
	Moment	Ply	Moment	Ply	Moment	Ply	Moment	Ply
Longitudinal - Fibre Failure	23652	8	18922	8	49203	7	39363	7
- Microcrack	7096	8	8785	1	14761	7	18583	3
Transverse - Resin/Fibre Fail	49203	7	39363	7	23652	8	18922	8
- Resin/Microcrack	14761	7	18583	3	7096	8	8785	1
Resin Shear	24370	7	24370	7	24370	7	24370	7
Skin Wrinkling	14355		14229		14355		14229	

BENDING - PLY FAILURE SEQUENCE (CYLINDRICAL BENDING)

Failure Sequence	Failure Moment [N.mm/mm]	Ply Number	Ply	Failure Strain [%]	Failure Mode
LONGITUDINAL - Top Skin Compression					
	14355				Skin Wrinkling
1	7096	8	1 x XE905 Ehfv @ 0°	0.45	Longitudinal Microcrack
2	7436	6	1 x XE905 Ehfv @ 0°	0.45	Longitudinal Microcrack
3	14761	7	1 x XE450 Ehfv @ 45°	0.45	Longitudinal Microcrack
4	14761	7	1 x XE450 Ehfv @ 45°	0.45	Transverse Resin/Microcrack
5	23652	8	1 x XE905 Ehfv @ 0°	1.50	Longitudinal Fibre
6	24053	2	1 x XE905 Ehfv @ 0°	-1.20	Longitudinal Fibre
LONGITUDINAL - Bottom Skin Compression					
	14229				Skin Wrinkling
1	8785	1	1 x WRE602 Ehfv @ 0°	0.45	Longitudinal Microcrack
2	9020	2	1 x XE905 Ehfv @ 0°	0.45	Longitudinal Microcrack
3	9578	4	1 x XE905 Ehfv @ 0°	0.45	Longitudinal Microcrack
4	18583	3	1 x XE450 Ehfv @ 45°	0.45	Longitudinal Microcrack
5	18583	3	1 x XE450 Ehfv @ 45°	0.45	Transverse Resin/Microcrack
6	18922	8	1 x XE905 Ehfv @ 0°	-1.20	Longitudinal Fibre
TRANSVERSE - Top Skin Compression					
	14355				Skin Wrinkling
1	7096	8	1 x XE905 Ehfv @ 0°	0.45	Transverse Resin/Microcrack
2	7436	6	1 x XE905 Ehfv @ 0°	0.45	Transverse Resin/Microcrack
3	14761	7	1 x XE450 Ehfv @ 45°	0.45	Transverse Resin/Microcrack
4	14761	7	1 x XE450 Ehfv @ 45°	0.45	Longitudinal Microcrack
5	23652	8	1 x XE905 Ehfv @ 0°	1.50	Transverse Resin/Fibre
6	24053	2	1 x XE905 Ehfv @ 0°	-1.20	Transverse Resin/Fibre
TRANSVERSE - Bottom Skin Compression					
	14229				Skin Wrinkling
1	8785	1	1 x WRE602 Ehfv @ 0°	0.45	Transverse Resin/Microcrack
2	9020	2	1 x XE905 Ehfv @ 0°	0.45	Transverse Resin/Microcrack
3	9578	4	1 x XE905 Ehfv @ 0°	0.45	Transverse Resin/Microcrack
4	18583	3	1 x XE450 Ehfv @ 45°	0.45	Transverse Resin/Microcrack
5	18583	3	1 x XE450 Ehfv @ 45°	0.45	Longitudinal Microcrack
6	18922	8	1 x XE905 Ehfv @ 0°	-1.20	Transverse Resin/Fibre

Figure A3: Superstructure calculations

Project: Kompas
Laminate: Wheelhouse deck, P100

26-maj-15
09:08

	LAYER		Panel	Zero Curv'e	Upper Skin	Lower Skin		ABD MATRIX		
1	1 x WRE602 Ehfv @ 0°	IN-PLANE								
2	1 x XE905 Ehfv @ 0°	Longitudinal Modulus	1.620E+03	1.642E+03	1.974E+04	1.954E+04	[Mpa]	A 11	9.267E+04	[N/mm]
3	1 x XE450 Ehfv @ 45°	Transverse Modulus	1.620E+03	1.642E+03	1.974E+04	1.954E+04	[Mpa]	A 12	1.811E+04	
4	1 x XE905 Ehfv @ 0°	Poissons Ratio - Vxy	0.197	0.195	0.175	0.190		A 16	0.000E+00	
5	50 mm P100	- Vyx	0.197	0.195	0.175	0.190		A 22	9.267E+04	
6	1 x XE905 Ehfv @ 0°	Shear Modulus	3.524E+02	3.548E+02	4.087E+03	4.309E+03	[Mpa]	A 26	0.000E+00	
7	1 x XE450 Ehfv @ 45°	FLEXURAL						A 66	1.926E+04	
8	1 x XE905 Ehfv @ 0°	Longitudinal Modulus	4.302E+03				[Mpa]			
9		Transverse Modulus	4.302E+03				[Mpa]			
10		STIFFNESSES								
11		Longitudinal Stiffness - E * T	8.793E+04	8.913E+04	4.719E+04	3.667E+04	[N/mm]	B 11	-2.649E+05	[N]
12		Transverse Stiffness - E * T	8.793E+04	8.913E+04	4.719E+04	3.667E+04	[N/mm]	B 12	-3.038E+04	
13		Shear Stiffness - G * T	1.912E+04	1.926E+04	9.772E+03	8.085E+03	[N/mm]	B 16	0.000E+00	
14					Asymmetric Laminate			B 22	-2.649E+05	
15		Longitudinal Bending - EI	5.729E+07		2.353E+04	1.165E+04	[N mm^2/mm]	B 26	0.000E+00	
16		Transverse Bending - EI	5.729E+07		2.353E+04	1.165E+04	[N mm^2/mm]	B 66	-4.081E+04	
17		Torsional - GJ	1.231E+07		3.737E+03	1.705E+03	[N mm^2/mm]			
18		NEUTRAL AXIS			Asymmetric Laminate					
19		Longitudinal Bending	2.95	0.00	0.01	0.00	[mm]	D 11	6.014E+07	[N.mm]
20		Transverse Bending	2.95	0.00	0.01	0.00	[mm]	D 12	1.115E+07	
21		LAMINATE						D 16	0.000E+00	
22		Weight	13.30		4.36	3.44	[kg/m^2]	D 22	6.014E+07	
23		Core Thickness	50		0	0	[mm]	D 26	0.000E+00	
24		Total Thickness	54.27		2.39	1.88	[mm]	D 66	1.239E+07	

ALLOWABLE MOMENTS - CYLINDRICAL BENDING [N mm/mm width]

	LONGITUDINAL MOMENT				TRANSVERSE MOMENT			
Compressive:	Top Skin		Bottom Skin		Top Skin		Bottom Skin	
	Moment	Ply	Moment	Ply	Moment	Ply	Moment	Ply
Longitudinal - Fibre Failure	29648	8	23719	8	61326	7	49061	7
- Microcrack	8894	8	11028	1	18398	7	23034	3
Transverse - Resin/Fibre Fail	61326	7	49061	7	29648	8	23719	8
- Resin/Microcrack	18398	7	23034	3	8894	8	11028	1
Resin Shear	30365	7	30365	7	30365	7	30365	7
Skin Wrinkling	17733		17575		17733		17575	

BENDING - PLY FAILURE SEQUENCE (CYLINDRICAL BENDING)

Failure Sequence	Failure Moment [N.mm/mm]	Ply Number	Ply	Failure Strain [%]	Failure Mode
LONGITUDINAL - Top Skin Compression					
	17733				Skin Wrinkling
1	8894	8	1 x XE905 Ehfv @ 0°	0.45	Longitudinal Microcrack
2	9240	6	1 x XE905 Ehfv @ 0°	0.45	Longitudinal Microcrack
3	18398	7	1 x XE450 Ehfv @ 45°	0.45	Longitudinal Microcrack
4	18398	7	1 x XE450 Ehfv @ 45°	0.45	Transverse Resin/Microcrack
5	29648	8	1 x XE905 Ehfv @ 0°	1.50	Longitudinal Fibre
6	30046	2	1 x XE905 Ehfv @ 0°	-1.20	Longitudinal Fibre
LONGITUDINAL - Bottom Skin Compression					
	17575				Skin Wrinkling
1	11028	1	1 x WRE602 Ehfv @ 0°	0.45	Longitudinal Microcrack
2	11267	2	1 x XE905 Ehfv @ 0°	0.45	Longitudinal Microcrack
3	11827	4	1 x XE905 Ehfv @ 0°	0.45	Longitudinal Microcrack
4	23034	3	1 x XE450 Ehfv @ 45°	0.45	Longitudinal Microcrack
5	23034	3	1 x XE450 Ehfv @ 45°	0.45	Transverse Resin/Microcrack
6	23719	8	1 x XE905 Ehfv @ 0°	-1.20	Longitudinal Fibre
TRANSVERSE - Top Skin Compression					
	17733				Skin Wrinkling
1	8894	8	1 x XE905 Ehfv @ 0°	0.45	Transverse Resin/Microcrack
2	9240	6	1 x XE905 Ehfv @ 0°	0.45	Transverse Resin/Microcrack
3	18398	7	1 x XE450 Ehfv @ 45°	0.45	Transverse Resin/Microcrack
4	18398	7	1 x XE450 Ehfv @ 45°	0.45	Longitudinal Microcrack
5	29648	8	1 x XE905 Ehfv @ 0°	1.50	Transverse Resin/Fibre
6	30046	2	1 x XE905 Ehfv @ 0°	-1.20	Transverse Resin/Fibre
TRANSVERSE - Bottom Skin Compression					
	17575				Skin Wrinkling
1	11028	1	1 x WRE602 Ehfv @ 0°	0.45	Transverse Resin/Microcrack
2	11267	2	1 x XE905 Ehfv @ 0°	0.45	Transverse Resin/Microcrack
3	11827	4	1 x XE905 Ehfv @ 0°	0.45	Transverse Resin/Microcrack
4	23034	3	1 x XE450 Ehfv @ 45°	0.45	Transverse Resin/Microcrack
5	23034	3	1 x XE450 Ehfv @ 45°	0.45	Longitudinal Microcrack
6	23719	8	1 x XE905 Ehfv @ 0°	-1.20	Transverse Resin/Fibre

Figure A4: Wheelhouse Deck calculations

Project: Kompas
Laminate: Wheelhouse panels, P100

26-maj-15
09:09

LAYER		Panel	Zero Curv'e	Upper Skin	Lower Skin		ABD MATRIX		
1	1 x WRE602 Ehfv @ 0°	IN-PLANE							
2	1 x XE905 Ehfv @ 0°	Longitudinal Modulus	2.136E+03	2.160E+03	1.868E+04	1.824E+04	[Mpa]		
3	1 x XE905 Ehfv @ 45°	Transverse Modulus	2.136E+03	2.160E+03	1.868E+04	1.824E+04	[Mpa]	A 11	1.031E+05 [N/mm]
4	1 x XE905 Ehfv @ 0°	Poissons Ratio - Vxy	0.241	0.238	0.220	0.244		A 12	2.460E+04
5	40 mm P100	- Vyx	0.241	0.238	0.220	0.244		A 16	0.000E+00
6	1 x XE905 Ehfv @ 0°	Shear Modulus	5.819E+02	5.838E+02	4.836E+03	5.190E+03	[Mpa]	A 22	1.031E+05
7	1 x XE905 Ehfv @ 45°	FLEXURAL						A 26	0.000E+00
8	1 x XE905 Ehfv @ 0°	Longitudinal Modulus	5.547E+03				[Mpa]	A 66	2.629E+04
9		Transverse Modulus	5.547E+03				[Mpa]		
10		STIFFNESSES							
11		Longitudinal Stiffness - E * T	9.619E+04	9.728E+04	5.188E+04	4.126E+04	[N/mm]	B 11	-2.131E+05 [N]
12		Transverse Stiffness - E * T	9.619E+04	9.728E+04	5.188E+04	4.126E+04	[N/mm]	B 12	-2.275E+04
13		Shear Stiffness - G * T	2.621E+04	2.629E+04	1.343E+04	1.174E+04	[N/mm]	B 16	0.000E+00
14					Asymmetric Laminate			B 22	-2.131E+05
15		Longitudinal Bending - EI	4.224E+07		3.654E+04	2.019E+04	[N mm^2/mm]	B 26	0.000E+00
16		Transverse Bending - EI	4.224E+07		3.654E+04	2.019E+04	[N mm^2/mm]	B 66	-3.122E+04
17		Torsional - GJ	1.144E+07		6.054E+03	3.173E+03	[N mm^2/mm]		
18		NEUTRAL AXIS			Asymmetric Laminate				
19		Longitudinal Bending	2.20	0.00	0.02	0.00	[mm]	D 11	4.514E+07 [N.mm]
20		Transverse Bending	2.20	0.00	0.02	0.00	[mm]	D 12	1.046E+07
21		LAMINATE						D 16	0.000E+00
22		Weight	13.50		5.01	4.09	[kg/m^2]	D 22	4.514E+07
23		Core Thickness	40		0	0	[mm]	D 26	0.000E+00
24		Total Thickness	45.04		2.78	2.26	[mm]	D 66	1.148E+07

ALLOWABLE MOMENTS - CYLINDRICAL BENDING [N mm/mm width]

	LONGITUDINAL MOMENT				TRANSVERSE MOMENT			
Compressive:	Top Skin		Bottom Skin		Top Skin		Bottom Skin	
	Moment	Ply	Moment	Ply	Moment	Ply	Moment	Ply
Longitudinal - Fibre Failure	26989	2	21751	8	55273	3	45424	7
- Microcrack	8157	8	9865	1	17034	7	20727	3
Transverse - Resin/Fibre Fail	55273	3	45424	7	26989	2	21751	8
- Resin/Microcrack	17034	7	20727	3	8157	8	9865	1
Resin Shear	27897	7	27897	7	27897	7	27897	7
Skin Wrinkling	16794		16801		16794		16801	

BENDING - PLY FAILURE SEQUENCE (CYLINDRICAL BENDING)

Failure Sequence	Failure Moment [N.mm/mm]	Ply Number	Ply	Failure Strain [%]	Failure Mode
LONGITUDINAL - Top Skin Compression					
	16794				Skin Wrinkling
1	8157	8	1 x XE905 Ehfv @ 0°	0.45	Longitudinal Microcrack
2	8688	6	1 x XE905 Ehfv @ 0°	0.45	Longitudinal Microcrack
3	17034	7	1 x XE905 Ehfv @ 45°	0.45	Longitudinal Microcrack
4	17034	7	1 x XE905 Ehfv @ 45°	0.45	Transverse Resin/Microcrack
5	26989	2	1 x XE905 Ehfv @ 0°	-1.20	Longitudinal Fibre
6	27189	8	1 x XE905 Ehfv @ 0°	1.50	Longitudinal Fibre
LONGITUDINAL - Bottom Skin Compression					
	16801				Skin Wrinkling
1	9865	1	1 x WRE602 Ehfv @ 0°	0.45	Longitudinal Microcrack
2	10121	2	1 x XE905 Ehfv @ 0°	0.45	Longitudinal Microcrack
3	10952	4	1 x XE905 Ehfv @ 0°	0.45	Longitudinal Microcrack
4	20727	3	1 x XE905 Ehfv @ 45°	0.45	Longitudinal Microcrack
5	20727	3	1 x XE905 Ehfv @ 45°	0.45	Transverse Resin/Microcrack
6	21751	8	1 x XE905 Ehfv @ 0°	-1.20	Longitudinal Fibre
TRANSVERSE - Top Skin Compression					
	16794				Skin Wrinkling
1	8157	8	1 x XE905 Ehfv @ 0°	0.45	Transverse Resin/Microcrack
2	8688	6	1 x XE905 Ehfv @ 0°	0.45	Transverse Resin/Microcrack
3	17034	7	1 x XE905 Ehfv @ 45°	0.45	Transverse Resin/Microcrack
4	17034	7	1 x XE905 Ehfv @ 45°	0.45	Longitudinal Microcrack
5	26989	2	1 x XE905 Ehfv @ 0°	-1.20	Transverse Resin/Fibre
6	27189	8	1 x XE905 Ehfv @ 0°	1.50	Transverse Resin/Fibre
TRANSVERSE - Bottom Skin Compression					
	16801				Skin Wrinkling
1	9865	1	1 x WRE602 Ehfv @ 0°	0.45	Transverse Resin/Microcrack
2	10121	2	1 x XE905 Ehfv @ 0°	0.45	Transverse Resin/Microcrack
3	10952	4	1 x XE905 Ehfv @ 0°	0.45	Transverse Resin/Microcrack
4	20727	3	1 x XE905 Ehfv @ 45°	0.45	Transverse Resin/Microcrack
5	20727	3	1 x XE905 Ehfv @ 45°	0.45	Longitudinal Microcrack
6	21751	8	1 x XE905 Ehfv @ 0°	-1.20	Transverse Resin/Fibre

Figure A4: Wheelhouse Panels calculations

Annex B: Effects on the ship

DTU Mechanical Engineering
Department of Mechanical Engineering

DTU Civil Engineering
Department of Civil Engineering

Date : April 2016
Project name : COMPASS – Composite superstructures for large PASSenger ships

Author : Vasileios Karatzas

Contents

1 Introduction

Conversions are becoming increasingly popular as ship owners try to overcome high newbuilding prices and long delivery times by adapting existing vessels for different roles. Alternatively, it is a general trend to try to increase the efficiency of vessels by reducing the cost per ton of payload cargo which results in increased revenue for the ship owners. The extent and kind of conversion varies depending on the intended operational plan with conversion from one type of ship to another, lengthening of the cargo area, widening and increasing the depth of the ship being among the most common ones. Retrofitting the superstructures is also among the conversion practices, although for most cargo vessels the superstructures represent a small fraction of the vessel's lightship as they are not of considerable extent. However, this is not the case for passenger ships as the superstructures constitute a significant percentage of the lightship. Additionally, depending on the size of the ship, the superstructure may tower several decks above the weather deck, affecting the stability of the ship. An appealing way to increase the efficiency of passenger ships is by designing superstructures made out of composites. The major advantage of composite materials is their increased specific stiffness and increased specific strength. Additionally, apart from being lightweight, composite materials exhibit very good fatigue performance and unlike steel they are not susceptible to corrosion.

Until recently, the existing regulatory frame did not allow the use of composites on ships, as combustible materials, were not accepted by the SOLAS convention. In 2002, SOLAS was extended by the so-called Rule 17 [1], enabling the use of combustible composite materials as long as the same level of safety could be demonstrated. This regulation, however, has rarely been used in practice, as both the technical safety analysis as the appropriate regulatory approval is very complex and time-consuming, and therefore costly

The work presented here has been performed under the scope of the COMPASS project. This project aims at providing a standardized approach for the implementation of composite superstructures for designers, ship-owners and authorities alike. The present report addresses the effects on an existing passenger ship due to the retrofitting of part of the superstructure with composite materials. The overall design along with changes in the lightship, stability and fuel consumption of the vessel are discussed.

2 Composite superstructure design

2.1 Case study description

The ship which was the study case is a double-ended RoPax ferry named PRINSESSE BENEDIKTE and is operated by Scandlines (Figure 1). The main characteristics of the vessel are listed in Table 1. The ship is powered by electric motors. The upper decks of the superstructure, which lie above 17.7 m measuring from the baseline (Figure 2) were selected for retrofitting. In detail the parts that were retrofitted include

- The Sun deck
- The Wheelhouse Deck
- The Wheelhouses
- The Funnels
- The Masts
- The Superstructure
- The Structural bulkheads in these areas

The deck positioned at 17.7m (Saloon deck) was made out of steel for both the existing and the retrofitted case.

Table 1: Main characteristics of the ship

PRINSESSE BENEDIKTE		
Length oa	142	[m]
Breadth	24.8	[m]
Depth	8.5	[m]
Service speed	18.5	[kn]
Lightship	6346	[t]
Gross tonnage	14822	[-]

Figure 1: RoPax ferry PRINSESSE BENEDIKTE

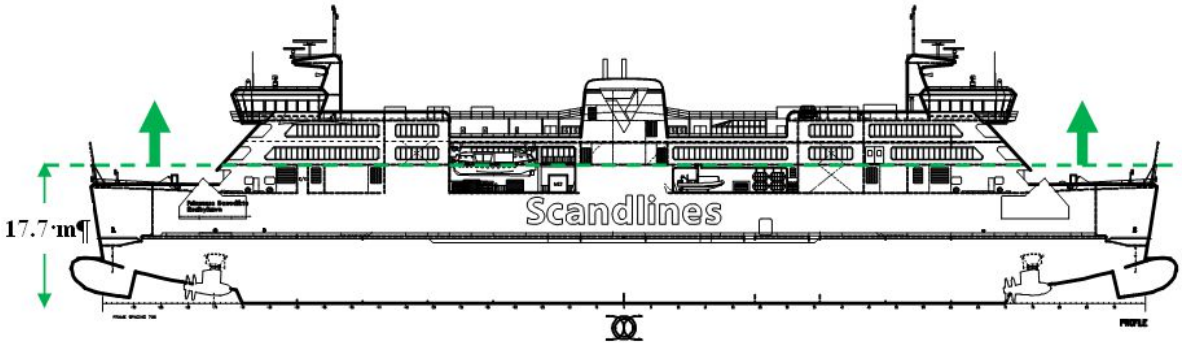

Figure 2: Part of the superstructure selected for retrofitting

There is a plethora of different design constraints and objectives to be considered when designing / retrofitting a ship, these typically reflect the interests of the various ship design stake holders such as the ship owners/operators, classification societies and shipyards to name but a few. Depending on the set of design requirements, which are often conflicting, an optimum design is sought [2].

Given that the original requirements and constraints were unknown and that it would be more interesting to have a direct comparison between the original and the retrofitted case, it was decided to keep the same general arrangement of the superstructure. Bearing this in mind, it is evident that the resulted design is the optimal one with respect to the ships' service and life cycle in general.

2.2 Materials

2.2.1 Face Sheet

In the early stages of the project different material configurations have been investigated for the design of the composite superstructure before concluding on the most appealing one for the case at hand. In all cases the elements consisted primarily of sandwich material solutions. From the first stages of this study it was deemed that glass fibres represent a more appealing material compared to carbon or other type of fibres as the raw material acquisition cost in the latter cases would be drastically increased for a composite structure of this size. Therefore in all configurations presented in this report the face sheets of the sandwich components consisted of glass fibers in an epoxy matrix. In particular E-glass biaxial stitched fabric and woven rovings along with Prime 20LV epoxy resin were selected. Representative mechanical properties of different E-glass/epoxy laminae are listed in Figure 3.

Material Properties	Type of material	Fibre direction	Fibre volume fraction	Cured ply thickness	Cured ply weight	Longitudinal tensile modulus	Transverse tensile modulus	Longitudinal compressive modulus	Transverse compressive modulus	In-Plane Shear Modulus	Longitudinal tensile strain	Transverse tensile strain	Longitudinal compressive strain	Transverse compressive strain
				[mm]	[g/m²]	[MPa]	[MPa]	[MPa]	[MPa]	[MPa]	[%]	[%]	[%]	[%]
UE800	Unidirectional E-glass	0°	0.48	0.641	1171	35910	8450	35910	8450	3190	1.80%	0.45%	-1.25%	-1.50%
BE900	E-glass Stitched fabric	0°/90°	0.46	0.754	1364	21220	21220	21220	21220	3050	1.50%	1.50%	-1.20%	-1.20%
WRE580	E-glass woven rovings	0°/90°	0.45	0.496	881	20380	20380	20380	20380	3278	1.50%	1.50%	-1.25%	-1.25%
XE905	E-glass Stitched fabric	+/-45°	0.46	0.750	1364	9737	9737	9737	9737	9471	1.50%	1.50%	-1.20%	-1.20%
UCHSC500	Unidirectional Carbon	0°	0.48	0.579	835	112110	6350	107540	6350	3390	1.00%	0.45%	-0.67%	-1.50%

Figure 3: Lamina material properties

2.2.2 Core materials

Regarding the core material, different types of core were considered namely, PVC, Balsa and PET cores. These represent some of the most widely used core types in industrial applications. A brief description of each types advantages and disadvantages is listed below

Balsa

Balsa cores are made out of balsa wood (Figure 4) and as such they are derived from a sustainable and renewable resource. Balsa exhibits higher shear and compression strength compared to foam cores and is inexpensive. In addition, it has exhibited better behaviour in fire-critical applications compared to other types of foams and the smoke released when burned is white and non-toxic.

On the other hand Balsa has higher density and its grain structure results in increased resin uptake during lamination therefore its use may lead introduce a weight penalty when compared to foam cores. A concern with Balsa is the risk of moisture uptake as with all wood materials, which makes it susceptible to rot if not properly installed or maintained [3]. In addition it takes from 6 to 10 years for Balsa trees to grow. Which means that the availability of such types of core might be problematic should the demand increase.

Figure 4: Balsa core material

PVC

Polyvinyl chloride foam cores (Figure 5) are less dense and more water resistant compared to Balsa. Nevertheless the material properties of such cores are lower and the acquisition cost more elevated than Balsa. In addition, PVC foams release toxic smoke when burnt which is a major concern in the unfortunate event of a fire.

Figure 5: PVC foam core sheets

PET

Polyethylene terephthalate cores (Figure 6) are thermoplastic and exhibit high thermal stability. Some other appealing characteristics are that they are thermoformable, remeltable and recyclable minimising process scrap during production as the material can be reused. From a mechanical point of view, PET cores require higher densities to reach the physical and mechanical properties of PVC and Balsa cores.

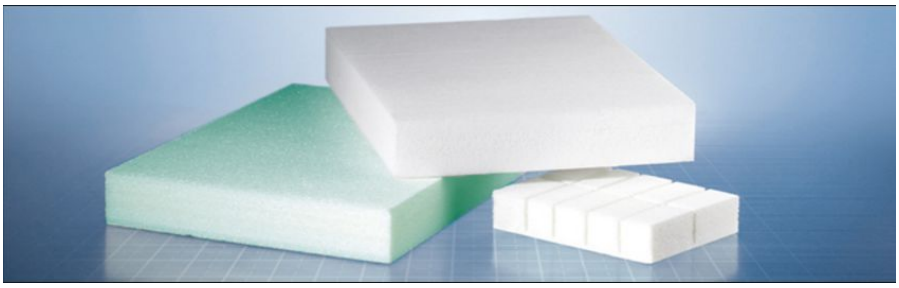

Figure 6: PET foam core sheets

The specific core for each type was selected form available commercial products. In particular for the PVC core Divinycell H80 and 100 series were selected, the lightweight ProBalsa LD7 for the Balsa and Divinycell P100 for the PET core. The nominal material properties for the core types were taken from the suppliers' data sheet and are presented in Figure 7.

Core Properties	Type of Core	Average density [kg/m³]	Shear strength [MPa]	Shear Modulus [MPa]	Tensile Strength [MPa]	Compressive Strength [MPa]	Compressive Modulus [MPa]
ProBalsa LD7	Balsa	90	1.60	96	7.00	5.4	1850
H80	PVC	80	1.15	27	2.50	1.4	90
H100	PVC	100	1.60	35	3.50	2	135
P100	PET	110	0.85	28	1.80	1.5	100

Figure 7: Nominal core properties

2.3 Design loads and scantling requirements

DNV's rules were used for the design of the composite superstructure. In particular, the scantling calculations were performed following DNV's Rules for Classification of High Speed, Light Craft and Naval Surface Craft [4,6] while the design loads were calculated according to DNV's Rules for Classifications of Ships [5,6].

2.4 Retrofitted design

Based on the selected design requirement, the different material configurations and the identification of the design loads and scantling requirements a 3D CAD model of the composite superstructure has been generated.

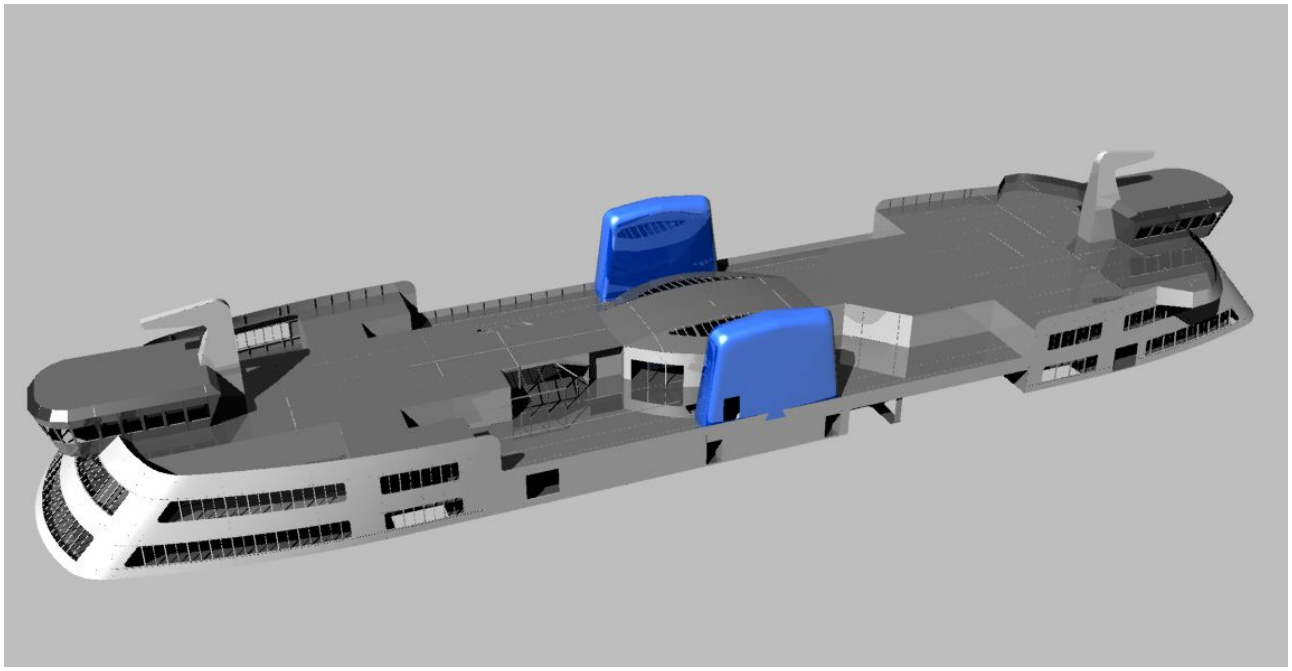

Figure 8: Generated 3D CAD model of the superstructure

What should be noted is that although the geometry and general arrangement is kept identical, the arrangement and number of stiffeners used differ substantially from the original steel design. A visual representation of the stiffeners is given in Figure 9. Two different stiffener geometries were used. The relevant details are presented in Figures 10 and 11. An indication of the substantially decreased number of stiffeners and in extent of the required manufacturing effort can be obtained by comparing the composite solution with the existing steel drawings of the ship for the Sun deck and the Wheelhouse deck (Figure 12).

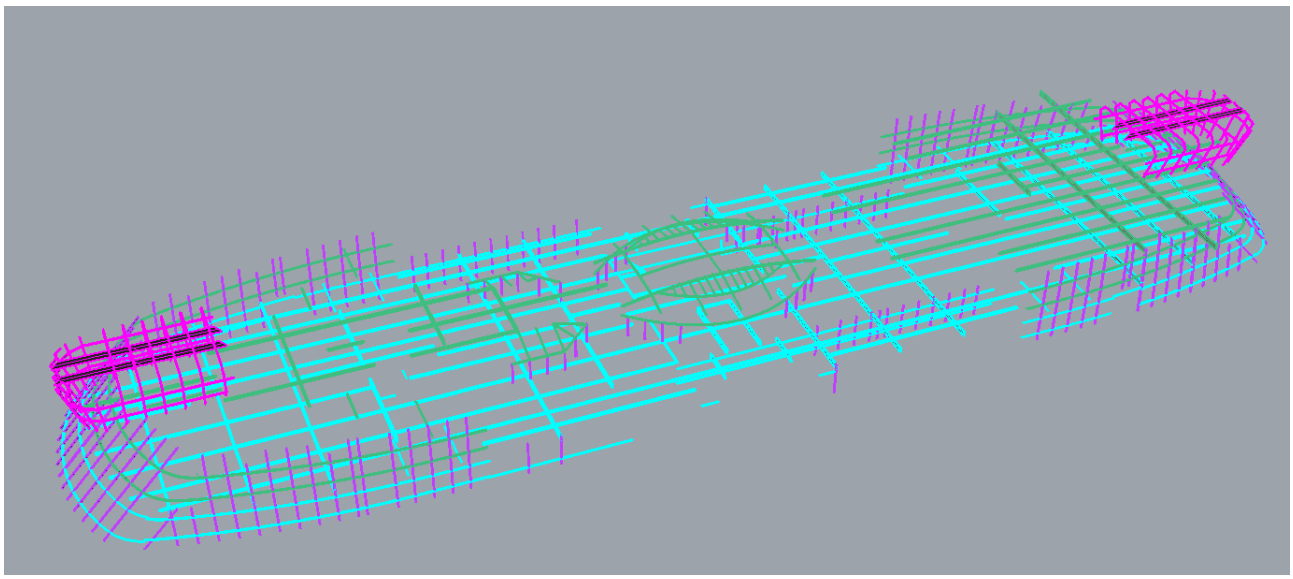

Figure 9: Stiffener arrangement for the composite case

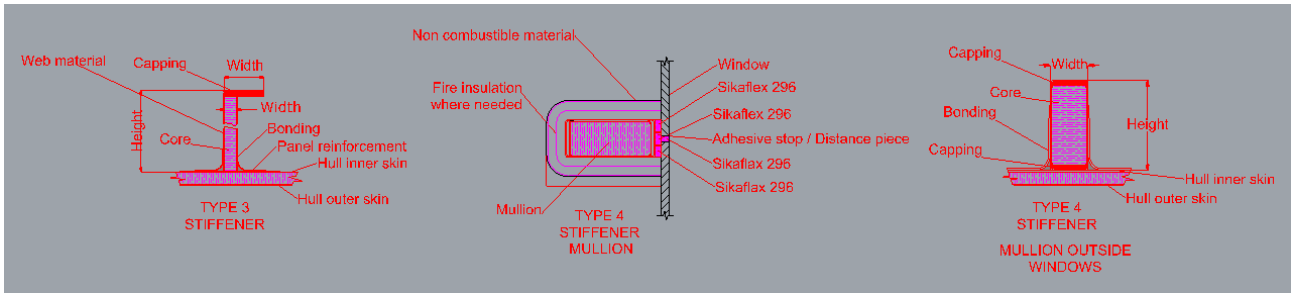

Figure 10: Stiffener Type

ITEM	Type	Height [mm]	Width [mm]	Web material	Capping	Bonding	Panel reinforcement/Capping
Vertical side stiffener	4	120	80	3 ply XE905	7 ply UCHSC500	3 ply XE905	7 ply UCHSC500/80 mm
Horizontal Side stiffener	4	120	60	3 ply XE905	8 ply UCHSC500	3 ply XE905	8 ply UCHSC500/60 mm
Vertical front stiffener	4	120	80	3 ply XE905	7 ply UCHSC500	3 ply XE905	7 ply UCHSC500/80 mm
Horizontal front stiffener	4	120	60	3 ply XE905	8 ply UCHSC500	3 ply XE905	8 ply UCHSC500/60 mm
Wheelhouse vertical stiffener	4	120	80	4 ply XE905	13 ply UCHSC500	4 ply XE905	13 ply UCHSC500/80 mm
Wheelhouse horizontal stiffener	4	100	60	2 ply XE905	4 ply UCHSC500	2 ply XE905	4 ply UCHSC500/80 mm
Longitudinal Wheelhouse deck beams	3	175	120	4 ply XE905	13 ply UCHSC500	4 ply XE905	4 ply UCHSC500/80 mm
Transverse wheelhouse deck beams	3	220	120	5 ply XE905	15 ply UCHSC500	5 ply XE905	6 ply UCHSC500/80 mm
Longitudinal Sun deck beams	3	250	120	5 ply XE905	15 ply UCHSC500	5 ply XE905	8 ply UCHSC500/80 mm
Transverse Sun deck beams	3	430	170	8 ply XE905	26ply UCHSC500	8 ply XE905	9 ply UCHSC500/80 mm

Figure 11: Stiffener details and location

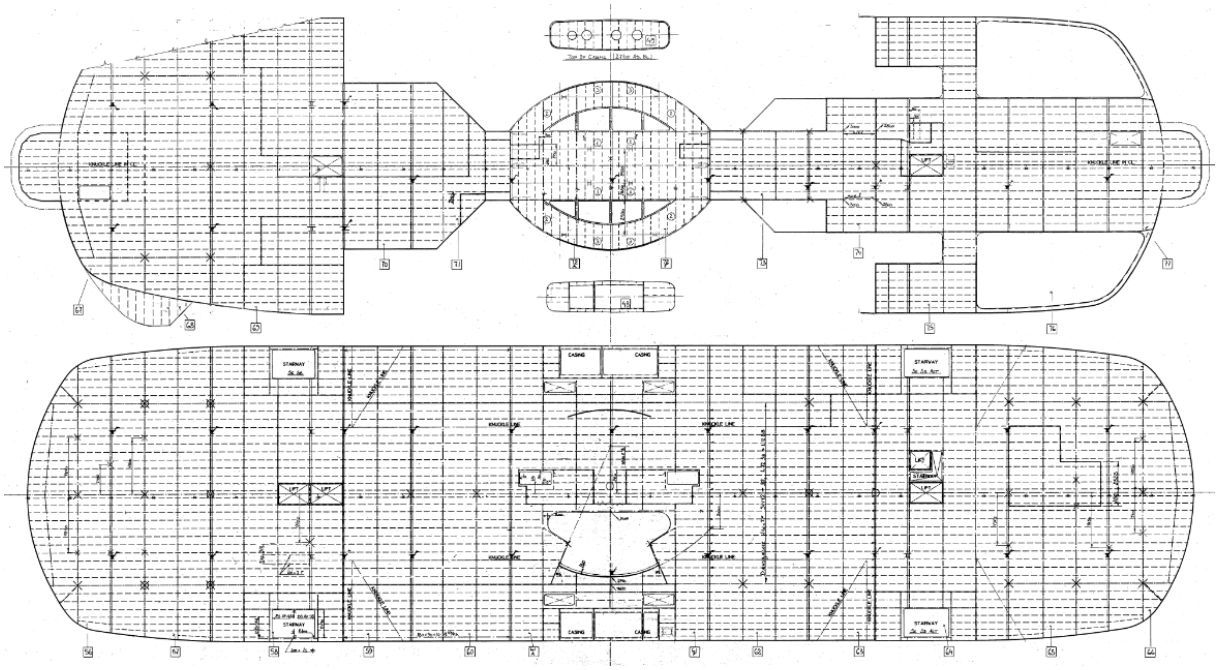

Figure 12: Steel drawings of the existing superstructure

The structural layup differed for each face sheet core combination. These are presented in detail in the Figure 13.

Balsa Core						
	Ply Number	Sun Deck 6 Material	Wheelhouse Deck 7 Material	Superstructure Material	Wheelhouse Panels Material	Structural Bulkheads Material
Outer Skin	1	600 g/m² E-glass, Woven Roving 0°/90°	600 g/m² E-glass, Woven Roving 0°/90°	600 g/m² E-glass, Woven Roving 0°/90°	600 g/m² E-glass, Woven Roving 0°/90°	900 g/m² E-glass, Stitched fabric 0°/90°
	2	600 g/m² E-glass, Stitched fabric 0°/90°	900 g/m² E-glass, Stitched fabric 0°/90°	900 g/m² E-glass, Stitched fabric 0°/90°	900 g/m² E-glass, Stitched fabric 0°/90°	900 g/m² E-glass, Biaxial Stitched fabric +/-45°
	3	900 g/m² E-glass, Biaxial Stitched fabric +/-45°	450 g/m² E-glass, Biaxial Stitched fabric +/-45°	450 g/m² E-glass, Biaxial Stitched fabric +/-45°	900 g/m² E-glass, Biaxial Stitched fabric +/-45°	+ Local reinforcement
	4	900 g/m² E-glass, Stitched fabric 0°/90°	900 g/m² E-glass, Stitched fabric 0°/90°	900 g/m² E-glass, Stitched fabric 0°/90°	900 g/m² E-glass, Stitched fabric 0°/90°	
Balsa Core		ProBalsa LD7/50mm	ProBalsa LD7/50mm	ProBalsa LD7/40mm	ProBalsa LD7/40mm	ProBalsa LD7/40mm
Inner Skin	1	600 g/m² E-glass, Stitched fabric 0°/90°	900 g/m² E-glass, Stitched fabric 0°/90°	900 g/m² E-glass, Stitched fabric 0°/90°	900 g/m² E-glass, Stitched fabric 0°/90°	900 g/m² E-glass, Stitched fabric 0°/90°
	2	900 g/m² E-glass, Biaxial Stitched fabric +/-45°	450 g/m² E-glass, Biaxial Stitched fabric +/-45°	450 g/m² E-glass, Biaxial Stitched fabric +/-45°	900 g/m² E-glass, Biaxial Stitched fabric +/-45°	900 g/m² E-glass, Biaxial Stitched fabric +/-45°
	3	900 g/m² E-glass, Stitched fabric 0°/90°	900 g/m² E-glass, Stitched fabric 0°/90°	900 g/m² E-glass, Stitched fabric 0°/90°		+ Local reinforcement

PET Core						
	Ply Number	Sun Deck 6 Material	Wheelhouse Deck 7 Material	Superstructure Material	Wheelhouse Panels Material	Structural Bulkheads Material
Outer Skin	1	600 g/m² E-glass, Woven Roving 0°/90°	600 g/m² E-glass, Woven Roving 0°/90°	600 g/m² E-glass, Woven Roving 0°/90°	600 g/m² E-glass, Woven Roving 0°/90°	900 g/m² E-glass, Stitched fabric 0°/90°
	2	600 g/m² E-glass, Stitched fabric 0°/90°	900 g/m² E-glass, Stitched fabric 0°/90°	900 g/m² E-glass, Stitched fabric 0°/90°	900 g/m² E-glass, Stitched fabric 0°/90°	900 g/m² E-glass, Biaxial Stitched fabric +/-45°
	3	900 g/m² E-glass, Biaxial Stitched fabric +/-45°	450 g/m² E-glass, Biaxial Stitched fabric +/-45°	450 g/m² E-glass, Biaxial Stitched fabric +/-45°	900 g/m² E-glass, Biaxial Stitched fabric +/-45°	+ Local reinforcement
	4	900 g/m² E-glass, Stitched fabric 0°/90°	900 g/m² E-glass, Stitched fabric 0°/90°	900 g/m² E-glass, Stitched fabric 0°/90°	900 g/m² E-glass, Stitched fabric 0°/90°	
PET Core		DIAB P100/50mm	DIAB P100/50mm	DIAB P100/40mm	DIAB P100/40mm	DIAB P100/40mm
Inner Skin	1	600 g/m² E-glass, Stitched fabric 0°/90°	900 g/m² E-glass, Stitched fabric 0°/90°	900 g/m² E-glass, Stitched fabric 0°/90°	900 g/m² E-glass, Stitched fabric 0°/90°	900 g/m² E-glass, Stitched fabric 0°/90°
	2	900 g/m² E-glass, Biaxial Stitched fabric +/-45°	450 g/m² E-glass, Biaxial Stitched fabric +/-45°	450 g/m² E-glass, Biaxial Stitched fabric +/-45°	900 g/m² E-glass, Biaxial Stitched fabric +/-45°	900 g/m² E-glass, Biaxial Stitched fabric +/-45°
	3	900 g/m² E-glass, Stitched fabric 0°/90°	900 g/m² E-glass, Stitched fabric 0°/90°	900 g/m² E-glass, Stitched fabric 0°/90°		+ Local reinforcement

PVC Core						
	Ply Number	Sun Deck 6 Material	Wheelhouse Deck 7 Material	Superstructure Material	Wheelhouse Panels Material	Structural Bulkheads Material
Outer Skin	1	600 g/m² E-glass, Woven Roving 0°/90°	600 g/m² E-glass, Woven Roving 0°/90°	600 g/m² E-glass, Woven Roving 0°/90°	600 g/m² E-glass, Woven Roving 0°/90°	900 g/m² E-glass, Stitched fabric 0°/90°
	2	600 g/m² E-glass, Stitched fabric 0°/90°	900 g/m² E-glass, Stitched fabric 0°/90°	900 g/m² E-glass, Stitched fabric 0°/90°	900 g/m² E-glass, Stitched fabric 0°/90°	900 g/m² E-glass, Biaxial Stitched fabric +/-45°
	3	900 g/m² E-glass, Biaxial Stitched fabric +/-45°	450 g/m² E-glass, Biaxial Stitched fabric +/-45°	450 g/m² E-glass, Biaxial Stitched fabric +/-45°	900 g/m² E-glass, Biaxial Stitched fabric +/-45°	+ Local reinforcement
	4	900 g/m² E-glass, Stitched fabric 0°/90°	900 g/m² E-glass, Stitched fabric 0°/90°	900 g/m² E-glass, Stitched fabric 0°/90°	900 g/m² E-glass, Stitched fabric 0°/90°	
PVC Core		DIAB P100/50mm	DIVINYCELL H100/50mm	DIVINYCELL H100/40mm	DIVINYCELL H80/40mm	DIVINYCELL H80/40mm
Inner Skin	1	600 g/m² E-glass, Stitched fabric 0°/90°	900 g/m² E-glass, Stitched fabric 0°/90°	900 g/m² E-glass, Stitched fabric 0°/90°	900 g/m² E-glass, Stitched fabric 0°/90°	900 g/m² E-glass, Stitched fabric 0°/90°
	2	900 g/m² E-glass, Biaxial Stitched fabric +/-45°	450 g/m² E-glass, Biaxial Stitched fabric +/-45°	450 g/m² E-glass, Biaxial Stitched fabric +/-45°	900 g/m² E-glass, Biaxial Stitched fabric +/-45°	900 g/m² E-glass, Biaxial Stitched fabric +/-45°
	3	900 g/m² E-glass, Stitched fabric 0°/90°	900 g/m² E-glass, Stitched fabric 0°/90°	900 g/m² E-glass, Stitched fabric 0°/90°		+ Local reinforcement

Figure 13: Structural lay up for the considered core options

3 Weight Calculations

Following the design of the new superstructure, weight calculations have been performed for all the aforementioned cases and compared to the calculated existing steel weight. The calculation of the steel weight has been performed based on available data from the ROPAX ferry PRINS RICHARD which is the sister ship of PRINSESS BENEDIKTE. At this point it is underlined that the calculated weight corresponds to the steel weight of the original superstructure excluding outfitting weights. Similarly the presented calculations for the composite cases solely consider the weight of the composite parts. Special considerations have been given to address structural and manufacturing details in the composite such as pillar support areas, local reinforcement at openings/edges and the resin intake based on the core type.

The weights have been calculated for the PVC, Balsa and PET core and listed along with the original steel weight in Table 2. Details on the calculations of these weights are provided at the appendix.

Table 2: Structural weight of the original and retrofitted parts of the superstructure

Structural weight		
Steel Superstructure	475.4	[t]
PVC core Superstructure	135.5	[t]
Balsa core Superstructure	140.5	[t]
PET core Superstructure	142.5	[t]

As it was expected the PVC results to the lighter option thanks to the core's lower density. The Balsa core option follows with 3.5 % increased weight compared to the PVC option and lastly the PET core being 4.9%heavier than the PVC option.

The Balsa core selected was lightweight having a density of only 90 kg/m^3, which is comparable to the PVC and PET core densities. This is the reason why there is not a notable difference between the calculated weights for the three types of cores. To demonstrate the impact of the core density on the weight, an additional case was investigated in which a balsa core with an average density of 166 kg/m^3 was used. The latter represents a typical average density value for balsa. For the typical core density the weight of the superstructure is higher than the PVC and the PET core

Table 2: Structural weight of the original and retrofitted parts of the superstructure

Structural weight		
Lightweight Balsa core case	140.5	[t]
Typical Balsa core density case	168.0	[t]

Comparing the composite superstructures to the original steel one it can be seen that the structural weight reduction is drastic with the reduction of the weight range between 64.7% for the typical balsa core to 71.5% for the light PVC one. The weight difference between the light balsa core the PET and the PVC core is not that pronounced. Based on the weight calculations the new Lightship weight for each case can be calculated. Additionally the weight of the superstructure has been expressed as a percentage of the lightship (Table 3). Results indicate that replacing part of the superstructure with sandwich materials leads to a reduction of the lightship of circa 5% which is considerable.

Table 3: Superstructure cases

Comparison of different cases				
Superstructure Case	Weight [t]	Lightship [t]	Percentage of Lightship	Percentage reduction of lightship
Steel	475.4	6346	7.49%	N/A
PVC core	135.5	6006	2.26%	5.36%
Light Balsa core	140.5	6011	2.34%	5.28%
Typical Balsa core	168.0	6038	2.78%	4.84%
PET core	142.5	6013	2.37%	5.25%

Eventually having investigated the different weight savings it was decided to proceed with the PET core, the reason being the smoke and toxicity hazards associated with the PVC and difficulties encountered with acquiring and fabricating panels out of Balsa. Additionally DIAB was willing to sponsor the project with the PET P100 core for the experimental tasks associated with this project. Therefore all subsequent calculations correspond to the P100 core case.

4 Stability

The implementation of composite materials in superstructures is particularly interesting in large passenger ships where the stability is one of the governing parameters for the number of decks towering above the main deck. To find out how the stability of the ship is affected two loading scenarios have been selected and compared between the retrofitted case and the original design. The first one was selected from the ship's stability booklet and referred to as loading condition 5. This loading condition represents the most conservative one with the ship carrying the maximum payload at this condition. The second case was based on the real average loading condition that the ship operates. Details about this condition were provided by Scandlines [7]. The specifics for each case are presented in the appendix.

To calculate the stability for the retrofitted cases the calculation of the new centre of gravity of the Lightship was necessary. This was done by considering that the outfitting weight (W_{OT}), the machinery weight (W_M) and the position of their centre of gravity are unaffected. This allows the decomposition of the Lightship in two groups namely the structural weight W_{ST} and the sum of W_M + W_{OT}.

Lightship = Wst + Wot +Wm

Knowing from the existing data for PRINS RICHARD the centre of gravity of the structural weight, the weight and centre of gravity for the sum W_M + W_{OT} was calculated (Figure 14). Additionally from the structural weight data for PRINS RICHARD the position and weight of the retrofitted parts were known. Replacing these weights with the ones calculated for the composite case allowed the calculation of the new Lightship weight and the new centre of gravity. In all cases the centre of gravity was measured from the Baseline of the vessel.

	Steel case		Retrofitted case	
	Weight [t]	KG [m]	Weight [t]	KG [m]
LS	6346.0	10.43	6013.1	9.88
W_{ST}	3769.1	10.73	3436.2	9.80
$W_M + W_{OT}$	2576.9	9.99	2576.9	9.99

Figure 14: Listing of the weight groups and center of gravity

Having calculated the new lightship, the new displacement was calculated by adding the deadweight that corresponded to each loading case. The draught and the other relevant hydrostatic data were taken from the ship's hydrostatic tables which enabled the calculation of the metacentric height (GM) and of the righting arm (GZ).

The metacentric height (GM) is a measurement of the initial static stability of a ship and is defined as the distance between the metacentre (KM) and the ship's centre of gravity (KG) for larger heeling angles stability is governed by the righting arm (GZ).

A larger metacentric height implies greater initial stability against overturning however the metacentric height also influences the natural period of rolling of the hull, with very large metacentric heights being associated with shorter periods of roll which are uncomfortable for passengers.

The results between the original and the composite case for the two loading conditions are presented in Figures 15 and 16. The modified GM and GZ curves are represented with solid lines in the diagrams while the dashed ones to the steel one.

Retrofitted case - Loading Condition 5

0	KM *	14.209	m
1	Deplacement	8505	t
2	GM=KM-KG	4.36	m

3	Krængningsvinkler β (degrees)	0	10	20	30	40	50	60
4	Sinβ	0	0.174	0.342	0.500	0.643	0.766	0.866
5	GM x Sinβ	0	0.757	1.491	2.180	2.803	3.340	3.776
6	MS *	0	-0.060	-0.097	-0.396	-0.778	-1.343	-2.210
7	GZ = (5) + (6)	0	0.697	1.394	1.784	2.024	1.997	1.566

Hydrostatiske data

8	LCB *	66.99	m
9	LCA *	67.00	m
10	LCG fra AP. = Sum E/SUM A	67.06	m
11	MCT x 100	16440	tm/m
12	Dybgang under Køl	5.675	m

Trim & Dybgang

13	Trim	-0.03	m
14	Kølpladetykkelse	0.015	m
15	dagter :	5.658	m
16	dfor :	5.69	m
17	Middeldybgang	5.675	m
	Steel Case		
18	Middeldybgang	5.815	m

* Tabel aflæasning

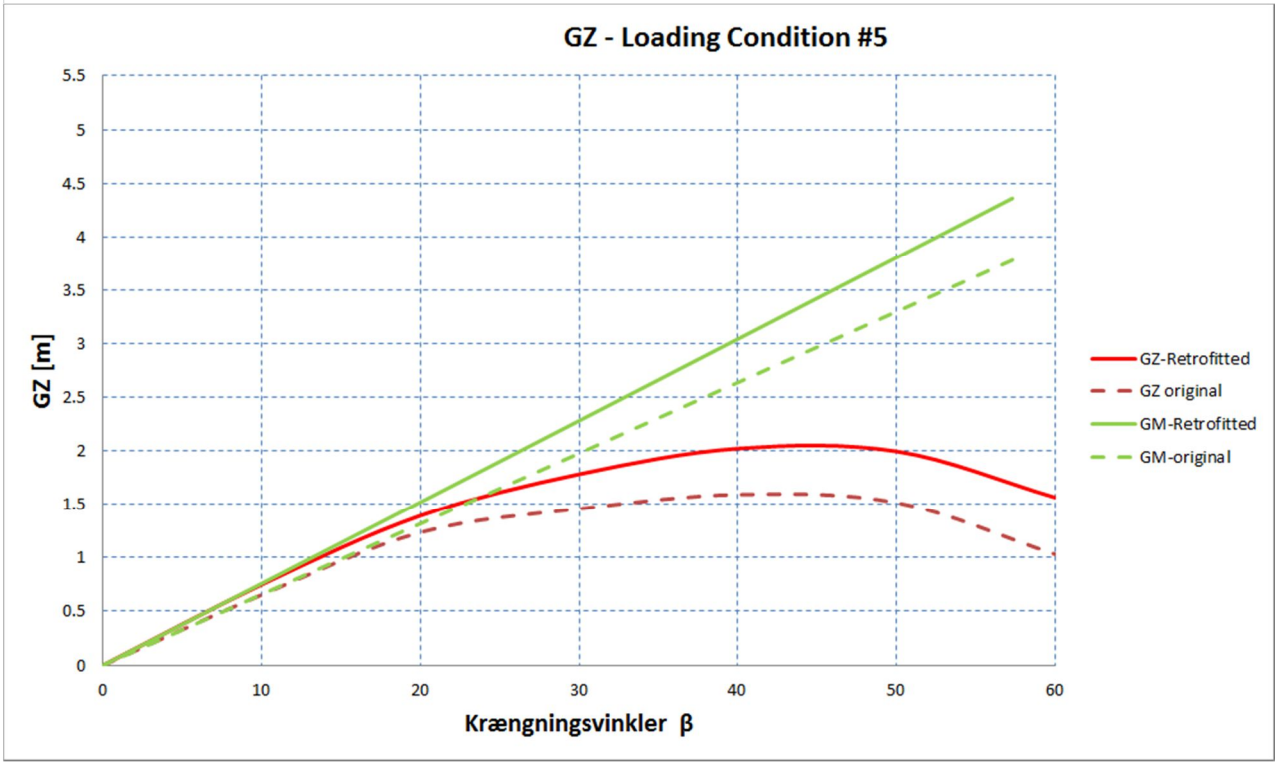

Figure 15: Hydrostatic data and stability for loading condition 5

Retrofitted case - Average Condition

0	KM *	14.838	m
1	Deplacement	6693.08	t
2	GM=KM-KG	5.088	m

3	Krængningsvinkler β (degrees)	0	10	20	30	40	50	60
4	Sinβ	0	0.174	0.342	0.500	0.643	0.766	0.866
5	GM x Sinβ	0	0.884	1.740	2.544	3.271	3.898	4.406
6	MS *	0	-0.034	-0.208	-0.603	-1.103	-1.603	-2.469
7	GZ = (5) + (6)	0	0.850	1.532	1.941	2.168	2.295	1.938

Hydrostatiske data

8	LCB *	66.99	m
9	LCA *	67.00	m
10	LCG fra AP. = Sum E/SUM A	66.67	m
11	MCT x 100	14290	tm/m
12	Dybgang under Køl	4.87	m

Trim & Dybgang

13	Trim	0.15	m
14	Kølpladetykkelse	0.015	m
15	dagter :	4.945	m
16	dfor :	4.80	m
17	Middeldybgang	4.87	m
	Steel Case		
18	Middeldybgang	5.035	m

* Tabel aflæasning

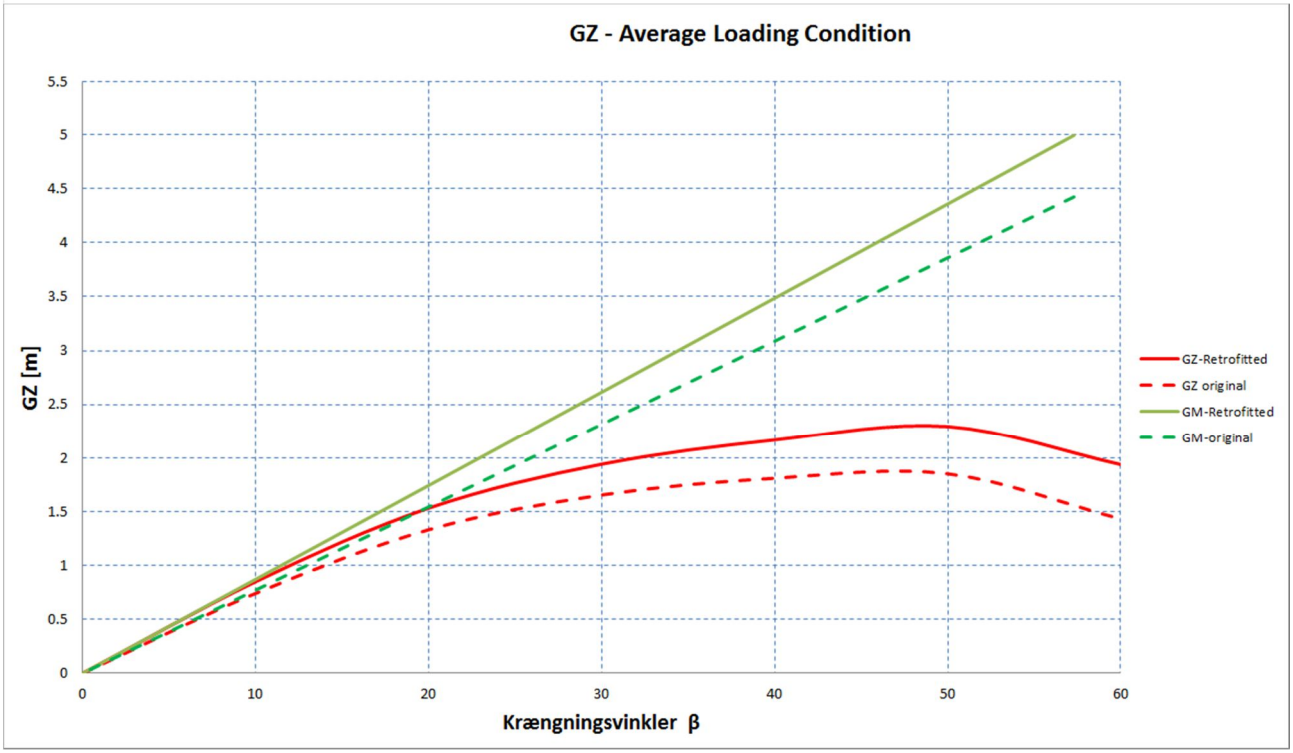

Figure 16: Hydrostatic data and stability for average loading condition

Comparing the GM values results indicate that by replacing part of the superstructure with composite materials leads to an increase of the GM values of 15.3 % for the loading condition 5 and of about 12.9% for the average condition. Additionally, the GZ values are increased as expected. The maximum value of GZ is increased by 27% and 24% for condition 5 and the average service condition respectively. In general the new design results in a bigger range of stability and in increased static and dynamic stability. Additionally, knowing the GM values for each case a simplified comparison between the periods of roll can be performed. The period of roll is given by the following equation:

$$T = \frac{2\pi k}{\sqrt{gGM}}$$

Where:

- k is the radius of gyration
- g is the acceleration of gravity and
- GM is the metacentric height

Assuming that the radius of gyration is kept constant, as the waterline area is not significantly affected in the studied cases, the change between in the period of roll can be given by the following equation

$$\frac{T_{steel}}{T_{composite}} = \sqrt{\frac{GM_{composite}}{GM_{steel}}}$$

For the examined cases the period of roll is reduced around 6% for both cases meaning that if the original period of roll was 12 seconds which is a typical value for passenger ships, the new one is decreased to 11 seconds. The fact that the decrease of the roll period is not that pronounced is desirable as shorter periods of roll which are uncomfortable for passengers.

5 Resistance and propulsion calculations

In this passage the effect of the conversion to the ship resistance and the required horsepower for propulsion are presented. Subsequently, an approximation of the fuel consumption reduction has been attempted. Unlike the previous passages where multiple conditions have been studied, only the "average" loading condition in which the vessel sails. This case has been selected as, in reality; the decision for the conversion of a vessel will be most likely based on the recorded service data. The followed approach could be repeated for different loading conditions should these be of interest.

The ship resistance components can be decomposed in different components as illustrated in Figure 17 [9]

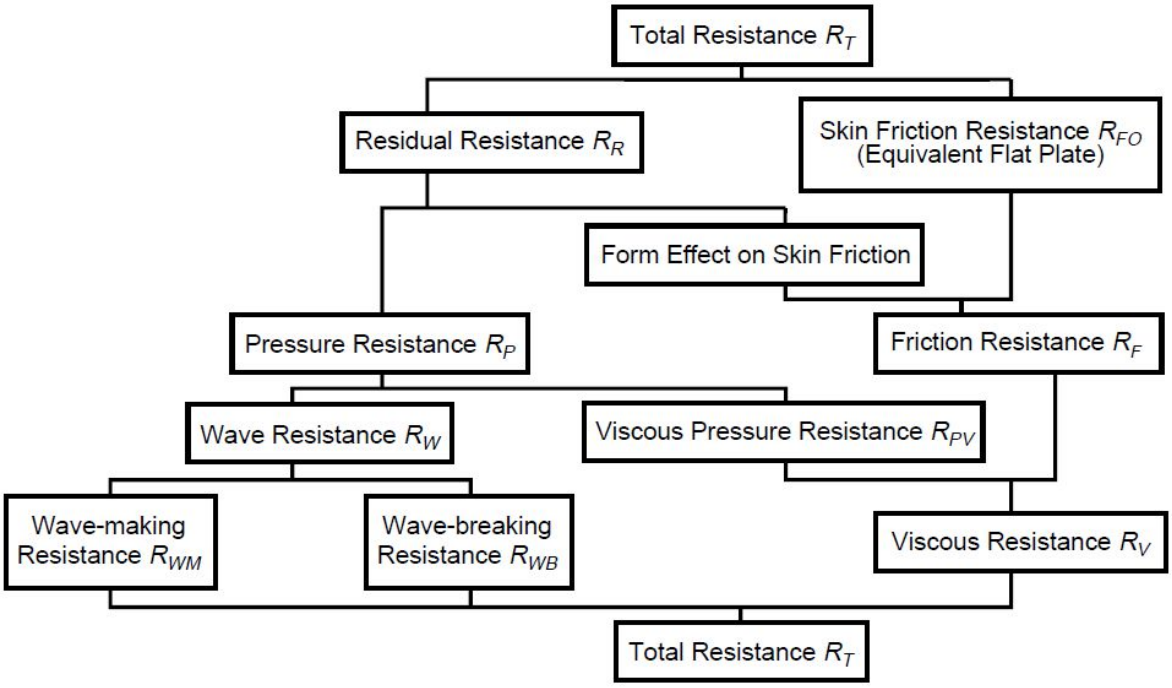

Figure 17: Decomposition of ship resistance components [9]

As the resistance of a full scale ship cannot be measured directly our knowledge comes from model tests. Different resistance prediction methods exist that yield reasonably accurate estimates of the resistance. This is necessary for the determination of the power requirements of the vessel

The resistance estimation methods depending on the ship type such as the ITTC, Hughes, SSPA, BSRA, Lap Keller, Holtrop & Mennen and Harvald methods. From the aforementioned Harvald's method was employed [8]. Harvald's method is relatively simple and yields satisfactory results. A short description of the method is presented in Figure 18 [9]

Year published: 1965, 1974

Basis for procedure: Evaluation of well-known resistance calculation procedures (Taylor, Lap, Series 60, Gothenborg, BSRA, etc.)

Description of main value: Residual resistance coefficient $C_R = R_R/((\rho/2) \cdot V^2 \cdot S)$ as $f(F_{nWL}$ or $V/\sqrt{L_{wl}}, L_{wl}/\nabla^{1/3}, C_{P,WL})$
Friction resistance coefficient $C_F = R_F/((\rho/2) \cdot V^2 \cdot S)$ as $f(L_{wl}, V_{kn})$

Target value: Total resistance R_T [kp]

Input values

L_{wl}, $F_{nWL} = V/\sqrt{g \cdot L_{wl}}$, B/T, lcb, frame form, A_{BT} (bulb), S, $C_{P,WL}$, $L_{wl}/\nabla^{1/3}$

Range of variation of input values

$0.15 \leq F_{n,WL} \leq 0.44$; $0.5 \leq C_{P,WL} \leq 0.8$; $4.0 \leq L_{wl}/\nabla^{1/3} \leq 8.0$; lcb before lcb standard; Correction for A_{BT} only for $0.5 \leq C_{P,WL} \leq 0.6$

Remarks

1. Influence of bulb taken into account.
2. Reference to length in WL.
3. Area of application: universal, tankers.
4. The correction for the centre of buoyancy appears (from area to area) overestimated.
5. The procedure underestimates resistance for ships with small L/B.

Figure 18: Resistance estimation procedure according to Guldhammer-Harvald [9]

The resistance estimation for PRINSESSE BENEDIKTE [10] at a mean draught of 5.30 m was available. Before calculating the resistance for the steel and the retrofitted case at the average loading condition it was decided to recreate the available resistance data using Harvald's method. As expected some deviation was noted between the method\s prediction and the available results for the ship. To minimize this it was decided to calibrate to match exactly the measured resistance from the model tests. The calibration was performed by changing the value of the appendages resistance coefficient for each speed. In reality this coefficient is to be kept constant as it is related to the vessel's appendages which are independent of speed.

In most cases the resistance measurements will not be available to the designer. In that case the resistance estimation will have to rely solely on the predictions of the selected method.

The ship's resistance for deep water after calibrating the method is depicted in Figure 19 and is identical to the resistance values of the vessel's resistance estimation report. The contribution of the wind/air resistance has not been taken into account in this case.

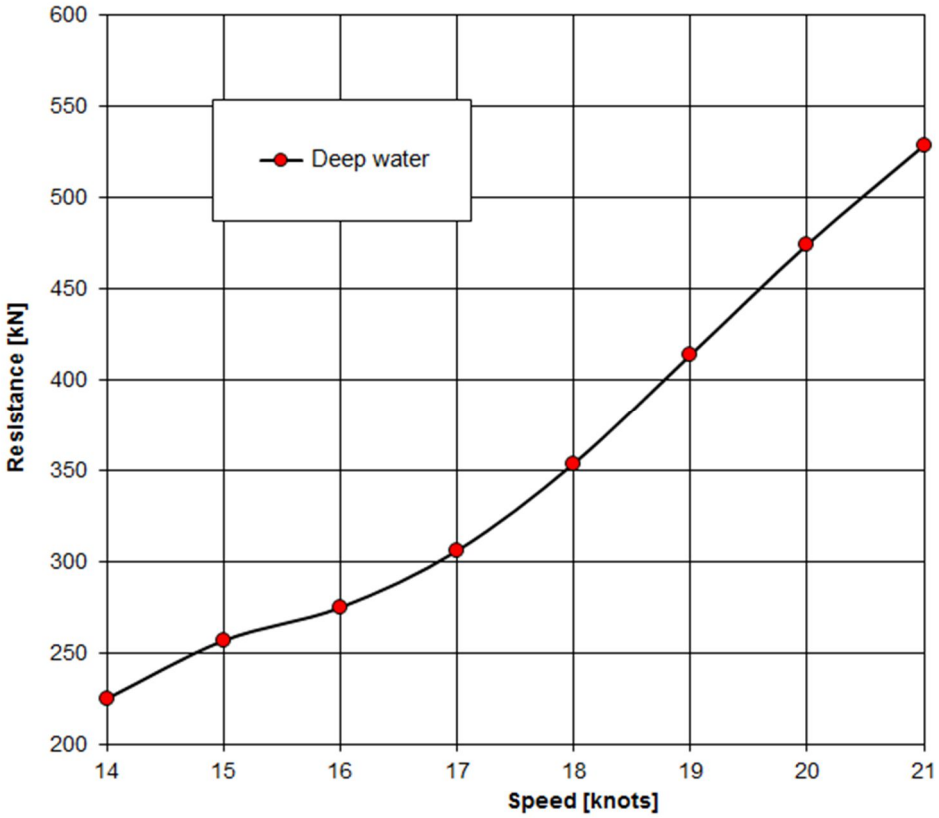

Figure 19: Resistance estimation

Table 4: Calculated resistance for

Speed [knots]	Resistance [kN]
14	225
15	256
16	275
17	306
18	353
19	413
20	417
21	528

After calibrating the method to reproduce the results from the towing tank tests, the input parameters corresponding to the draught of the steel case for the average loading conditions have been input. The resistance and propulsion power at both shallow and deep waters have been calculated. The ship resistance increases with decreasing water depth. For the given route an average depth of 18 m was considered. As the draught decreases the area the friction resistance is reduced. At the same time the area above the waterline increases which lead to an increase on the added resistance due to the wind. Typically for commercial ships air resistance represents about 2% of the total resistance [11]. Nevertheless in ship types such as containerships, RORO and ferries the added wind resistance can be significant. At the present study an average wind speed of 6m/s was taken into account which corresponds to the annual average wind speed in the Rødby area [12]

As stated in the previous chapter the draught changed from 5.035m to 4.87m after the conversion. Based on the existing hydrostatic tables and line plans the new values for the relevant input parameter values have been identified and the resistance of the ship for these conditions calculated. The resistance calculations have been performed with and without the contribution of wind for deep water and shallow water assuming that the water depth is 18m.

For the derivation of the propulsion power, apart from the total propulsion coefficient an additional electrical/mechanical transmission efficiency factor was implemented to account for the efficiency of the electric motors. The results are presented in Tables 5 and 6.

Table 5: Resistance & propulsion power for the original design at the average loading condition

Original design average loading case				
	Deep Water			
Speed [knots]	Total Resistance (no wind resistance) [kN]	Propulsion Power [kW]	Total Resistance (+ wind resistance) [kN]	Propulsion Power [kW]
14	219	2798.9	249	3220.0
15	249	3421.1	281	3894.4
16	267	3892.2	301	4416.7
17	297	4594.4	332	5176.7
18	343	5628.9	380	6274.4
19	400	6953.3	438	7666.7
20	457	8378.9	497	9162.2
21	507	9754.4	548	10610.0
	Shallow Water			
Speed [knots]	Total Resistance excluding the wind resistance [kN]	Propulsion Power [kW]	Total Resistance including the wind resistance [kN]	Propulsion Power [kW]
13.6	219	2725.6	249	3128.9
14.5	249	3323.3	281	3774.4
15.41	267	3768.9	301	4266.7
16.31	297	4433.3	332	4982.2
17.18	343	5407.8	380	6011.1
18.01	400	6644.4	438	7304.4
18.81	457	7954.4	497	8671.1
19.57	507	9188.9	548	9961.1

Table 6: Resistance & propulsion power for the retrofitted design at the average loading condition

Retrofitted design average loading case				
	Deep Water			
Speed [knots]	Total Resistance (no wind resistance) [kN]	Propulsion Power [kW]	Total Resistance (+ wind resistance) [kN]	Propulsion Power [kW]
14	216	2482	246	2864

15	246	3035	278	3464
16	264	3456	298	3932
17	294	4083	329	4610
18	339	5004	376	5588
19	396	6183	434	6829
20	452	7456	492	8166
21	502	8693	543	9467
	Shallow Water			
Speed [knots]	Total Resistance (no wind resistance) [kN]	Propulsion Power [kW]	Total Resistance (+ wind resistance) [kN]	Propulsion Power [kW]
13.6	216	2423	246	2790
14.54	246	2955	278	3365
15.46	264	3354	298	3807
16.35	294	3949	329	4447
17.22	339	4817	376	5365
18.06	396	5920	434	6520
18.85	452	7092	492	7744
19.61	502	8204	543	8906

The propulsion power at shallow waters as a function of the vessel's speed is illustrated in Figure 20 for the original case and the conversion. Additionally the effect of the wind resistance to the propulsion power is illustrated by performing the calculations for both when the wind resistance is added and when it is ignored.

Evaluating the results it seems that the reduction in resistance is practically negligible ranging from 1.2% for low speeds to 0.8% for high speeds. This is caused by the fact that the draught change is not significant resulting in a reduction of the wetted area by merely 67 m^2 (2.5%) and an increase of 5m^2 (<1%) for the projected area needed for the calculation of the wind resistance.

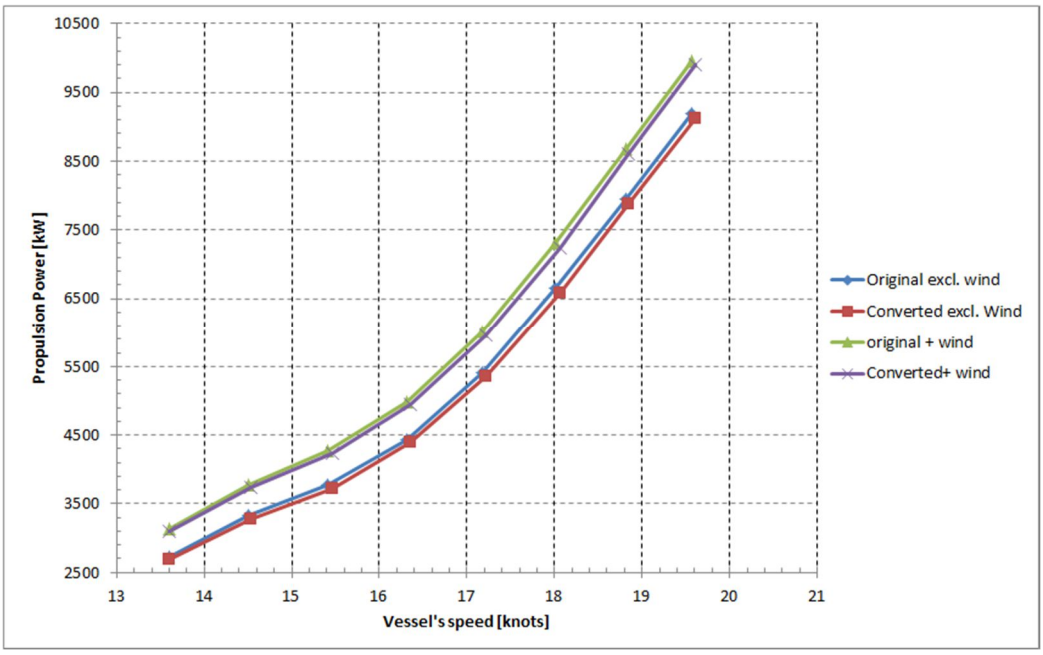

Figure 20: Propulsion power versus speed

6 Fuel consumption

Having calculated the propulsion power, the fuel consumption can be estimated considering the ship's route. According to the available data provided by Scandlines the ferry completes 8300 journeys per year and the annual fuel consumption is 7300 tons. At each trip the vessel spends 45 minutes sailing between the two ports at an average speed of 15 kn. Approximately 15 minutes are needed at the port for the embarkation and disembarkation of passengers

At the port, power is not needed for the propulsion. Instead, the power consumption corresponds to other purposes such as lighting, communication, refrigeration, climate control and others. The power consumption at the port is referred to as the hotel load. The estimated hotel load for PRINSESSE BENEDIKTE is 1000kWh [13]. The specific fuel consumption is considered equal to 220 gr/kwh [2].

The propulsion power for the shallow water has been selected for the calculations in an attempt to be more realistic. Based on these data the fuel consumption per trip is equal to:

Original case:

Estimated consumption per trip

0.75 [h] x 4044.8 [kW] x 220 [gr/kWh] + 0.25 [h] x 1000 [kW] x 220 [gr/kWh] = 667.4 kg/trip

Estimated consumption per year

8300 x 667.4 = 5540 tons

Retrofitted case:

Estimated consumption per trip

0.75 [h] x 3984.4 [kW] x 220 [gr/kWh] + 0.25 [h] x 1000 [kW] x 220 [gr/kWh] = 657.4 kg/trip

Estimated consumption per year

8300 x 657.4 = 5456.4 tons

Comparing the estimated fuel consumption with the annual recorded fuel consumption a notable deviation of 25% is noted. This deviation stems from the fact that the followed approach does not account for the fuel consumption of the acceleration and deceleration times which for such a sort route make up for a significant part of the vessels service time (17 minutes per trip). In addition, in the areas close to the ports the water depth is less than 10m which further increases the ship resistance during the acceleration periods. Other factors that affect the resistance and have not been accounted for are the wave resistance and the additional consumption due to steering/manoeuvring. Nonetheless, the followed approach can provide a simple estimation of how the fuel consumption can be affected.

Comparing the fuel consumption for the original and retrofitted case the fuel savings are about 1.5 % (84 tons) of the initial annual estimation which reflects the reduction of the ship's resistance due to the reduced draught. In reality this percentage would be higher as higher fuel savings are expected during the acceleration and deceleration of the vessel.

7 Conclusions

Evaluating the effects that the implementation of composite materials has had on the ship the following conclusions can be drawn.

The design procedure is more complicated compared to the steel analysis nevertheless it is possible to be accounted for by combining existing rules and regulations. The final design is less complicated than the equivalent steel one with the number of stiffeners being dramatically reduced.

The partial conversion of the vessel's superstructure results to a reduction of the Lightship ranging from 4.8% to 5.4% depending on the core material selected. Therefore in the studied case the weight change does not represent the most important parameter for the selection of the core. Other parameters such as the availability, acquisition and sandwich production cost and the behavior of the core in the case of fire are deemed more governing.

The reduction of the Lightship in combination with the position of the center of gravity of the converted parts led to a significant increase of the vessel's overall stability, improving static, dynamic and the range of stability.

The draught change in the average loading condition does not significantly affect the resistance of the ship as the propulsion power reduction was around 1% for the service speed of 15 knots. This in turn led to a small fuel consumption decrease of about 1.5% per year which does not signify a potential source of cost saving for the ship-owner.

This observation does not come as a surprise given that it was decided to keep the same general arrangement of the superstructure, given that the original requirements and constraints were unknown. It is considered more profitable to increase the payload to displacement ratio by decreasing the lightship mass than to try to save on fuel by reducing the draught. In addition, the ship that was selected as the demonstration case does not encounter any challenges in reality that would necessitate such a conversion.

Last but not least it should be emphasized that the material acquisition and fuel consumption costs do not account for the total of the vessel's life cycle cost and should not be regarded as the sole criteria for such options. On the contrary these could be misleading if all the associated costs are not well estimated and taken into consideration.

8 References

[1] International Maritime Organization. SOLAS, Consolidated Edition 2009. International Convention for the Safety of Life at Sea. (2009)
[2] A. Papanikolaou, Ship Design Methodologies of Preliminary Design, Springer, Dordrecht, 2014, pp. 14-27
[3] DIAB, Guide to core and sandwich, 2012
[4] DNV Rules for Classification of Ships, January 2014, Det Norske Veritas
[5] DNV Rules for Classification of High Speed Light Craft and Naval Surface Craft, January 2014, Det Norske Veritas
[6] M. D. Jacobsen, N. Hjørnet Private communication, 2014
[7] C. Nicolajsen, V. Karatzas Private communication, 2015
[8] Harvald S. A. (1983), Resistance and Propulsion of Ships, Wiley 1983
[9] H. Schneekluth (1998), Ship Design for Efficiency and Economy
[10] Force Technology 107-27425 Report No.1 Rødby-Putgarten Ferry-Final Thruster Head Boxes, 2007
[11] MAN Diesel & Turbo, Basic Principles of Ship Propulsion
[12] https://weather-and-climate.com
[13] H. O. Kristensen, V. Karatzas, Private communication, 2016

9 Appendix

PET core

Saloon Deck 17700 o. BL

Item	Area [m^2]	Length [m]	Weight [kg/m^2]	Extra resin [kg/m^2]	Weight [kg/m]	Total weight [kg]
Superstructure Panel	1440.13		12.2	4		23330.1
Horizontal side stiffeners		312.5			3.067	958.4
Vertical front stiffener		833.5			3.464	2887.5
Bonding/closing tape		644.6			0.651	419.9
Bulkheads	74.751		9.85	3		960.6
Bulkhead stiffeners		62			4.812	299.7
Bulkhead bonding		348			0.651	226.7
Bulkhead lower closing tape (Connection to steel)		265.97			0.651	173.3
Bulkhead reinforcement	46.4		0.835			38.7
Bulkhead/deck connection, adhesive		265.97			2.231	593.4
Deck/superstructure connection, adhesive		258.39			2.231	576.5
Pillar deck support (hot spots)	9.5		10.377	2		117.6
Various 5 %						1529
Σ:						**32111**

Sun Deck 20600 o. BL

Item	Area [m^2]	Length [m]	Weight [kg/m^2]	Extra resin [kg/m^2]	Weight [kg/m]	Total weight [kg]
Deck	2101.44		14.6	3		36985.3
Long. Sun deck beam		738.05			13.081	9654.7
Trans. Sun deck beam		291.82			31.145	9088.8
Bonding/closing tape		426.78			0.651	278.0
Bulkheads	94.261		9.85	3		1211.3
Bulkhead stiffeners		79			4.812	377.9
Bulkhead bonding		365.4			0.651	238.0
Bulkhead reinforcement	19.72		0.835			16.5
Horizontal side stiffeners		260.4			3.067	798.6
Pillar deck support (hot spots)	8.25		10.377	2		102.1
Various 5 %						2938
Σ:						**61689**

Wheelhouse Deck 23500 o. BL

Item	Area [m^2]	Length [m]	Weight [kg/m^2]	Extra resin [kg/m^2]	Weight [kg/m]	Total weight [kg]
Deck	1393.26		13.3	3		22710.1
Wheelhouse Panel	379.12		13.5	3		6255.5
Wheelhouse vertical stiffener		180.76			5.052	1826.4
Wheelhouse horizontal stiffener	14.1	100.52	13.3	3	2.002	862.1
Funnel	488.27		12.2	3		7421.7
Mast	127.432		13.02	3		2041.5
Mast bonding		140.2			0.651	91.3
Long. Wheelhouse deck beam		333.46			6.899	2300.7
Trans. Wheelhouse deck beam		233.7			11.02	2576.2
Bonding/closing tape		510			0.651	332.2
Various 5 %						2320.9
Σ:						**48739**

Total composite superstructure weight

Item	Total weight [kg]
Saloon Deck 17700 o. BL	32111
Sun Deck 20600 o. BL	61689
Wheelhouse Deck 23500 o. BL	48739
Σ:	**142539**

Figure A1: PET core weight details

PVC core

Saloon Deck 17700 o. BL

Item	Area [m^2]	Length [m]	Weight [kg/m^2]	Extra resin [kg/m^2]	Weight [kg/m]	Total weight [kg]
Superstructure Panel	1440.13		11.77	4		22710.9
Horizontal side stiffeners		312.5			2.793	872.9
Vertical front stiffener		833.5			3.100	2583.5
Bonding/closing tape		644.6			0.651	419.9
Bulkheads	74.751		8.65	3		870.8
Bulkhead stiffeners		62			4.44672	277.0
Bulkhead bonding		348			0.651	226.7
Bulkhead lower closing tape (Connection to steel)		265.97			0.651	173.3
Bulkhead reinforcement	46.4		0.835			38.7
Bulkhead/deck connection, adhesive		265.97			2.231	593.4
Deck/superstructure connection, adhesive		258.39			2.231	576.5
Pillar deck support (hot spots)	9.5		10.377	2		117.6
Various 5 %						1473
Σ:						30934

Sun Deck 20600 o. BL

Item	Area [m^2]	Length [m]	Weight [kg/m^2]	Extra resin [kg/m^2]	Weight [kg/m]	Total weight [kg]
Deck	2101.44		14.06	3		35850.6
Long. Sun deck beam		738.05			11.941	8813.4
Trans. Sun deck beam		291.82			28.368	8278.2
Bonding/closing tape		426.78			0.651	278.0
Bulkheads	94.261		8.65	3		1098.1
Bulkhead stiffeners		79			4.44672	349.3
Bulkhead bonding		365.4			0.651	238.0
Bulkhead reinforcement	19.72		0.835			16.5
Horizontal side stiffeners		260.4			2.793	727.3
Pillar deck support (hot spots)	8.25		10.377	2		102.1
Various 5 %						2788
Σ:						58539

Wheelhouse Deck 23500 o. BL

Item	Area [m^2]	Length [m]	Weight [kg/m^2]	Extra resin [kg/m^2]	Weight [kg/m]	Total weight [kg]
Deck	1393.26		12.77	3		21971.7
Wheelhouse Panel	379.12		10.58	3		5148.4
Wheelhouse vertical stiffener		180.76			4.669	1688.0
Wheelhouse horizontal stiffener	14.1	100.52	12.77	3	1.762	799.0
Funnel	488.27		11.77	3		7211.7
Mast	127.432		14.69	3		2254.3
Mast bonding		140.2			0.651	91.3
Long. Wheelhouse deck beam		333.46			6.101	2034.6
Trans. Wheelhouse deck beam		233.7			10.02	2341.8
Bonding/closing tape		510			0.651	332.2
Various 5 %						2193.7
Σ:						46067

Total composite superstructure weight

Item	Total weight [kg]
Saloon Deck 17700 o. BL	30934
Sun Deck 20600 o. BL	58539
Wheelhouse Deck 23500 o. BL	46067
Σ:	135540

Figure A2: PVC core weight details

Balsa Core

Saloon Deck 17700 o. BL

Item	Area [m^2]	Length [m]	Weight [kg/m^2]	Extra resin [kg/m^2]	Weight [kg/m]	Total weight [kg]
Superstructure Panel	1440.13		11.4	4		22178.0
Horizontal side stiffeners		312.5			2.923	913.4
Vertical front stiffener		833.5			3.272	2727.5
Bonding/closing tape		644.6			0.651	419.9
Bulkheads	74.751		9.05	5		1050.3
Bulkhead stiffener		79			4.620	364.9
Bulkhead bonding		348			0.651	226.7
Bulkhead lower closing tape (Connection to steel)		265.97			0.651	173.3
Bulkhead reinforcement	46.4		0.835			38.7
Bulkhead/deck connection, adhesive		265.97			2.231	593.4
Deck/superstructure connection, adhesive		258.39			2.231	576.5
Pillar deck support (hot spots)	9.5		10.377	2		117.6
Various 5 %						1469
Σ:						30849

Sun Deck 20600 o. BL

Item	Area [m^2]	Length [m]	Weight [kg/m^2]	Extra resin [kg/m^2]	Weight [kg/m]	Total weight [kg]
Deck	2101.44		13.6	4		36985.3
Long. Sun deck beam		738.05			12.481	9211.9
Trans. Sun deck beam		291.82			29.683	8662.2
Bonding/closing tape		426.78			0.651	278.0
Bulkheads	94.261		9.05	5		1324.4
Bulkhead Stiffener		79			4.62	364.9
Bulkhead bonding		365.4			0.651	238.0
Bulkhead reinforcement	19.72		0.835			16.5
Horizontal side stiffeners		260.4			2.923	761.1
Pillar deck support (hot spots)	8.25		10.377	2		102.1
Various 5 %						2897
Σ:						60842

Wheelhouse Deck 23500 o. BL

Item	Area [m^2]	Length [m]	Weight [kg/m^2]	Extra resin [kg/m^2]	Weight [kg/m]	Total weight [kg]
Deck	1393.26		12.3	4		22710.1
Wheelhouse Panel	379.12		12.7	4		6331.3
Wheelhouse vertical stiffener		180.76			4.850	1753.6
Wheelhouse horizontal stiffener	14.1	100.52	12.3	3	1.876	808.6
Funnel	488.27		11.37	4		7504.7
Mast	127.432		14.68	4		2380.4
Mast bonding		140.2			0.651	91.3
Long. Wheelhouse deck beam		333.46			6.479	2160.6
Trans. Wheelhouse deck beam		233.7			10.50	2452.8
Bonding/closing tape		510			0.651	332.2
Various 5 %						2326.3
Σ:						48852

Total composite superstructure weight

Item	Total weight [kg]
Saloon Deck 17700 o. BL	30849
Sun Deck 20600 o. BL	60842
Wheelhouse Deck 23500 o. BL	48852
Σ:	140543

Figure A3: Balsa core weight details

DWT breakdown for CONDITION 5

Loading Condition 5: Trailers, cars & Pass. 100% bunkers

Contents in tanks	Weight	LCG	TCG	VCG	FSM	LCG*W	VCG*W	TCG*W
	t	m	m	m	tm	tm	tm	tm
DIESEL OIL	217	85.96	-5.35	3.75	260.76	18653.32	813.75	-1160.95
FRESH WATER	90	37.56	-0.96	4.76	91.70	3380.40	428.40	-86.40
HEELING WATER	258	65.61	-1.48	4.02	186.23	16927.38	1037.16	-381.84
LUBRICATING OIL	44	88.30	2.58	5.50	8.29	3885.20	242.00	113.52
MISCELLANEOUS	35	65.12	8.38	4.52	9.12	2279.20	158.20	293.30
WATER BALLAST	95	67.00	0.00	5.90	189.55	6365.00	560.50	0.00
TOTAL	739	69.68	-1.65	4.38	745.65	51490.50	3240.01	-1222.37

Description	# Number	Weight	LCG	TCG	VCG	Aft	FWD	Weight per unit	LCG*W	VCG*W	TCG*W
		t	m	m	m	m	m	t	tm	tm	tm
Provisions	-	40	67.0	10.0	22.00	18.00	116.00	-	2680.00	880.00	400.00
Stores	-	45	67.0	0.0	19.00	44.60	86.40	-	3015.00	855.00	0.00
Crew	-	5	33.4	0.0	22.00	21.50	44.60	-	167.00	110.00	0.00
Passengers	900	68	67.0	0.0	22.00	21.50	112.50	0.08	4556.00	1496.00	0.00
Trailers on main deck	580	1438	67.0	0.0	10.80	7.50	126.50	2.48	96346.00	15530.40	0.00
Cars on upper Deck	126	158	67.0	0.0	15.10	16.60	117.40	1.25	10586.00	2385.80	0.00
TOTAL		1754	66.9	0.2	12.12				117350.00	21257.20	400.00

Figure A4: Deadweight details for loading condition 5

DWT breakdown for Average Loading Condition

Average Loading Condition : 181 pass. 13 Trailers, 46 cars

Contents in tanks	Weight	LCG	TCG	VCG	FSM	LCG*W	VCG*W	TCG*W
	t	m	m	m	tm	tm	tm	tm
DIESEL OIL	60	85.96	-5.35	3.75	260.76	5157.60	225.00	-321.00
FRESH WATER	90	37.56	-0.96	4.76	91.70	3380.40	428.40	-86.40
HEELING WATER	258	65.61	-1.48	4.02	186.23	16927.38	1037.16	-381.84
LUBRICATING OIL	44	88.30	2.58	5.50	8.29	3885.20	242.00	113.52
MISCELLANEOUS	35	65.12	8.38	4.52	9.12	2279.20	158.20	293.30
WATER BALLAST	0	67.00	0.00	5.90	0.00	0.00	0.00	0.00
TOTAL	487	64.95	-0.79	4.29	556.10	31629.78	2090.76	-382.42

Description	# Number	Weight	LCG	TCG	VCG	Aft	FWD	Weight per unit	LCG*W	VCG*W	TCG*W
		t	m	m	m	m	m	t	tm	tm	tm
Provisions	-	40.00	67.00	10.00	22.00	18.00	116.00	-	2680.00	880.00	400.00
Stores	-	45.00	67.00	0.00	19.00	44.60	86.40	-	3015.00	855.00	0.00
Crew	-	5.00	33.40	0.00	22.00	21.50	44.60	-	167.00	110.00	0.00
Passengers	181	13.68	67.00	0.00	22.00	21.50	112.50	0.08	916.26	300.86	0.00
Trailers on main deck	13	32.23	67.00	0.00	10.80	7.50	126.50	2.48	2159.48	348.10	0.00
Cars on upper Deck	46	57.68	67.00	0.00	15.10	16.60	117.40	1.25	3864.73	871.01	0.00
TOTAL		193.59	66.13	2.07	17.38				12802.47	3364.96	400.00

Figure A5: Deadweight details for average loading condition

Annex C: Thermal numerical modelling of joints at steel/FRP interface

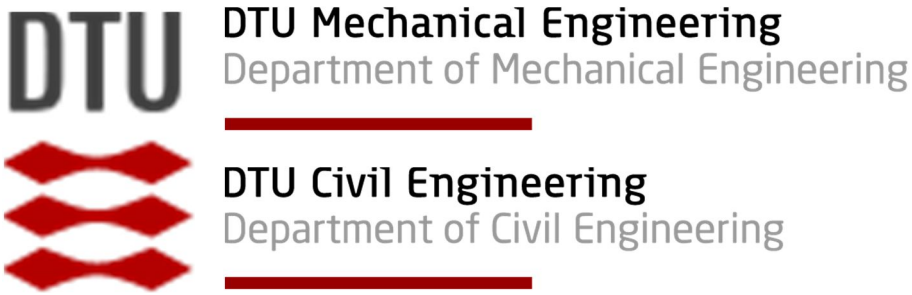

Date : January 2016
Project name : COMPASS – COMposite superstructures for large PASsenger Ships

Author : Thomas Hulin

Content

1 Introduction

The present document is focussed on the numerical study at elevated temperatures of joints between the steel hull and Glass Fibre Reinforced Polymer (GFRP) superstructure proposed as a case study for the passenger ship Prinsesse Benedikte. The report presents the various challenges connected with this approach, their respective influence on results and predictions, and preliminary conclusions. Under several assumptions outlined further in the report, the evolution of temperatures within the joint, and a study of different ways to protect the structural integrity of the joint in the case of a fire are proposed and discussed.

It is important to remember that no experimental verification of the model could be performed due to time constrains. The proposed results should be taken with care, and within the limits set in the discussions. They address the safety concerns around the use of FRP materials for passenger ships, and outline the possibilities to use such materials in such applications.

1.1 Problem definition

FRP materials are made with fibres (most often glass fibres) held by polymer binders, such as epoxy resins, which are not temperature resistant. When exposed to heat, such polymers will undergo changes of their material state (Figure 1), progressive softening of their molecular bonds and ultimately breakage of these bonds. At ambient and low temperatures, their state is qualified as glassy and their E-modulus remains constant at its maximum value. When temperature rises, the material enters the glass transition phase in which it softens and E-modulus decreases. It then experiences a sudden and sharp drop down to 1/4th of its original E-modulus and enters the leathery state (Mahieux and Reifsnider 2001, Bai et al. 2008, Bai and Keller 2009). The glass transition temperature (T_g) defines the point at which the shift between glassy and leathery states occurs. The Heat Deflection Temperature (HDT) indicates the temperature at which the polymer starts losing its stiffness and enters the glass transition zone. In structural applications, where stiffness is a key design parameter, it is critical that the material remains below the HDT.
For most commercially available epoxy resins, the HDT is located around 65 °C. To stay on the safe side it is considered that even high temperature epoxies cured with a specific curing agent should remain below HDT. It is however difficult to estimate until which temperature the ambient mechanical properties remain, and how fast they degrade with temperature. To preserve the structural integrity of the joint, it is suggested that the temperature of FRP reach a maximum of 45 °C.
Such a low temperature could be reached during normal operation of the ship due to exposure to sun. It is a concern for all surfaces on the outside of the ship and calls for direct protection from sunlight.

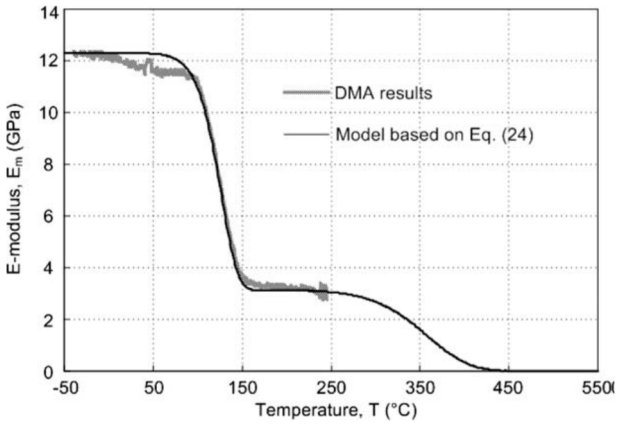

Figure 1 – Material states of softening polymer and decrease of E-modulus with temperature (Bai et al. 2008).

1.2 Limitations

The modelling work is proposed as a preliminary assessment, and should be investigated further before definite conclusions can be given. Several limitations should be taken into account:

- For some materials, thermal properties are difficult to obtain, and usually not well described in literature. Temperature dependent values are seldom available. This is particularly true for insulation materials (mineral wool), polymers used as insulation (PET, PUR, EPS) or as matrix for FRPs (epoxy). The values chosen for the present study are to the author's best knowledge.
- Heat conduction between two materials is not perfect, due to contact resistance. This is due to the microscopic asperities of the surfaces of the materials in contact, leading to a dependence of heat conduction on the real area of contact between the two materials (Mikić 1974, Matsumoto et al. 1977, Madhusudana 1993, Savija et al. 2003, Singhal et al. 2005). The real area of contact depends on the surface roughness, size of asperities, and applied pressure.
  These interfaces have been described for a limited range of materials, and though literature is available for steel/polymer interface at high temperature (when the polymer can flow, Bendada et al. 2004, Massé 2004, Dawson et al. 2008), there is little or no data at lower temperature ranges.
- Heat input is difficult to characterize. The steel part of the joint is not exposed to heat directly, but placed on top of the deck of the car park of the ship. A fire could occur below this deck and then heat up the joint. The deck is fire insulated with non-combustible mineral wool which is not a well characterised material. Numerical modelling of the deck for heat transfer remains a challenge; therefore the heat input for the joint model is a major concern.
- No experimental verification is produced so far for the behaviour of the joint at high temperature, which calls for great care when analysing the modelling results.

1.3 Geometry of the joint

The general geometry of the joint is shown in Figure 2. Component A is made of steel and used to distribute the stress coming from bolt tensioning. Component B is a thermal insulator which will be subsequently investigated in the report. Steel/FRP, steel/insulator and insulator/FRP interfaces are sealed using Sikaflex 221 (PUR based material). FRP is introduced under the form of a sandwich element with GFRP skins and a core made of Divinycell P (PET material).

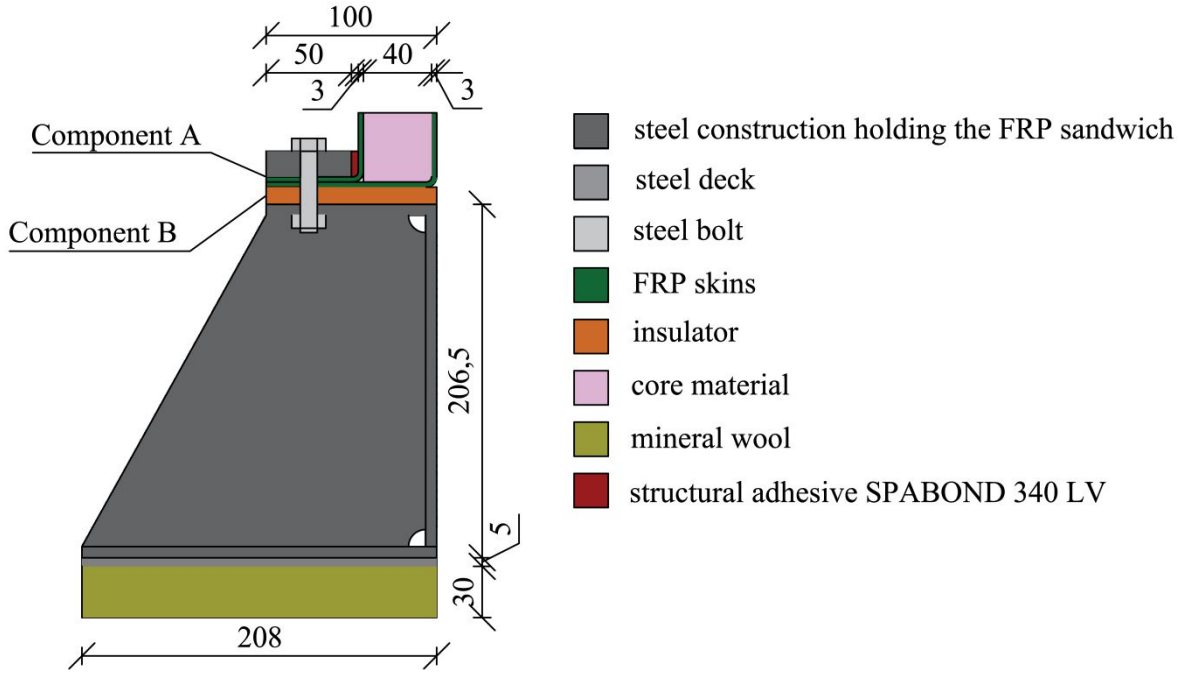

Figure 2 – Geometry of the studied joint

The spacing between the axis of two bolts is 100 mm. Bolts have a diameter of Ø10 mm. The steel plates chosen for the structure have a thickness of 6.5 mm. The sealing choice between the sandwich element and Component A is presented in Figure 2, and the gap between Component A and the sandwich element is filled with the structural adhesive SPABOND 340LV.

2 MODEL PRESENTATION

2.1 Procedure, assumptions, and geometry

The interface between steel and GFRP is assumed to be fully conductive. This approach is conservative, but can be justified. In fact, the thin layer of sealing material gluing GFRP to steel is applied in a viscous state, and can be assumed to create an enhanced real area of contact between the two materials, filling in the larger asperities. Furthermore, the interface is maintained tight by the bolt, which applies additional pressure (pre-tensioned at 75% of their proof load) increasing heat conduction at the interface.

Symmetry is used to simplify the modelling carried out in 3D. The model describes the bolt and bracket. Only the first 100 mm of the height of the sandwich element are considered then sealed as a perfect insulator. This assumption is made on account of the low temperatures reached, and that the length of core material in the vertical direction is high so it can be assumed to perform as a perfect insulator. The geometry reproduces Figure 2, and is presented in Figure 3.

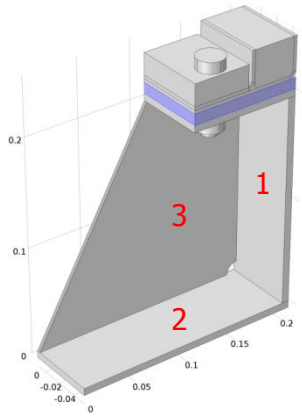

Figure 3 – Model geometry. The blue part represents the insulator, which is not present in all simulations.
1: vertical steel plate; 2: lower horizontal steel plate; 3: bracket

2.2 Modelling equations

Field equation
The model follows the standard heat equation. When possible, the material properties are temperature dependent.

Boundary conditions
Heat input is applied as an incident heat flux. Additional discussion will be provided further in the report.
When applicable, cooling heat transfer with the environment is allowed via convection and radiation, respectively Eq.1 and Eq.2.

$$\boldsymbol{n}.\boldsymbol{q} = h(T - T_{ambient}) \quad (1)$$

$$\boldsymbol{n}.\boldsymbol{q} = \varepsilon\sigma(T^4 - T_{ambient}^4) \quad (2)$$

where h is the convective heat transfer coefficient, ε is the surface emissivity of the material, σ is the Stefan-Boltzmann constant, $T_{ambient}$ is the temperature of the environment in contact with the boundary, $\boldsymbol{q}$ is the heat flux passing through this boundary, and $\boldsymbol{n}$ is the direction normal to the boundary.
The heat transfer coefficient for convection is taken in the Eurocode recommendations (Eurocode 1-1-2) which propose h_{in} = 25 W.m^{-2}.K^{-1} when using the ISO time-temperature curve, and h_{out} = 9 W.m^{-2}.K^{-1} when combined with radiation. These values are assumed valid for all materials by lack of other proposed values.

The cooling boundary conditions depend on the situation. This joint will be used both inside the ship and for the outer structure. The boundary conditions are therefore defined as:

- BC1 – The joint is considered in full contact with the outside environment. Heat exchange with the outside environment is allowed from all surfaces via convection and radiation.
- BC2 – It corresponds to the inside of the ship. The joint is insulated from all sides and heat transfer is totally prevented. This condition is severe and conservative, since an air gap will most likely exist between the fire insulation and parts of the joint structure.
- BC3 – It corresponds to the outside of the ship. The joint is insulated only on the surface turned towards the ship. The surface turned towards the water is allowed to exchange heat with the outside environment, via convection and radiation. This condition might change if special protection against corrosion, fire, or sun exposure is chosen.

2.3 Thermal material properties

The values are given for all materials except the candidates for insulator. These will be described individually in their respective parts.
Thermal material properties are temperature-dependent when possible. The values are given to the author's best knowledge from published literature. Further refinements are encouraged.

Steel
Naval construction uses Grade A steel. Ambient temperature values are given by Ruukki, structural steel producer from Finland. Temperature dependencies are taken from the Eurocode 3-1-2 recommendations.
Density is taken as 7850 kg.m^{-3}. Surface emissivity for steel is set as 0.7. Thermal conductivity [W.m^{-1}.K^{-1}] is given by Eq.3 and specific heat at constant pressure [J.kg^{-1}.K^{-1}] by Eq.4.

$$k_s = 54 - 3.33 \times 10^{-2} T \quad (3)$$

$$C_{p,s} = 425 + 7.73 \times 10^{-1} T - 1.69 \times 10^{-3} T^2 + 2.22 \times 10^{-6} T^3 \quad (4)$$

Composite materials
Thermal properties for FRP skins, core material in sandwich panel, and sealant adhesive are difficult to obtain since these materials are not well characterised. The main chemical constituent has been used as reference, and associated values used for the material. All values are presented in Table 1.

Table 1 – Values for material thermal properties for composite materials

Material	Base component	Property	Value
FRP skins	Epoxy	C_p [J.kg^{-1}.K^{-1}]	1400
		k [W.m^{-1}.K^{-1}]	0.5
		ρ [kg.m^{-3}]	1851.5
Core material	PET	C_p [J.kg^{-1}.K^{-1}]	1400
		k [W.m^{-1}.K^{-1}]	0.033
		ρ [kg.m^{-3}]	110
Sealant adhesive	PUR	C_p [J.kg^{-1}.K^{-1}]	1400
		k [W.m^{-1}.K^{-1}]	0.035
		ρ [kg.m^{-3}]	1270

Thermal properties for candidate materials for the insulator
The candidate materials considered are high performance concrete, gypsum board, and structural wood.
Values for concrete are taken from the Eurocode 2.
Values for gypsum boards are from Rahmanian (2011). At the temperatures involved in this study, the specific heat can be taken as $C_{p,gypsum}$ = 950 J.kg^{-1}.K^{-1}; the thermal conductivity k_{gypsum} = 0.24 W.m^{-1}.K^{-1}; and the density ρ_{gypsum} = 800 kg.m^{-3}.
Values for wood are taken from the **Eurocode 5**.

3 HEAT INPUT INVESTIGATION

3.1 Procedure

The heat input is one of the major challenges related to the study of the joint at elevated temperatures. The joint receives heat from the fire insulated deck below. The deck consists of a steel plate protected by mineral wool. Since the behaviour of mineral wool at high temperatures is not well understood, and its thermal properties extracted so far unreliable, modelling the deck is a challenging project.
Equivalent properties (thermal conductivity, heat capacity and density) for the composite steel+wool can reproduce the temperature profile on the unexposed side of the deck at early and late exposure times on the scale of a 1 h test. Figure 4 presents a comparison between a test recording and the prediction from the model. The experimental data corresponds to the unexposed side temperature of a standard steel deck protected with mineral wool and tested in-house. As seen on Figure 4, the model cannot reproduce the heat generated in the wool during exposure to fire. Applying such a heating scenario to the joint would underestimate the actual exposure. Describing the behaviour of mineral wool is out of the scope of this project and is being carried out in the FIRETOOLS[1] project.

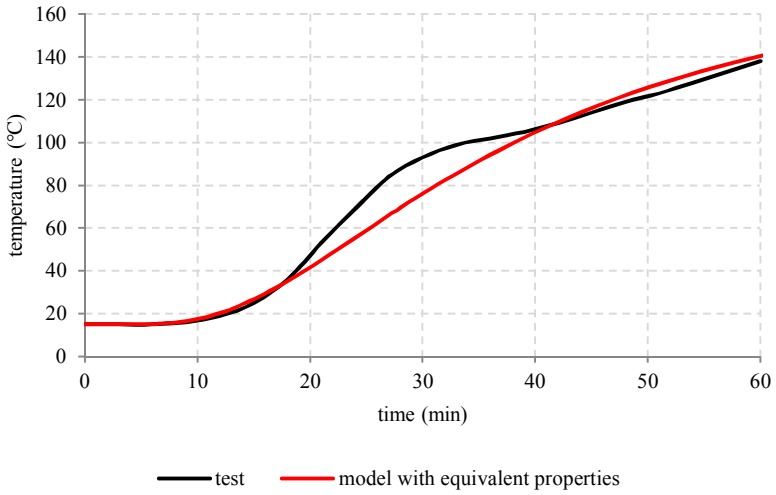

Figure 4 – Comparison between test and numerical model using equivalent thermal properties to fit data for a composite steel/mineral wool deck exposed to the ISO 834 curve

The approach proposed here is to use the experimental temperature recordings to calculate the heat flux entering the steel plate of the deck at its interface with mineral wool. This heat flux and the steel plate of the deck can then be added to the joint model for temperature calculations.

3.2 Incident heat flux calculation

In the case of a fire insulated deck taken alone and tested in a furnace under standard conditions, the unexposed side is allowed to exchange heat with the external environment. The amount of energy entering the plate should then cover the temperature rise of the plate and the losses at its unexposed surface. The calculation is based on experimental temperature recordings at the unexposed surface, performed at fixed time intervals which define a time step (3 min, 180 s). It is postulated that the temperature of the steel plate is constant through its thickness, which is reasonable considering the presence of the insulation layer.

The amount of energy entering the plate can then be expressed as

$$E_{in} = E_{T,rise} + E_{out} \quad (5)$$

[1] http://www.firetools-fp7.eu/ - the project is led by DBI and Lund University

where E_{in} is the amount of energy entering the steel plate, $E_{T,rise}$ is the amount of energy necessary to rise the temperature of the plate, and E_{out} are the energy losses from the unexposed surface. $E_{T,rise}$ and E_{out} can be expressed respectively by Eq.6 and Eq.7

$$E_{T,rise} = \rho C_p V \Delta T \quad (6)$$

$$E_{out} = At[h(T - T_{amb}) + \varepsilon\sigma(T^4 - T_{amb}^4)] \quad (7)$$

where ρ is the density of steel, C_p is the specific heat of steel, V is the volume of the plate, ΔT is the temperature rise, A is the exposed area, t is the time step, h is the convective heat transfer coefficient, ε is the emissivity, σ is the Stefan-Boltzmann constant, and T_{amb} is the temperature of the environment in contact with the unexposed surface.
Combining Eq.6 and Eq.7 together, considering the time step and a unit area, the incident heat flux can be expressed as

$$Q_{in} = \frac{\rho C_p e}{t}\Delta T + h(T - T_{amb}) + \varepsilon\sigma(T^4 - T_{amb}^4) \quad (8)$$

where e is the thickness of the steel plate.
The incident heat flux is then calculated and used in COMSOL Multiphysics to recalculate the unexposed side temperature. Two input parameters are adjusted to fit the experimental results with a proper incident heat flux, the convective heat transfer coefficient and the ambient temperature. The default values for these are h = 9 W.m^{-2}.K^{-1} and T_{amb} = 20 °C. Results for the default values are presented in Figure 5.

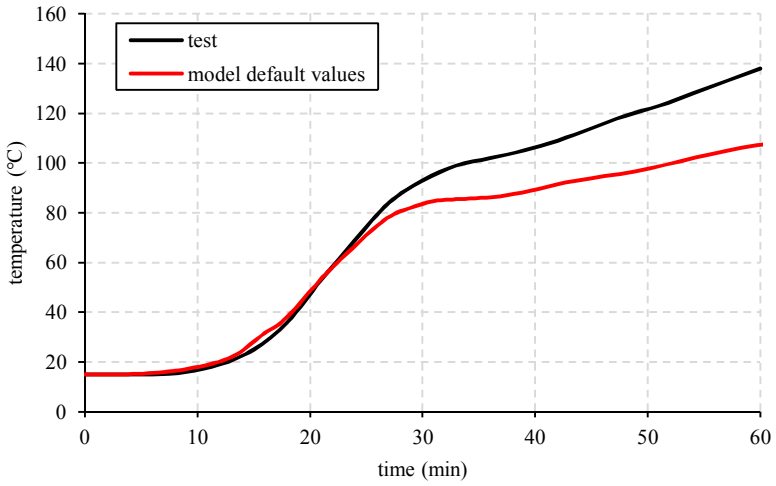

Figure 5 – Experimental recording vs. model with calculated incident heat flux for the unexposed side of the steel plate, with default values

The curves match rather well at low temperatures but the fit diverges after 25 min and 70 °C to reach a difference of 35 °C at 60 min. To get an acceptable fit, parameters h and T_{amb} can be adjusted. Changing these values will impact the amount of energy entering the plate. Lowering h leads to lower temperatures as the energy input is reduced but the exchange by radiation is still permitted. Rising h leads to higher temperatures until a limit is reached for h = 40 W.m^{-2}.K^{-1}. At that limit the fit is still not good and rising h further does not change the result. Moreover, the resulting heat flux entering the steel plate is comparable to the heat flux imposed by the furnace on the wool at 30 min of exposure, which is unrealistic (Hulin et al. 2015)
It is evident that not all the processes occurring at the boundary are fully described by the values of the parameters appearing in the equations. Further knowledge of the behaviour of the boundaries is critical to describe all fluxes in a consistent way. The results presented here should be regarded within these limitations.

An acceptable fit for the temperature of the unexposed side is obtained by raising the energy entering the plate by 50% after 27 min. The resulting temperature curve and incident heat flux are given in Figure 6. This additional energy may correspond to the heat generated within the wool by the pyrolysis of the binder used to produce it. This phenomenon also explains the difference between model and experiment seen on Figure 4.

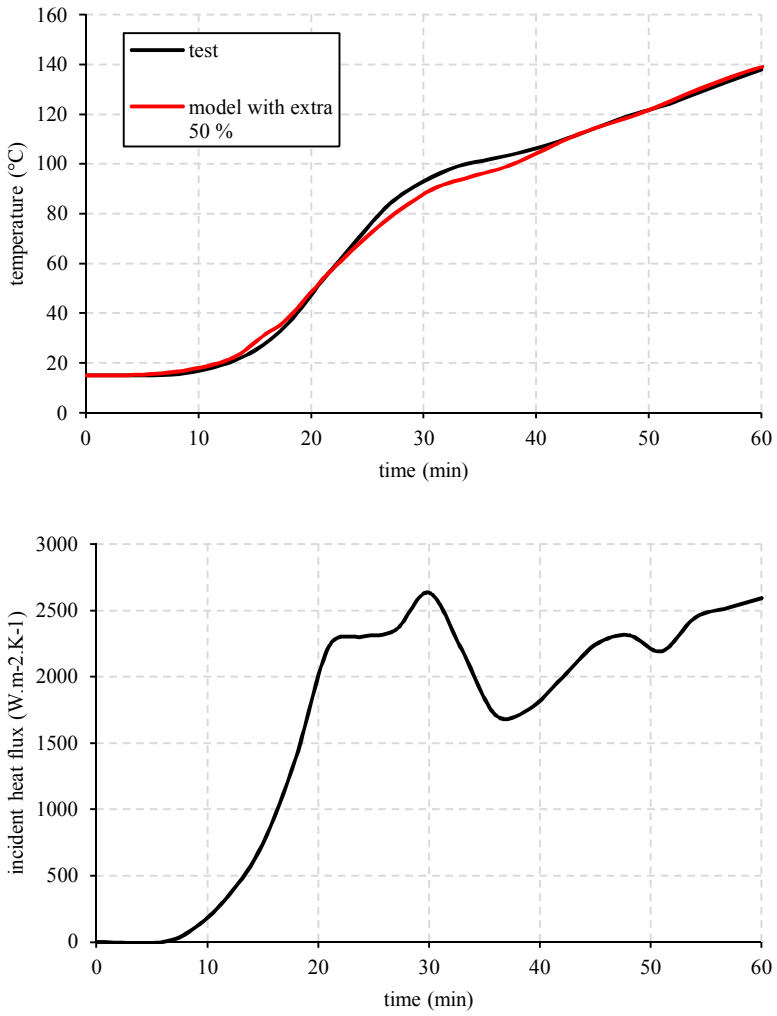

Figure 6 – Temperature curve on the unexposed surface of the steel plate (top) and associated heat flux entering the plate (bottom) for a fit with an artificial rise of incident energy of 50% after 27 min

4 INVESTIGATION OF THE JOINT

4.1 Overview of the models

The investigation for the protection of the joint in case of fire has been done using two models. An overview of the parametric variations is proposed in Table 2.
The first model considers direct contact between the steel part and the FRP material. In this model, a parametric study is performed on the influence of the initial temperature to account for the impact of the environmental conditions. The impact of a 10% deviation of the steel thermal properties is given for information. All three boundary conditions are described in this model.
The second model considers the influence of an insulator placed between the steel part and the FRP material. The thickness of the insulator is taken as 10 mm, and various materials are considered to compare their respective impacts on the temperature profile. Candidate materials must have suitable mechanical properties to ensure a satisfying behaviour of the joint, particularly concerning shear resistance.
In all models, the temperature is calculated along the steel/FRP or insulator/FRP interface above the bracket and at the bolt level. Probes record the evolution with time of the temperature at the boundary between FRP and the air gap around the bolt, at the steel/FRP or insulator/FRP boundaries at the edge of the joint. Figure 7 shows the location of the recording points.

Table 2 – Parametric variations carried out on the model

Model	Insulator	Parametric variations
Model 1	No	Boundary conditions (BC1, BC2, BC3)
		Initial temperature (0 °C, 15 °C, 30 °C)
		Deviation of steel thermal properties (10% on C_p and k)
Model 2	Yes	Concrete insulator
		Gypsum board insulator
		Wood insulator
		Fantasy material

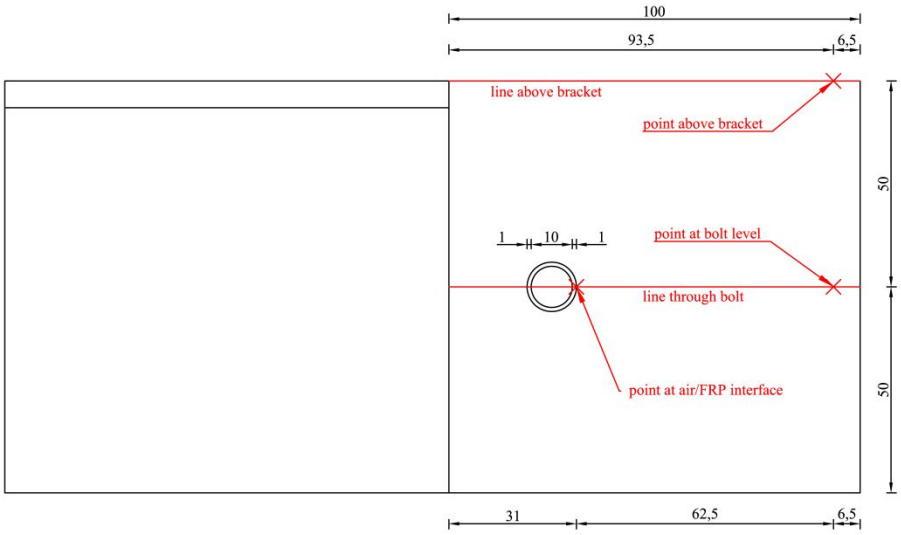

Figure 7 – Location of recording points on the numerical model, on a view from the top of the steel/FRP or insulator/FRP interface

4.2 Case without insulator

The variation on the boundary conditions shows that, as expected, the fully insulated case (BC2) leads to the highest temperatures at steel/FRP interface (Figure 8). This graph proposes results for the most common

summer air temperature at sea in Denmark, 15 °C. In this case, every situation shows temperature at the steel/FRP interface below the defined limit of 45 °C. This means that, on a regulatory perspective, the most common situation should not require additional insulation between joint and deck.
The slope of the curve after 1 h of exposure suggests that the glass transition temperature might be reached after 1 h 30 min of exposure. With this in mind, it is advised to increase the insulation of the joint.

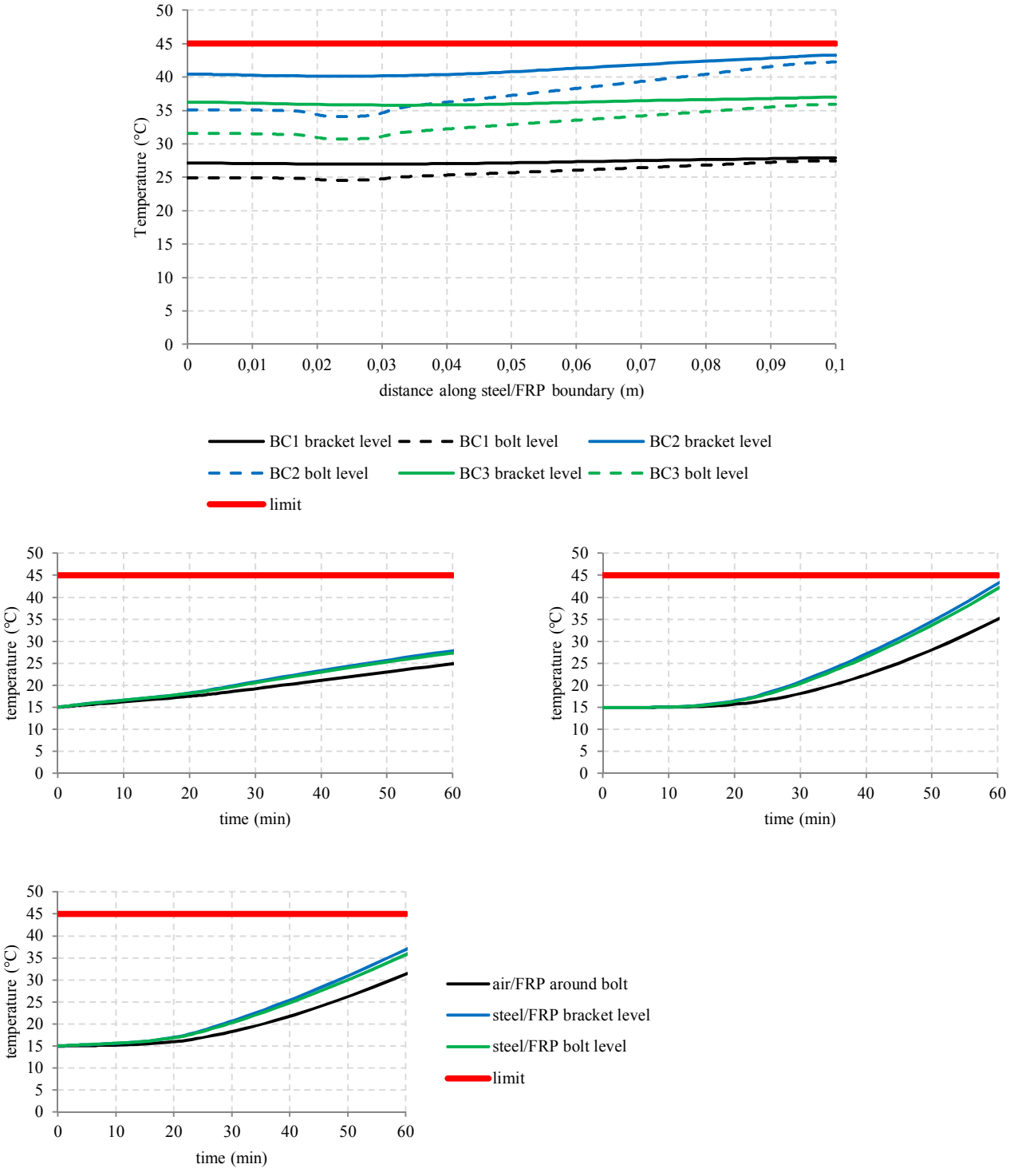

Figure 8 – Temperature predictions for each boundary condition, along recording lines at 1 h of exposure (top graph) and at recording points (lower 3 graphs)

It is visible on Figure 9 that the initial temperature has a critical influence. Reducing it lowers the interfacial temperature, which means that the joint should be safer in cold months. However, on a hot summer day the temperature at port could rise up to 30 °C or more. In this case the defined temperature limit for the steel/FRP interface is exceeded at 45 min (Figure 9) and approaches the glass transition region at 1 h of exposure.

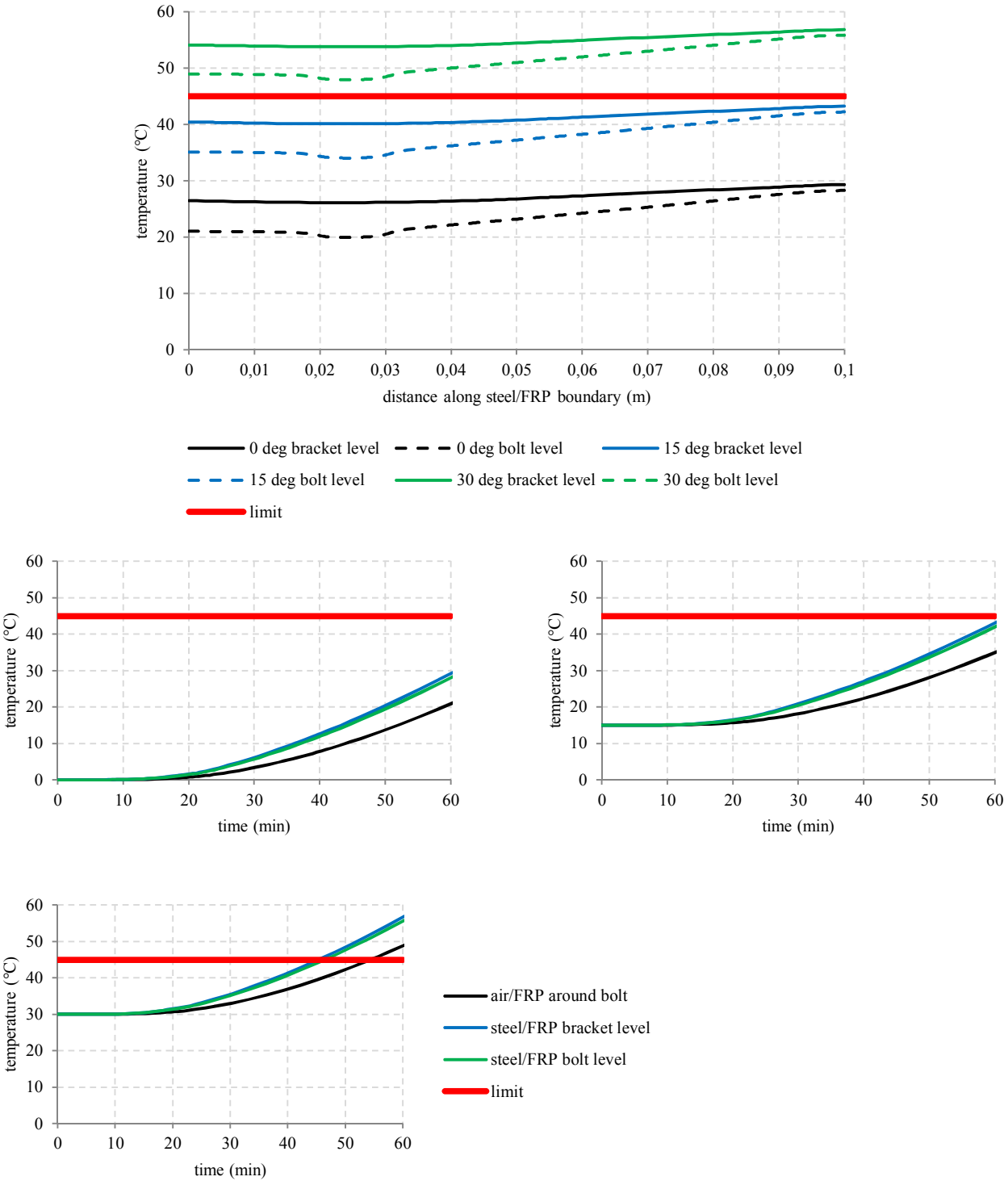

Figure 9 – Temperature predictions for various environmental temperatures, along recording lines at 1 h of exposure (top graph) and at recording points (lower 3 graphs)

The variations on steel properties are given in Figure 10. The industry considers a 10 % safety margin on the thermal properties of marine steel commonly used for ship structures (Grade A steel). The worst case scenario for the joint would be an increase in thermal conductivity of steel, or a decrease in heat capacity. Both scenarios are considered separately. A combination of worst case scenarios is not investigated here. The simulations are performed for an initial temperature of 15 °C.
Both situations lead to a temperature rise, and at 1 h of exposure the defined temperature limit is exceeded on the part of the interface located above the vertical steel plate (see Figure 3 for location). The temperature reached is less than 50 °C and the limit is exceeded at 58 min. On a regulatory perspective, the temperatures are acceptable. Keeping in mind the fact that a fire might last more than 1 h, some additional protection could be considered.

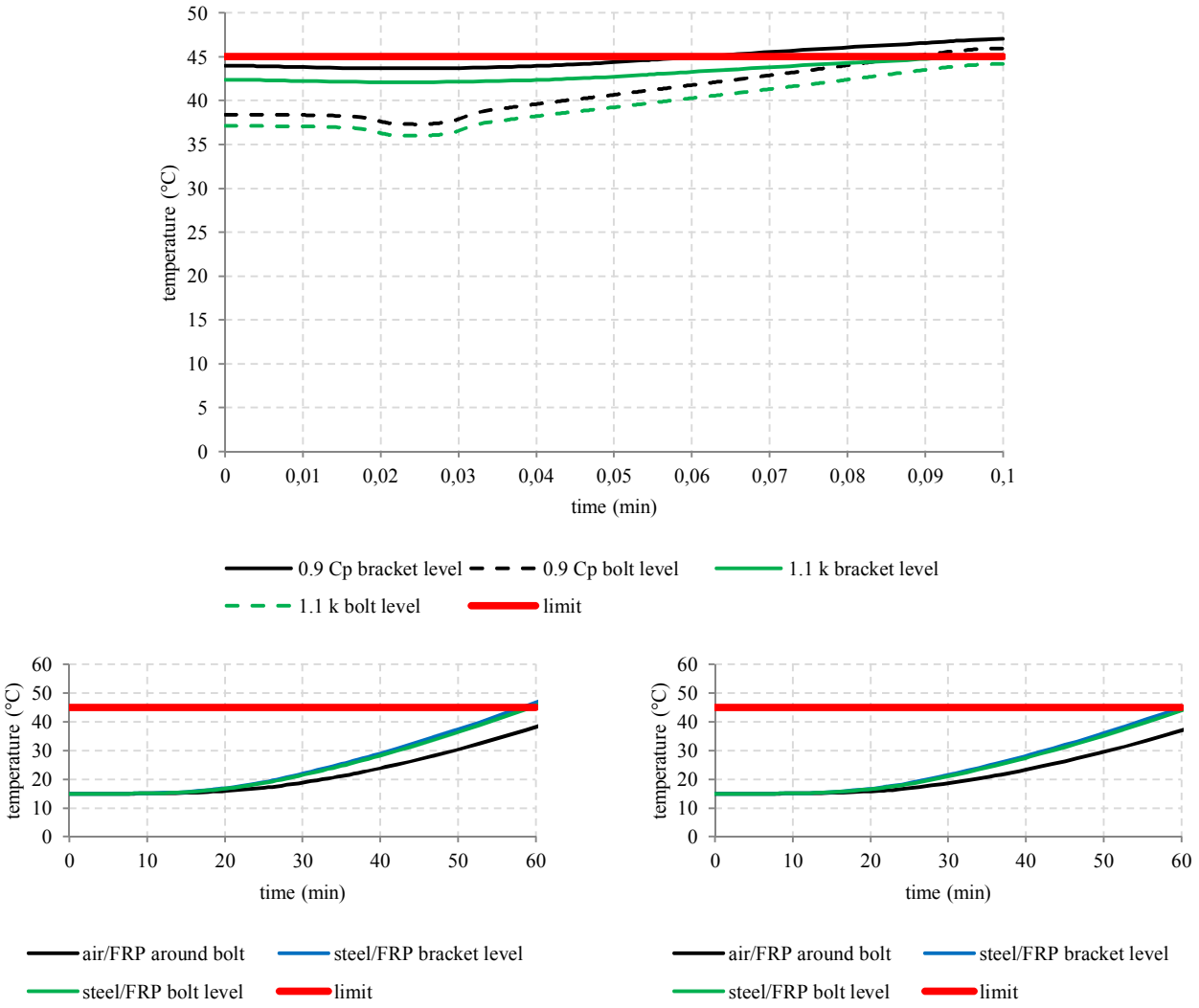

Figure 10 – Temperature predictions for variations on steel properties, along recording lines at 1 h of exposure (top graph) and at recording points (lower 3 graphs)

Among the investigations of the joint without insulator, almost all scenarios displayed temperatures below the defined limit after 1 h of exposure of the deck to the standard ISO curve. Only the case of high environmental temperatures is of concern, since the glass transition temperature region is reached after 1 h of exposure of the deck to the standard fire. Since this report is part of the investigation on the feasibility of using FRP materials on board a ship, it is interesting if a safe solution can be provided for all scenarios, especially concerning the general level of concern for such materials in hazardous applications.
The investigation with insulator will then be based on the critical situation found in the investigations without insulator.

4.3 Case with insulator

The investigation of the insulator is carried out with the worst boundary condition (BC2) and the highest expected environmental temperature (30 °C). It is suggested that such a combination is sufficient to take into account the potential deviation of the steel properties, and the fact that such hot days in the operational area of the ferry are exceptional.
The parametric variation is led on the candidate materials, namely concrete, gypsum board and wood. Material properties for concrete are from the Eurocode 2, gypsum board from Rahmanian (2011), and the properties of wood are taken from the Eurocode 5. An additional fantasy material has been introduced to highlight the critical values for thermal properties.

All results are presented in Figure 11. On the curves at bolt level (solid lines), the high plateau corresponds to the bolt. Materials with higher insulation properties will prevent the progression of heat which will pass through the bolt. This area is of importance for the contact between the air layer surrounding the bolt and the FRP material, to keep the stiffness at this critical interface. The sudden rise in temperature at the right hand side of the graph is explained by the curvature of the FRP skins of the sandwich superstructure, which induces a short area in contact with the external environment.

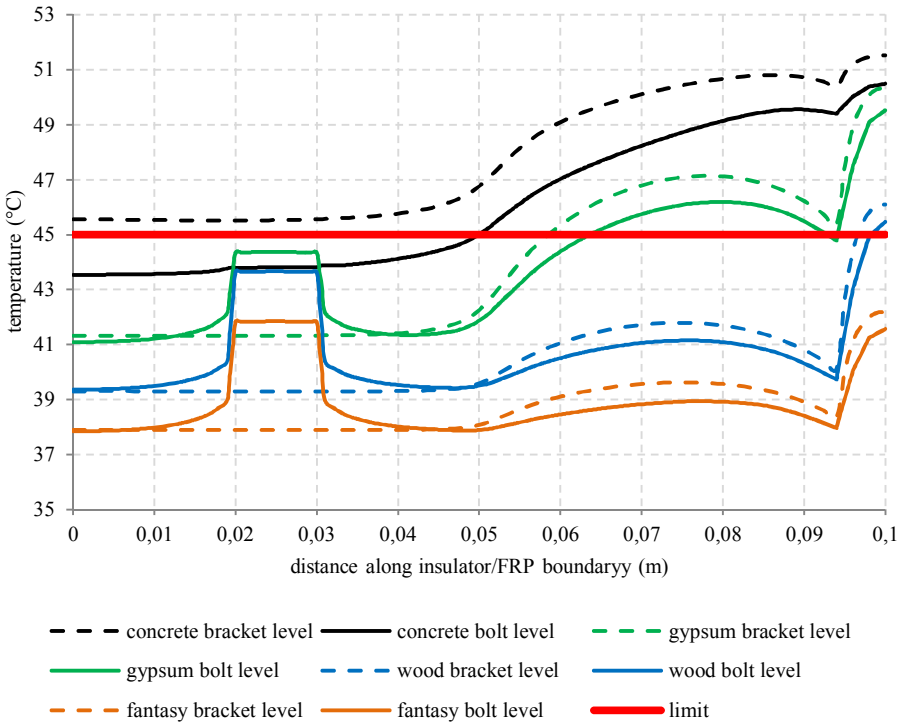

Figure 11 – Temperature predictions for all candidate materials as insulators, along the recording lines at 1 h of exposure

Wood performs best of the usual construction materials. All temperatures are below the defined limit, even for the bolt. If all issues related to its use in a wet and aggressive environment can be cleared, it would be the material of choice. Its potential use should be validated with respect to compressive and shear loading in service conditions. It is expected that its fibrous structure can be oriented in a suitable direction to provide the necessary resistance in the desired directions.

Concrete appears as the worst candidate. At the level of the bracket after 1 h of exposure, the temperature is above the defined limit along the entire interface with FRP. Despite its rather high heat capacity, the relatively high thermal conductivity of concrete compared to the other studied materials impairs its performance as an insulator. Indeed, the temperature in the bolt does not rise. The temperatures reached are too low to benefit from the effect of water evaporation.

Gypsum board could also be a possible candidate if wood appears unsuitable for mechanical or environmental reasons. The temperature remains mostly below the defined limit, exceeding it only by 2 °C which remains acceptable on a regulatory perspective. The lower heat capacity of gypsum board is compensated by its lower thermal conductivity (this is also visible by the temperature rise in the bolt).

The fantasy material proposed combines the benefits of a high heat capacity, a high density, and a low thermal conductivity. Values are presented in **Table 3** and given as constants. Heat capacity would ideally increase with temperature; thermal conductivity would ideally decrease with temperature.
As expected, the material behaves the best of all the candidates. Temperatures are kept very low, which ensure a high level of protection even for prolonged exposures.

Table 3 – Proposed properties for fantasy material

Property	**Value**
ρ [kg.m^{-3}]	2400
k [W.m^{-1}.K^{-1}]	0.24
C_p [J.kg^{-1}.K^{-1}]	950

5 CONCLUSION

5.1 Conclusion and recommendations

It is reminded that the presented results are only theoretical, and no experimental validation of the model has been performed so far. Before any direct application is considered, additional testing to validate numerical finding must be carried out.

A numerical investigation has been carried out to describe the behaviour at elevated temperatures of the joint between steel hull and FRP superstructure of a passenger ship. Two models were used, with and without the use of an insulator between steel and FRP. The results and discussions show that it is achievable to protect the FRP material from a fire coming from the level below and heating through the deck. The use of FRP on board a passenger ship is therefore a possibility which can be made safe.

The model without insulator highlighted that the joint is protected by the structure itself in the most common situations, namely common air temperatures and fully insulated parts. In the less likely cases of high air temperatures and poor steel quality, the structure itself is not sufficient to protect the joint.

The model with insulator showed that, in the worst case represented by elevated air temperatures and fully insulated parts, high protection levels are achievable. In the available structural materials, wood is the preferred choice if it can be validated structurally. A proposition for a fantasy material has been given to suggest development directions to potential associated producers.

Another possibility to achieve the properties proposed for the fantasy material would be the use of a two-layer composite insulator, combining both a high specific heat and a low thermal conductivity. Such an approach requires validation for mechanical behaviour, since the composite layer would then become more complex and ensuring the shear transfer between layers could be a challenge.

An alternative guideline for a safe fire design, especially considering the lack of experimental validation of the model, would be to use a thicker insulation layer for the deck construction and avoid adding an insulator which can increase the complexity of the composite joint on a mechanical point of view. It is recommended to use a total thickness of dense mineral wool (150 $kg.m^{-3}$) of minimum 50 mm below the deck. Such a solution might prove overestimated, but at this point in time it cannot be refined before experimental validation of the model and reliable characterisation of the heat input.

5.2 Needs for future work

Two activities should be performed to raise the confidence level of the numerical investigations.

- An experimental program, and potentially implementation of some of the findings from the FIRETOOLS project, should be carried out on the deck construction to define reliable heat input ;
- A test program should be carried out directly on the joint, in order to validate the numerical model without and with insulator.

Another investigation track should consider a fire coming from a room with FRP walls, in order to define the appropriate thickness of fire insulation on the sides of the FRP skins.
A last possibility, particularly interesting when considering FRP materials, would be to implement natural fire curves. This implies extending the scope of a potential experimental program characterising the deck construction.

6 BIBLIOGRAPHY

Bai Y, Keller T (2009) Modelling of mechanical response of FRP composites in fire. *Composites Part A* 40:731-738

Bai Y, Keller T, Vallée T (2008) Modelling of stiffness of FRP composites under elevated and high temperatures. *Composite Science and Technology* 68:3099-3106

Bendada A, Derdouri A, Lamontagne M, Simard Y (2004) Analysis of thermal contact resistance between polymer and mold in injection molding. *Applied Thermal Engineering* 24:2029-2040

Dawson A, Rides M, Allen CRG, Urquhart JM (2008) Polymer-mould interface heat transfer coefficient measurements for polymer processing. *Polymer Testing* 27:555-565

Eurocode 1: Actions on structures – Part 1-2: General actions – Actions on structures exposed to fire

Eurocode 2: Design of concrete structures – Part 1-2: General rules – Structural fire design

Eurocode 3: Design of steel structures – Part 1-2: General rules – Structural fire design

Eurocode 5: Design of timber structures – Part 1-2: General – Structural fire design

Hulin T, Maluk C, Bisby L, Hodicky K, Schmidt JW, Stang H (2015) Experimental studies on the fire behavior of high performance concrete thin plates. *Fire Technology* DOI: 10.1007/s10694-015-0486x

Madhusudana CV (1993) Thermal contact conductance and rectification at low joint pressures. *International Communications in Heat and Mass Transfer* 20:123-132

Mahieux CA, Reifsnider KL (2001) Property modelling across transition temperatures in polymers: a robust stiffness-temperature model. *Polymer* 42:3281-3291

Massé H, Arquis E, Delaunay D, Quilliet S, Le Bot PH (2004) Heat transfer with mechanically driven thermal contact resistance at the polymer-mold interface in injection molding of polymers. *International Journal of Heat and Mass Transfer* 47:2015-2027

Mikić BB (1974) Thermal contact conductance; theoretical considerations. *International Journal of Heat and Mass Transfer* 17:205-214

Rahmanian I (2011) *Thermal and mechanical properties of gypsum boards and their influences on fire resistance of gypsum board based systems*. Ph.D. thesis, University of Manchester

Savija I, Culham JR, Yovanovich MM, Marotta EE (2003) Teview of thermal conductance models for joints incorporating enhancement materials. *Journal of Thermophysics and Heat Transfer* 17:43-52

Singhal V, Litke PJ, Black AF, Garimella SV (2005) An experimentally validated thermos-mechanical model for the prediction of thermal contact conductance. *International Journal of Heat and Mass Transfer* 48:5446-5459

Annex D: Large-scale bulkhead fire tests – summary report

Date : July 2016
Project name : COMPASS – COMposite superstructures for large PASsenger Ships

Author : Dan Lauridsen

Content

1 Purpose

The purpose of this document is to provide a general overview of eight tests conducted on different bulkhead. In the test series consists of the following test:

File number	Structural core	Exposure
PGA10758A	Steel	ISO834
PGA10758B	Steel	NFC50
PGA10758C	Steel	NFC100
PGA10758D	Aluminium	ISO834
PGA10758E	Aluminium	NFC50
PGA10758F	Aluminium	NFC100
PGA10758G	FRP (Fibre reinforced plastic)	ISO834
PGA10758H	FRP (Fibre reinforced plastic)	NFC50

2 Apparatus

2.1 Testing hardware

2.1.1 Furnace

The furnace is designed to test vertically placed test specimens with a maximum dimension of 3200 x 3200 mm. The furnace includes 12 burners fuelled with propane. Twelve plate thermocouples are mounted to ensure a uniform temperature distribution inside the furnace.

2.1.2 Test frame

The test frame is specially designed to test loaded constructions. It is made of reinforced concrete. A concrete beam at the top is pushed down using hydraulics to apply load onto the bulkheads.

2.1.3 Deflection measuring units

The deflections of the bulkheads are measured with two instruments:

- 3D image analysis software (Primary):
  - By using two cameras and painting some spots on the bulkheads it is possible to analyse the displacement of the different points of the bulkhead.
- Mechanical measurement (Backup):
  - A thin wire is fixed to the bulkhead. This will pull on a fish wheel which measures the displacements.

2.1.4 Dataloggers

The dataloggers used for the measurements are Agilent 34970A and the unexposed surface temperatures are measured using Type K thermocouples insulated with fibreglass.
The combined accuracy of the apparatus is ± 2 °C.

2.2 Instrumentation

Temperature observations were taken continually during the entire testing time.

The furnace temperature was determined by means of plate thermocouples uniformly distributed at a distance of approximately 100 mm from the exposed side of the test specimens. The furnace temperature was continuously controlled so as to follow the relevant time temperature curve.

The surface temperatures were measured on the unexposed surface of the test specimens as specified in the 2010 FTP Code part 3.

The thermocouples were constructed according to the description in IMO Resolution MSC.307(88), 2010 FTP Code.

Observations were made on the general behaviour of the test specimens.

The pressure in the furnace was equal to the pressure in the laboratory at a point located approximately 500 mm above notional floor level as specified in IMO Resolution MSC307(88), 2010 FTP Code.

The load applied to the test specimens was logged during the entire testing time.

The deflections of the bulkheads were measured at five points on the bulkheads.

3 Test specimens

External dimensions:	Width:	Height:	Thickness:
Steel bulkhead:	2930 mm	3120 mm	131.5 mm
Aluminium bulkhead:	2930 mm	3120 mm	136 mm
FRP bulkhead:	2930 mm	3144 mm	143 mm

3.1 Steel bulkhead

The steel bulkhead was made of a 6.5 mm steel plate stiffened using Mannstaedt bulb flats, 100 x 7 mm with c/c = 700 mm. 10 mm thick steel plates were welded to the top and bottom of the bulkhead for load distribution and stability during the test.

The bulkhead was insulated using ceramic fibre designated FireMaster Marine Plus Blanket, produced by Morgan Thermal Ceramics. The insulation material had a measured density of 75 kg/m².

The exposed face of the steel bulkhead (insulated) before the fire test.

The unexposed face of the steel bulkhead (painted) after 3 hours of exposure.

3.2 Aluminium bulkhead

The aluminium bulkhead is made of 6 mm aluminium plate stiffened using angle bars, 80 x 40 x 6 mm with c/c = 700 mm. 10 mm thick aluminium plates were welded to the top and bottom of the bulkhead for load distribution and stability during the test.

The bulkhead was insulated using ceramic fibre designated FireMaster Marine Plus Blanket, produced by Morgan Thermal Ceramics. The insulation material had a measured density of 74.4 kg/m².

The aluminium bulkhead is getting insulated. Only one layer is used which is rolled over the stiffeners.

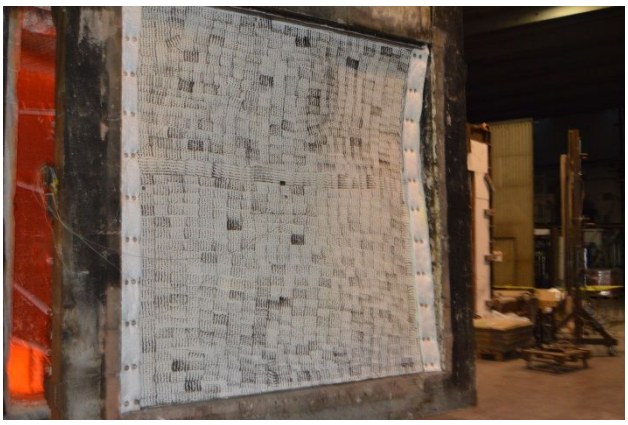

The aluminium bulkhead as it is removed from the furnace. The bulkhead failed when the load was increased.

3.3 FRP bulkhead

The FRP bulkhead is constructed of a core of 40 mm Divinycell P100 with FRP skin on both sides. These bulkheads were produced without stiffeners. 22 mm thick plywood was fixed to the top and bottom of the bulkheads for weight distribution and stability.

The bulkhead was insulated using four layers of ceramic fibre designated FireMaster Marine Plus Blanket, produced by Morgan Thermal Ceramics with layers of aluminium foil in between the layers of insulation. The insulation material had measured densities of 75 kg/m² and 74.4 kg/m².

The FRP bulkhead as it is getting insulated.

The FRP bulkhead collapsed after 82 minutes of exposure to ISO 834-1.

4 Test procedure

The tests will be conducted in the DBI test laboratory.

4.1 Mounting

The test specimens were fixed. They were loosely mounted into the test frame where they can deflect freely. Of safety reasons the bulkheads were mounted in a way disabling them from falling out of the test frame but still allow free movement.

4.2 Load

The load was applied in two or three steps (depending on the load percentage). In between every step it was ensured that the deflections were stable. The maximum load was reached before the furnace was turned on.

The load was focused on the gravitational centre of the bulkheads to avoid any eccentricity.

Bulkheads tested to the standard time-temperature curve were loaded with 7 kN/m as stated in the FTP Code.

Bulkheads tested to the natural fire curve were loaded to approximately 50 % of the maximum load bearing capacity:

- Steel: Applied load = 40 Tons (≈ 134 kN/m)
  Load bearing capacity = 510 kN/m
  Utilization: = 26 %

- Aluminium: Applied load = 18.3 Tons (≈ 61 kN/m)
  Load bearing capacity = 123 kN/m
  Utilization: = 50 %

- FRP: Applied load = 5.4 Tons (≈ 18.1 kN/m)
  Load bearing capacity = 36 kN/m
  Utilization: = 50 %

The steel bulkhead was only utilized 26% because the testing equipment was not approved to apply more than 40 tons of load.

4.3 Fire/heat exposure

There were 6 test specimens in total; 2 of each type and a total of 8 tests. One of each bulkhead was exposed to the standard time-temperature curve as defined by ISO 834-1. The others were exposed to natural fire curves. The steel and aluminium bulkheads exposed to the natural fire curve took very little damage from the first test and were therefore tested again with a second natural fire curve

The natural fire curves were defined by the following expressions:

Low curve (NFC50):

$$T_g = 20 + \frac{345 * \log_{10}(8 * 0.6987 * t + 1)}{1 + 0.04 * \left(\frac{t}{110.5}\right)^{3.5}}$$

Where: T_g = Gas temperature
t = Time (minutes)

The maximum temperature is reached after 110.5 minutes at 946 °C. After it has topped the temperature curve slowly drops towards zero.

High curve (NFC100):

$$T_g = 20 + \frac{345 * \log_{10}(8 * 2.7949 * t + 1)}{1 + 0.04 * \left(\frac{t}{55.3}\right)^{3.5}}$$

Where: T_g = Gas temperature
t = Time (minutes)

The maximum temperature is reached after 55.3 minutes at 1045 °C. After it has topped the temperature curve slowly drops towards zero.

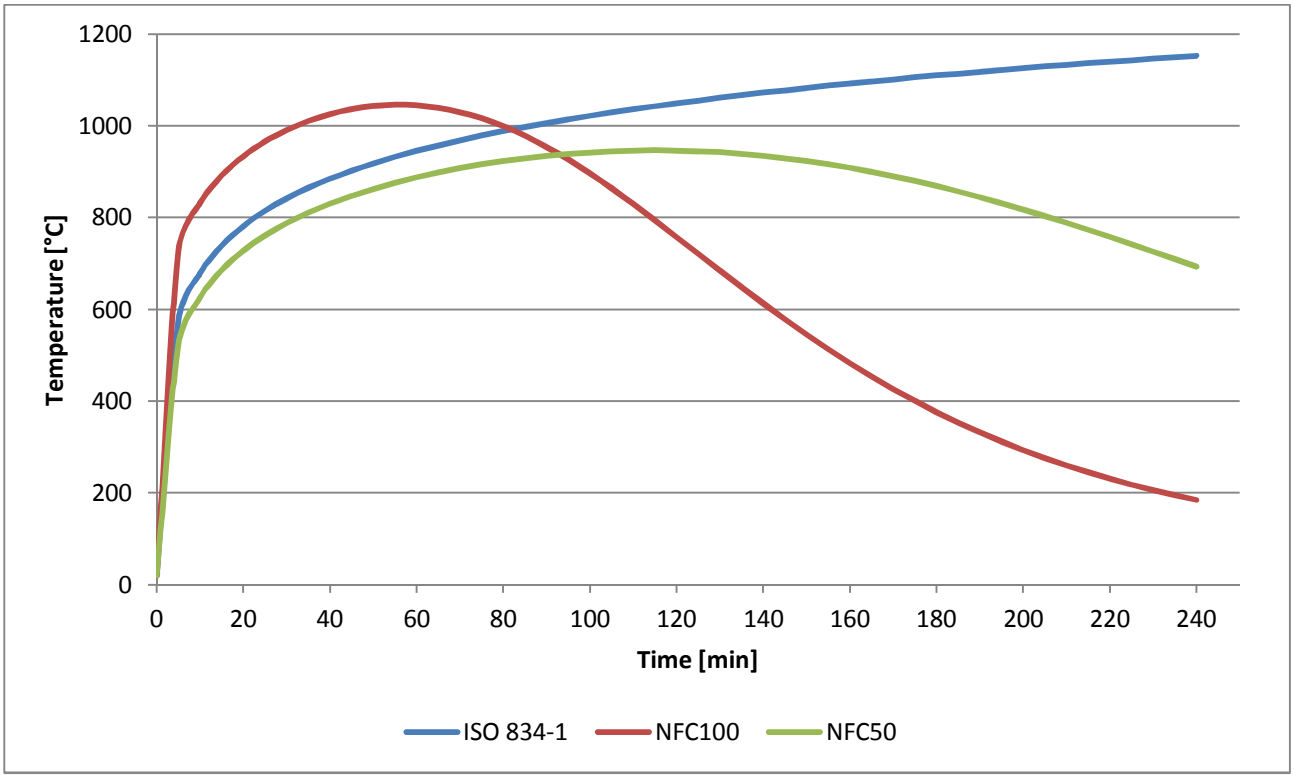

Comparison between the different time-temperature curves. The natural fire curves cools down as the fuel inside the room burns out. The peak for the natural fire curves are determined by the opening factors.
The tests without failure were stopped after around 3.5 hours.

5 Test results

For details of each of the tests performed, please refer to the individual test reports. The following text gives main results and performance recorded during the tests.

PG10758A: Steel – ISO834 thermal exposure
Insulation failure according to FTP-code, Part 3 occurred after 68 minutes of testing as the maximum temperature rise measured on the unexposed surface exceeded 180°C - at that time the average steel temperature rise measured in the stiffeners towards the exposed side was 390°C. The maximum temperature in the steel and on the unexposed surface was reached at the end of the test (210 minutes) - at that time the average temperature rise measured on the unexposed surface was approximately 190°C and 642°C measured in the steel stiffeners toward the exposed side.

PG10758B Steel – NFC50 thermal exposure
Insulation failure according to FTP-code, Part 3 occurred after 71 minutes of testing as the maximum temperature rise measured on the unexposed surface exceeded 180°C - at that time the average steel temperature measured in the stiffeners towards the exposed side was approximately 190°C. The maximum temperature in the steel stiffeners and on the unexposed surface was reached after approximately 145-165 minutes - at that time the average temperature rise measured on the unexposed surface was approximately 125°C and 255°C measured in steel stiffeners towards the exposed side. From the time at which the maximum temperatures had been reached to the end of the test (210 minutes) the temperatures in the steel stiffeners towards the exposed side and the temperature measured on the unexposed side was declining.

PG10758C Steel – NFC100 thermal exposure
Insulation failure according to FTP-code, Part 3 occurred after 46 minutes of testing as the maximum temperature rise measured on the unexposed surface exceeded 180°C - at that time the average steel temperature measured in the stiffeners towards the exposed side was approximately 210°C. The maximum temperature in the steel stiffeners and on the unexposed surface was reached after approximately 84-94 minutes - at that time the average temperature rise measured on the unexposed surface was approximately 138°C and 254°C measured in steel stiffeners towards the exposed side. From the time at which the maximum temperatures had been reached to the end of the test (160 minutes) the temperatures in the steel stiffeners towards the exposed side and the temperature measured on the unexposed side was declining.

PG10758D Aluminium – ISO834 thermal exposure
Insulation failure according to FTP-code, Part 3 occurred after 58 minutes of testing as the average temperature rise measured on the unexposed surface exceeded 140°C - at that time the average aluminium temperature rise measured in the stiffeners towards the exposed side was 188°C. The maximum and average temperature rise in the aluminium and on the unexposed surface was reached at the end of the test (217 minutes) - at that time the average temperature rise was approximately 210°C and 315°C measured on respectively the unexposed side and in the aluminium stiffeners towards the exposed side.

PG10758E Aluminium - NFC50 thermal exposure
Insulation failure according to FTP-code, Part 3 occurred after 72 minutes of testing as the average temperature rise measured on the unexposed surface exceeded 140°C - at that time the average aluminium temperature rise measured in the stiffeners towards the exposed side was 185°C. The maximum temperature rise in the aluminium stiffeners the unexposed surface was reached after approximately 130-140 minutes - at that time the average temperature rise was approximately 165°C and 185°C measured in the aluminium stiffeners towards the exposed side. From the time at which the maximum temperature has been reached to the end of the test (240 minutes) both the aluminium temperatures measured towards the exposed side and the unexposed surface temperature was declining.

PG10758F Aluminium – NFC100 thermal exposure
Insulation failure according to FTP-code, Part 3 occurred after 32 minutes of testing as the average temperature rise measured on the unexposed surface exceeded 140°C - at that time the average aluminium temperature rise measured in the stiffeners towards the exposed side was 175°C.
Structural occurred after 73 minutes of testing - at that time the average temperature rise measured on the unexposed surface was 201° and 285° measured in the aluminium stiffeners towards the exposed side. Note that the maximum temperature rise measured on an aluminium stiffener after 73 minutes of testing was 364°C and it was increasing by 25°C per minute.

PG10758G FRP – ISO834 thermal exposure
Insulation failure according to FTP-code, Part 3 did not occur before structural collapse (82 minutes). The maximum average temperature rise and the maximum temperature rise measured on the laminate towards the exposed side, before 82 minutes, was respectively approximately 258°C and 280°C. No significant temperature rise was recorded on the unexposed surface during the test.

PG10758H FRP - - NFC50 thermal exposure
Insulation failure according to FTP-code, Part 3 did not occur before structural collapse (61 minutes). The maximum average temperature rise and the maximum temperature rise measured on the laminate towards the exposed side, before 61 minutes, was respectively approximately 140°C and 150°C. No significant temperature rise was recorded on the unexposed surface during the test.

6 Conclusion

The peculiarity of this series of tests has been the desire to evaluate all the three classic failure criteria's that is used in relation to resistance to fire testing according to IMO regulations – integrity, insulation and loadbearing capacity.

IMO regulations indirectly ranks the three failure criteria's the following way

1. Load bearing ability (it give no meaning to evaluate integrity or insulation performance after structural collapse)
2. Integrity (Flaming on the unexposed side or glowing of the cotton wool pad as a result of hot gasses passing through the specimen is not allowed during 60 minutes in an "A" class division)
3. Insulation (The difference between A-0 and A-60 is the insulation criteria - both classifications require integrity performance for 60 minutes)

The conducted tests show that the steel bulkheads fail on the insulation performance first and load bearing ability remains for a considerable time. The aluminium bulkhead displays the same trend - insulation failure before structural failure. For the aluminium bulkhead the timespan between the two failure modes is significantly less that what was observed on the steel bulkhead. On the FRP bulkhead structural failure comes before insulation failure.

The thickness of the fire protection (insulation) on the FRP bulkhead is designed to avoid a load bearing failure and on the steel and aluminium bulkhead to avoid an insulation failure.

The time span between insulation failure and loadbearing failure can be regarded as an implicit robustness that is built into a conventional steel or aluminium ship. Although implicit robustness related to the aluminium bulkheads is significantly lower than for the steel bulkheads.

The significance of implicit robustness on fire safety can be argued. Collapse of a loadbearing construction, local or total, is generally negative for fire safety. A localized collapse may not be a significant event for the fire safety on board a ship and a localized may lead to progressive collapse and become a significant event.

The tested bulkheads is one sided exposed to fire, like it is the case for the outer skin on a ship. Based on this investigation DBI is of the opinion that it is not likely that a structural collapse will occur in the outer skin on the ship that have been used as case study for this project. A fire is likely to burnout before the implicit robustness towards structural collapse is exhausted. Regarding the aluminium bulkhead DBI consider that it is possible to that a fire on board will coarse a structural collapse. The fire must be severe which requires both fuel and ventilation conditions which can feed the fire. With regard to the FRP structure, a strong but realistic fire will result in structural collapse.

It is important to note that steel bulkheads or construction can suffer a structural collapse but the load level or utilization of the structural member must be high. Furthermore it must be noted that the FRP structure in the tests is a simple sandwich construction, other more advanced sandwich constructions made using improved fibers and matrixes can change the outcome.

ANNEX E: Material characterization tests at elevated temperatures

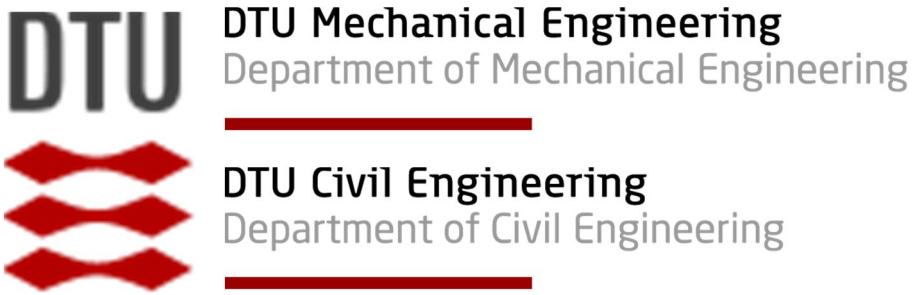

Date : August 2016
Project name : COMPASS – Composite superstructures for large PASSenger ships

Author : Mohsen Rezaei

Content

1 Experimental procedure

Tests for characterization of the mechanical properties were performed in different temperatures starting from room temperature and proceeding to elevated temperatures. The temperatures are listed for each test type. The tests are based on the ASTM standards. In the case of the lamina tests, the specimen dimensions may be different from those described in the standards, so as to fit the testing machine and setup. The geometry of the specimens is listed underneath the corresponding test type. The composite structure was designed using GBX450L-1250 E-glass Stitched fabric and Prime 20LV epoxy resin with fibre orientation of $0^o/90^o$, the structural core selected for sandwich structures is Divinycell P100. Volume fraction of fibre contents for the E-glass/epoxy composites in these tests is 50%. For each test and temperature at least three specimens were produced and tested. All the tests were performed on an Instron servo-hydraulic testing machine with a 100 kN capacity. A circulating air oven was mounted to the testing machine, see

Figure 1. The Environmental chamber can maintain temperatures from -60 °C to +180 °C. Samples were kept in the oven at the desired temperature for at least 1 h to achieve a uniform thermal distribution in the specimens. In all cases, the specimens were exposed at the prescribed temperature up to the point that thermal equilibrium is reached. By the use of eq. 1 [1] using typical values taken from the literature for the magnitudeses that were not measured,

$$\frac{\rho vc}{hA_s}\ln\frac{\theta_i}{\theta} \qquad (1$$

Where h is convection coefficient A_s is the exposure area, ρ is density, $\theta_i and\ \theta$ are initial ambient and target temperature, v is volume and c is specific heat. Typical values taken from the literature for the magnitudes that were measured as below and a safety factor of 1.5 was used.

$\rho_{Composite} = 1900\ Kg/m^3$
$\rho_{Foam} = 104\ Kg/m^3$
$C_{Composite} = 1600\ J/Kg\ K$
$C_{Foam} = 1116\ J/Kg\ K$
$h = 5\ W/m^2\ K$

1.1. Tensile Properties of E-glass/epoxy Composite Material

Aim of this test method is to determine the in-plane tensile properties of glass epoxy composite materials. This test was carried out following the standard ASTM D3039/D3039M−14 [2]. The tensile specimens used were E-glass/Epoxy composites with dimension 250 mm×25 mm cut from the panel of 635 mm×490 mm. The longitudinal direction is the direction parallel to the fibres. To avoid deboning of tabs at elevated temperatures, tabs were made in the specimen by milling the gauge length area using CNC machine. Figure 2 shows the geometry and dimension of tensile specimens in detail. The testing speed was set as 2 mm/min in all the tests. To measure the elastic modulus of the specimens one strain gauge capable of working at maximum 180 °C was installed on the front side of the specimen. The maximum measuring range of the extensometer is a strain of 2.5%. The elastic moduli of the samples were measured in the strain range of 0.01% to 0.20%. Ultimate tensile strength is calculated using eq.2. where F^{tu} is ultimate tensile strength P^{max} is maximum force before failure and A is average cross-sectional area.

$$F^{tu} = \frac{p^{max}}{A} \qquad (2$$

The elevated temperatures were chosen as 25 °C, 50 °C, 75 °C, 100 °C, 125 °C and 150 °C. Samples were kept in the oven at the targeted temperature for minimum the time calculated using eq.1 to achieve thermal equilibrium inside of the specimens.
Figure 3 shows the experimental setup for tensile properties test.

Figure 1. Environmental chamber mounted to the testing machine

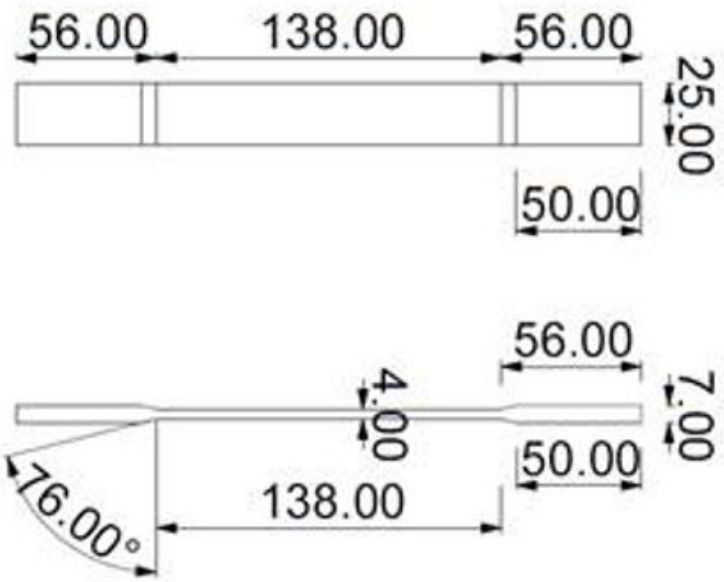

Figure 2. Geometry and dimension of tensile specimens

Figure 3. Experimental setup for tensile properties test

1.2. Compressive Properties of E-glass/epoxy Composite Material

This test method is used to determine the in-plane compressive properties of E-glass/epoxy composite material. This test was conducted following the standard D3410/D3410M−03 [3]. The Compressive specimens used were E-glass/Epoxy composites with dimension 150 mm×25 mm cut from the panel of 435 mm×490 mm. The longitudinal direction is the direction parallel to the fibres. To avoid deboning of the tabs at elevated temperatures, the tabs were made in the specimen by milling the gauge length area using CNC machine. Figure 4 shows the geometry and dimension of tensile specimens in detail. The testing speed was set as 1 mm/min in all the tests. To measure the elastic modulus of the specimens and control the bending ratio, two strain gauges of HBM 350 Ohm capable of working at high temperatures were installed on both sides of the specimen. The IITRI test fixture was used for this test. Its configuration incorporates flat wedge

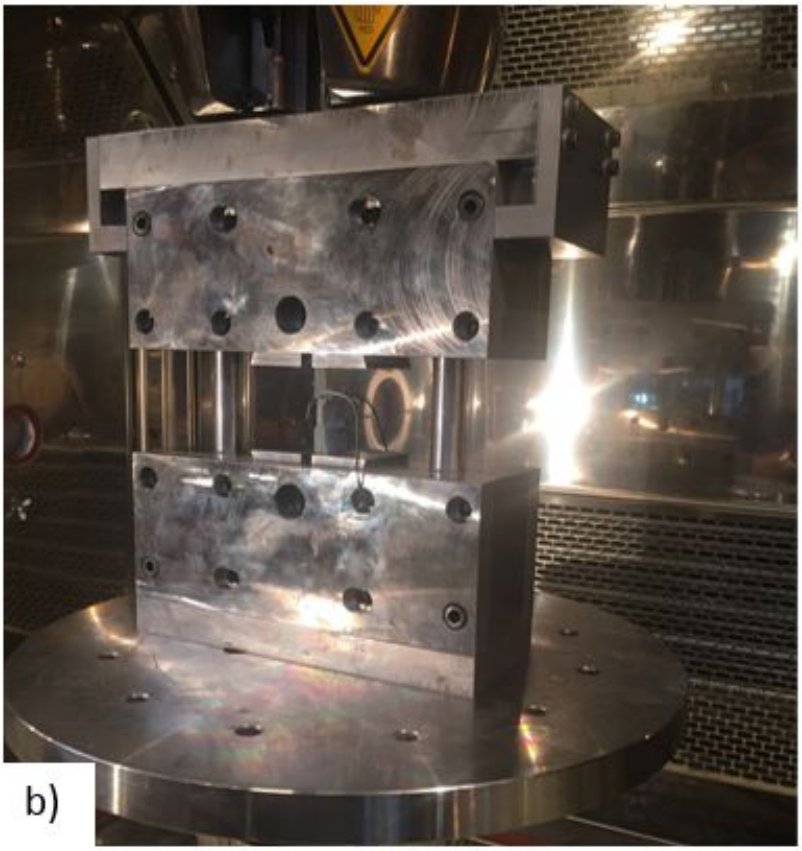

grips, as shown in Figure 5 , which helps full surface contact with the mating blocks, independent of the tabbed specimen thickness. The elastic modulus of each specimen was measured in the strain range of from 0.1% to 0.30%. The bending ratio should be below 10% according to the standard. The checkpoint for bending is at 0.2% strain. The bending ratio is calculated following by eq. 3. where ε_1 and ε_2 are the strain measured by strain gage 1 and 2 respectively.

$$\text{Percent Bending} = \frac{\varepsilon_1 - \varepsilon_2}{\varepsilon_1 + \varepsilon_2} \times 100 \qquad (3$$

Ultimate tensile strength is calculated using eq.4 where F^{cu} is ultimate Compressive strength, P^{max} is maximum force before failure and A is cross-sectional area. The temperature range was chosen as 25 °C, 50 °C, 75 °C and 100 °C.

$$F^{cu} = \frac{p^{\max}}{A} \quad (4$$

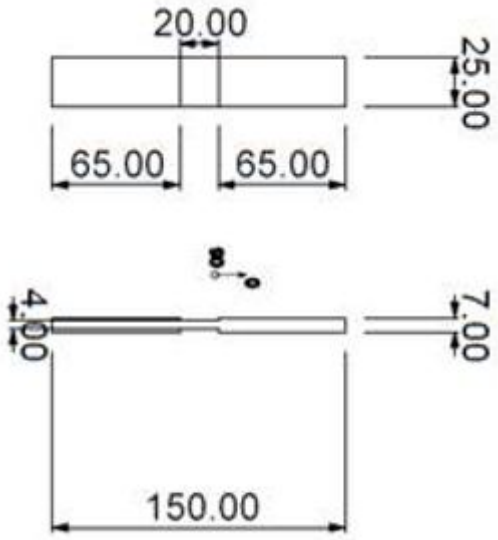

Figure 4. Geometry and dimension of Compressive specimens

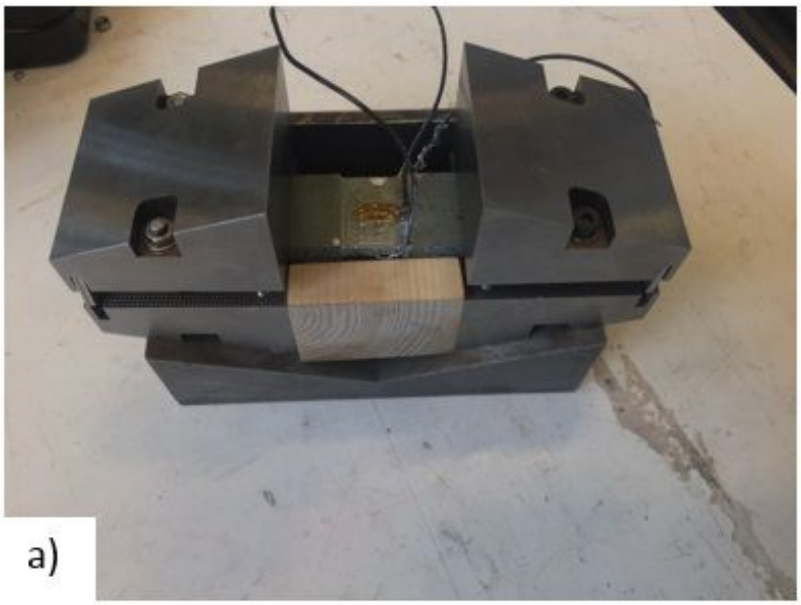

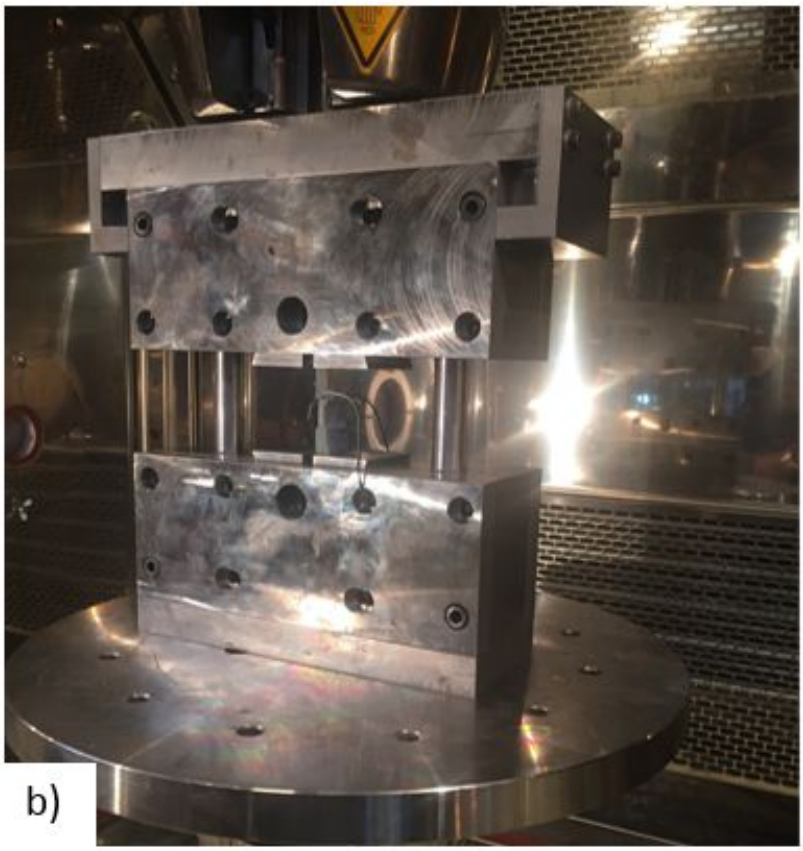

Figure 5. Compressive Test setup a) flat wedge grips b) IITRI Compression Test Fixture

1.3. Shear Properties of E-glass/epoxy Composite Material by V-notched rail shear method

This test method is used to define the shear properties of E-glass/epoxy composite material. This test was performed following standard D7078/D7078M–12[4]. The shear specimens used were V-notched E-glass/Epoxy composites cut from the panel of 425 mm×470 mm. They were installed between two pairs of loading rails. The longitudinal direction is the direction parallel to the fibres. Figure 6 shows the geometry and dimension of V-notched shear specimens in detail. The testing speed was set as 1 mm/min in all the tests.

To investigate the strain distribution and shear modulus in the test specimens a digital image correlation (DIC) measurement technique is employed. The software used for processing is Aramis from GOM. The system uses two 12 megapixel digital cameras to determine the movement in the specimen by processing the deformation of the pattern. A calibration plate of 175x140 was used to calibrate the DIC system through glass. A measurement through glass (window of climate chamber) is always connected with a higher calibration deviation (depending on the glass type and thickness), therefore the calibration influence was needed to be verified. To check the influence of the glass, the speckle pattern was sprayed on a rigid plate It was placed inside of the oven and it was moved manually in x,y directions for 1 mm, 2 mm and 5 mm . Thereby a noise which depends on the place and the influence of the glass in each direction was measured. The result was with a homogeneous noise of strain computation and accuracy of above 99%. To measure the shear modulus of the specimens two virtual Extensometer introduced and centred between the notch tips in the gauge section of the specimen. The virtual extensometers presented at the +45° and -45° orientations shown in Figure 7. Shear modulus were measured followed by eq. 5 in the strain range of 0.15% to 0.25%, where γ is the engineering shear strain, ε_{+45} and ε_{-45} are the strain measured by virtual strain gage 1 and 2 at +45° and -45° respectively. The ultimate engineering shear strength is determined from eq.6. The elevated temperatures were chosen as 25 °C, 50 °C,62.5 °C, 75 °C and 100 °C.
Figure 8 shows the experimental setup and DIC cameras for V-notched shear properties test.

$$\gamma = |\varepsilon_{+45}| + |\varepsilon_{-45}| \quad (5$$

γ^{μ} =min of 5% strain or γ at ultimate load (6

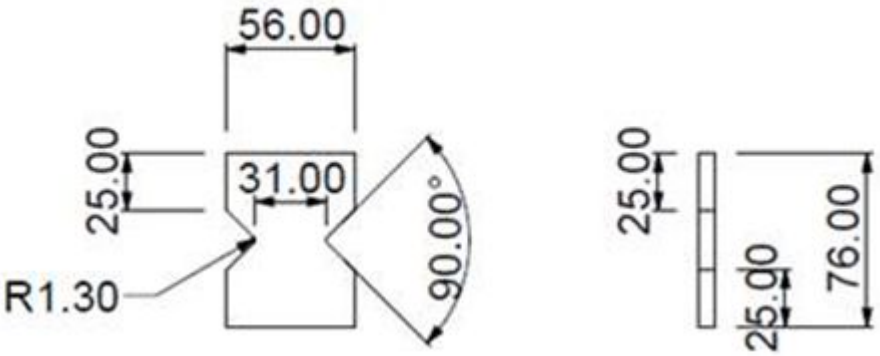

Figure 6. Geometry and dimension of V-notched shear specimens

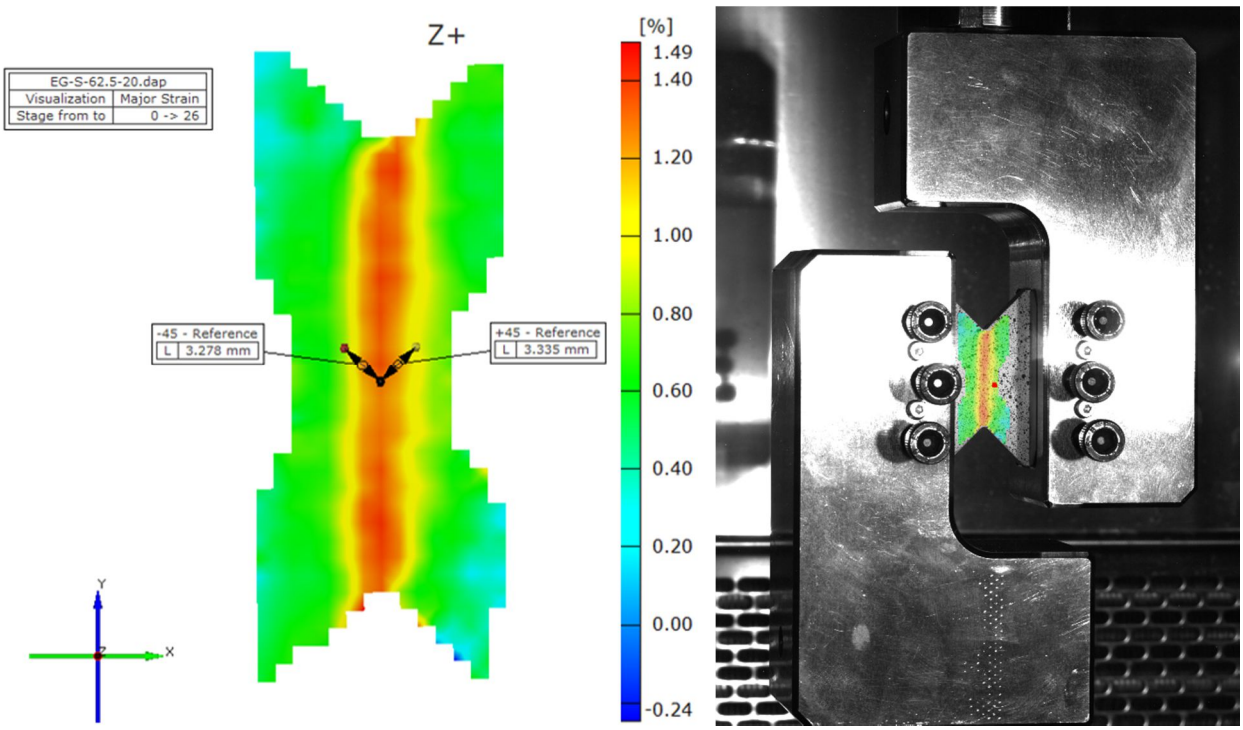

Figure 7. virtual extensometers presented at +45° and -45° orientations using DIC

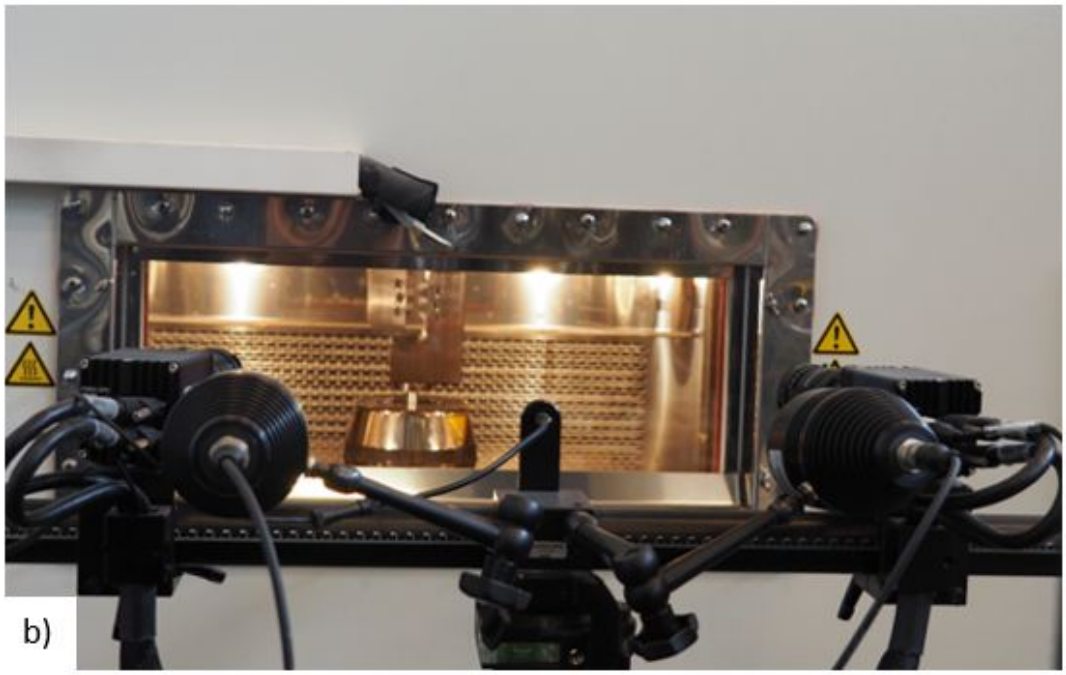

Figure 8. Experimental setup a) v-notched shear properties test b) DIC cameras

1.4. Core Shear Properties of Sandwich Structure by Beam Flexure

This test method covers the determination of core shear properties of flat sandwich structures subjected to flexure. The applied moment maintains curvature of the sandwich facing panels. This test was performed following the standard C393/C393M–11[5]. The sandwich specimens used were E-glass/Epoxy face sheet with foam core composites (P100 by DIAB). Figure 9 shows sandwich panel thickness dimensions. The testing speed was set as 3 mm/ min in all the tests. Cylindrical steel rollers with diameter 35 mm were used to load and support the sandwich specimens with a Load span length *L* = 160 mm, support span S= 450 and Sandwich width= 90 mm. A thick layer of rubbers placed on beneath of the steel rollers to reduce the stress concentration. Five different temperatures, namely 25°C (room temperature, RT), 50°C, 75°C and 100°C, were considered in the experiments.
Core Shear modulus were measured followed by eq. 7-9 [6]. The beam mid-span deflections were measured using Aramis system. Values were calculated for a minimum of ten force levels evenly spaced over the force range and the average value is selected. Core shear ultimate strength is determined from eq.10. The temperatures chosen were 25 °C, 50 °C, 75 °C and 100 °C.
Figure 8 shows the experimental setup and DIC cameras for four point bending test of sandwich beams.

$$D = \frac{E(d^3 - c^3)b}{12} \quad (7$$

$$U = \frac{P(S_1 - L_1)}{4\left[\Delta - \frac{P(2S^3 - 3SL^2 + L^3)}{96D}\right]} \quad (8$$

$$G = \frac{U(d-2t)}{(d-t)^2 b} \quad (9$$

$$F_s^{ult} = \frac{P_{max}}{(d+c)b} \quad (10$$

Δ = beam mid-span deflection
P = total applied force
d = sandwich thickness, mm
b = sandwich width
t = facing thickness
S = support span length
L = load span length
G = core shear modulus
D = flexural stiffness
U = transverse shear rigidity
F_s^{ult} = core shear ultimate strength
c = core thickness

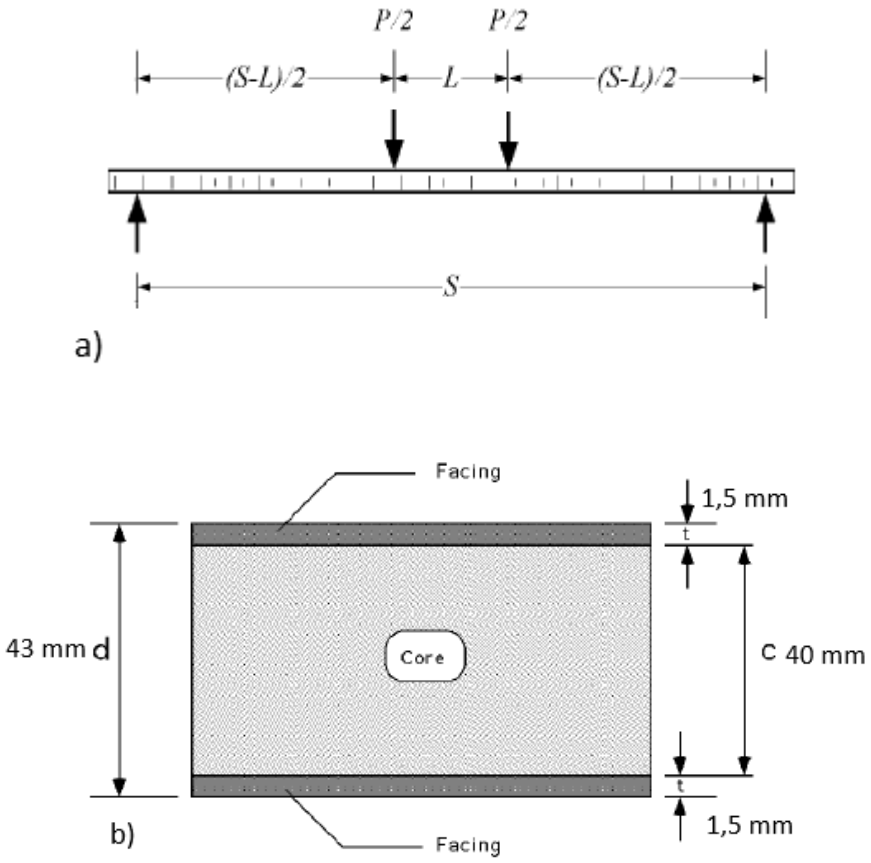

Figure 9. Four point bending a) sandwich beam b) panel thickness dimensions

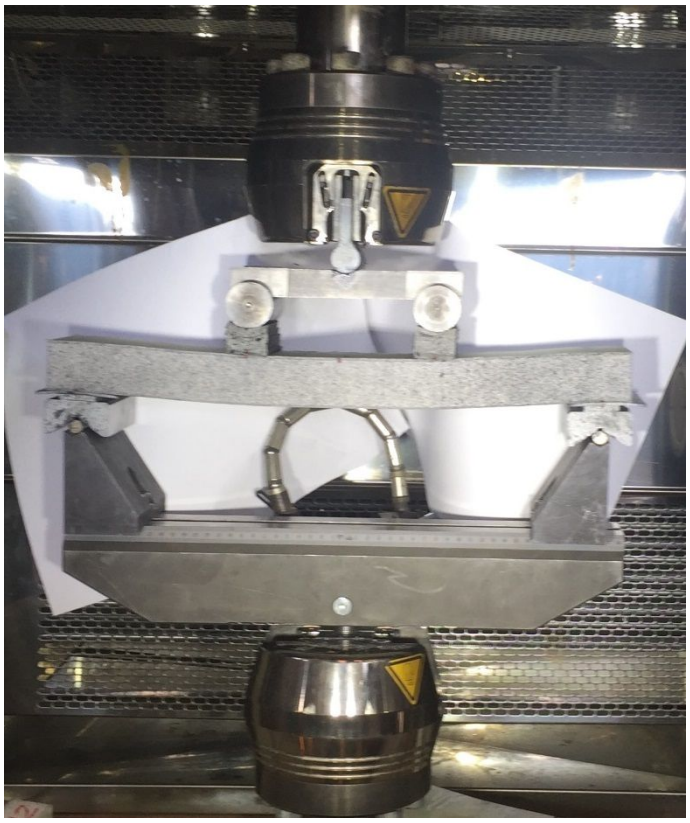

Figure 10. Experimental setup for four-point bending test of sandwich beams

1.5. Flatwise Compressive Properties of Sandwich Core

This test method covers the determination of compressive strength and modulus of sandwich cores. These properties are verified in a direction normal to the plane of facings. This test was performed following the standard C365/C365M−16[7]. The sandwich specimens used were E-glass/Epoxy face sheet with foam core. The same panel as four-point bending test is used for this test. Panel is cut to the specimens with 60 mm × 60 mm dimensions. The testing speed was set as 0.5 mm/ min in all the tests. Platens Force was introduced into the specimen using one fixed flat platen and one spherical seat platen. Five different temperatures, namely 25°C (room temperature, RT), 50°C, 75°C and 100°C, were considered in the experiments.
Compressive modulus were measured followed by eq.11. Deflections of the sandwich panel were measured using Aramis system by measuring the deflection of upper platen. Core shear ultimate strength is determined from eq.12. If 2 % deflection is achieved prior to stopping the test, then the flatwise compressive Stress would be calculated at 2 % deflection. The chosen temperatures were 25 °C, 50 °C, 75 °C and 100 °C.
Figure 11 shows the experimental setup for Flatwise Compressive Properties test of Sandwich Core

$$E_z^{fc} = \frac{(p_{0.004-}p_{0.002})t}{(\delta_{0.004-}\delta_{0.002})A} \quad (11$$

$$F_z^{fcu} = \frac{p^{\max}}{A} \quad (12$$

E_z^{fc} = core flatwise compressive chord modulus
$P_{0.004}$ = applied force corresponding to δ0.004
$P_{0.002}$ = applied force corresponding to δ0.002
$\delta_{0.004}$ = recorded deflection value such that δ/t is closest to 0.004,
$\delta_{0.002}$ = recorded deflection value such that δ/t is closest to 0.002.
A = cross-sectional area
t = measured thickness of core specimen prior to loading
F_z^{fcu} = ultimate flatwise compressive strength
P_{max} = ultimate force until failure, or until the measured deflection equals 2 % of the initial core thickness

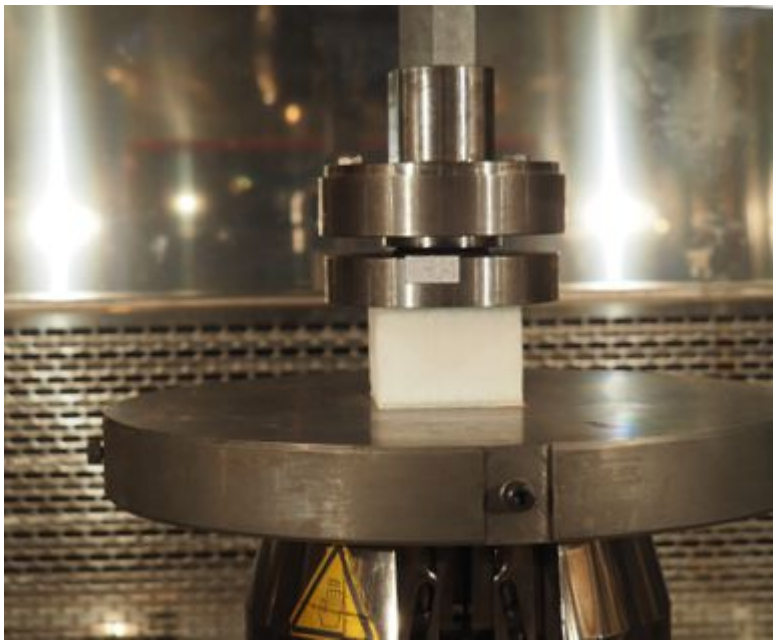

Figure 11. Experimental setup for Flatwise Compressive Properties test of Sandwich Core

2 Results

2.1. Elastic modulus and ultimate strength

Results from the Tensile, Compression, Shear, Core shear and Core compression tests of composite laminates and sandwich structures are reported below. Tables for material properties tests are available in appendix A.As previously mentioned elevated temperature for Tensile tests were chosen as 25 °C, 50 °C, 75 °C, 100 °C, 125 °C, 150 °C and 175 °C.

a and b show the reduction in tensile elastic modulus and tensile strength as a function of temperature. In general, it can be noticed that the reduction in elastic modulus is significant up to 100 °C and then it remained stable. Similar behaviour observed with Tensile strength reduction. Above 100 °C, specimens failed in the tab area (see Figure 13) therefore the ultimate strength values cannot be used. Failure surface of specimens after different exposure temperatures are shown in Figure 13. Specimens exposed to the temperature from 25 °C to 100 °C were failed in the gauge length area with acceptable typical failure mode of Angled Gauge Middle (AGM). whilst specimens exposed to the temperature from 125 °C to 175 °C were failed in the tab area and their failure mode is not acceptable followed by ASTM D3039/D3039M [2]. This happened due to sofftening of the composite material at elevated temperature. Conequently it was decided to reach maximum 100 °C for the rest of the test series.

The temperatures for the compression tests were 25 °C, 50 °C, 75 °C and 100 °C. Similar graphs to tensile tests, have been provided for compression test (see Figure 14a and b). Due to technical problems, test results for compressive modulus at 75 °C are not available. At 100 °C the resin of the composite became rubbery which caused significant bending during the test. Therefore compressive modulus of the composite components at 100 °C cannot be recorded with this test. Results show the reduction in Elastic modulus and Tensile strength as a function of temperature especially this reduction is more dramatic after 50 °C. Failure surface of specimens after different exposure temperatures are shown in Figure 15. Specimens exposed to the temperature from 25 °C to 100 °C were failed in the gauge length area with acceptable typical failure mode of Through thickness At Tab (HAT)[3].

Elevated temperature for Shear tests were chosen as 25 °C, 50 °C, 65 °C, 75 °C and 100 °C. Figure 16 a and b show the reduction in shear modulus and ultimate shear strength as a function of temperature. Results show reduction in Elastic modulus and Tensile strength as a function of temperature especially this reduction is more sever after 62.5 °C which is close to glass temperature transient of the resin. Failure surface of specimens after different exposure temperatures are shown in Figure 17. Specimens exposed to the temperature from 25 °C to 100 °C were failed in the gauge section with acceptable typical failure mode of Multi-mode Gage section between Notches (MGN)[4].

The temperatures for core Shear tests were chosen equal to 25 °C, 50 °C, 75 °C and 100 °C. Figure 18 shows reduction in the core shear modulus as a function of temperature. Results show reduction in elastic modulus as a function of temperature similar to the previous tests. This reduction is more sever after 50 °C. some of the Specimens at room temperature were failed due to core shear failure (see Figure 19.a) and some due to indentation. Core shear strength measured at room temperature is equal to 0.88 MPa whilst all the specimens at elevated temperatures were failed due to indentation (see Figure 19.b). Therefore, considering the effect of temperature on core shear strength is not achieved. Failure surface of specimens after different exposure temperatures are shown in

Figure 20.

Elevated temperature for flatwise core compression tests were chosen as 25 °C, 50 °C, 75 °C and 100 °C.

Figure 21 a and b show the reduction in core compression modulus and ultimate core compression strength as a function of temperature. This reduction is more sever after 50 °C like the other tests. Failure surface of specimens after different exposure temperatures are shown in Figure 22.

Figure 23 compares the Elastic modulus and strength reduction in percentage for all the tests. Tensile test shows less reduction comparing the other tests which is due to fibre dominant behaviour of material properties in 0° fibre orientation. Compression and shear tests show higher reduction as exposed to elevated temperature which is due to matrix dominant behaviour of material properties. Both have similar trend in strength and elastic modulus reduction and they show dramatic reduction after 75 °C which is above the matrix glass temperature transient.

2.2. Curve fitting

All the materials with thermosetting resin system including strength and modulus can be fitted to a cure as in Figure 24 [8]. On heating thermoset resin system materials as amorphous polymers, from room temperature the only transformation which will happen before decomposition is the glass transition. So it is needed to find a suitable relationship to the property-temperature relationship in this area. In this study curve fitting function has been extracted based on tanh equation model which is described in eq. 13. where P_U and P_R are the unrelaxed (low temperature) and relaxed (high temperature) values of that property, respectively, k is a constant describing the breadth of the relaxation and T_g (in Kelvin) is the temperature of the mechanically observed glass transition, corresponding to a 50% reduction in the property value.

$$P(T) = P_U - \frac{P_U - P_R}{2}(1 + \tanh(k(T - T_g))) \quad (13$$

All the curve fitting function applied to the test results had good agreement with equation 13. Figure 25 shows curve fitting for tensile Elastic modulus with P(T)=23.321×(1-0.5×0.2778×(1+tanh(K×(T-65) ×π/180))) and K=2.866. Due to failure of the tabs after 100 °C and lack of data afterward, curve fit cannot be precisely produced for tensile ultimate strength.

Figure 26 shows curve fitting for compressive ultimate strength with P(T)=323×(1-0.5×0.92×(1+tanh(K×(T-71) ×π/180))) and K=3.926. . Due to lack of data, curve fit for compressive modulus cannot be maintained.

Figure 27 shows curve fitting for shear modulus with P(T)=3,1379×(1 0.5×0.96899×(1+tanh(K×(T-65) ×π/180))) and K=3.241. Figure 28 shows curve fitting for shear ultimate strength with P(T)=56.53×(1 0.5×0.92354×(1+tanh(K×(T-65) ×π/180))) and K=2.786.

Figure 29 shows curve fitting for core shear modulus with P(T)=25.997×(1 0.5×0.8729×(1+tanh(K×(T-63) ×π/180))) and K=2,771. Due to failure of the sandwich specimens in indentation at elevated temperatures, curve fit cannot be produced for core shear ultimate strength.

Figure 30 shows curve fitting for core compressive modulus with P(T)=83,46×(1-0.5×0.90545×(1+tanh(K×(T-65) ×π/180))) and K=3.429. Figure 31 shows curve fitting for Compressive ultimate strength with P(T)=-1.76×(1-0.5×0.90189×(1+tanh(K×(T-60) ×π/180))) and K=2.288

3 Conclusion

Material properties of the E-glass/ Epoxy composite and Sandwich structures with E-glass/epoxy face sheet and the Divinycell P100 core have been measured by performing tensile, compression, shear, core shear and core compression experiments. The effect of exposure to elevated temperature has been investigated. General reduction for both modulus and strength of the materials at elevated temperatures was visible. Tensile test showed less elastic modulus and ultimate strength reduction comparing other tests. The reduction of strength and elastic modulus was greater in case of compression and shear tests, both had similar trend in reductions and they showed dramatic decrease after 75 ^{o}C which is above the matrix glass temperature transient. Curve fitting function applied to the test results; all had good agreement with the tanh equation.

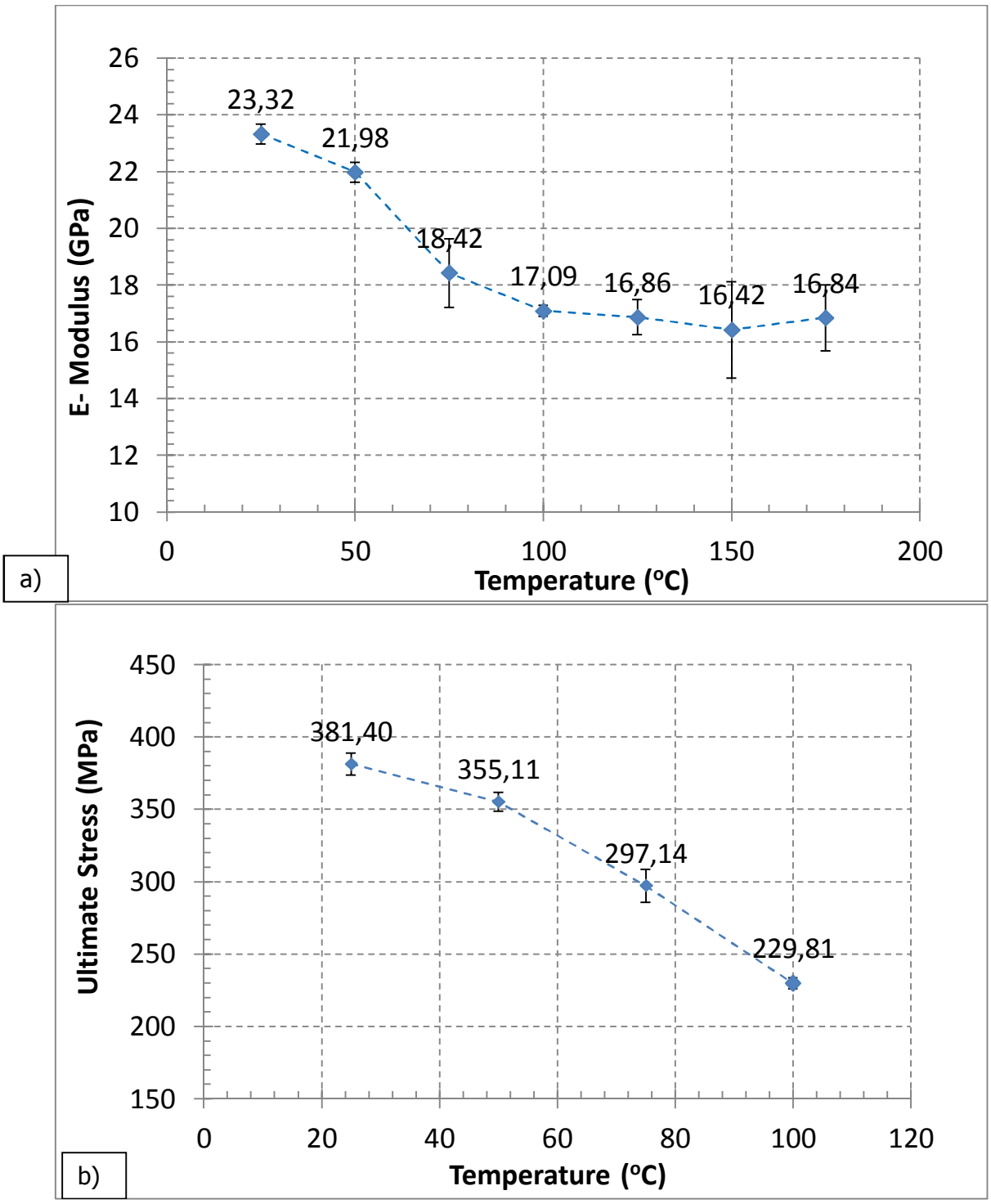

Figure 12. a) Tensile elastic modulus b) Tensile Ultimate strength, reduction due to exposure to elevated temperatures.

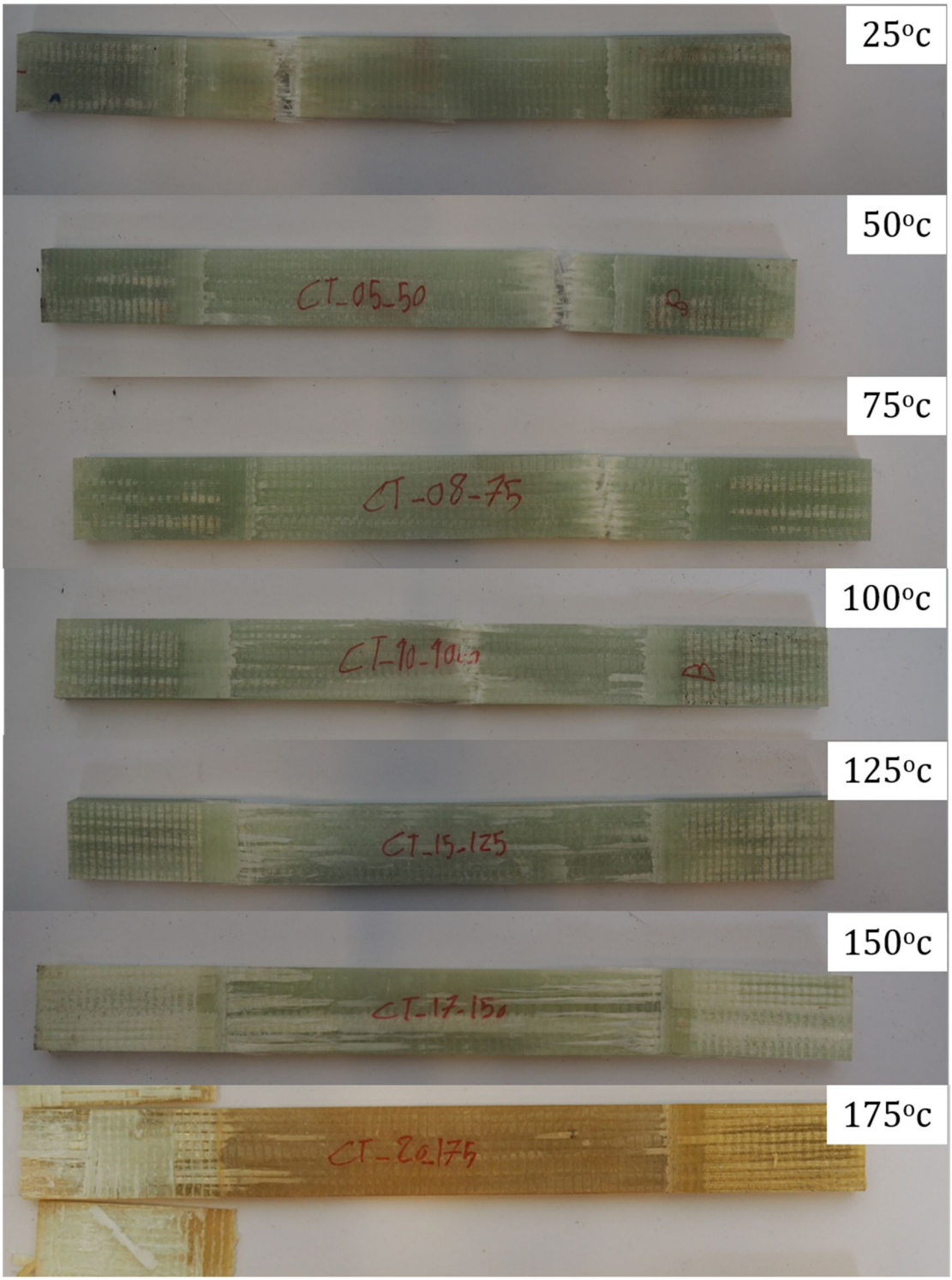

Figure 13. Failure surface of Tensile test specimens after different exposure temperatures (one specimen per exposure time).

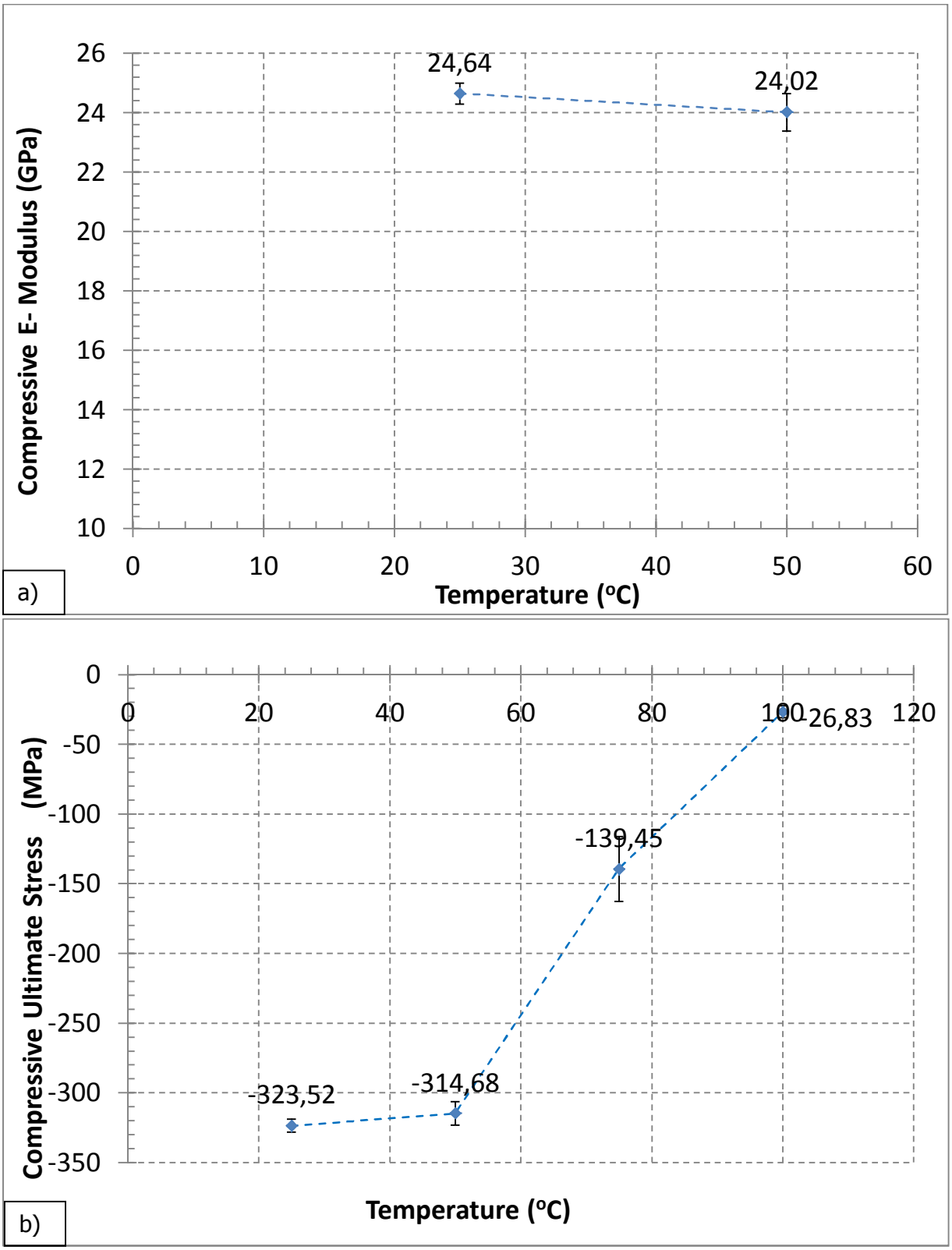

Figure 14. a) Compressive Elastic modulus b) Compressive Ultimate strength, reduction due to exposure to elevated temperatures.

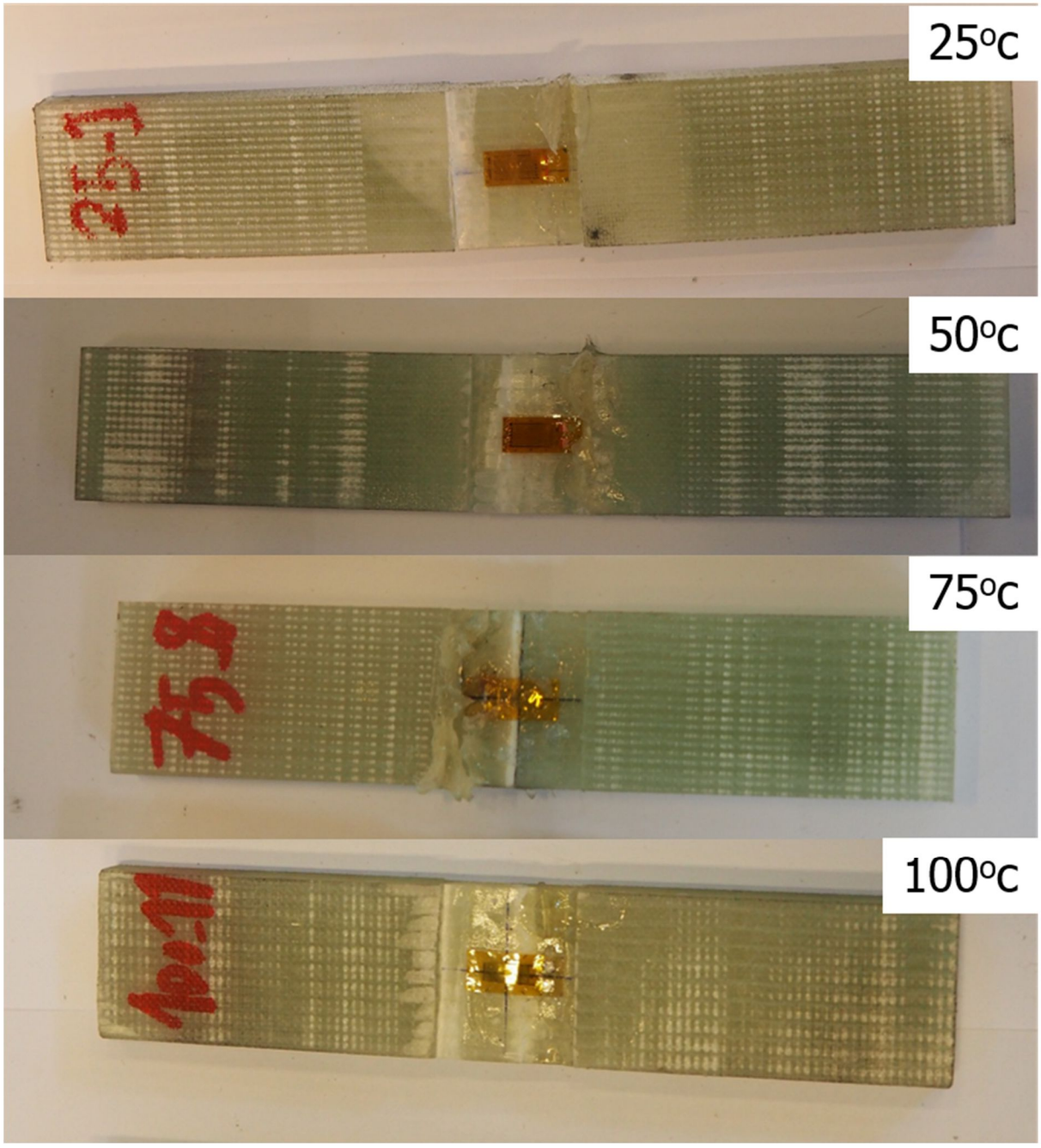

Figure 15. Failure surface of Compressive test specimens after different exposure temperatures (one specimen per exposure time).

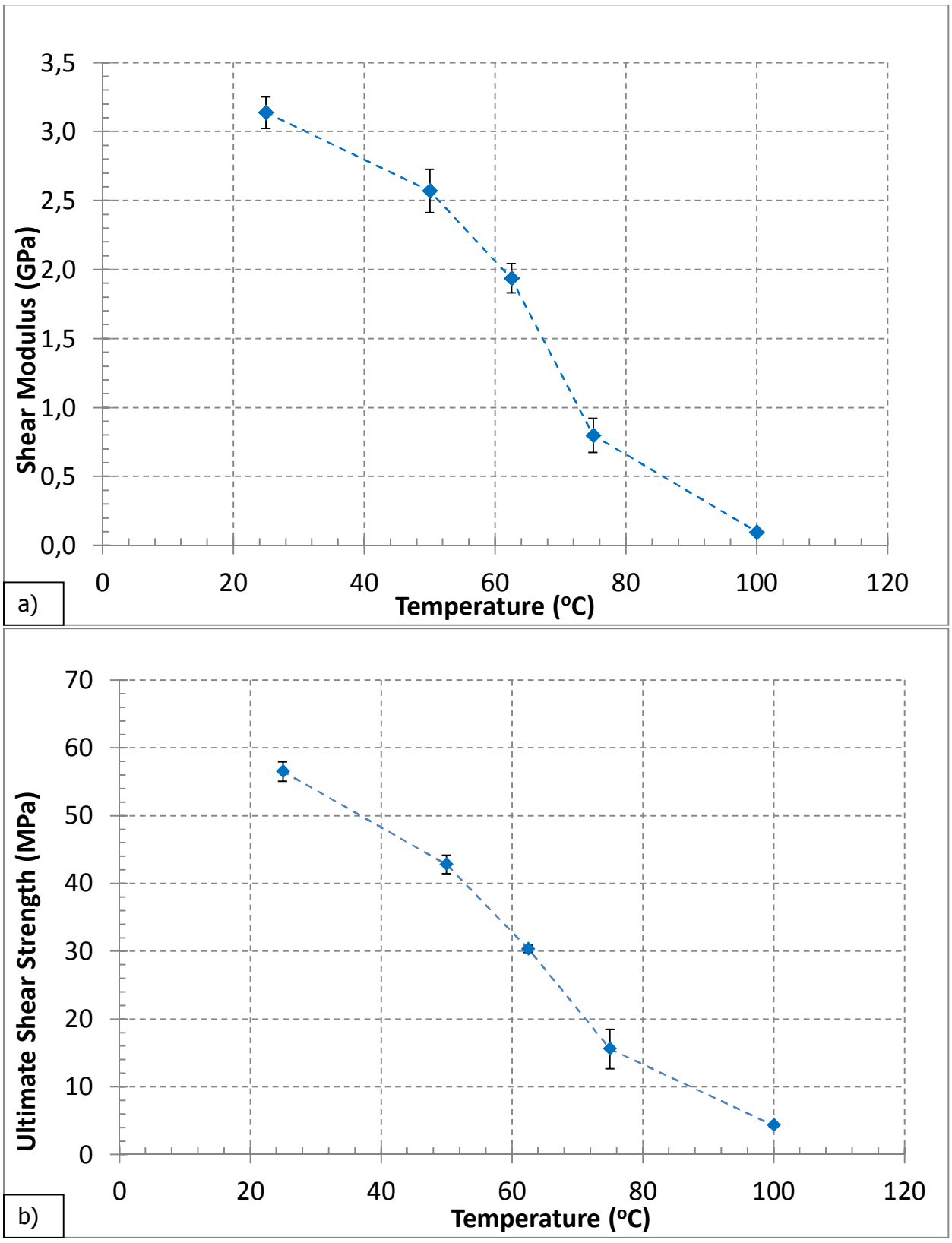

Figure 16. a) Shear modulus b) Shear Ultimate strength, reduction due to exposure to elevated temperatures.

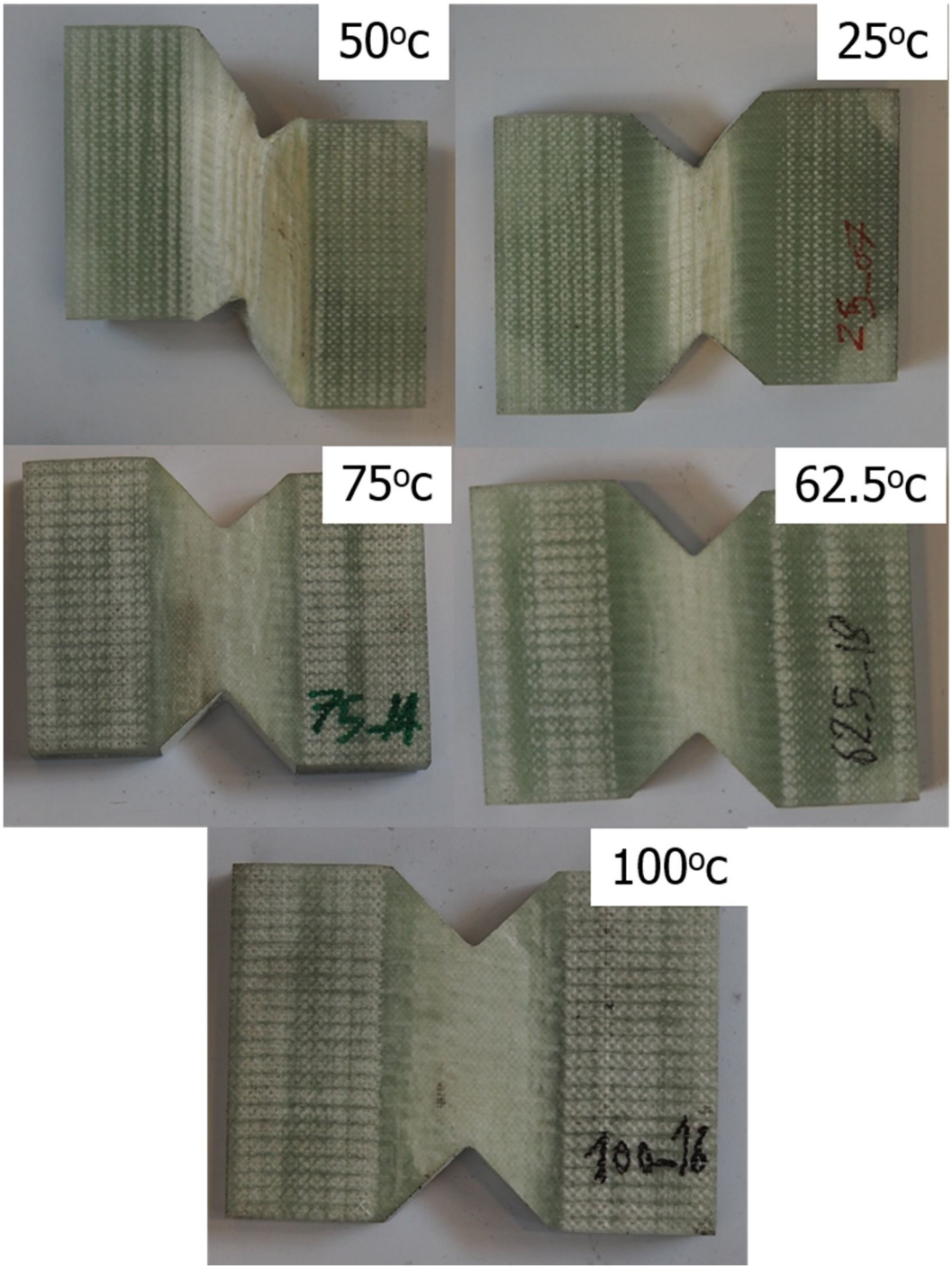

Figure 17. Failure surface of Shear test specimens after different exposure temperatures (one specimen per exposure time).

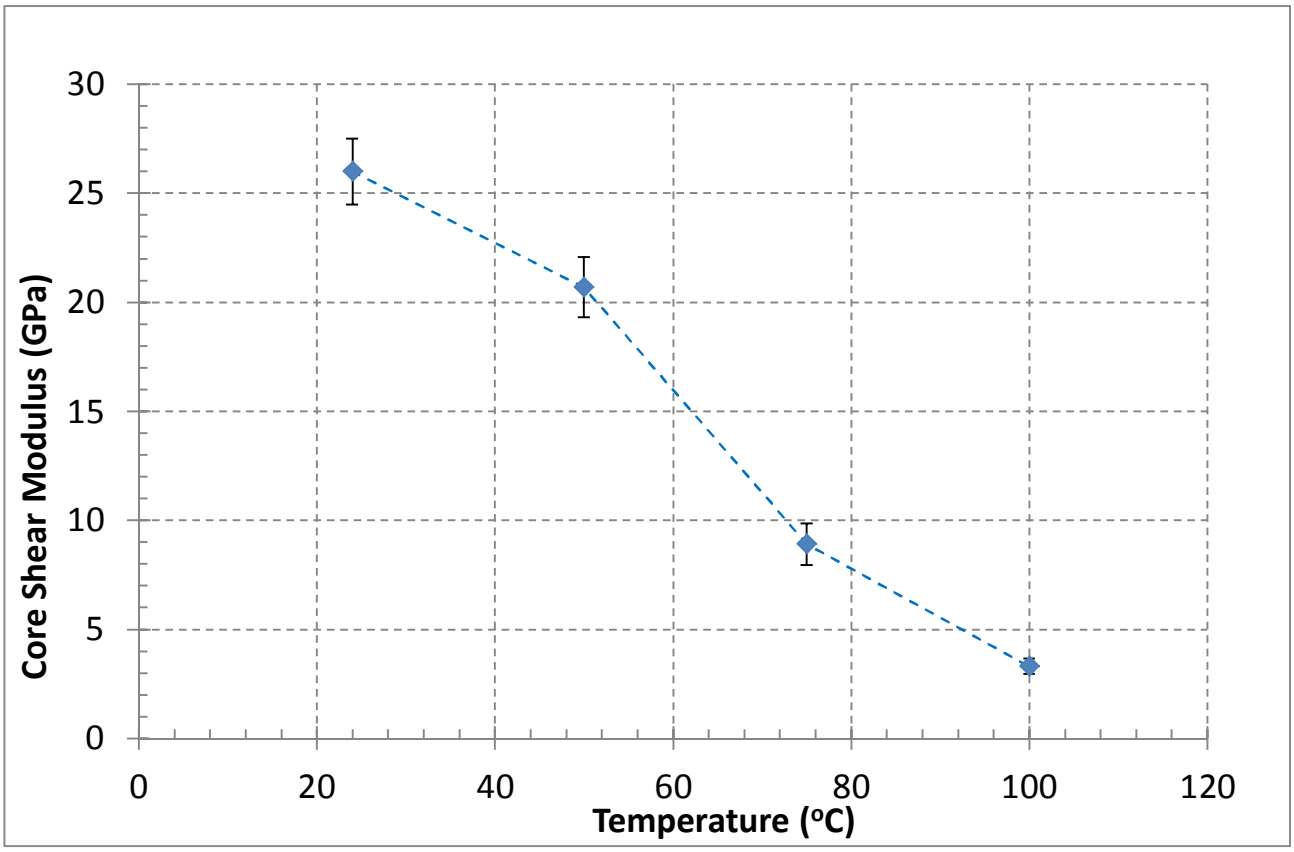

Figure 18. a) Core Shear modulus reduction due to exposure to elevated temperatures.

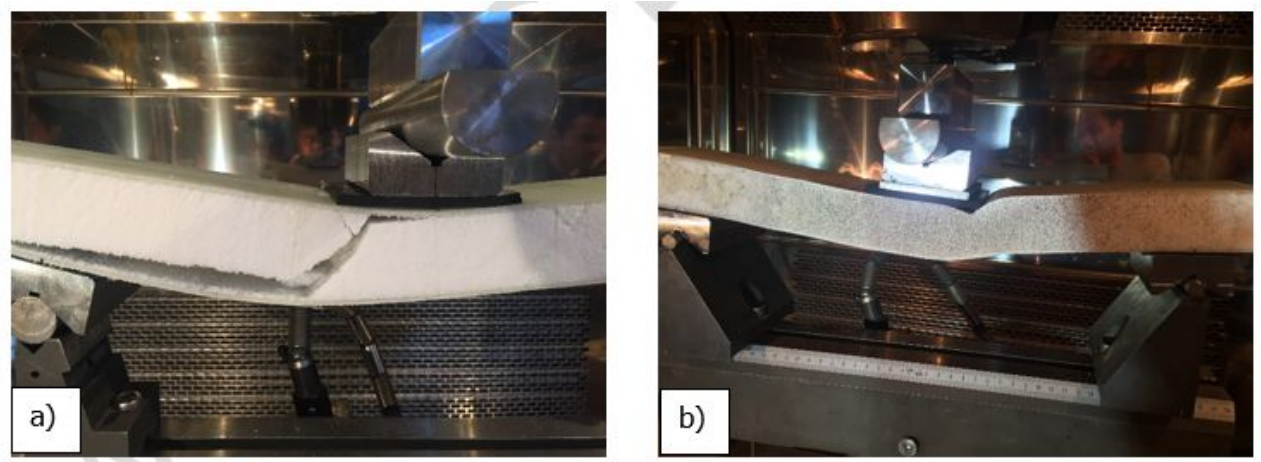

Figure 19 a) Failure due to a) core shear failure at room temperature b) indentation at elevated temperature (50 °C and above) of foam core sandwiches observed in experiments.

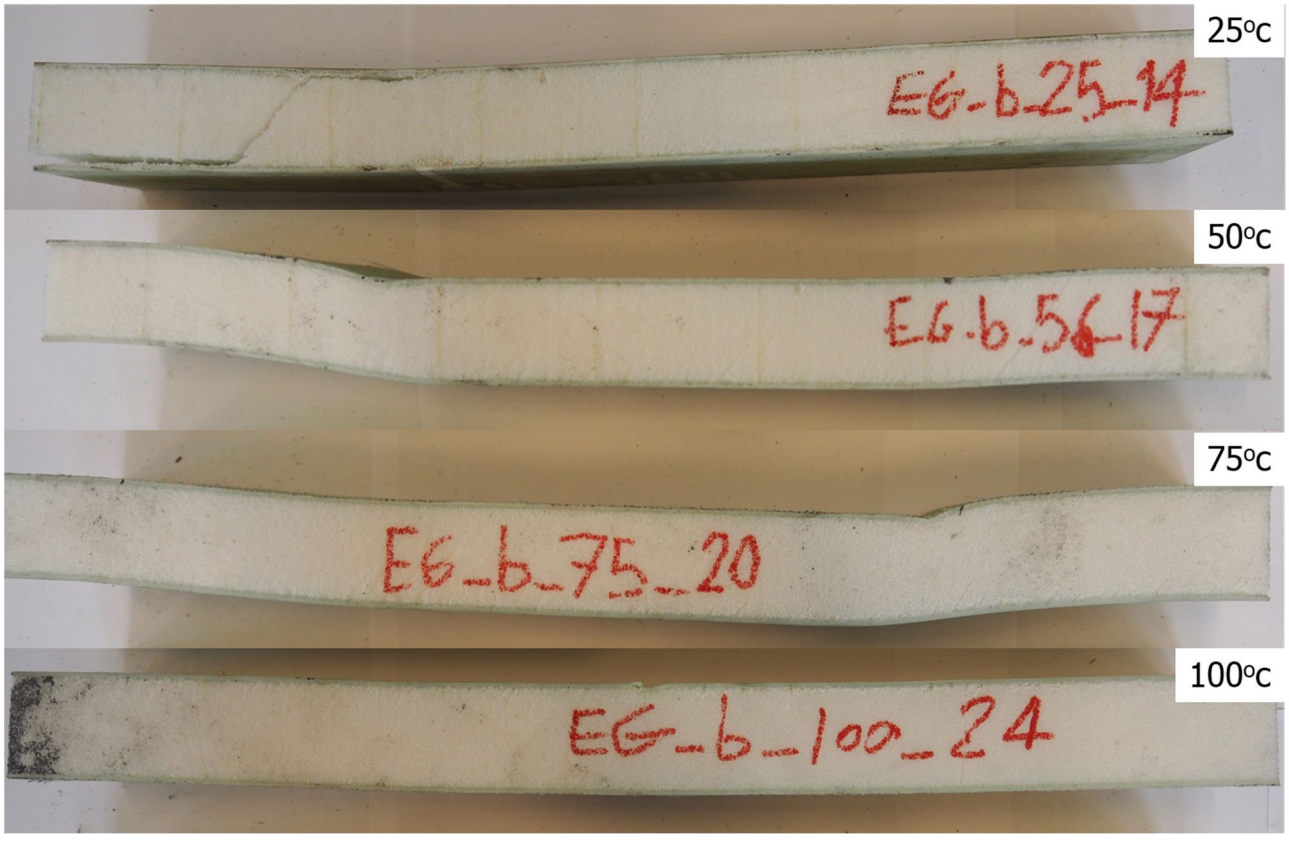

Figure 20**.** Failure surface of Core shear test specimens after different exposure temperatures (one specimen per exposure time).

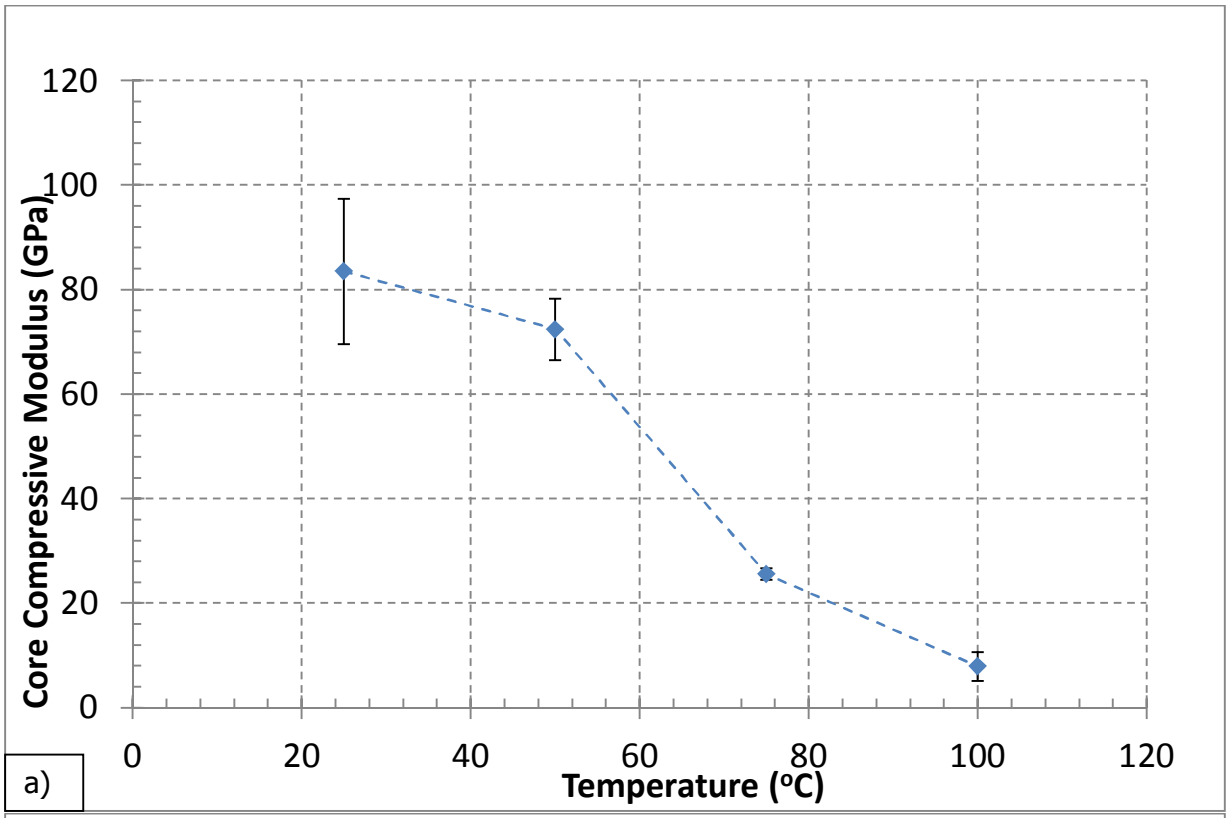

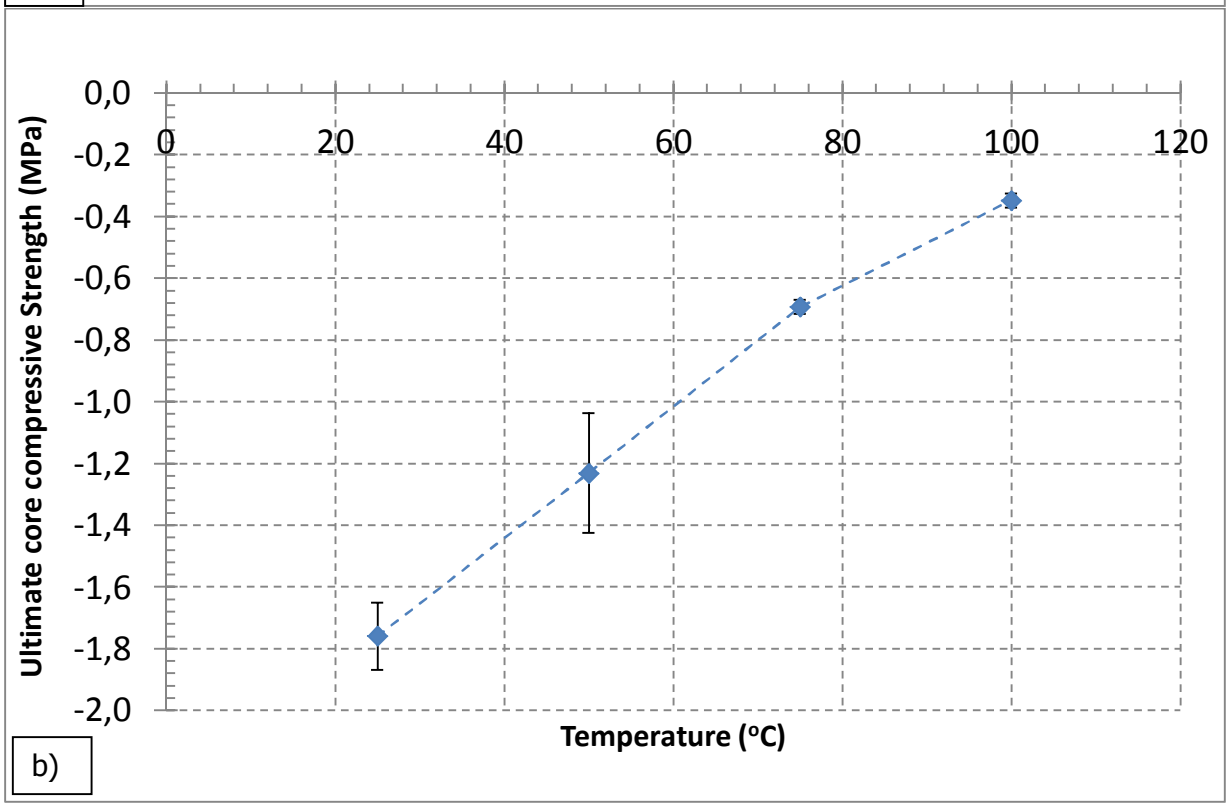

Figure 21. a) Core compressive modulus b) Core compressive Ultimate strength, reduction due to exposure to elevated temperatures.

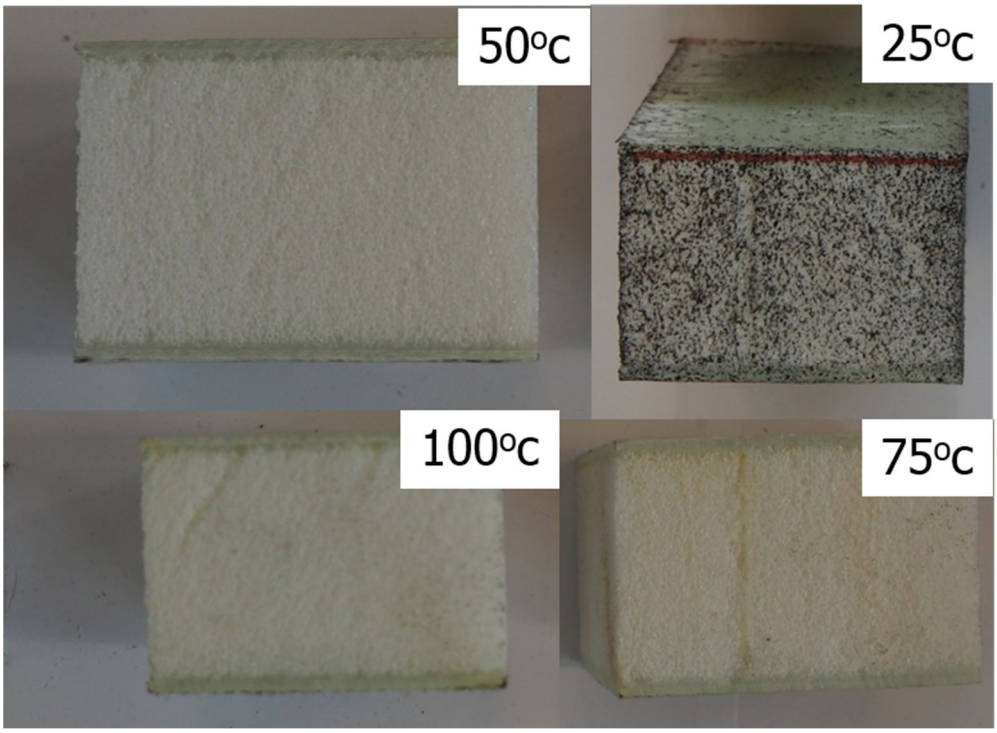

Figure 22. Failure surface of Core shear test specimens after different exposure temperatures (one specimen per exposure time).

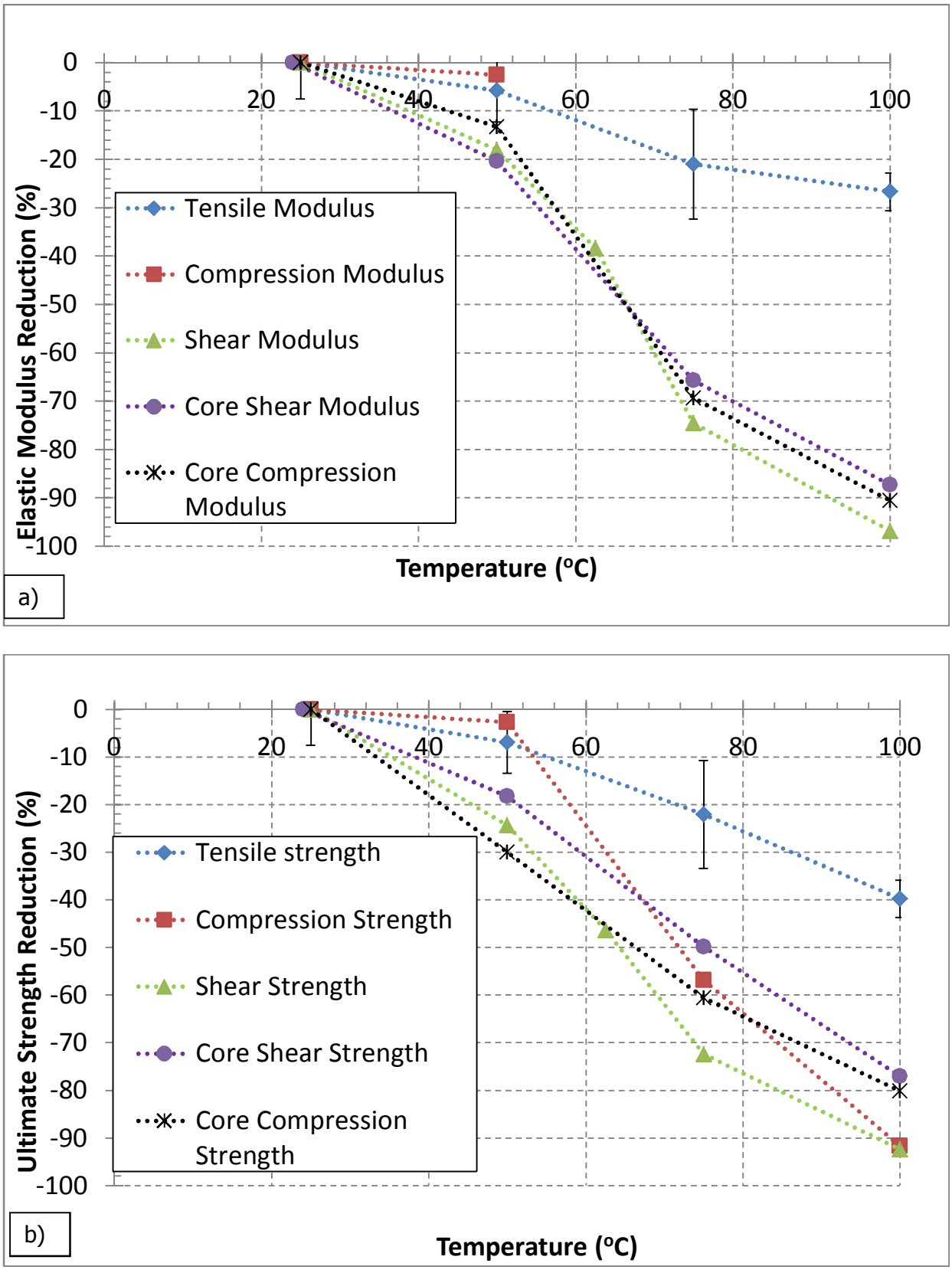

Figure 23. percentage of a) Elastic modulus b) Ultimate strength reduction, due to exposure to elevated temperatures with different tests.

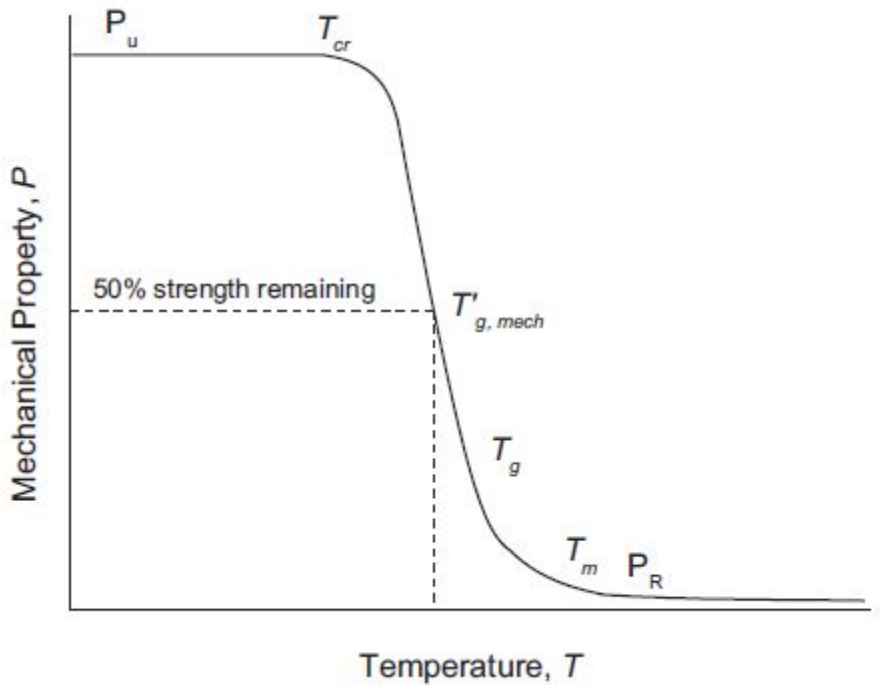

Figure 24. Schematic of the effect of thermal heating on the mechanical property of a laminate [8].

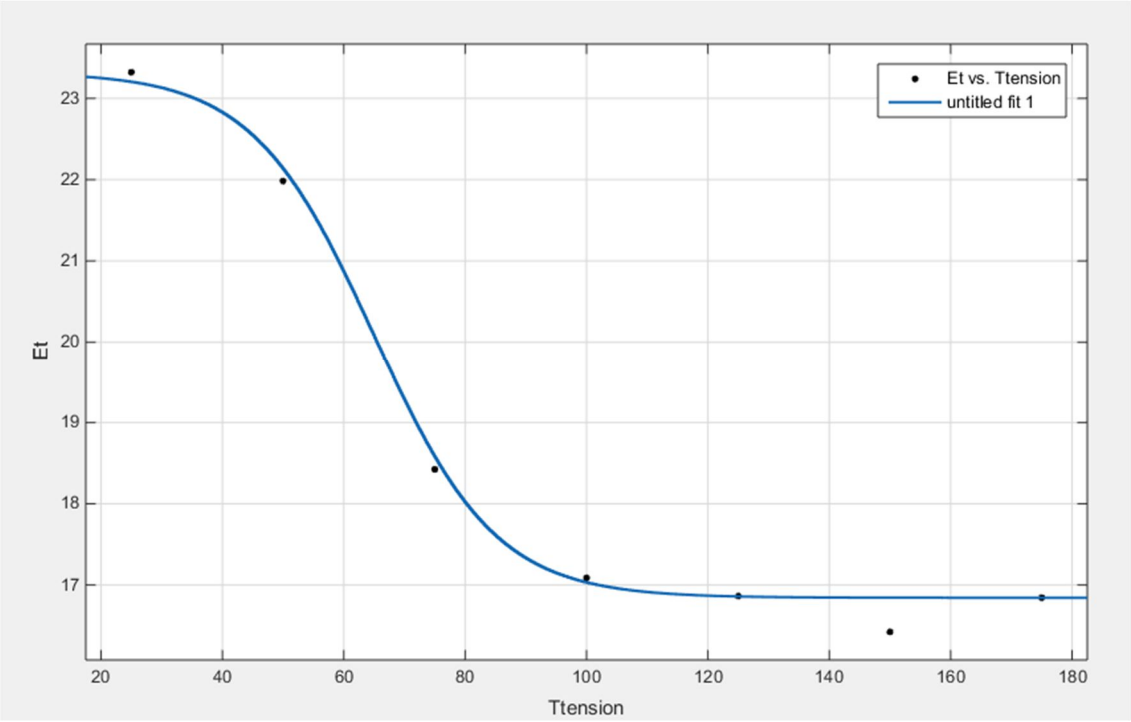

Figure 25. Curve fitting for tensile Elastic modulus with P(T)=23.321×(1-0.5×0.2778×(1+tanh(K×(T-65)×π/180))) and K=2.866)

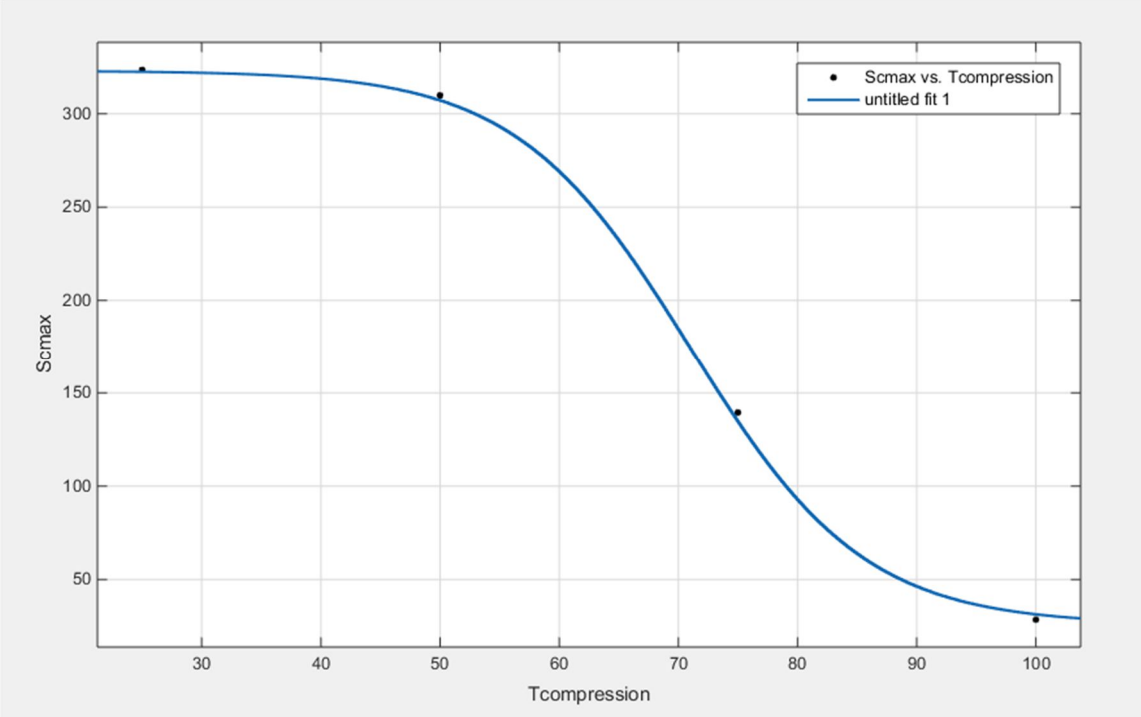

Figure 26. Curve fitting for Compressive ultimate strength with P(T)=323×(1-0.5×0.92×(1+tanh(K×(T-71)×π/180))) and K=3.926

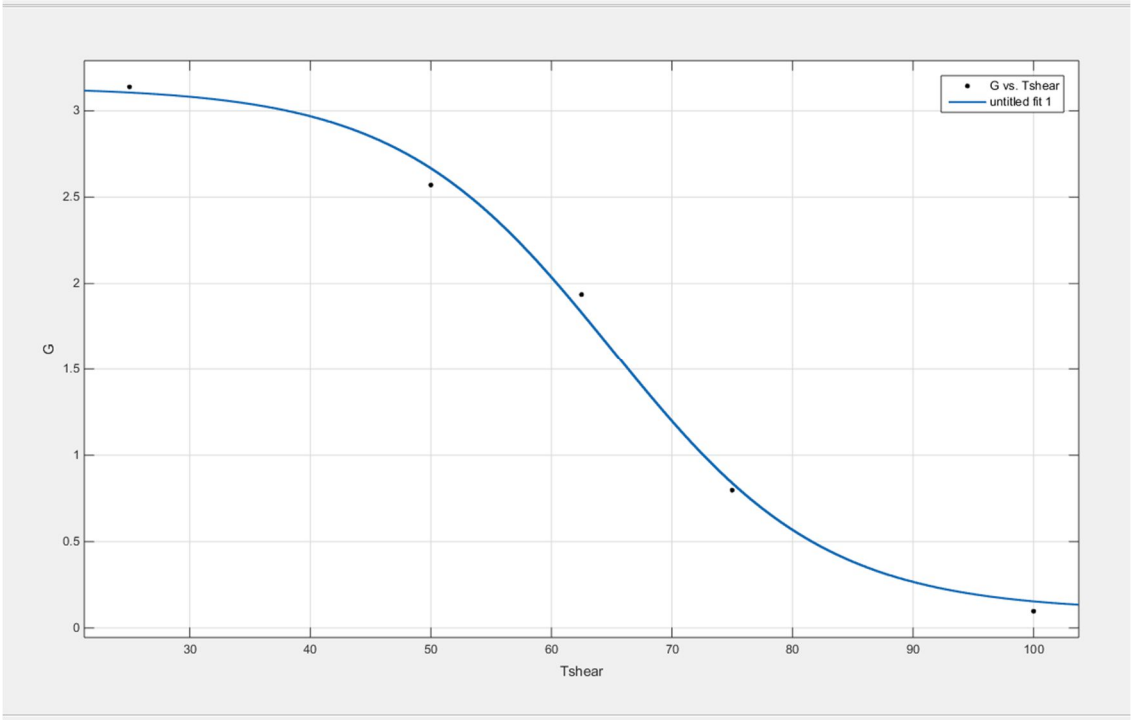

Figure 27. Curve fitting for shear modulus with P(T)=3.1379×(1-0.5×0.96899×(1+tanh(K×(T-65)×π/180))) and K=3.241)

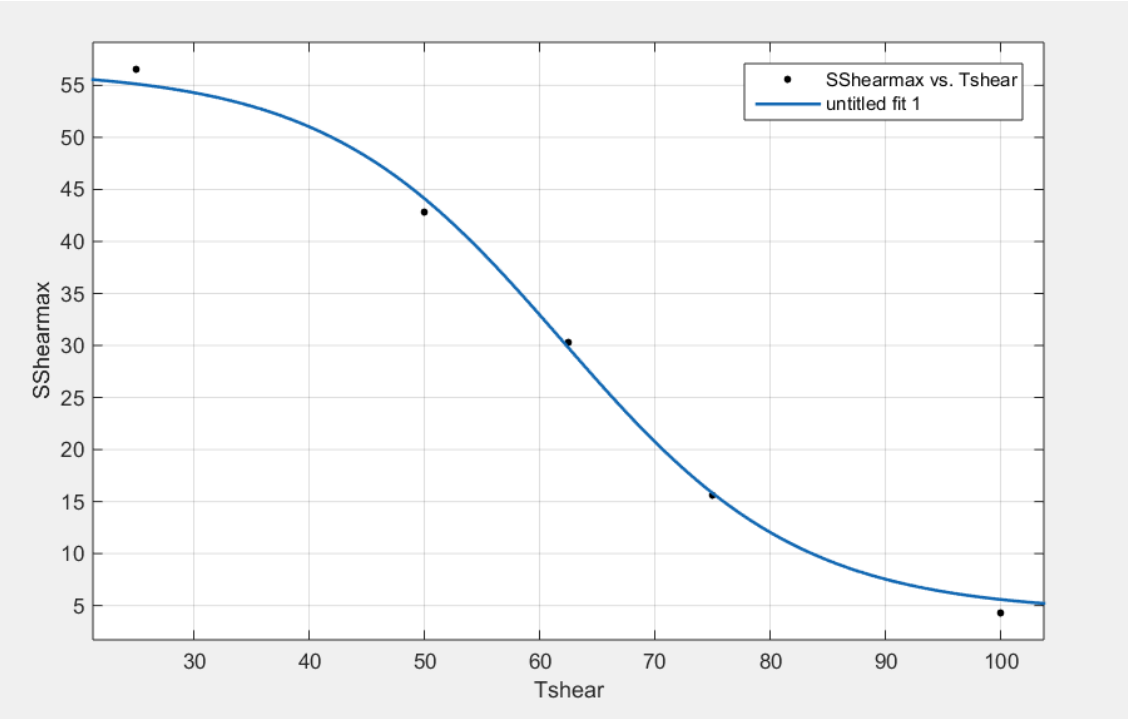

Figure 28. Curve fitting for shear ultimate strength with P(T)=56.53×(1 0.5×0.92354×(1+tanh(K×(T-65) ×π/180))) and K=2.786

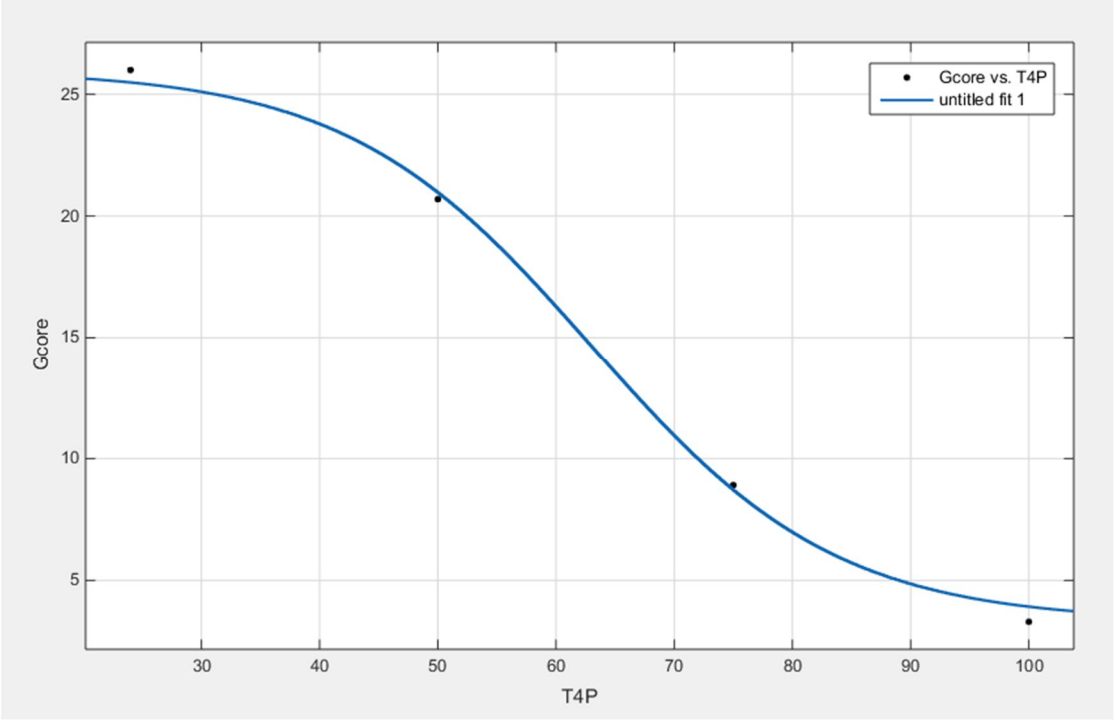

Figure 29. curve fitting for core shear modulus with P(T)=25,997×(1 0.5×0.8729×(1+tanh(K×(T-63) ×π/180))) and K=2,771.

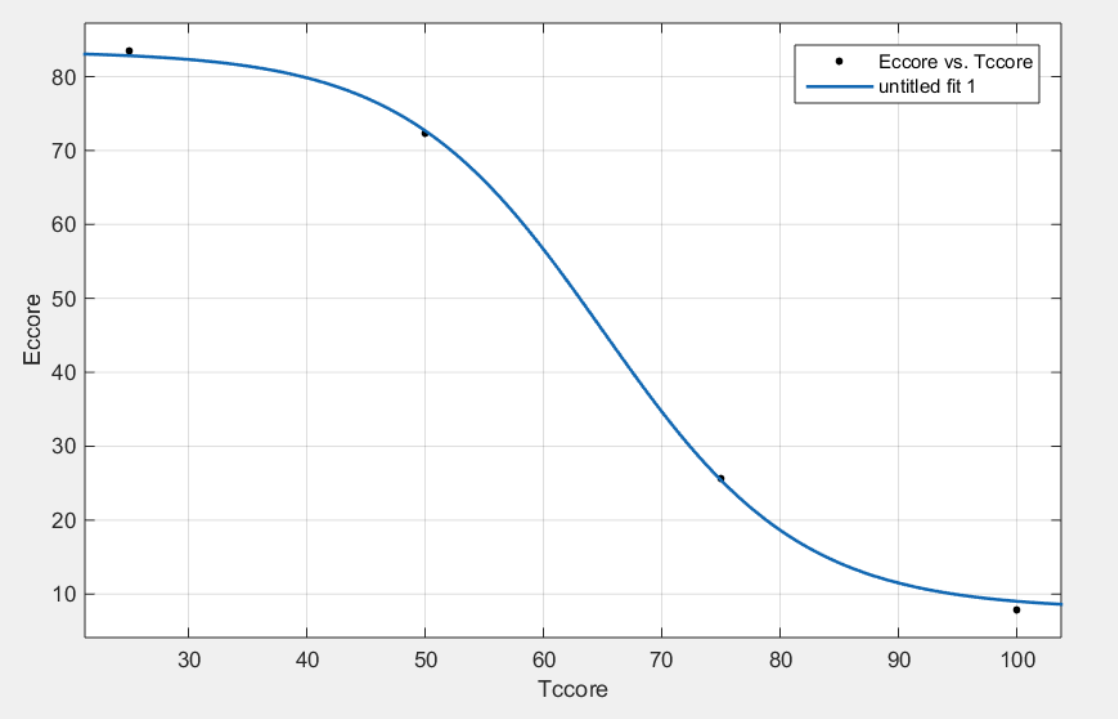

Figure 30. curve fitting for core compressive modulus with P(T)=83,46×(1-0.5×0.90545×(1+tanh(K×(T-65) ×π/180))) and K=3.429

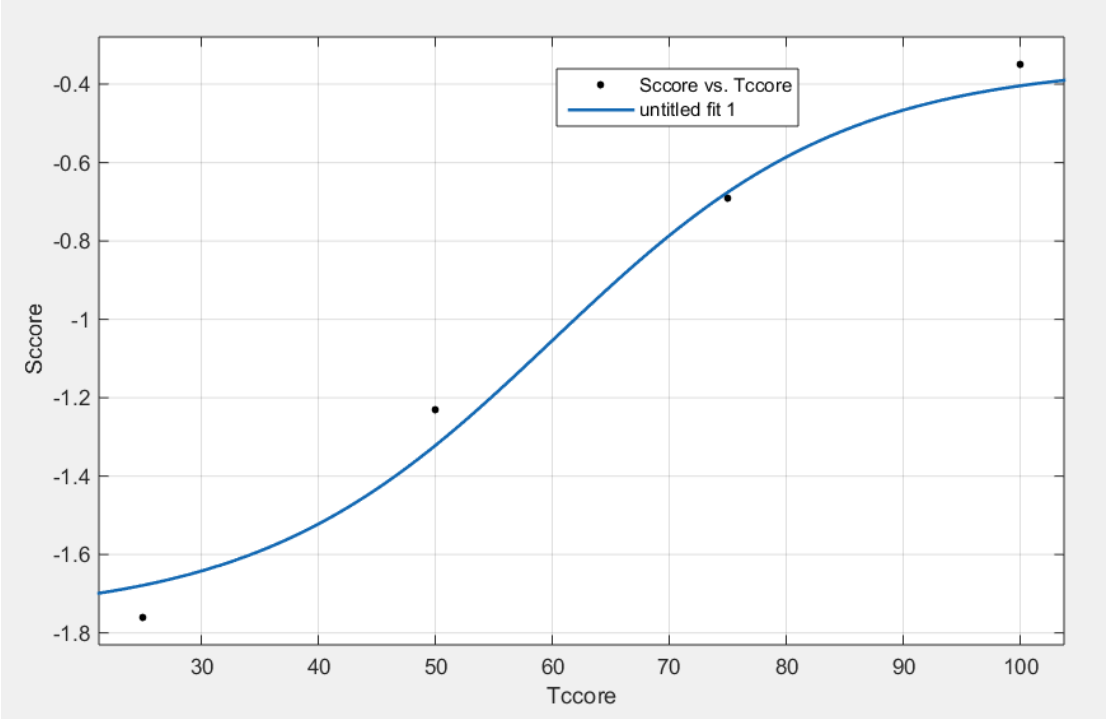

Figure 31. curve fitting for Compressive ultimate strength with P(T)=-1.76×(1-0.5×0.90189×(1+tanh(K×(T-60) ×π/180))) and K=2.288

4 Refrences

[1] T. L. Bergman and F. P. Incropera, *Fundamentals of heat and mass transfer.* Wiley, 2011.

[2] "ASTM D3039/D3039M – 14, Standard Test Method for Tensile Properties of Polymer Matrix Composite Materials 1," *ASTM International*, 2014.

[3] "ASTM D3410/D3410M – 16, Standard Test Method for Compressive Properties of Polymer Matrix Composite Materials with Unsupported Gage Section by Shear Loading 1," *ASTM Int.*, 2016.

[4] ASTM International, "ASTM D7078/D7078M – 12, Standard Test Method for Shear Properties of Composite Materials by V-Notched Rail Shear Method 1," 2012.

[5] "ASTM Standard C393/C393M – 11, Test Method for Core Shear Properties of Sandwich Constructions by Beam Flexure 1," *ASTM Int.*, 2011.

[6] "ASTM D7250/D7250M – 16 Standard, Standard Practice for Determining Sandwich Beam Flexural and Shear Stiffness 1," *ASTM Int.*, 2016.

[7] "ASTM C365/C365M – 16, Standard Test Method for Flatwise Compressive Properties of Sandwich Cores 1," *ASTM Int.*, 2016.

[8] D. R. Tobergte and S. Curtis, *Fire Properties of Polymer Composite Materials*, vol. 53, no. 9. 2013.

[9] R. A. Schapery, "Thermal Expansion Coefficients of Composite Materials Based on Energy Principles," *J. Compos. Mater.*, vol. 2, no. 3, pp. 380–404, Jul. 1968.

Appendix A

Tensile test results

Ultimate Failure load (KN)

Testing Temperature	SP-1	SP-2	SP-3	Average	Standard Deviation	Reduction	Coefficient of Variation	Sample Size	Confidence level (95%)	Margin of Error	Upper Bound	Lower Bound	Max	Min	Range
°C	KN	KN	KN	KN		%					KN	KN	KN	KN	
25	38,60	39,58	39,23	39,14	0,50	0,00	0,01	3,00	1,96	0,56	39,70	38,58	39,58	38,60	0,98
50	36,02	35,59	36,83	36,15	0,63	-7,63	0,02	3,00	1,96	0,71	36,86	35,44	36,83	35,59	1,24
75	31,45	28,67	30,09	30,07	1,39	-23,16	0,05	3,00	1,96	1,58	31,65	28,50	31,45	28,67	2,78
100	22,96	22,96	23,63	23,18	0,39	-40,76	0,02	3,00	1,96	0,44	23,62	22,74	23,63	22,96	0,68
125	20,07	18,20	18,45	18,91	1,01	-51,69	0,05	3,00	1,96	1,14	20,05	17,76	20,07	18,20	1,86
150	13,00	14,01	17,97	14,99	2,63	-61,69	0,18	3,00	1,96	2,97	17,97	12,02	17,97	13,00	4,97
175	11,16	8,80	8,63	9,53	1,41	-75,65	0,15	3,00	1,96	1,60	11,13	7,93	11,16	8,63	2,52

* Specimens failed at tab area

Ultimate Stress (Mpa)

Testing Temperature	SP-1	SP-2	SP-3	Average	Standard Deviation	Reduction	Coefficient of Variation	Sample Size	Confidence level (95%)	Margin of Error	Upper Bound	Lower Bound	Max	Min	Range
°C	MPa	MPa	MPa	MPa		%					MPa	MPa	MPa	MPa	
25	372,82	387,09	384,29	381,40	7,56	0,00	0,02	3,00	1,96	8,56	389,96	372,84	387,09	372,82	14,27
50	354,48	348,96	361,91	355,11	6,50	-6,89	0,02	3,00	1,96	7,35	362,47	347,76	361,91	348,96	12,95
75	307,89	285,28	298,25	297,14	11,35	-22,09	0,04	3,00	1,96	12,84	309,98	284,30	307,89	285,28	22,61
100	227,93	227,20	234,30	229,81	3,90	-39,75	0,02	3,00	1,96	4,41	234,23	225,40	234,30	227,20	7,09
125	198,41	180,08	183,08	187,19	9,83	-50,92	0,05	3,00	1,96	11,13	198,31	176,06	198,41	180,08	18,33
150	129,21	138,91	178,86	148,99	26,31	-60,93	0,18	3,00	1,96	29,77	178,77	119,22	178,86	129,21	49,64
175	111,23	87,40	85,56	94,73	14,32	-75,16	0,15	3,00	1,96	16,20	110,93	78,53	111,23	85,56	25,67

Elastic modulus (Gpa)

Testing Temperature	SP-1	SP-2	SP-3	Average	Standard Deviation	Reduction	Coefficient of Variation	Sample Size	Confidence level (95%)	Margin of Error	Upper Bound	Lower Bound	Max	Min	Range
°C	GPa	GPa	GPa	GPa		%					GPa	GPa	GPa	Gpa	
25	23,67	22,99	23,31	23,32	0,34	0,00	0,01	3,00	1,96	0,39	23,71	22,93	23,67	22,99	0,69
50	22,38	21,86	21,71	21,98	0,35	-5,75	0,02	3,00	1,96	0,40	22,38	21,59	22,38	21,71	0,67
75	18,04	17,44	19,78	18,42	1,21	-21,01	0,07	3,00	1,96	1,37	19,80	17,05	19,78	17,44	2,34
100	16,91	17,29	17,06	17,09	0,19	-26,74	0,01	3,00	1,96	0,22	17,30	16,87	17,29	16,91	0,38
125	16,46	16,55	17,57	16,86	0,62	-27,70	0,04	3,00	1,96	0,70	17,56	16,16	17,57	16,46	1,11
150	14,58	16,75	17,93	16,42	1,70	-29,59	0,10	3,00	1,96	1,92	18,35	14,50	17,93	14,58	3,35
175	15,67	18,00	16,85	16,84	1,17	-27,78	0,07	3,00	1,96	1,32	18,16	15,52	18,00	15,67	2,33

Compressive test results

Ultimate Failure load (KN)

Testing Temperature	SP-1	SP-2	SP-3	Average	Standard Deviation	Reduction	Coefficient of Variation	Sample Size	Confidence level (95%)	Margin of Error	Upper Bound	Lower Bound	Max	Min	Range
°C	KN	KN	KN	KN		%					KN	KN	KN	KN	
25	-32,09	-32,08	-32,88	-32,35	0,46	0,00	-0,01	3,00	1,96	0,52	-31,83	-32,87	-32,08	-32,88	0,81
50	-31,18	-30,80	-32,43	-31,47	0,85	-2,73	-0,03	3,00	1,96	0,96	-30,51	-32,43	-30,80	-32,43	1,63
75	-11,83	-13,58	-16,43	-13,95	2,32	-56,89	-0,17	3,00	1,96	2,63	-11,32	-16,57	-11,83	-16,43	4,60
100	-3,16	-2,54	-2,33	-2,68	0,43	-91,72	-0,16	3,00	1,96	0,49	-2,19	-3,17	-2,33	-3,16	0,83

Ultimate Stress (Mpa)

Testing Temperature	SP-1	SP-2	SP-3	Average	Standard Deviation	Reduction	Coefficient of Variation	Sample Size	Confidence level (95%)	Margin of Error	Upper Bound	Lower Bound	Max	Min	Range
°C	MPa	MPa	MPa	MPa		%					MPa	MPa	MPa	MPa	
25	-320,91	-320,79	-328,85	-323,52	4,62	0,00	-0,01	3,00	1,96	5,22	-318,30	-328,74	-320,79	-328,85	8,05
50	-311,81	-307,98	-324,26	-314,68	8,51	-2,73	-0,03	3,00	1,96	9,63	-305,05	-324,31	-307,98	-324,26	16,28
75	-118,29	-135,80	-164,27	-139,45	23,21	-56,89	-0,17	3,00	1,96	26,26	-113,19	-165,71	-118,29	-164,27	45,98
100	-31,68	-25,38	-23,43	-26,83	4,31	-91,71	-0,16	3,00	1,96	4,88	-21,95	-31,71	-23,43	-31,68	8,25

Elastic modulus (Gpa)

Testing Temperature	SP-1	SP-2	SP-3	Average	Standard Deviation	Reduction	Coefficient of Variation	Sample Size	Confidence level (95%)	Margin of Error	Upper Bound	Lower Bound	Max	Min	Range
°C	GPa	GPa	GPa	GPa		%					GPa	GPa	GPa	Gpa	
25	24,24	24,86	24,84	24,64	0,35	0,00	0,01	3,00	1,96	0,40	25,04	24,24	24,86	24,24	0,62
50	23,31	24,51	24,25	24,02	0,63	-2,53	0,03	3,00	1,96	0,71	24,73	23,31	24,51	23,31	1,20

Shear test results

Ultimate Shear Strength (Mpa)

Testing Temperature	SP-1	SP-2	SP-3	Average	Standard Deviation	Reduction	Coefficient of Variation	Sample Size	Confidence level (95%)	Margin of Error	Upper Bound	Lower Bound	Max	Min	Range
°C	MPa	MPa	MPa	MPa		%					MPa	MPa	MPa	MPa	
25	58,04	55,16	56,38	**56,53**	**1,45**	**0,00**	0,03	3,00	1,96	1,64	58,17	54,89	58,04	55,16	2,89
50	**42,00**	41,97	44,35	**42,77**	**1,37**	**-24,33**	0,03	3,00	1,96	1,55	44,32	41,23	44,35	41,97	2,38
62,5	**30,97**	30,10	29,96	**30,34**	**0,55**	**-46,32**	0,02	3,00	1,96	0,62	30,97	29,72	30,97	29,96	1,01
75	12,30	17,78	16,64	**15,57**	**2,89**	**-72,45**	0,19	3,00	1,96	3,27	18,85	12,30	17,78	12,30	5,48
100	4,38	4,47	4,11	**4,32**	**0,19**	**-92,35**	0,04	3,00	1,96	0,22	4,54	4,11	4,47	4,11	0,37

Shear modulus (Gpa)

Testing Temperature	SP-1	SP-2	SP-3	Average	Standard Deviation	Reduction	Coefficient of Variation	Sample Size	Confidence level (95%)	Margin of Error	Upper Bound	Lower Bound	Max	Min	Range
°C	GPa	GPa	GPa	GPa		%					GPa	GPa	GPa	Gpa	
25	3,06	3,27	3,09	**3,14**	**0,11**	**0,00**	0,04	3,00	1,96	0,13	3,27	3,01	3,27	3,06	0,21
50	2,40	2,70	2,62	**2,57**	**0,16**	**-18,09**	0,06	3,00	1,96	0,18	2,75	2,39	2,70	2,40	0,30
62,5	2,03	1,82	1,96	**1,94**	**0,11**	**-38,30**	0,05	3,00	1,96	0,12	2,06	1,82	2,03	1,82	0,21
75	0,71	0,74	0,94	**0,80**	**0,12**	**-74,57**	0,15	3,00	1,96	0,14	0,94	0,66	0,94	0,71	0,23
100	0,09	0,09	0,11	**0,10**	**0,01**	**-96,90**	0,14	3,00	1,96	0,02	0,11	0,08	0,11	0,09	0,03

Core Shear test results

Ultimate Stress (Mpa)

Testing Temperature	SP-1	SP-2	SP-3	Average	Standard Deviation	Reduction	Coefficient of Variation	Sample Size	Confidence level (95%)	Margin of Error	Upper Bound	Lower Bound	Max	Min	Range
°C	MPa	MPa	MPa	MPa		%					MPa	MPa	MPa	MPa	
24	0,89	0,84	0,90	**0,88**	**0,04**	**0,00**	0,04	3,00	1,96	0,04	0,92	0,84	0,90	0,84	0,07
50	0,71	0,73	0,72	**0,72**	**0,01**	**-18,23**	0,01	3,00	1,96	0,01	0,73	0,71	0,73	0,71	0,02
75	0,44	0,43	0,44	**0,44**	**0,01**	**-49,88**	0,02	3,00	1,96	0,01	0,45	0,43	0,44	0,43	0,01
100	0,17	0,24	0,20	**0,20**	**0,04**	**-77,08**	0,18	3,00	1,96	0,04	0,24	0,16	0,24	0,17	0,07

* Just the Specimens failed Due to shear

Shear modulus (Mpa)

Testing Temperature	SP-1	SP-2	SP-3	Average	Standard Deviation	Reduction	Coefficient of Variation	Sample Size	Confidence level (95%)	Margin of Error	Upper Bound	Lower Bound	Max	Min	Range
°C	MPa	MPa	MPa	MPa		%					GPa	GPa	GPa	Gpa	
24	24,91	25,37	27,71	**26,00**	**1,50**	**0,00**	0,06	3,00	1,96	1,70	27,70	24,29	27,71	24,91	2,81
50	19,14	21,17	21,76	**20,69**	**1,38**	**-20,40**	0,07	3,00	1,96	1,56	22,25	19,14	21,76	19,14	2,62
75	8,87	7,96	9,89	**8,91**	**0,97**	**-65,74**	0,11	3,00	1,96	1,09	10,00	7,81	9,89	7,96	1,93
100	2,89	3,48	3,54	**3,30**	**0,36**	**-87,29**	0,11	3,00	1,96	0,40	3,71	2,90	3,54	2,89	0,65

Core Compression test results

Ultimate Failure load (KN)

Testing Temperature	SP-1	SP-2	SP-3	Average	Standard Deviation	Reduction	Coefficient of Variation	Sample Size	Confidence level (95%)	Margin of Error	Upper Bound	Lower Bound	Max	Min	Range
°C	KN	KN	KN	KN		%					KN	KN	KN	KN	
25	-4,88	-5,88	-5,36	**-5,37**	**0,50**	**0,00**	-0,09	3,00	1,96	0,57	-4,81	-5,94	-4,88	-5,88	1,00
50	-4,87	-1,45	-4,02	**-3,45**	**1,78**	**-35,79**	-0,52	3,00	1,96	2,01	-1,44	-5,46	-1,45	-4,87	3,42
75	-1,71	-1,77	-1,64	**-1,70**	**0,07**	**-68,28**	-0,04	3,00	1,96	0,07	-1,63	-1,78	-1,64	-1,77	0,13
100	-0,70	-0,53		**-0,61**	**0,12**	**-88,56**	-0,20	2,00	1,96	0,17	-0,45	-0,78	-0,53	-0,70	0,17

Ultimate Stress (Mpa)

Testing Temperature	SP-1	SP-2	SP-3	Average	Standard Deviation	Reduction	Coefficient of Variation	Sample Size	Confidence level (95%)	Margin of Error	Upper Bound	Lower Bound	Max	Min	Range
°C	MPa	MPa	MPa	MPa		%					MPa	MPa	MPa	MPa	
25	-1,88	-1,66	-1,74	**-1,76**	**0,11**	**0,00**	-0,06	3,00	1,96	0,12	-1,64	-1,88	-1,66	-1,88	0,22
50	-1,45	-1,11	-1,12	**-1,23**	**0,19**	**-30,01**	-0,16	3,00	1,96	0,22	-1,01	-1,45	-1,11	-1,45	0,34
75	-0,70	-0,71	-0,67	**-0,69**	**0,02**	**-60,60**	-0,03	3,00	1,96	0,03	-0,67	-0,72	-0,67	-0,71	0,05
100	-0,36	-0,33		**-0,35**	**0,02**	**-80,19**	-0,06	2,00	1,96	0,03	-0,32	-0,38	-0,33	-0,36	0,03

Elastic modulus (Gpa)

Testing Temperature	SP-1	SP-2	SP-3	Average	Standard Deviation	Reduction	Coefficient of Variation	Sample Size	Confidence level (95%)	Margin of Error	Upper Bound	Lower Bound	Max	Min	Range
°C	GPa	GPa	GPa	GPa		%					GPa	GPa	GPa	Gpa	
25	71,25	98,61	80,52	**83,46**	**13,92**	**0,00**	0,17	3,00	1,96	15,75	99,21	67,71	98,61	71,25	27,36
50	76,00	75,54	65,64	**72,39**	**5,86**	**-13,26**	0,08	3,00	1,96	6,63	79,02	65,77	76,00	65,64	10,37
75	25,28	26,76	24,61	**25,55**	**1,10**	**-69,39**	0,04	3,00	1,96	1,24	26,79	24,30	26,76	24,61	2,15
100	10,73	7,65	5,29	**7,89**	**2,73**	**-90,54**	0,35	3,00	1,96	3,09	10,98	4,80	10,73	5,29	5,44

Annex F: Reaction to fire of composite sandwich-materials

Cone Calorimeter tests and ignition temperature

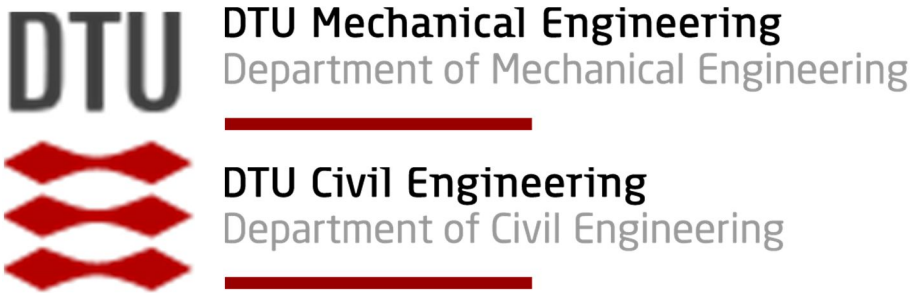

Date : September 2016
Project name : COMPASS – Composite superstructures for large PASSenger ships

Author : Mindykowski Pierrick – DTU Byg

Content

Summary

This appendix presents all the tests that were performed to study the reaction to fire of two composite sandwich-materials. A cone calorimeter was used, following the ISO 5660 standard.
From these tests, the spontaneous and piloted temperatures of ignition were determined.
The first type of skin, a geopolymer type, showed a non-combustible behaviour.
Ignition temperatures of the core material were lesser than that of the epoxy-based skin and the sandwich assembly. As a result, it can be concluded that the core material is the weakness of these types of sandwich, which is as expected.
It is important to point out that all of these ignition temperatures were much higher than the glass transition temperature of the core material. Therefore, before ignition can occur, the building element made by these types of sandwich will most likely already have collapsed.

1. Introduction

The goal of the COMPASS project is to give an answer, or at least to provide an avenue of reflection on the question: Can we use fibre reinforced polymer as composite in the construction of the superstructure of passenger ships?
This question is important due to the fact that composite materials offer a large range of advantages for the marine industry such as light weight, reduction of the maintenance costs and the possibility to create complex shapes. However, in order to have the approval of the authorities for building a SOLAS vessel with composite materials, this alternative design has to show an equivalent level of safety as the prescriptive requirement which is based on the use of metals 0.
The topic is the reaction to fire of two composite sandwiches. For this study, a cone calorimeter has been used to determine one of the main key parameter for the fire protection: the temperature of ignition.
The studied sandwiches have the same core material: DIAB Divinycell P100, but present two different types of skin: geopolymer and epoxy.

2. Cone calorimeter and its use for the present study

2.1 Cone calorimeter and ISO 5660

The reaction to fire of the sandwich specimen was studied in a cone calorimeter developed by Fire Testing Technology (ISO 5660 standard [2.]) under well-ventilated conditions. The ISO 5660 standard specifies a method for assessing the heat release rate and dynamic smoke production rate of specimens exposed in the horizontal orientation to controlled levels of irradiance with an external igniter.
In the present study, the Annex H of the ISO 5660 standard is used. This annex presents the methodology for the calculation of effective critical heat flux for ignition. "*This critical heat flux for ignition is the minimum heat flux needed to sustain ignition. It can be determined empirically using the cone calorimeter by exposing specimens to different heat fluxes and measuring the ignition times for sustained flaming* (with the presence of an igniter, i.e. electrical spark)*. It is determined by trial and error with repeated tests in search of the heat flux for no ignition occurring within 15 minutes duration*." [2.] .
The standard specifies that three specimens shall be tested at each level of irradiance selected; each tested specimen shall be square with sides measuring 100 mm (+0/-2 mm). The procedure according the standard is the following:
"*Expose news specimens in each successive experiment to a different heat flux exposure and measure and record the time to sustained ignition of the vapours for each. The minimum heat flux is determined by trial and error. It shall first be determined to a coarse resolution of 5kW/m^2, and then more finely to 1 kW/m^2.*
Determine the lowest value of heat flux at which sustained ignition is achieved, and the highest value at which ignition is not achieved. The minimum heat flux for ignition is defined as the average between the lowest heat flux at which there is ignition, and the highest heat flux at which there is no ignition for 15 minutes. For example, if the specimen ignites at 30 kW/m^2 within 15 minutes, then repeat the same procedure at 25 kW/m^2, 20 kW/m^2, 15 kW/m^2 and 10 kW/m^2 (in that order) until there is no ignition for 15 minutes.

If test results show a crossover, in that the lowest heat flux at which ignition occurs is lower than the highest heat flux at which no ignition was found it will be necessary to carry out triplicate tests for each determination and average results. The average of the (averaged) highest flux for non-ignition in 15 minutes and the averaged lowest heat fluxes for ignition within 15 minutes is the reported value for the minimum heat flux for ignition."

2.2 Use of the cone calorimeter in the present study

In the present study, some deviations from the ISO 5660 should be noted. As the studied material is a sandwich composite element used on board ships (described in the introduction), it should show a resistance to fire for 60 minutes [2.]. That is why the minimum time of testing in this study was 30 minutes instead of the 15 minutes described in the standard.
Additionally, as the number of specimen was low, the methodology to find out the temperature of ignition was not a trial and error methodology, but the use of the methodology and results developed by Spearpoint and Quintiere [3.]. The authors have shown that from few experimental data points, it is easy to find the critical heat flux using a simple relation between these data points [3.].
And finally, two different set of experiments have been performed. The first one used a spark as igniter to find the critical temperature of the piloted ignition. But as the specimen is usually used with the presence of thermal insulation (several layers of insulation, separated by aluminium foils), it is clearly understandable that in this case, the piloted ignition by a flame is not the main process. That is why the second set of experiments is non-piloted ignition (without presence of igniter, i.e. the electrical spark).

3. Results of experiments on the cone calorimeter

3.1 Piloted ignition

3.1.1 Sandwich: Geopolymer skin and DIAB Divinycell P100 core

The first set of experiments was performed on the sandwich made by a geopolymer skin and core material provided by DIAB and called Divinycell P100.
The results are presented on the following table. Remark: only two tests for each heat flux were performed).

Table 1: Time to piloted ignition vs. Radiant heat flux for the sandwich made by Geopolymer skin and DIAB Divinycell P100 core.

Radiant heat flux (kW/m^2)	Time to ignition (s)	Remarks
15	No ignition	-
15	No ignition	-
20	No ignition	Collapse of the skin
20	No ignition	Collapse of the skin
25	810	Flame from the core
25	750	Flame from the core
30	332	Flame from the core
30	389	Flame from the core

The first results show that the geopolymer skin was not combustible but that the core material can burn under the skin. Also, it seems that the core material, in the present case, starts to melt or regress before its ignition. This conclusion is made by the result of the test under 20 kW/m^2.
This regression of the core is visible on the following picture. The thickness of the core material was reduced by 50 percent.

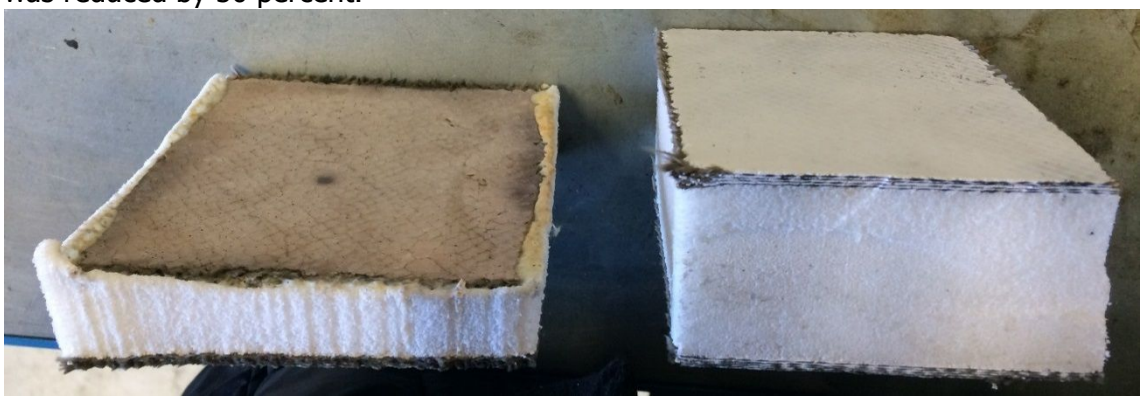

Figure 1: Sandwich made with geopolymer skin and DIAB Divinycell P100 core before and after an ignition test under the cone calorimeter at 20 kW/m^2.

This results lead to this conclusion: In order to test the ignitability of a sandwich, the study should imply three different tests as test for the skin itself, test for the core itself and test for the sandwich.

3.1.2 Geopolymer skin

As shown by the previous results, the ignition of the skin itself was studied to make uncorrelated the time to ignition of the core to the time to ignition of the skin.

Table 2: Time to piloted ignition vs. Radiant heat flux for the Geopolymer skin.

Radiant heat flux (kW/m^2)	Time to ignition (s)	Remarks
30	No ignition	-
30	No ignition	-
40	No ignition	Collapse of the skin
40	No ignition	Collapse of the skin

3.1.3 Sandwich: Epoxy skin and DIAB Divinycell P100 core

Results of the ignition tests of the sandwich made by epoxy skin and the DIAB Divinycell P100 core are presented in the Table 3.

Table 3: Time to piloted ignition vs. Radiant heat flux for the sandwich made by epoxy skin and DIAB Divinycell P100 core.

Radiant heat flux (kW/m^2)	Time to ignition (s)
7.5	No ignition
7.5	No ignition
7.5	No ignition
13.1	268
13.1	264
13.1	262
18.9	135
18.9	132
18.9	137
24.3	100
24.3	96
24.3	101
30.3	70
30.3	71
30.3	72
35.7	58
35.7	57
35.7	58

3.1.4 Epoxy skin

As advised previously, the test of the ignitability of the skin itself should be done. In the present case, results of the time to ignition of the epoxy skin are shown in the Table 4.

Table 4: Time to piloted ignition vs. Radiant heat flux for the epoxy skin.

Radiant heat flux (kW/m^2)	Time to ignition (s)
7.5	No ignition
7.5	No ignition
7.5	No ignition
13.1	241
13.1	243
13.1	244
18.9	120
18.9	123
18.9	119
24.3	91
24.3	88
24.3	93
30.3	65
30.3	64
30.3	64
35.7	56
35.7	54
35.7	55

3.1.5 Core of the sandwich: DIAB Divinycell P100

As explained, the two different sandwiches have the same core material: DIAB Divinycell P100. The results of its ignition tests are as follows.

Table 5: Time to piloted ignition vs. Radiant heat flux for the core material DIAB Divinycell P100.

Radiant heat flux (kW/m^2)	Time to ignition (s)
7.5	No ignition
7.5	No ignition
7.5	No ignition
13.1	184
13.1	178
13.1	180
18.9	60
18.9	58
18.9	57
24.3	28
24.3	27
24.3	27
30.3	16
30.3	15
30.3	16
35.7	11
35.7	12
35.7	12

3.2 Non-piloted (spontaneous) ignition

As advised for the piloted ignition case, the study of the spontaneous ignition was performed for each part of the sandwich and for the sandwich itself.

3.2.1 Sandwich: Geopolymer skin and DIAB Divinycell P100 core

For this case, only two heat fluxes have been tested: 30 and 40 kW/m^2. The explanation is given by the results: in each case, no ignition appears but the whole core of the sandwich was gasified at 30 minutes and 45 minutes for 30 and 40 kW/m^2, respectively.

3.2.2 Geopolymer skin

Again, in this case only two heat fluxes have been tested: 30 and 40 kW/m^2 according to previous results. Without any surprise, the skin material did not ignite, even after 60 minutes of testing.

3.2.3 Sandwich: Epoxy skin and DIAB Divinycell P100 core

From the fire safety point of view, this configuration of sandwich seems to be the most important (spontaneous configuration close to the reality, with a combustible skin and core material). That is why the number of experiments is large.

Table 6: Time to spontaneous ignition vs. Radiant heat flux for the sandwich made by epoxy skin and DIAB Divinycell P100 core.

Radiant heat flux (kW/m^2)	Time to ignition (s)
13.1	No ignition
13.1	No ignition
13.1	No ignition
18.9	No ignition
18.9	No ignition
18.9	No ignition
24.3	No ignition
24.3	No ignition
24.3	No ignition
27.5	146
27.5	142
27.5	144
30.3	101
30.3	98
30.3	99
35.8	64
35.8	65
35.8	65
40	53
40	52
40	52
45	42
45	42
45	42

3.2.4 Epoxy skin

The results of the spontaneous ignition tests of the epoxy skin are presented in Table 7.

Table 7: Time to spontaneous ignition vs. Radiant heat flux for the Epoxy skin.

Radiant heat flux (kW/m^2)	Time to ignition (s)
13.1	No ignition
13.1	No ignition
13.1	No ignition
18.9	No ignition
18.9	No ignition
18.9	No ignition
24.3	No ignition
24.3	No ignition
24.3	No ignition
27.5	139
27.5	144
27.5	142
30.3	98
30.3	97
30.3	97
35.8	61
35.8	63
35.8	62
40	51
40	50
40	52
45	40
45	41
45	40

3.2.5 Core of the sandwich: DIAB Divinycell P100

The last set of spontaneous ignition is about the spontaneous ignition of the core material.

Table 8: Time to spontaneous ignition vs. Radiant heat flux for the core material DIAB Divinycell P100.

Radiant heat flux (kW/m^2)	Time to ignition (s)
13.1	No ignition
13.1	No ignition
13.1	No ignition
18.9	No ignition
18.9	No ignition
18.9	No ignition
22	699
22	654
22	675
24.3	418
24.3	406
24.3	401
27.5	204
27.5	197
27.5	195
30.3	132
30.3	129
30.3	130
35.8	79
35.8	83
35.8	82
40	59
40	61
40	60

4. Discussion

4.1 Piloted ignition – Determination of the ignition temperature

In Fig. 2 all the results from the piloted time to ignition for all types of specimen (Sandwich made by epoxy skin and DIAB core, sandwich made by geopolymer skin and DIAB core, epoxy skin, and DIAB core) are presented.

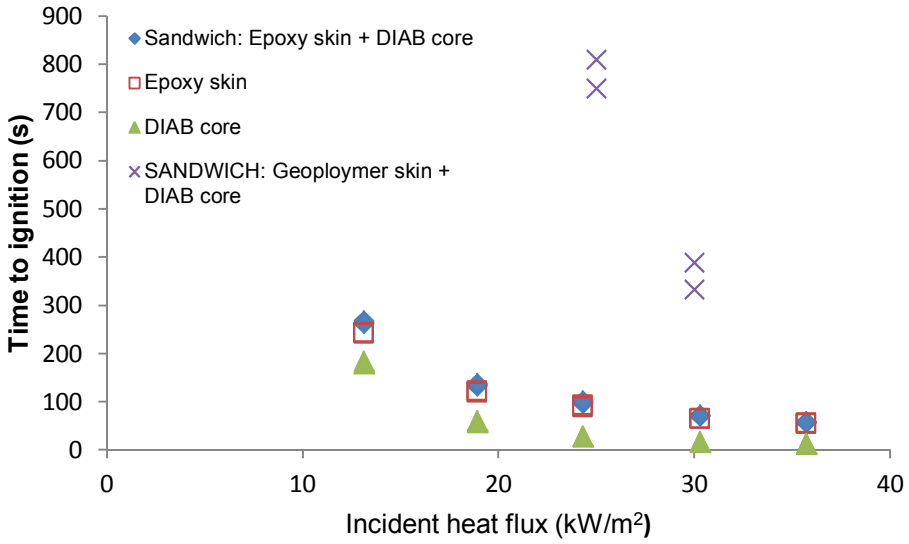

Figure 2: Time to ignition (piloted) for all the materials tested for the present study.

The most visible result is that the geopolymer skin shows a non-combustible behaviour.
The second main result is that the sandwich (epoxy skin + DIAB core) shows the same behaviour as the epoxy skin alone. This similarity will be explained later, after the determination of the temperature of ignition and the underlying theory.

As explained, the methodology for the study of the ignition is not exactly the same as the one presented in ISO 5660, as the methodology used here is from [3.].
The ignition of combustible can be easily understood with an integral model that shows that ignition occurs when the surface reaches a critical value $T=T_{ig}$. This condition allows the determination of the ignition time using the heat conduction into the solid while ignoring the chemical kinetics of pyrolysis and the chemical kinetics of ignition of evolved gases with air.
For thermally thick conditions, as theory and experience suggest, the ignition data should be plotted as $\frac{1}{\sqrt{t_{ig}}}$ in function of the imposed heat flux in the cone calorimeter, $\dot{q}''_{ext}$.
For thermally thin condition, the plot is done in function of $\frac{1}{t_{ig}}$. This method to plot the experimental data is also a way to show the thermal behaviour of a specimen. Indeed, experimental data of a thermally thick specimen show a straight line when they are plotted on a graph presenting $\frac{1}{\sqrt{t_{ig}}}$ in function of the imposed heat flux, $\dot{q}''_{ext}$.

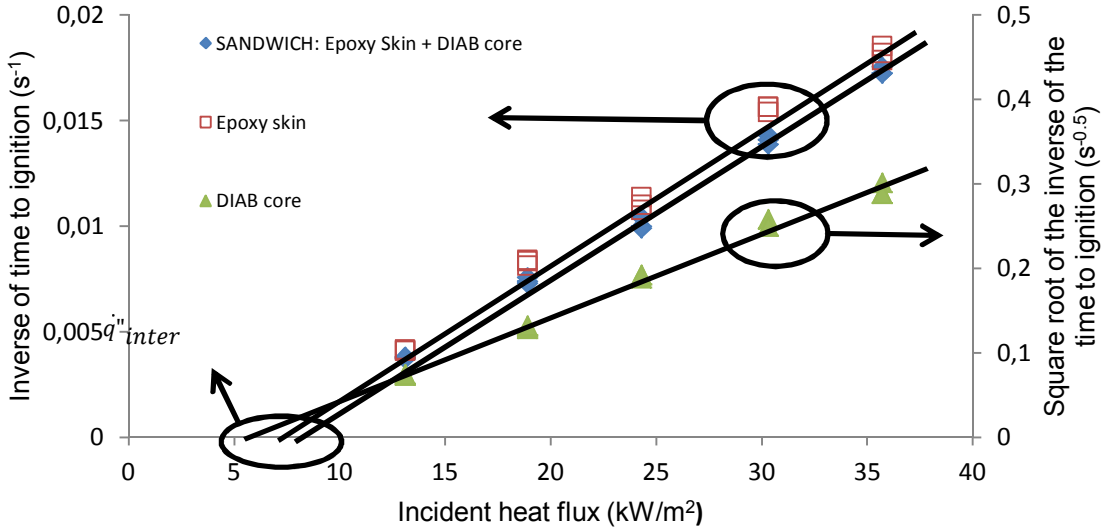

Figure 3: Transformed ignition time vs. Heat flux.

It should be noticed that only results with epoxy skin are presented on the previous graph. Indeed, the geopolymer skin has been shown as a non-combustible material.
The previous graph shows that the sandwich (epoxy Skin + DIAB core) and the epoxy skin present a thermally thin behaviour, and that the DIAB core a thermally thick one.
The theory [3.] explains that the straight lines (clearly visible on the previous graph) represent the following equation:

- For the thermally thick case:

$$\dot{q}''_{ext} = \frac{1}{\sqrt{t_{ig}}}\left[\frac{\sqrt{\pi k \rho C_p}\left(T_{ig} - T_0\right)}{2}\right] + \dot{q}''_{inter}$$

- For the thermally thin case:

$$\dot{q}''_{ext} = \frac{\delta \rho C_p \left(T_{ig} - T_0\right)}{t_{ig}} + \dot{q}''_{inter}$$

Furthermore, one can link $\dot{q}''_{inter}$ with the critical heat flux $\dot{q}''_{cr}$ through the following equation:

$$\dot{q}''_{inter} = A \times \dot{q}''_{cr}$$

With (for a charring material):

- A=0.76 for the thermally thick case
- A=0.64 for the thermally thin case

It means that from the value of $\dot{q}''_{inter}$, it's easy to find the temperature of ignition, T_{ig}.

Table 9: Temperature of the piloted ignition of materials.

Material	$\dot{q}''_{inter}$ (kW/m^2)	$\dot{q}''_{cr}$ (kW/m^2)	T_{ig} (°C)
Sandwich	6.82	8.99	308
Epoxy Skin	6.25	8.22	305
DIAB Core	6.00	7.90	288

From the previous table, it comes that the DIAB core is the weakest part of the sandwich. But the most interesting result is that the ignition temperature of the sandwich is 308 °C. This temperature is higher than the temperature of glass transition of the DIAB core, which is around 90 °C.

4.2 Non-piloted ignition – Determination of the ignition temperature

In order to determine the non-piloted (spontaneous) ignition temperature, the methodology is the same as for the piloted ignition study.
And in the same was as for the piloted ignition, only the results with the epoxy- skin are presented.

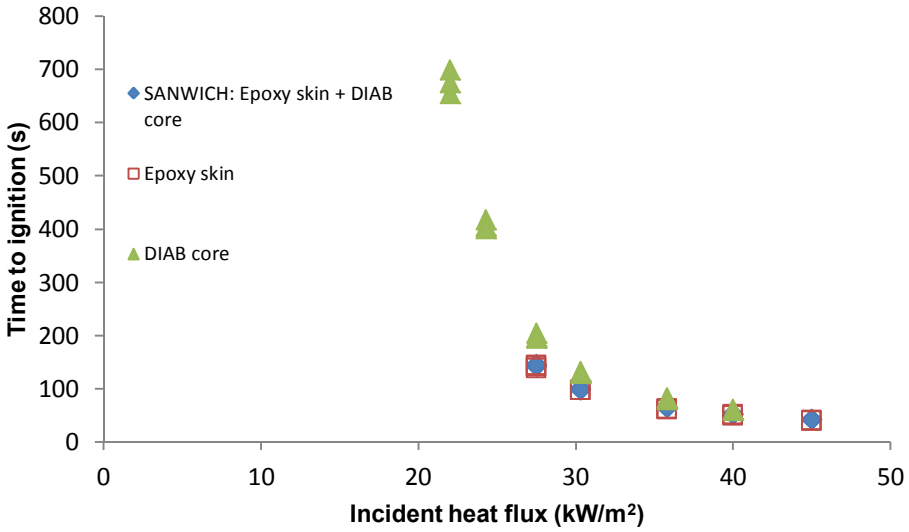

Figure 4: Time to ignition (spontaneous) for all material tested for the present study.

As expected and following the results of the piloted ignition tests, the sandwich and the skin show the same behaviour.

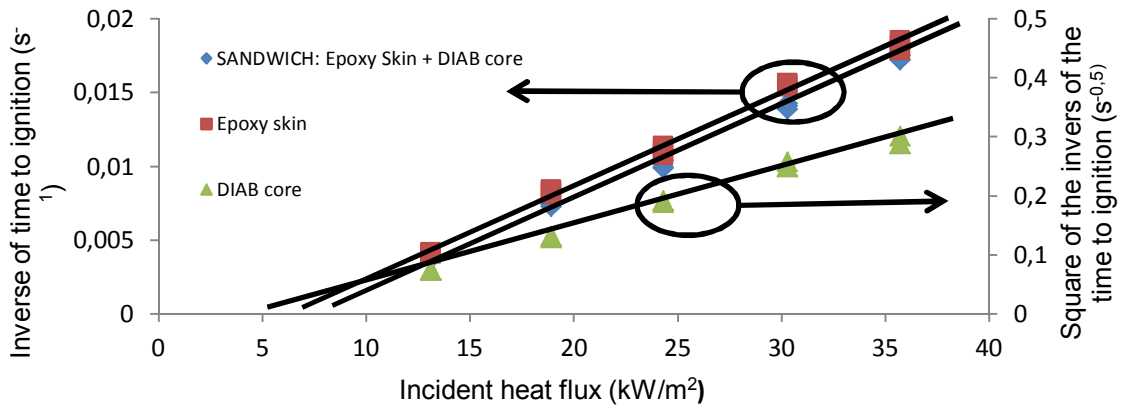

Figure 5: Transformed ignition time vs. Heat flux.

The transformed ignition time for the sandwich and the skin show a thermally thin behaviour, whereas the DIAB core displays a thermally thick behaviour.
As explained, the spontaneous temperature of ignition for each material can then be readily estimated. The results are presented in table 10.

Table 10: Temperature of the spontaneous ignition of materials.

	$\dot{q}''_{inter}$ (kW/m^2)	$\dot{q}''_{cr}$ (kW/m^2)	T_{ig} (°C)
Sandwich	19.4	25.5	508
Epoxy Skin	20.2	26.6	516
DIAB Core	14.3	21.6	472

The temperature of ignition (both case: piloted and spontaneous) follows the same tendency. We can split the results in two groups: DIAB core and sandwich-Epoxy skin. The lowest temperature of ignition is for the DIAB core compared with the group formed by the sandwich and the epoxy skin. The difference is around 20°C in the case of the piloted ignition and around 40 °C in the case of the spontaneous ignition.

5. Conclusion

Several tests were performed in order to study the time to ignition of two different types a sandwich composite. For each of them, the same core material has been used: DIAB Divinycell P100. The difference is the type of the skin: the first one is a geopolymer one, and the second one is epoxy skin.
The present study shows the results of tests on the piloted and spontaneous ignition. Indeed, the piloted ignition shows usually a lower temperature of ignition compared to the spontaneous ignition. But, in the COMPASS project, the sandwich composite is used on shipping construction, and in this case, is protected by thermal insulation that prohibit the presence of flame (as igniter).
Piloted and spontaneous ignition tests show the same behaviour:

- The geopolymer skin can be seen like a non-combustible material
- The sandwich (core + epoxy skin) and the epoxy skin show a thermally thin behaviour in front of ignition, with an higher temperature of ignition (piloted: 305 °C and spontaneous: 510 °C) than the core material
- The DIAB core material shows a thermally thick behaviour with a lower ignition temperature (piloted: 288 °C and spontaneous: 472 °C) than other material

Even if the ignition temperature of the core material is lower than the sandwich composite, the main conclusion is that the sandwich composite has a temperature of piloted of ignition of 308 °C that is really higher than the temperature of glass transition, It leads to the fact that the sandwich composite will lose its stiffness long time before its ignition

References

[1.] Regulation 17, International Maritime Organization. SOLAS Consolidated Edition 2009. International Convention for the Safety of Life at Sea.
[2.] ISO 5660-1:2002, Reaction-to-fire tests -- Heat release, smoke production and mass loss rate -- Part 1: Heat release rate (cone calorimeter method)
[3.] Spearpoint MJ, Quintiere JG. Predicting the piloted ignition of wood in the cone calorimeter using an integral model - effect of species, grain orientation and heat flux. *Fire Safety Journal* 2001; **36**: 391–402.

Annex G: Fire Resistance for small scale composite specimen

On the use of the H-TRIS

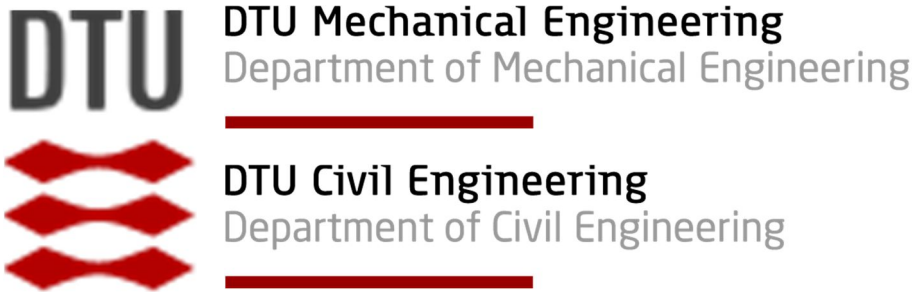

Date : May 2016
Project name : COMPASS – Composite superstructures for large PASSenger ships

Author : Pierrick Mindykowski – DTU Byg

Content

1. Introduction

Composite materials offer a large range of advantages for the marine industry such as being lightweight [1], reduction of the maintenance costs [2] and the possibility to create complex shapes [3]. However, in order to have the approval of the authorities for building a SOLAS (International Convention for the Safety of Life at Sea) vessel with composite materials (a SOLAS vessel is a Passenger ship engaged on international voyage or Cargo Ship of 500GT and upward engaged on international voyage), this alternative design has to show an equivalent level of safety as the prescriptive requirement that is based on the use of steel [4]. Several solutions have been proposed to define new methodologies that demonstrate the required fire safety, and these can be divided into two main approaches; A) The tradeoff approach, i.e. staying as close as possible to the prescriptive regulations by making conservative equivalences, often in terms of passive protection, that are then compared to an equivalent prescriptive design [5], and B) The performance based approach, which looks into the overall performance in a fire situation [6].

In A), the solution requires experimental testing of different structural components as prescribed by the FTP code [7]. These tests are large scale and consist of exposing the structural element (generally with a size of 3 meter for length and width) to a predefined temperature curve from one side with the use of a gas fueled oven. Due to the scale and the human resources required to carrying these tests out, they often result in high operating costs, poor repeatability, unrealistic and/or inappropriate boundary conditions, and poor statistical confidence [8].

The second approach (B) requires more fire engineering analysis and uses risk analysis along with validated simulation tools that consider the full range of degradation of the materials, including combustion. Furthermore, to obtain all the required data (thermal and mechanical properties of the composite) for the simulation of different fire scenarios, experiments have to be carried out.

2. The H-TRIS

A new system that can answer the main issue of both the aforementioned approaches will be presented in the following. The Heat Transfer Rate Inducing System (H-TRIS) is an experimental rig developed by Maluk et al. [9] that can replicate, at a small scale, the thermal and mechanical stresses required by the FTP code (ISO 834 temperature time curve [10]), and provide thermal and mechanical properties of the studied composite. This can be seen as the link between small scale tests, which are used to determine properties of specimen and develop thermal and thermomechanical model as the TGA-DSC [11] [12], cone calorimeter [13], LIFT [14] and Dynamic Mechanical Analysis [15], and the real scale tests as the furnace tests with the ISO 834 temperature curve.

An H-TRIS consists of two parts; a radiant panel as thermal source and a mechanically loaded specimen as target, as shown in Figure 1.

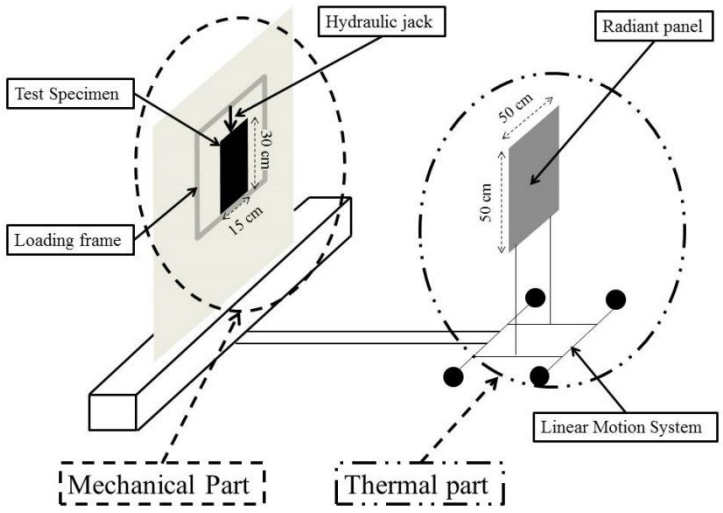

Figure 1: The two parts of the H-TRIS

2.1 Mechanical part of the H-TRIS

The mechanical part of the H-TRIS consists of two parts. The first part is the frame as presented in
Figure 2 (dimensions of the frame are presented in the Appendix A). The two HEB beams act as vertical columns in the rig. These will be connected to the 65mm base plate via two UPN 200 beams with the use of bolts screwed to the base of the plate and the base of the HEB columns. On the top of the rig, two UPN 200 beams will be positioned horizontally in the height specified in the drawings and will act as a fixed crosshead. It is in these UPN beams that the 20mm thick plate and the UPN beam will be attached to form the upper grip of the rig with the additional use of the two double plates.

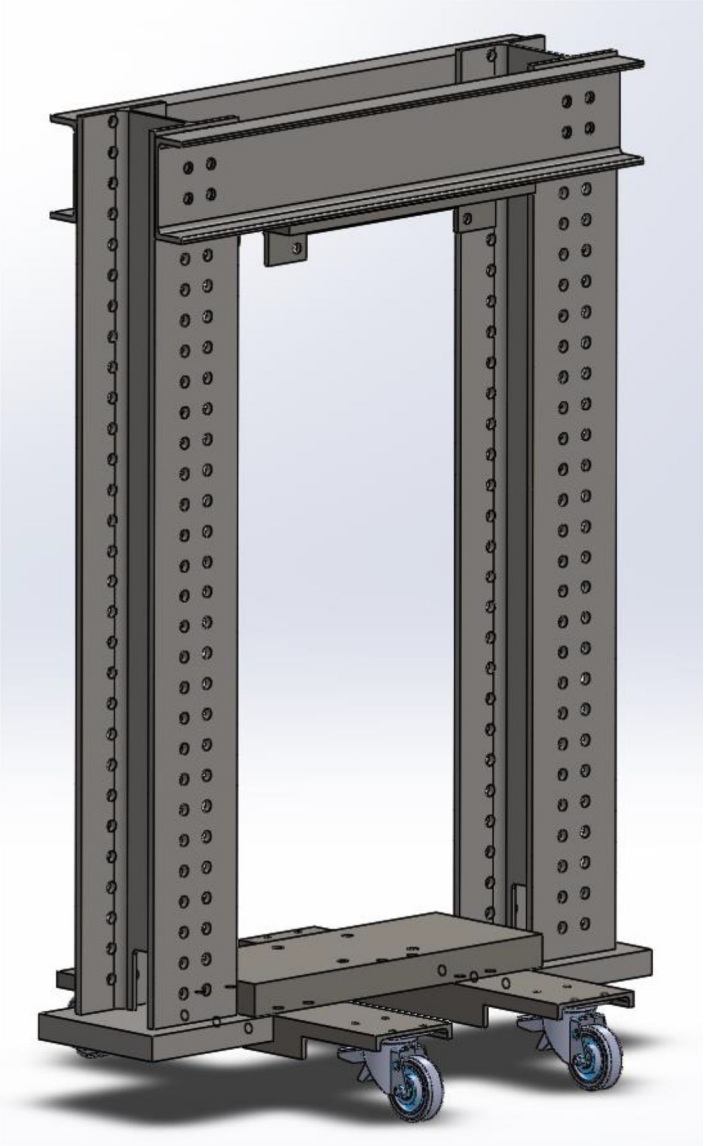

Figure 2: Frame of the mechanical part of the H-TRIS.

The second part of the mechanical part of the H-TRIS is the actuator system (Figure 3). This system is able to apply a maximum load of 222 kN, and is powered by an hydraulic pump. Obviously, the entire system is protected from heating radiant heat flux by a thermal protection plate.

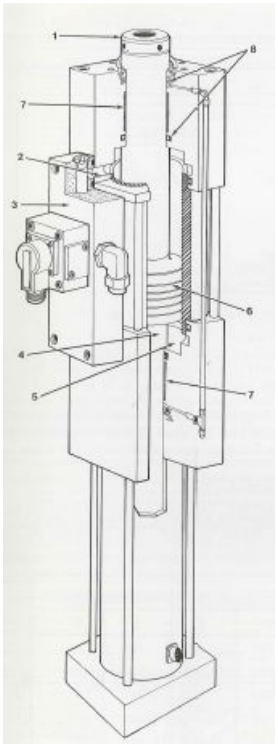

Figure 3: Actuator system of the mechanical part of the H-TRIS.

2.2 Thermal part of the H-TRIS

Due to the size of the specimen in the current design (area of 30 x 15 cm^2), the square gas-fired radiant panel is only a 50 cm wide but capable of providing a radiant heat flux up to 100 kW/m^2 (Figure 4).

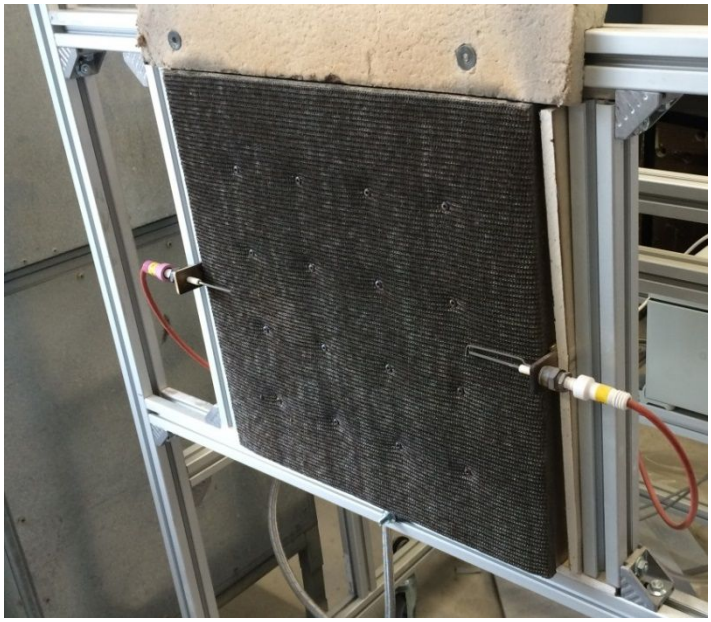

Figure 4: Burner of the H-TRIS.

Additionally, in order to be able to provide any kind of radiant heat flux, two systems have been developed to drive the burner (see the Figure 6). The first one is a simply track on which the burner can move, and by this, increase the incident heat flux on the target (as the incident heat flux is inversely proportional to the distance emitter-target). The second system is the possibility to drive the burner in order to provide a power from 0% to 100 %. This last system can be done in live manually (through a control box) or at priori through the software LabView from National Instruments.

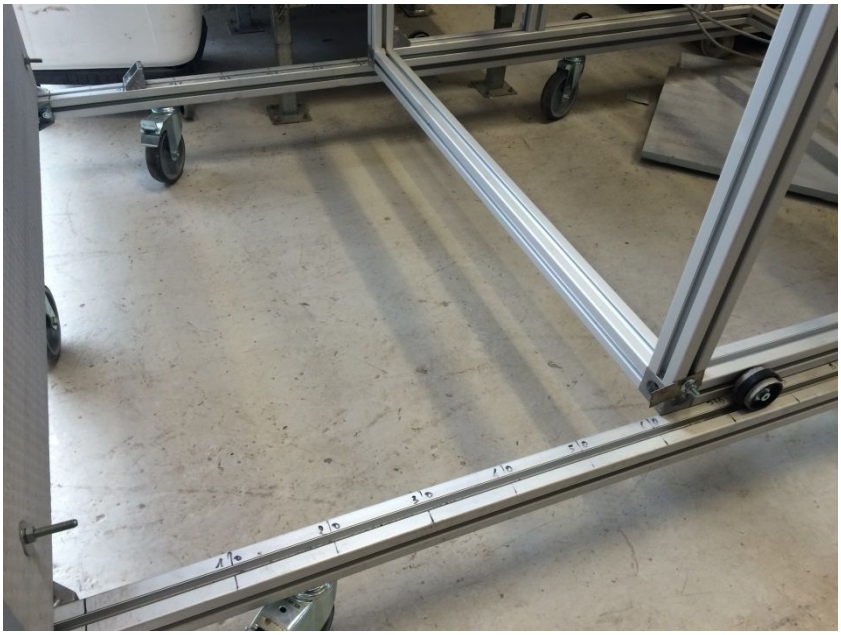

Figure 5: Tracks of the H-TRIS.

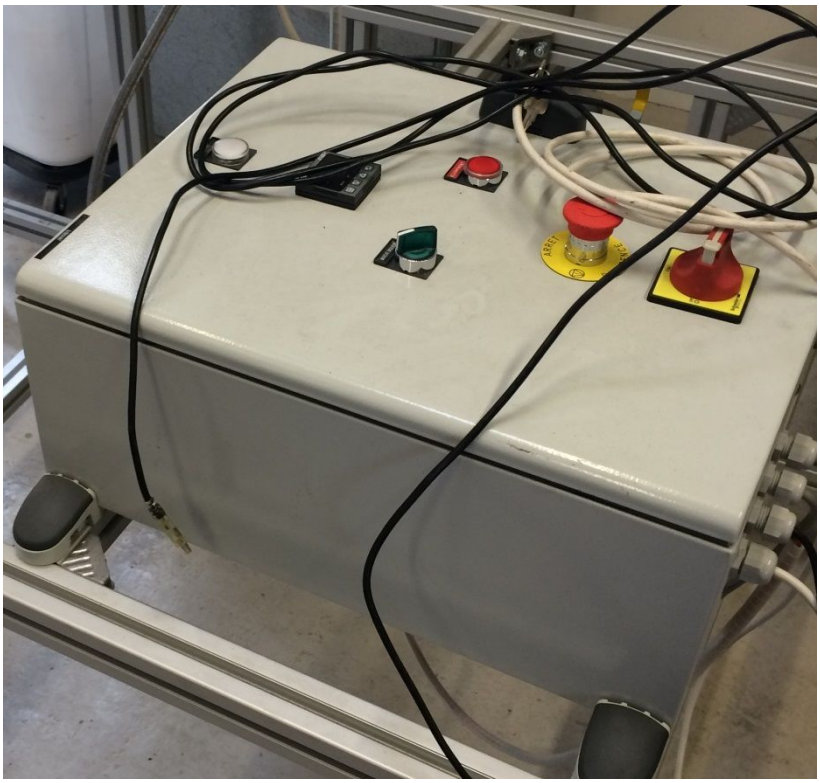

Figure 6: Control box of the H-TRIS.

3. THE H-TRIS IN COMPASS

The operating cost of the H-TRIS is low because of the small size of the sample, the low consumption of gas, and because it requires only one operator. From the mechanical point of view, as the experiment is at a small scale, the H-TRIS does not require a high performance system. It implies that the mechanical failure mode might be not comparable to the large scale one. But the H-TRIS is a new experimental rig that can be used as a screening experimental rig to test different composite and/or thermal insulation, to obtain experimental data used to simulate or prepare big scale tests, and finally its use requires knowing the thermal properties of the material in order to determine the equivalent radiant heat flux through a thermal model.

3.1 Three steps to describe the entire heating process

Maluk [8] developed the H-TRIS for studying a composite concrete. Then, to replicate the thermal stress from the ISO 834 temperature time curve, he developed an inverse thermal model based on 1D conduction model, which has the following steps: a) Performing oven test in order to obtain the time function temperature gradient caused due to convection and radiation from the oven, b) inverse thermal model including the radiant heat flux as boundary condition, c) the final result: the required history of the incident radiant heat flux from the radiant panel.

In the present study, the inverse method proves to be too complicated to implement, because composites are multi-layered with several compounds and protected by thermal insulation. As a result, too many unknowns arise in the problem, especially related to the contact resistances. Indeed, the sandwich material is composed by three layers, skin made by epoxy or geopolymer for each side, and by the core material (DIAB Divinycell P100). Both type of sandwich are shown on the following picture (Figure 7).

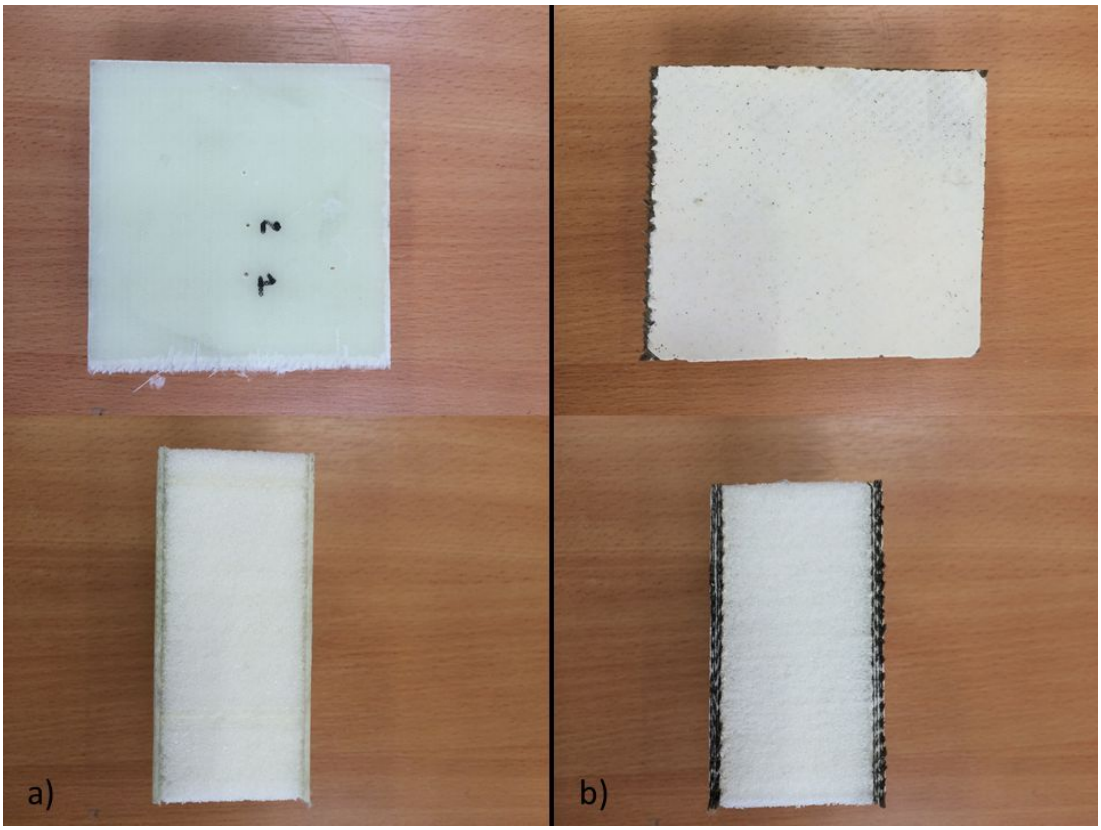

Figure 7: Pictures of the sandwiches, a) Epoxy skin sandwich, b) Geopolymer skin sandwich

The adopted solution is a direct approach based on 1D conduction model with test loops.
The method consists of testing different radiant heat fluxes and comparing the resulting temperature gradient of the material with the one from the oven test. These two models are described in Figure 8.

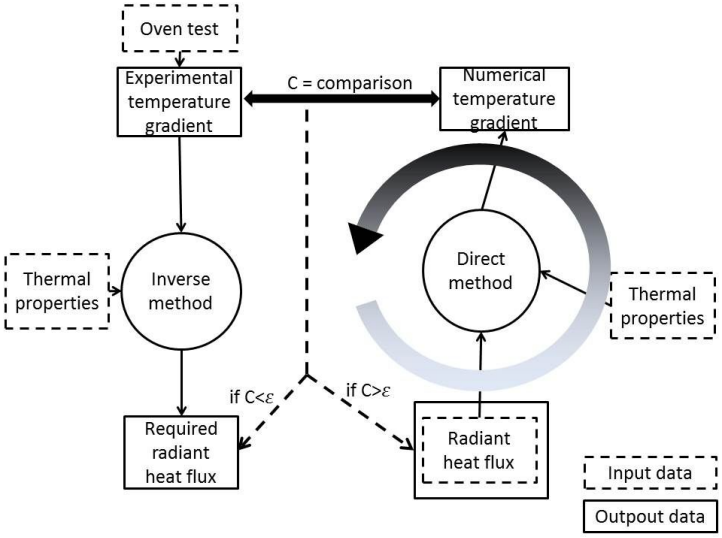

Figure 8: Schematic of inverse and direct method

Whatever the adopted model, one of the key parameters is the thermal properties of the specimen, meaning the conductivity, the density, the heat capacity and the emissivity of the material. Contrary to the case of concrete, thermal properties of composites vary considerably with temperature. Furthermore, apart from the skin properties, the homogeneity of the core material poses significant challenges to the accurate measurement of the thermal properties. As the model should stay as simple as possible, the real thermal properties are replaced by apparent properties. These properties might be close or not to the real one, but their primary function is to provide realistic results for different radiant heat flux inputs.
To determine these apparent properties, a cone calorimeter is used to inflict a calibrated radiant heat flux to the specimens under study. Subsequently with the use of genetic algorithms and by applying the direct approach the apparent thermal properties are defined (see Figure 9). The scope is that the numerical model is able to simulate the temperature gradient (which is strongly dependent of apparent thermal properties) as measured during the mass loss cone tests.

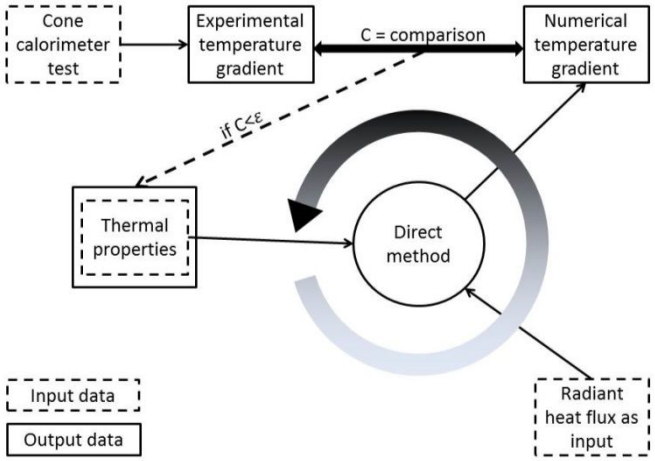

Figure 9: Schematic method to determine apparent thermal properties of the specimen

A comparison of experimental and numerical temperature gradient leads to the most fitting properties.
Additionally, as the numerical code is only mono layer, an attempt is made in order to represent artificially the influence of the thermal insulation. This influence is represented here by two terms: a time delay value and a coefficient of radiant heat flux. The values of these two terms are deduced by mass loss cone tests applying different heat flux and using different thermal insulations. A generalization of the values of these two terms has been attempted using the methodology of the thermal quadrupoles.
Finally, after these two steps (apparent thermal properties of the studied sandwich and the influence of the thermal insulation for the numerical code), the last one is obtaining the equivalent radiant heat flux, that one which gives the same gradient temperature in the sandwich when exposed at the ISO 834 temperature time curve during an oven test required by the FTP code.
In conclusion, in order to be able to use the H-TRIS, three couples of experiment/numerical test are required. These three steps are summarized in the Figure 10.

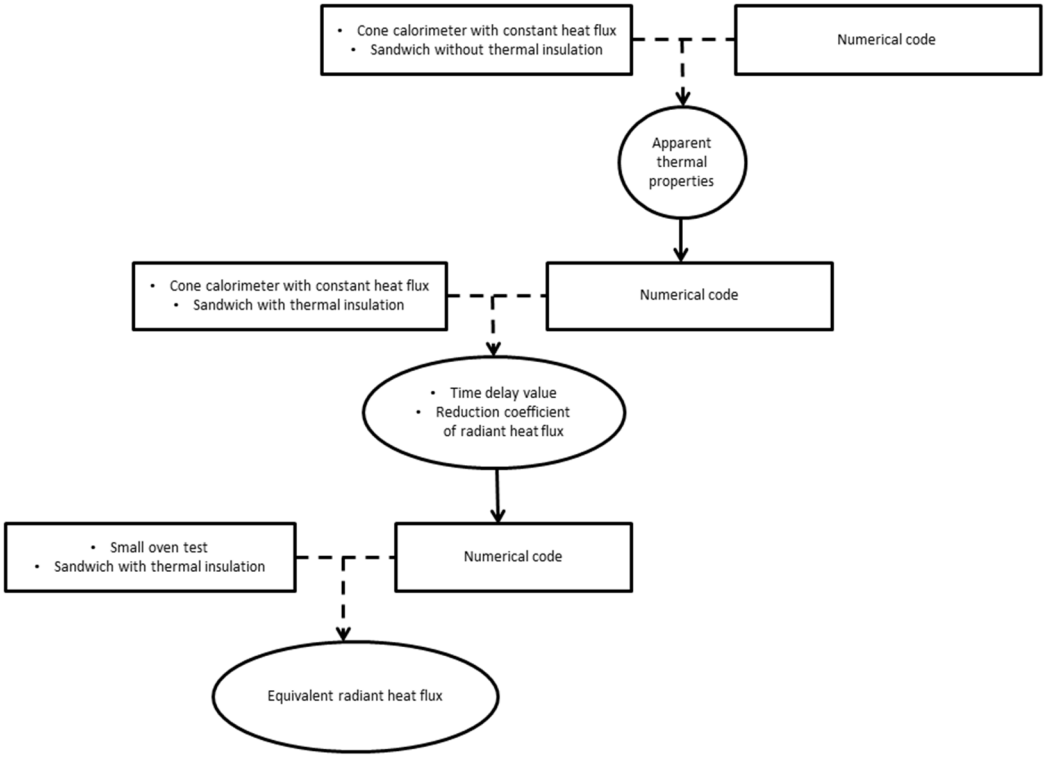

Figure 10: Steps to obtain the equivalent radiant heat flux as input for the H-TRIS

3.2 Determination of the apparent thermal properties of the sandwich

3.2.1 Experiments under the mass loss cone

As explained previously, the first step is the determination of the apparent thermal properties of the sandwich material using in COMPASS. In order to make the numerical code very light, the calculation and the confronted experiments are made only for the core material.

The experimental procedure used here is based on the ISO 5660 standard [16]. A specimen is placed under the mass loss cone and exposed to a calibrated incident heat flux. The important data here is the temperature gradient along the time. This gradient is taken through the thickness of the specimen at three different positions (10, 20 and 30 mm from the surface) and recorded by thermocouples, as shown on the following figure.

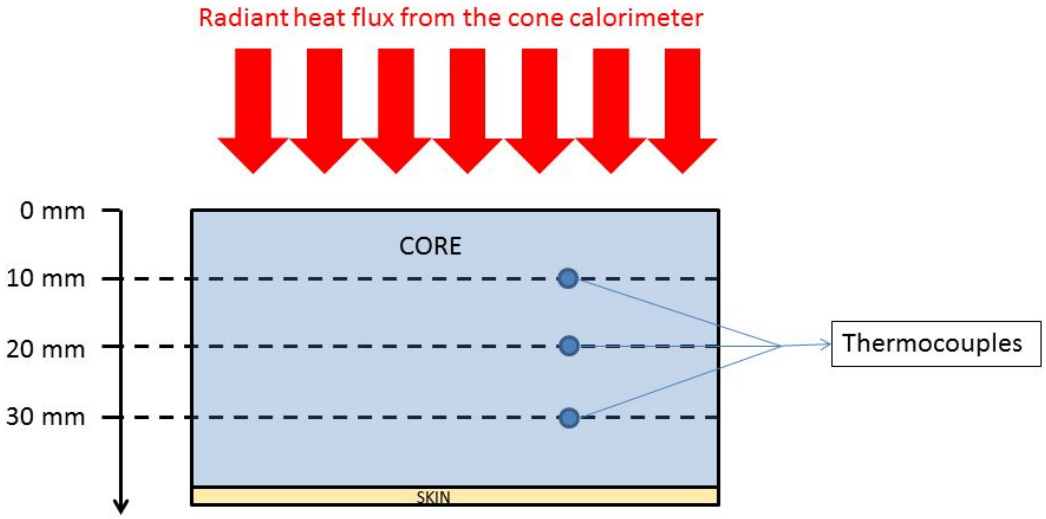

Figure 11: Position of the thermocouples

In the following paragraph, experimental results are an average of 3 different tests.

3.2.2 Comparison with the numerical code

The numerical code developed for the project is a simple one dimension code simulating the conduction in a mono layer specimen.

For this, the heat transfer equation has been discretized with a finite elements space, and Neumann boundary conditions at the top and the bottom of the specimen.

As said previously, the method direct is used in addition with an algorithm genetic. The principle of the algorithm genetic is to select the most fitting population to a problem. In the present case, the population is composed by N individuals formed by different genes: $\text{Ind}_n = \{\varepsilon_i, Cp_j, \rho_k, \lambda_l, Tvap_m, Lv_r\}$

With:

- ε_i: Emissivity of the core material / $0.7 < \varepsilon_i < 1$
- Cp_j: Heat capacity of the core material - $800 < Cp_j < 1200$ [J/K]
- ρ_k: Density of the core material / $80 < \rho_k < 130$ [kg/m^3]

- λ_l: Conductivity of the core material / $1 \times 10^{-3} < \lambda_l < 1$ [*W/(m.K)*]
- $Tvap_m$: Temperature of vaporisation of the core material / $500 < Tvap_m < 600$ [*K*]
- Lv_r: Latent heat of sublimation (assumption) / $1 \times 10^6 < Lv_r < 10 \times 10^6$ [*J/kg*]

The process of the selection of the best individual is explained on the following Figure 12. It consists on testing combinations of thermal properties, simulating the impact of incident radiant heat flux and comparing the temperature gradient obtained with experimental data. And finally, when the difference between experiment and numerical results reaches a correct pre-established value, the genes of the selected individual are considered has the solution.

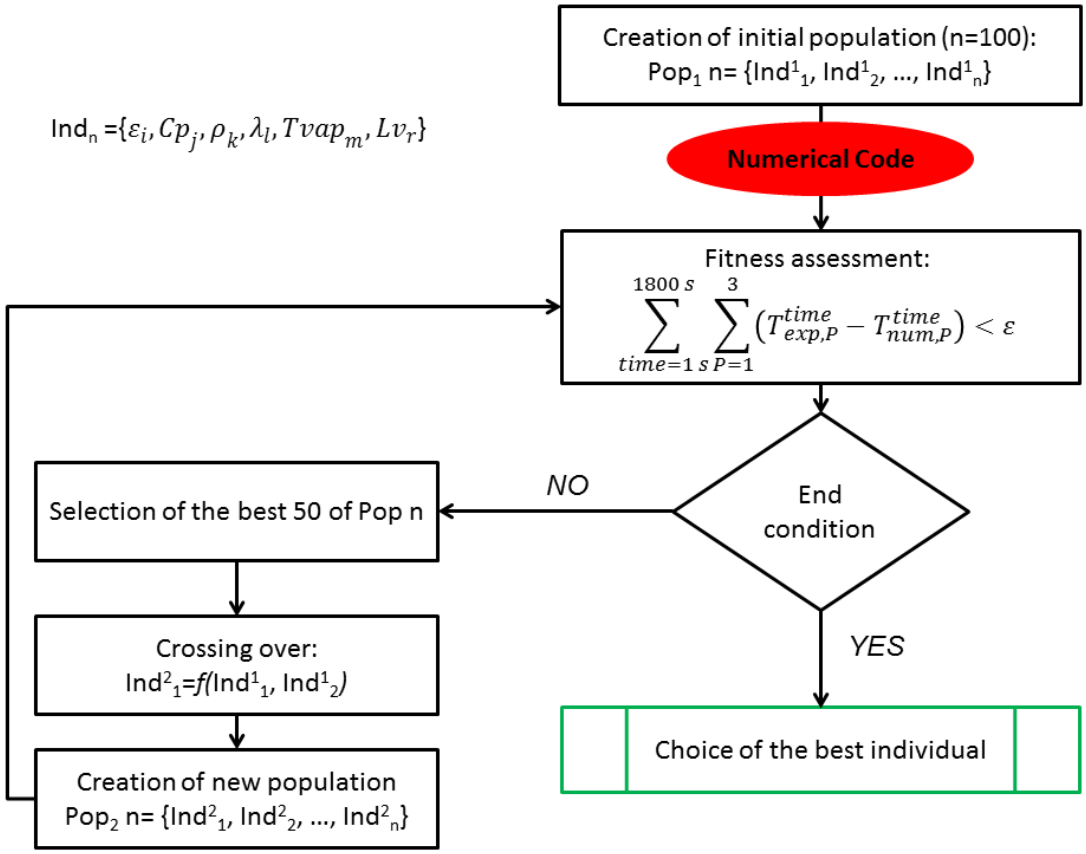

Figure 12: Numerical code and algorithm genetic

Three different heat fluxes have been used for this kind of tests (5, 7.5 and 10 kW/m^2), knowing that the heat flux should be less than the spontaneous ignition critical heat flux (around 21 kW/m^2). But as the piloted ignition critical heat flux is around 8 kW/m^2, the maximum heat flux used here is 10 kW/m^2.
For each experiment, P1 represents the temperature of the thermocouple at 10 mm from the top of the specimen. In the same way, P2 represents the temperature of the thermocouple at 20 mm and P3 represents the temperature of the thermocouple at 30 mm.
The three following figures show the numerical results compared to the experimental data.

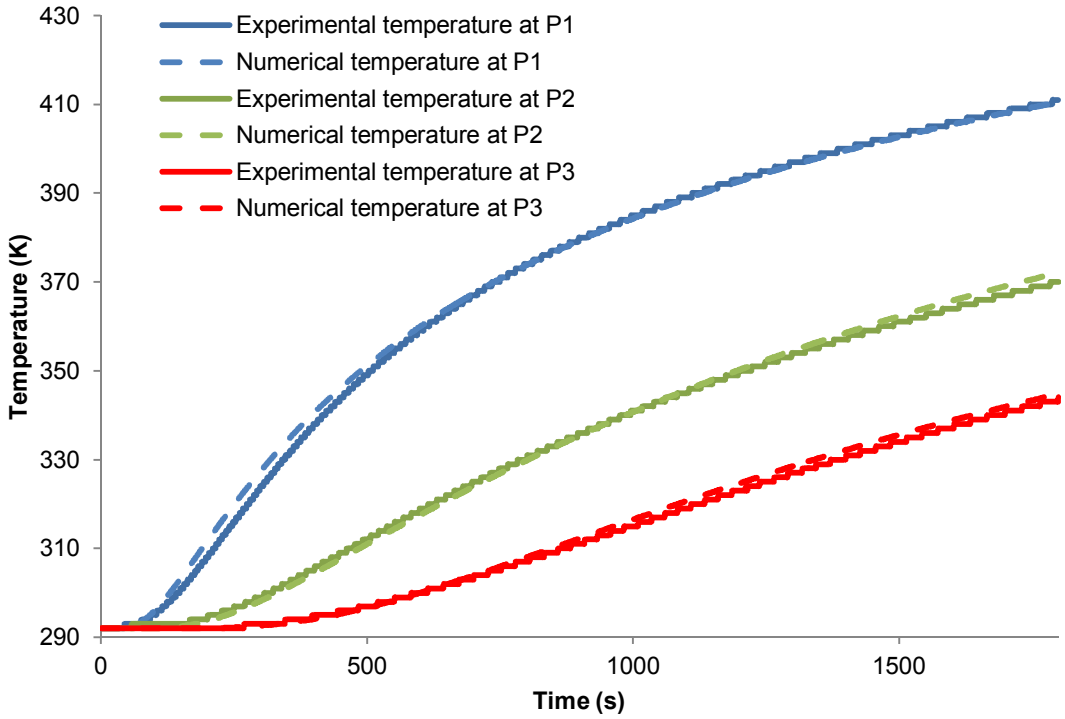

Figure 13: Comparison of the gradient temperature at 5 kW/m^2

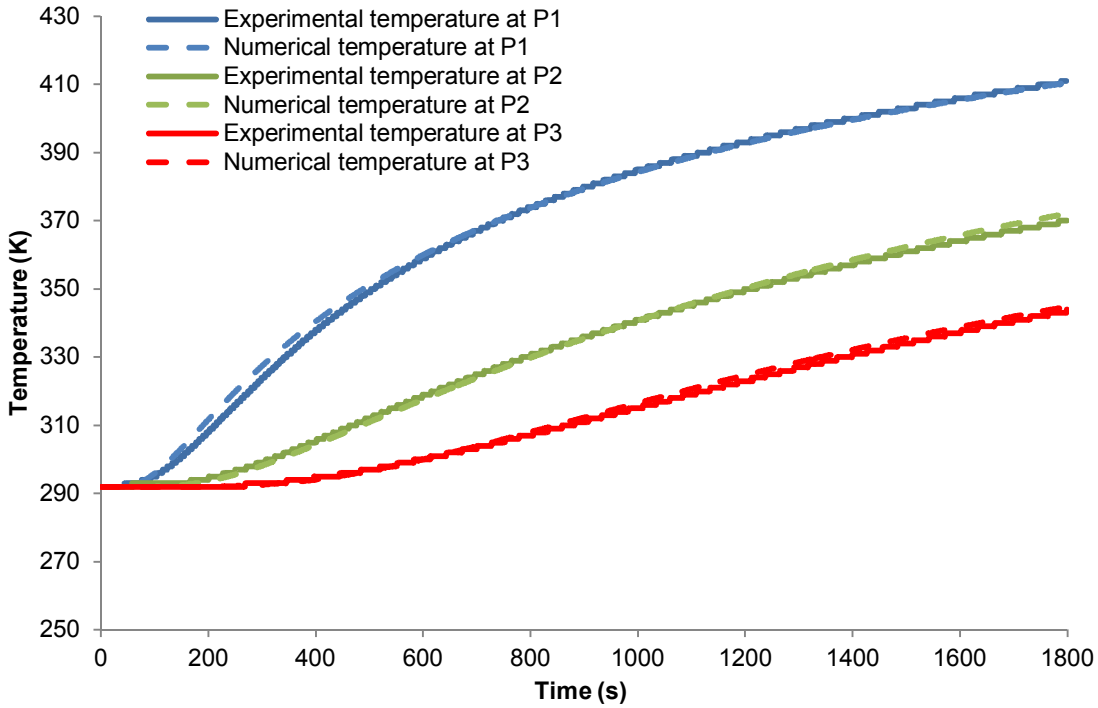

Figure 14: Comparison of the gradient temperature at 7.5 kW/m2

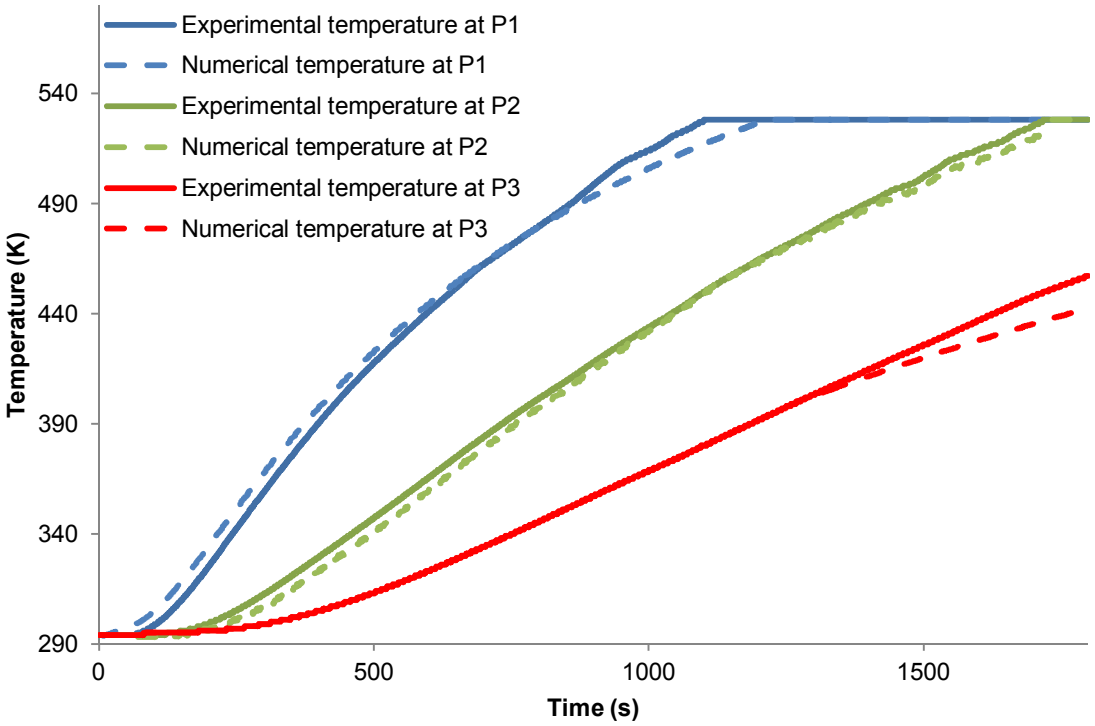

Figure 15: Comparison of the gradient temperature at 10 kW/m2

All results given but the simulation show a maximal error of 4.8% (in the case of the thermocouple situated at 30 mm from the top, for the test at 10 kW/m^2).

3.2.3 Results

The results from the use of the numerical code and the algorithm genetic are summarized in the following table.

Table 1: Apparent thermal properties of the core material, as results of the numerical code

Thermal property	Value deduced from the numerical study
Emissivity ε	0.83
Heat capacity Cp [*J/K*]	1100
Density ρ [*kg/m^3*]	110
Conductivity λ [*W/(m.K)*]	2.2×10^{-2}
Temperature of vaporisation $Tvap$ [*K*]	530
Latent heat of sublimation Lv [*J/kg*]	0.75

These values can be now compared to the values given by the supplier: DIAB. In case of the data is not provided by the supplier, this data is found in the literature as the core material is made by 97% of PET.

Table 2: Comparison of numerical and literature thermal properties

Thermal property	Values deduced from the numerical study	Values from DIAB[1] or literature
Emissivity ε	0.83	0.78 [17] - 0.9 [18]
Heat capacity Cp [*J/K*]	1100	1300 – 1700 [19]
Density ρ [*kg/m^3*]	110	110[1]
Conductivity λ [*W/(m.K)*]	2.2×10^{-2}	3.3×10^{-2} [1]
Temperature of vaporisation $Tvap$ [*K*]	530	539 [19]
Latent heat of sublimation Lv [*J/kg*]	0.15	0.12 – 0.14 [19]

The comparison between values of the thermal properties of the core material obtained by simulation/experiments and provided/found in the literature, leads to the conclusion that the model used in the numerical simulation is close to the reality as the thermal properties are close to real one and not only apparent one.

3.3 Determination of the time delay and reduction coefficient of radiant heat flux

As explained previously, the second step is the determination of the delay time and the reduction coefficient of the radiant heat flux. This step has been decided in order to keep light the numerical code, avoiding modelling the heat transfer through the multi-layer thermal insulation (and the skin of the sandwich material). Then the philosophy of this step is testing a sandwich material with insulation under a constant heat flux, and numerically reproducing the resulted temperature gradient within a core under submitted to a reduced heat flux triggered with a certain time delay. In this step, the numerical code and the algorithm genetic are the same, but for this last, the way to use it is different. Indeed, here the individual has the following form:

$$\text{Ind}_n = \{A, t_{delay}\}$$

From these different couple of result obtained through experiments, a generalized law will be deduced.

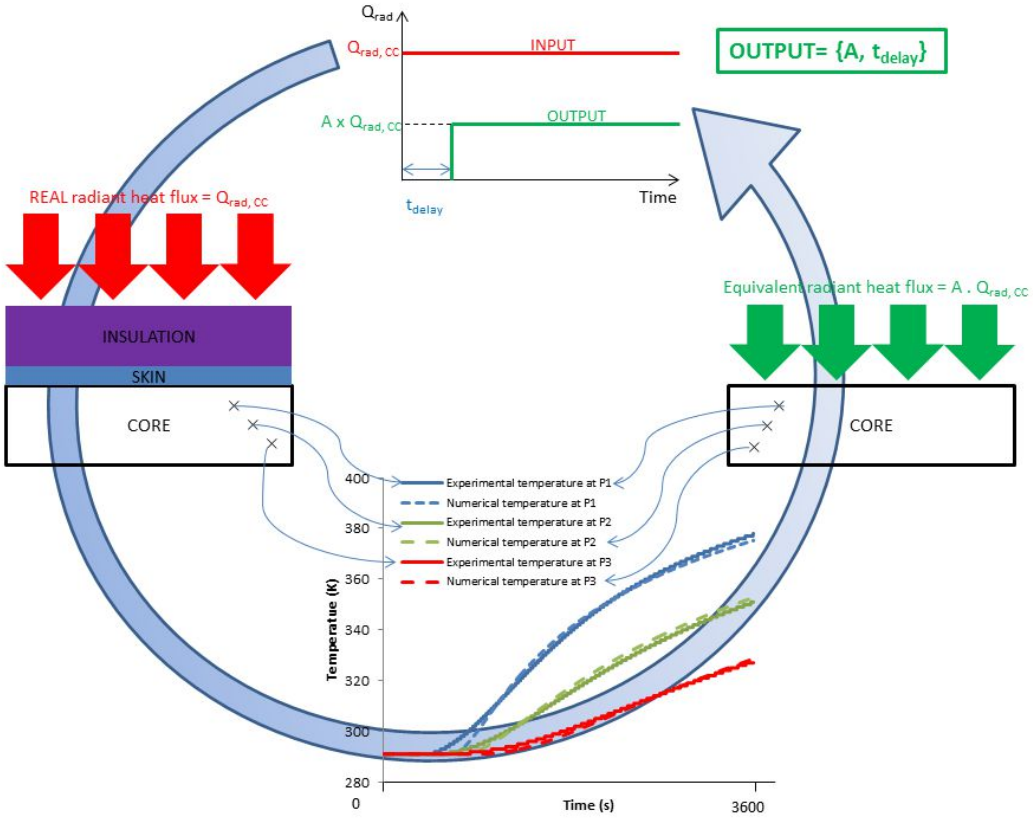

Figure 16: Principle to determine the time delay and the reduction coefficient of the radiant heat flux

3.3.1 Experiments under the mass loss cone

As reminder, the experiments are conducted in the same way as for the first step.

As for the project the two different provided thermal insulations have only 8% of difference for the density (64 kg/m^3 and 70 kg/m^3), only one type is selected (64 kg/m^3) to avoid the mixing of the influence of the density and the error from the numerical results (for the previous part, the error was already around 5%). In order to be able to develop a generalized law, the experiments cover a wide expanse of configurations. The following table shows all experiments performed for this step.

Table 3: Summary of experiments under mass loss cone to find the time delay and the reduction coefficient of the radiant heat flux

Test number	Heat flux (kW/m^2)	Thermal Insulation (mm)	Type of skin
1	75	50	Epoxy
2	50	25	Epoxy
3	50	50	Epoxy
4	25	25	Epoxy
5	25	25	No Skin
6	50	50	No Skin
7	100	100	Epoxy
8	2.5	No Thermal Insulation	Epoxy
9	5	No Thermal Insulation	Epoxy
10	7.5	No Thermal Insulation	Epoxy
11	10	No Thermal Insulation	Epoxy
12	2.5	No Thermal Insulation	Geopolymer
13	7.5	No Thermal Insulation	Geopolymer
14	10	No Thermal Insulation	Geopolymer

Only one example is given to show the general behaviour of the temperature gradient inside the core material, but more results exist.

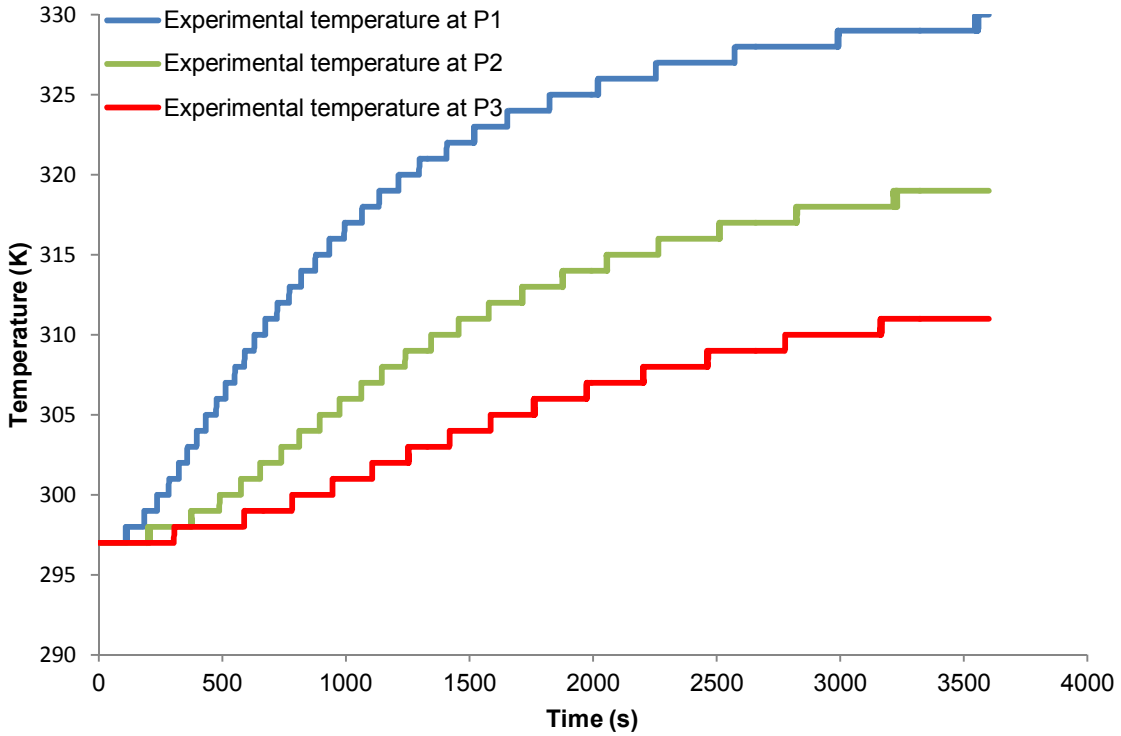

Figure 17: Temperature gradient for the test at 100 kW/m2 and 100 mm of thermal insulation

3.3.2 Comparison with the numerical code

The attended results here are the time delay and the reduction coefficient for each experiment.

Before presenting these two values, the comparison between experiments and numerical studies are presented on the following figures. From the Figure 18 to the Figure 28, results are shown for the case of sandwich made with epoxy skin. Indeed, comparison for sandwich with geopolymer are absent due to the fact that the numerical code doesn't work for this case.

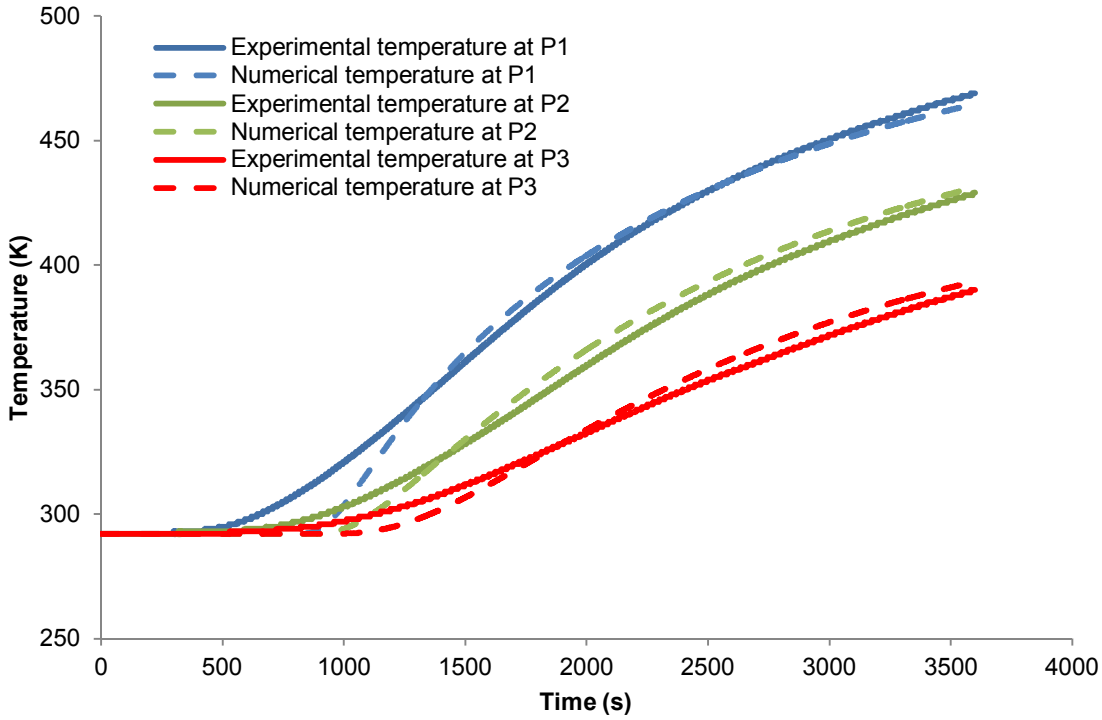

Figure 18: Comparison of the gradient temperature for the case 75kW/m2 and 50mm of thermal insulation

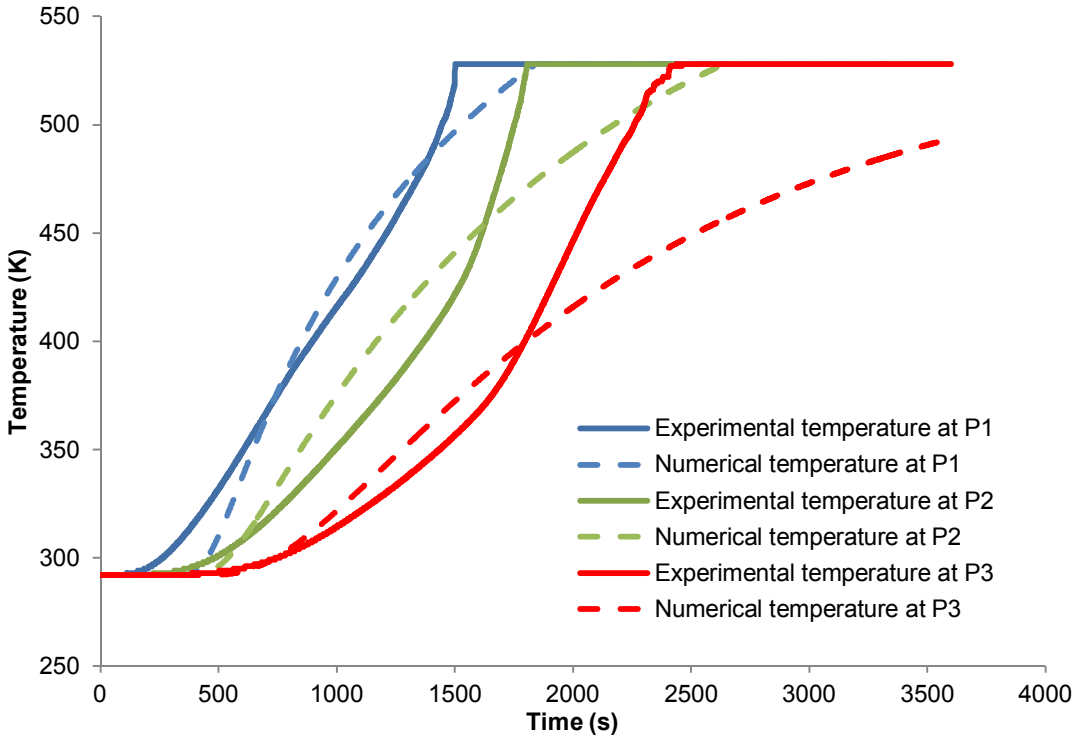

Figure 19: Comparison of the gradient temperature for the case 50kW/m2 and 25mm of thermal insulation

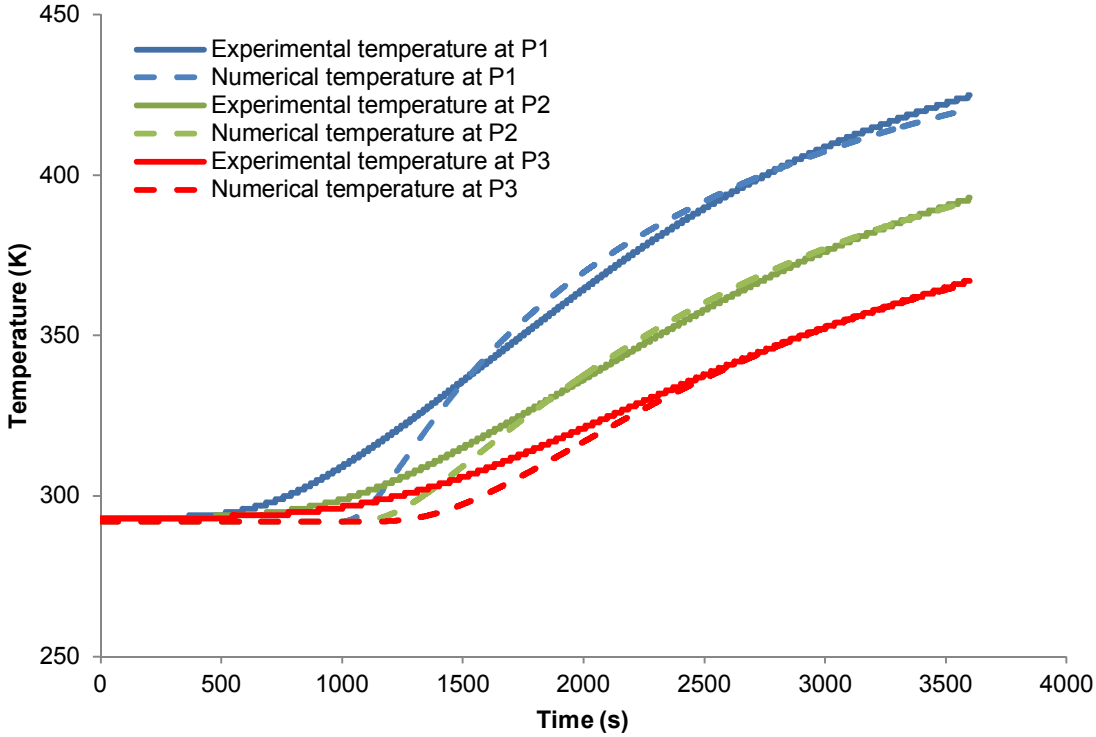

Figure 20: Comparison of the gradient temperature for the case 50kW/m2 and 50mm of thermal insulation

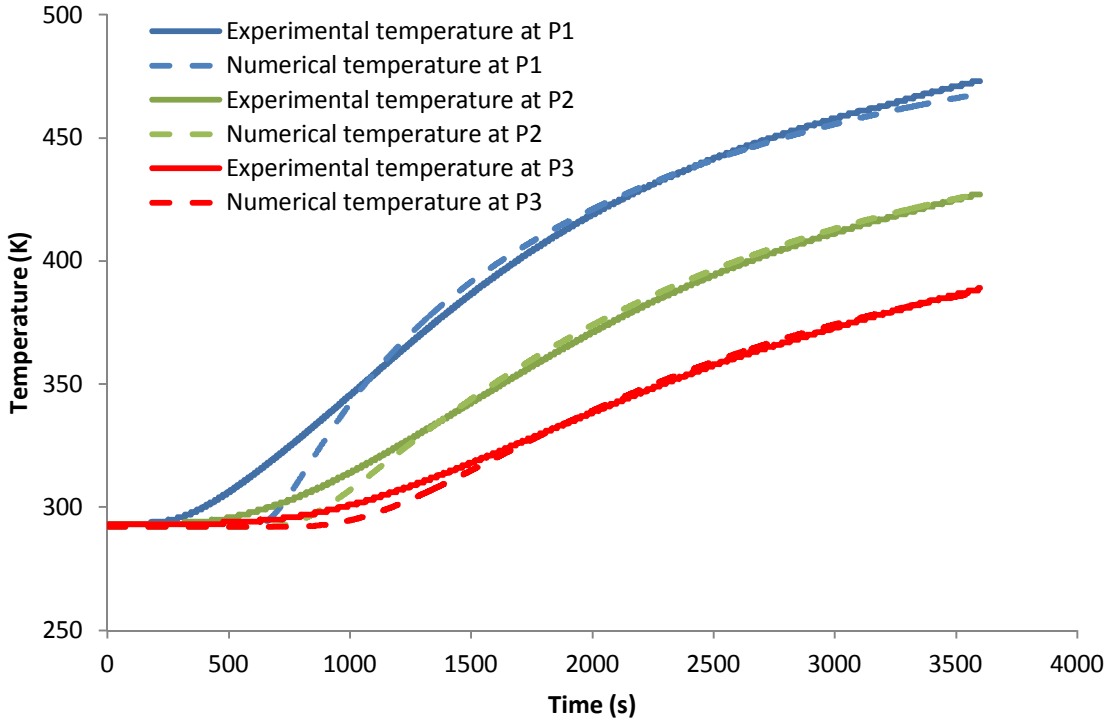

Figure 21: Comparison of the gradient temperature for the case 25kW/m2 and 25mm of thermal insulation

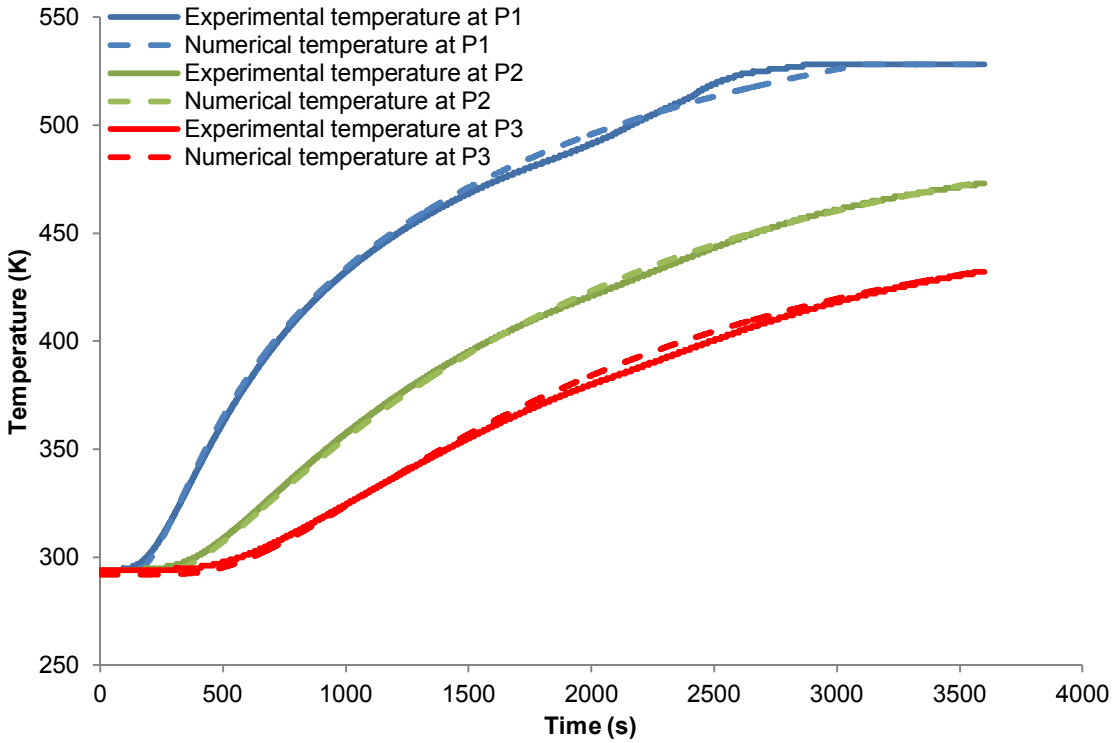

Figure 22: Comparison of the gradient temperature for the case 25kW/m2 and 25mm of thermal insulation, without Skin

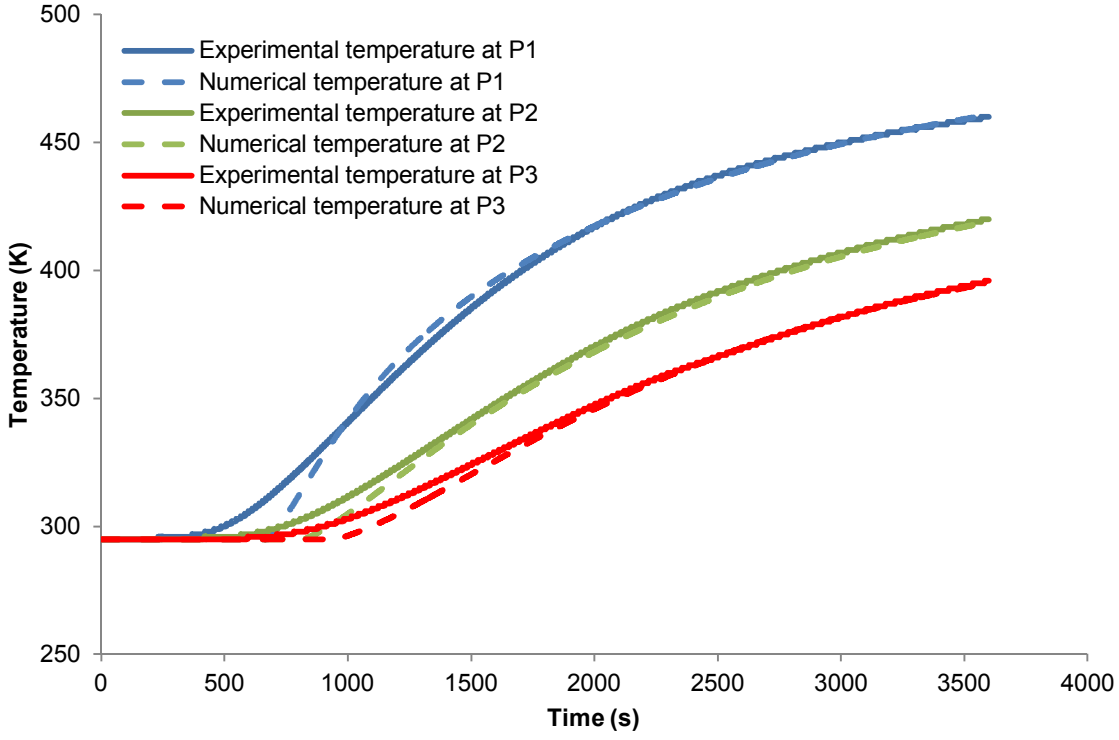

Figure 23: Comparison of the gradient temperature for the case 50kW/m2 and 50mm of thermal insulation, without Skin

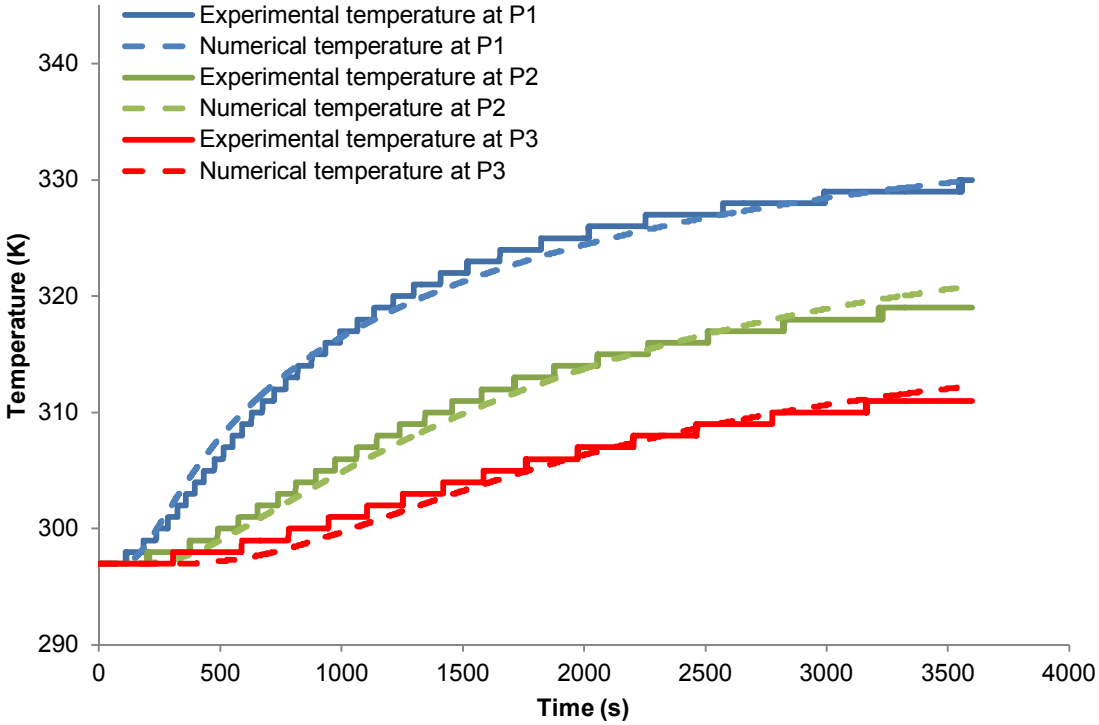

Figure 24: Comparison of the gradient temperature for the case 100kW/m2 and 100mm of thermal insulation

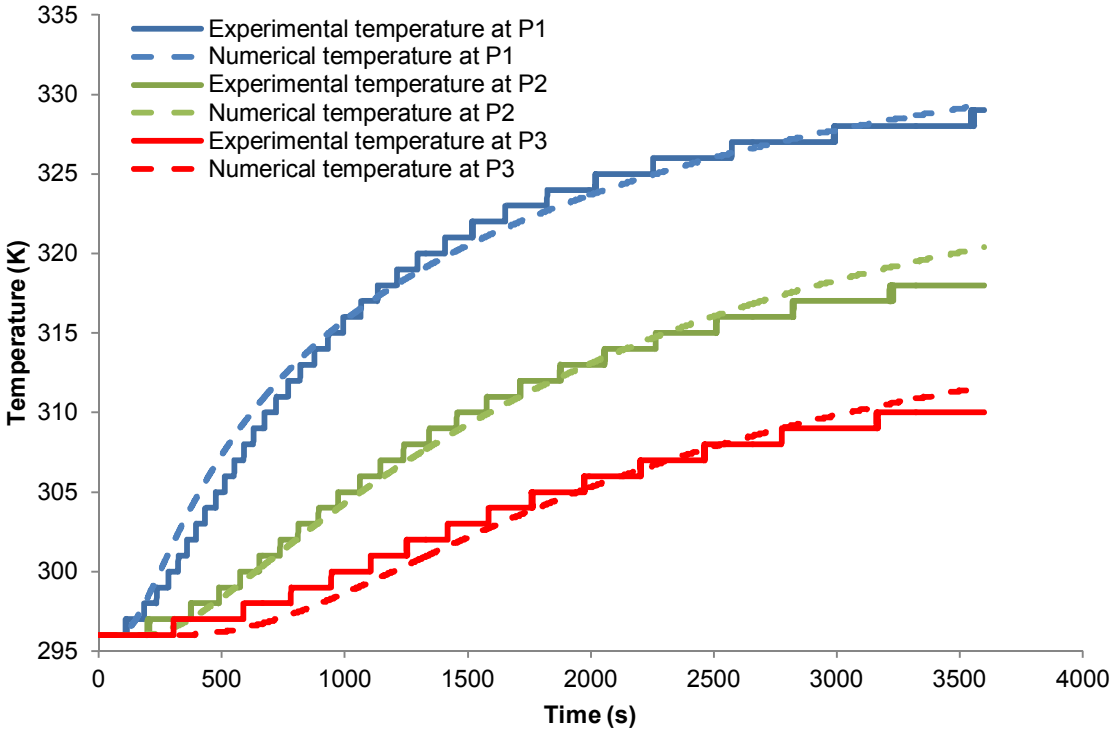

Figure 25: Comparison of the gradient temperature for the case 2.5kW/m2 and NO thermal insulation

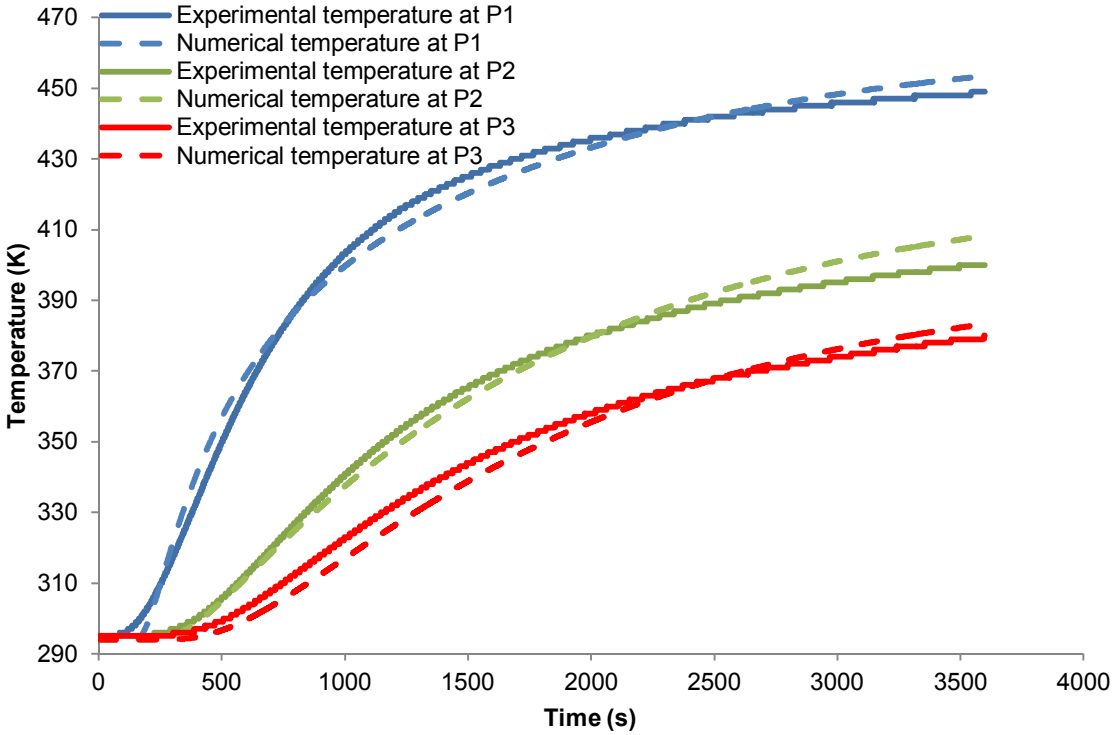

Figure 26: Comparison of the gradient temperature for the case 5kW/m2 and NO thermal insulation

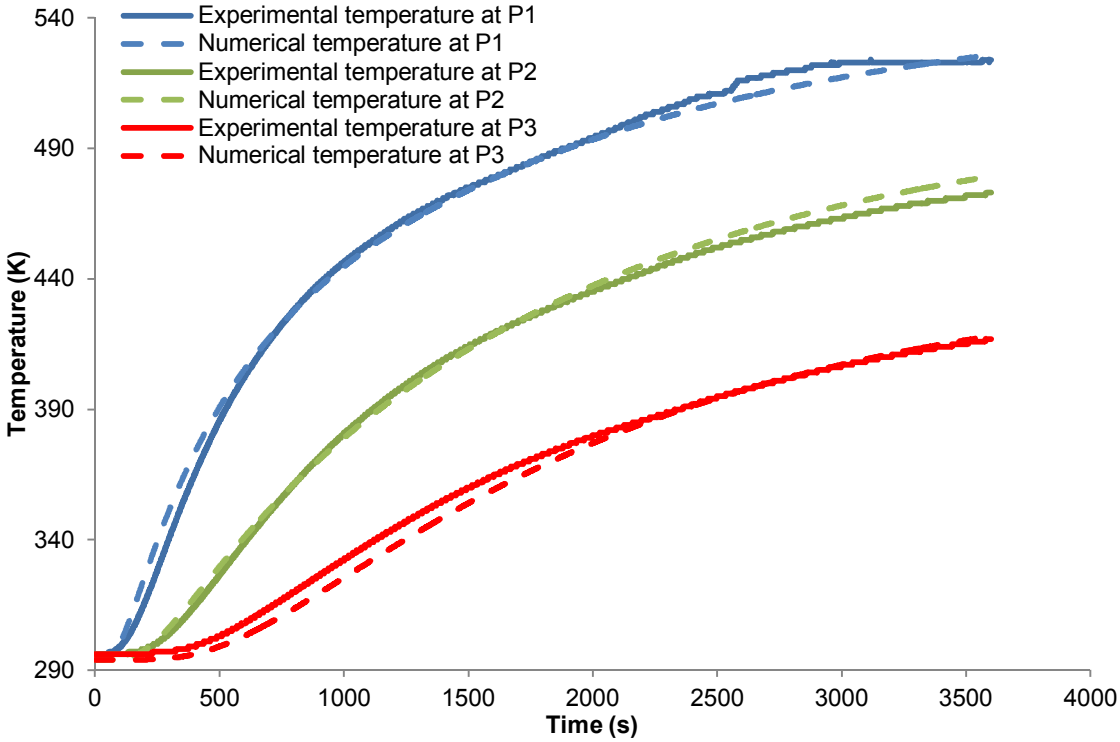

Figure 27: Comparison of the gradient temperature for the case 7.5kW/m2 and NO thermal insulation

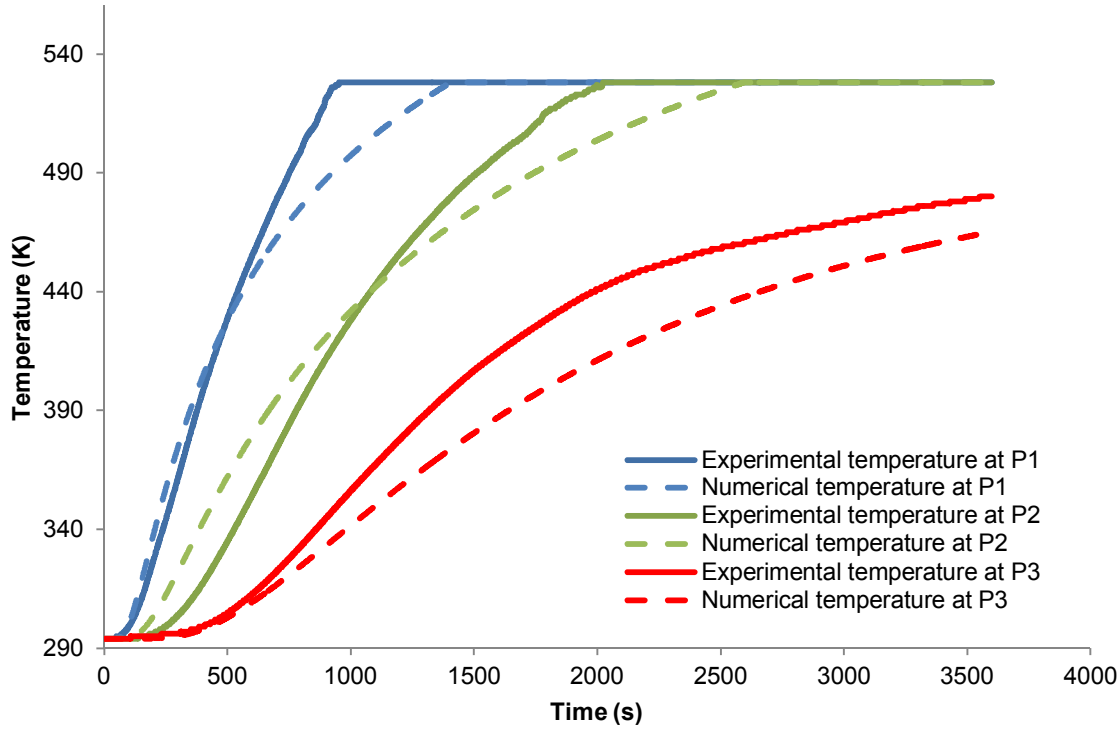

Figure 28: Comparison of the gradient temperature for the case 10kW/m2 and NO thermal insulation

Three results can already be underlined from the previous curves:
A big discrepancy between the numerical solution and the experiment for tests where the temperature of melting is reached (for instance: Figure 19).
In case of the presence of the skin and the thermal insulation, the numerical cannot reproduce correctly the beginning of the rise of temperature (between 500 and 1000 seconds for the Figure 18).
For the case of the geopolymer skin, results from the numerical simulation are not able to reproduce the reality (it might be due to the releasing of water vapour).

These results are summarized in Table 4.

Table 4: Results of numerical tests to determine the delay and the reduction coefficient of the radiant heat flux

Test number	Heat flux (kW/m^2)	Thermal Insulation (TI) (mm)	Type of skin	Time delay (s)	Equivalent Heat Flux (kW/m^2)	Reduction coefficient (%)
1	75	50	Epoxy	861	10.4	87
2	50	25	Epoxy	484	28.9	43
3	50	50	Epoxy	827	6.5	87
4	25	25	Epoxy	508	13.3	46
5	25	25	No Skin	214	14.1	43
6	50	50	No Skin	553	7.4	85
7	100	100	Epoxy	0	1.3	98
8	2.5	No Thermal Insulation	Epoxy	0	1.2	48
9	5	No Thermal Insulation	Epoxy	144	5.2	-4
10	7.5	No Thermal Insulation	Epoxy	137	7.2	4
11	10	No Thermal Insulation	Epoxy	152	9.6	4
12	2.5	No Thermal Insulation	Geopolymer	For the geopolymer case, the numerical is not adapted (due to release of water from geopolymer)		
13	7.5	No Thermal Insulation	Geopolymer			
14	10	No Thermal Insulation	Geopolymer			

The previous results show some important things. The behaviour of the sandwich specimen with geopolymer skin cannot be reproduced by the numerical code, as it may release water vapour during the heating process. This conclusion could also be seen on the results obtained during the experiments with a small oven test with the temperature curve ISO 834.

When the time delay is equal to zero, a differentiation should be done between the test at 2.5 kW/m^2 and the test at 100. Indeed, in the second case the thermal wave doesn't have time to reach the core material while in the first case, the incident heat flux is so low that its influence is not clearly taken in account by the numerical code.

From the Table 4, all the results are summarized in the following table.

Table 5: laws deduced from the comparison between numerical and experimental heating process of sandwich and thermal insulation

Material	Time delay (s)
50 mm TI + SKIN	844
25 mm TI + SKIN	496
SKIN	144
25 mm TI	214
50 mm TI	553

Material	Reduction coefficient (%)
50 mm TI	86
25 mm TI	44
100 mm TI	98
SKIN	±4

3.4 Determination of the equivalent radiant heat flux

The third and final step of this methodology is the comparison between numerical tests and experimental test on a small oven with the temperature curve ISO 834. This standard curve is shown on the Figure 29.

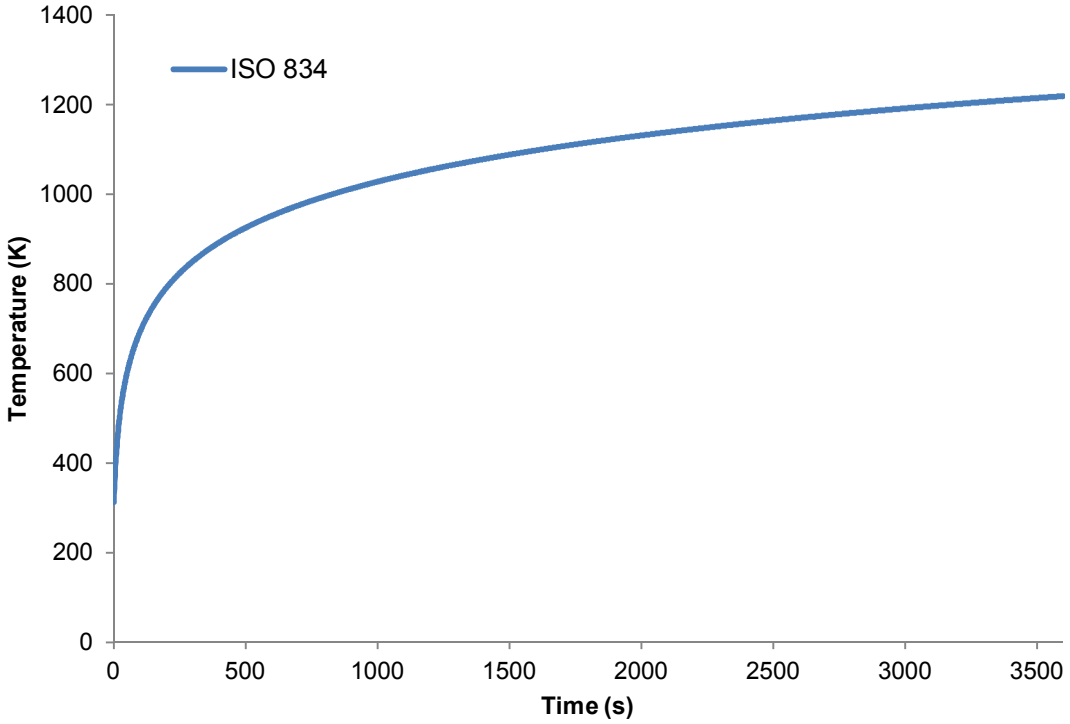

Figure 29: temperature curve ISO 834

3.4.1 Experiments on small oven (ISO 834)

One test has been performed with the small oven of DBI. The oven is able to reproduce the temperature curve ISO 834 in a relatively small oven, comparing with the standard one.
During this test, four plates of the two different sandwiches (2 plates of epoxy skin and 2 plates with geopolymer skin) have been tested. The size of each plate was 500 x 500 mm, with 4 layers of thermal insulation (25mm*64 kg/m^3-25mm*70 kg/m^3-25mm*70 kg/m^3-25mm*64 kg/m^3) separated by an aluminium foil layer.
As in all previous steps, three thermocouples have been mounted through the thickness of specimens, at 10 mm from the top of the specimen (P1), at 20 mm (P2) and P3 represents the thermocouple at 30 mm.

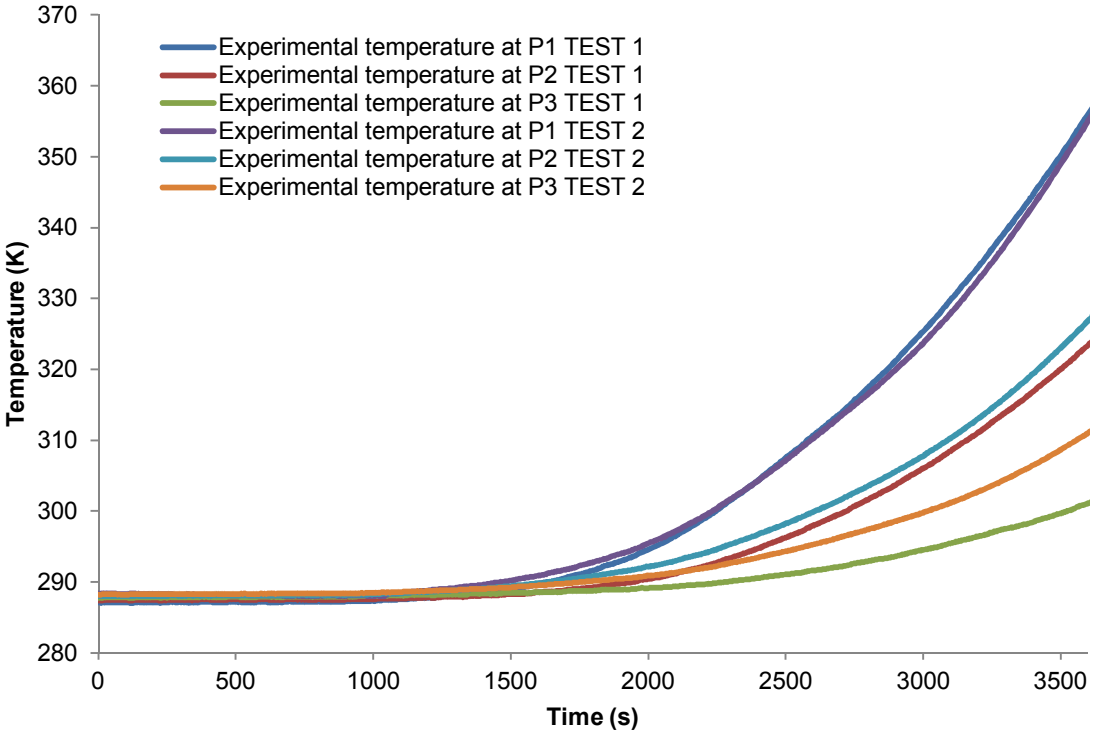

Figure 30: Temperature of the core of the Epoxy skin sandwich for the small oven test (ISO 834)

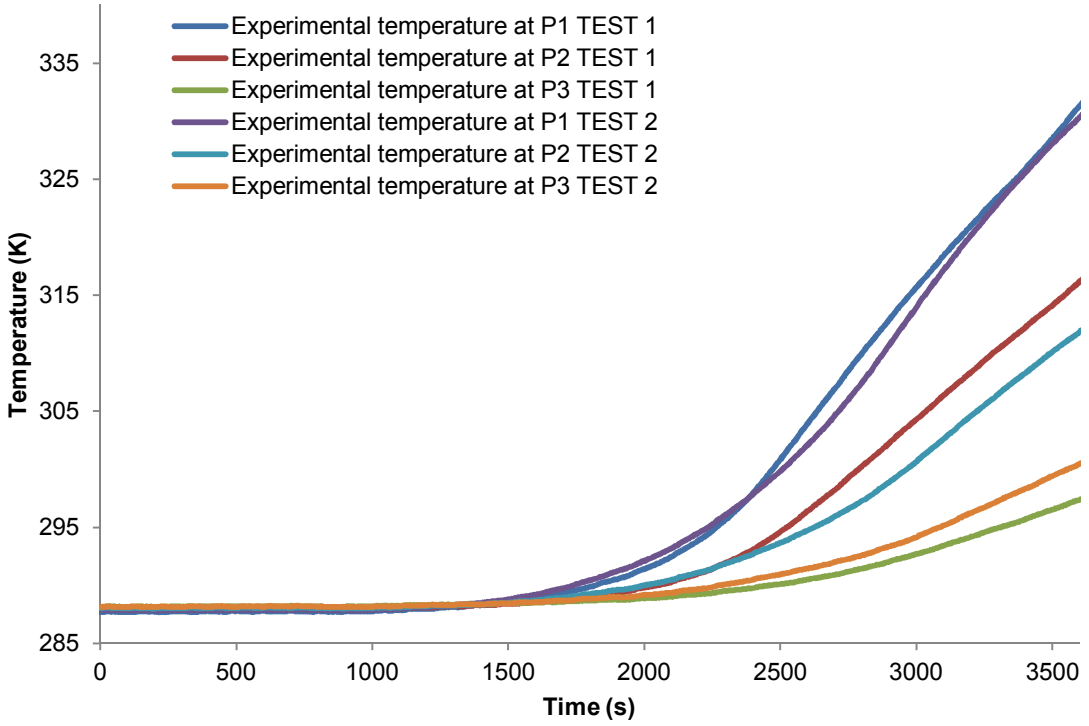

Figure 31: Temperature of the core of the Geopolymer skin sandwich for the small oven test (ISO 834)

It can be noticed that, as overserved previously, the geopolymer skin shows a better resistance to the heating process than the epoxy skin. At the end of the test (after 3600 s), the temperature are 335 K, 310 K and 300 K for the geopolymer skin and 355 K, 325 K and 300 K for the epoxy skin for P1, P2 and P3 respectively. This better resistance is also due to the release of water vapour as seen in the paragraph 3.2.2, but also in the following graph. It represents the temperature of the skin (bottom part, close to the contact between the skin and the core of the sandwich) during the small oven test.

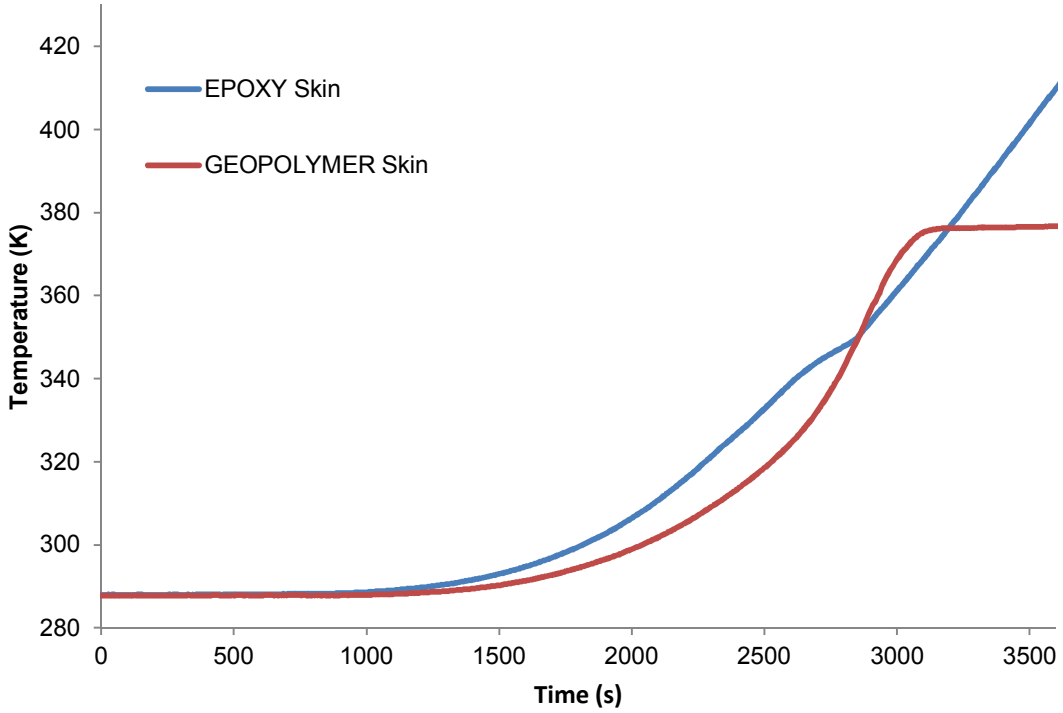

Figure 32: Temperature of the bottom part of the Geopolymer (red) and Epoxy (blue) skin for the small oven test (ISO 834)

From the Figure 32, the release of water vapour is clearly visible because appearing around 374K. And because of this release of water vapour, the sandwich with geopolymer skin cannot be studied deeper, i.e. it cannot be tested with the H-TRIS.
Additionally, a change of behaviour of the heating process is already visible for the epoxy skin. It happens between 344 and 349K. It might due to the glass transition temperature of the epoxy skin (according to the data from the skin producer the glass transition temperature is around 342-344 K).

3.4.2 Comparison with the numerical code

In the same way as the paragraph 3.3.2, the numerical code is used to determine an equivalent heat and a time delay. In the present case, as the heat stress from the oven is not constant, the equivalent heat flux and its time delay is in reality a composition of two groups of heat flux and time delay. The change of incident heat flux is clearly identifiable on the following curve.

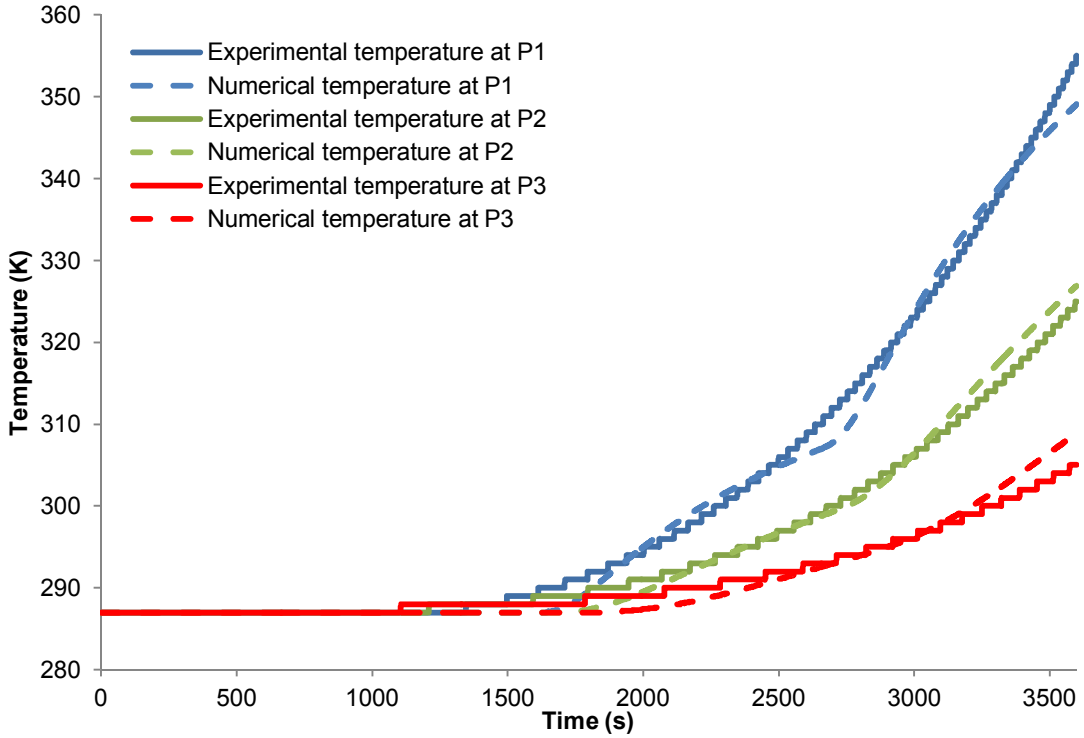

Figure 33: Comparison of the gradient temperature for the small oven test

3.4.3 Results

With the experiments and its comparison with the numerical code, the equivalent heat flux has been determined. This heat flux is the combination of two constant heat fluxes (Q_1 and Q_2) with their time delay:

- t_{delay}=150 s (taken in account for the time of appliance for $Q_1$and Q_2)
- Q_1= 1.3 kW/m^2 from 1564 seconds to 2603seconds
- Q_2= 3.6 kW/m^2 from 2603 seconds to 3600 seconds

The following curve represents the equivalent heat flux (capable to reproduce the heating of the small oven ISO 834).

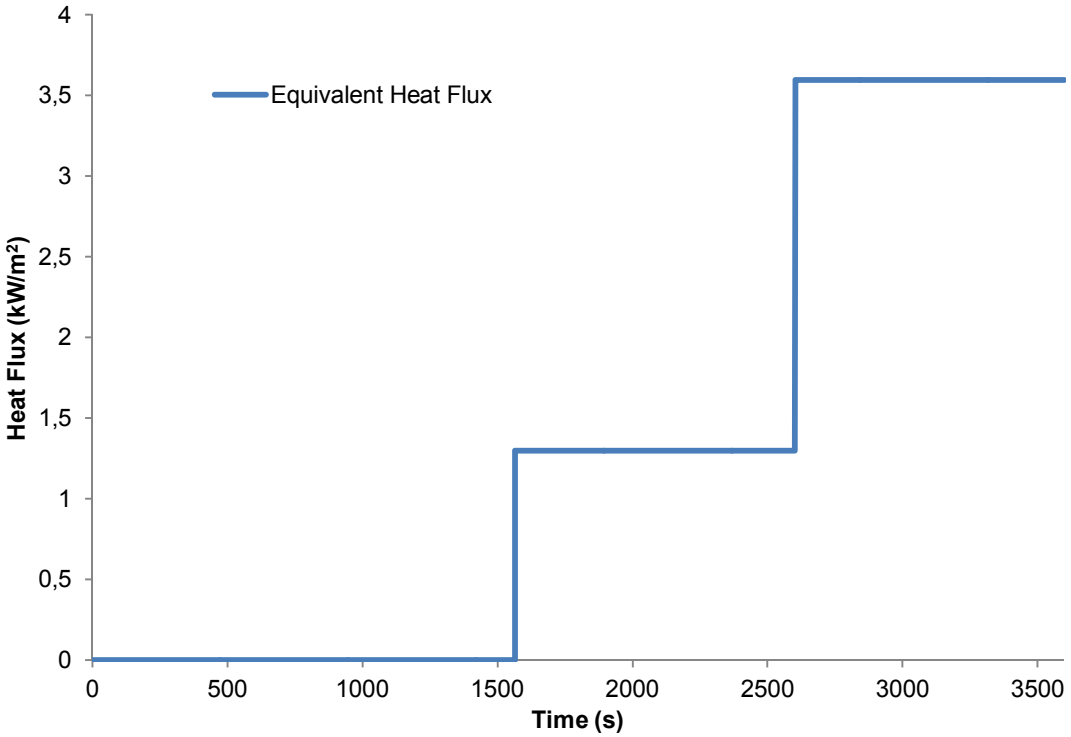

Figure 34: Equivalent heat flux as input, to reproduce the heating process of an epoxy skin sandwich by an oven with the ISO 834 temperature curve.

The result from the Figure 34 allows the performing of a test to compare the result obtained by an experiment with a mass loss cone applying the equivalent radiant heat flux on an epoxy skin sandwich. The mass loss cone is used because the H-TRIS doesn't have its mechanical part build. But the heating process is the same and the result should be as well.

3.5 Comparison of the gradient temperature obtained with the small oven and the mass loss cone

The Figure 35 corresponds to the comparison of the temperature obtained by the numerical code (same as the Figure 33) and by the equivalent heaty flux found previously (Figure 34) applies by the mass loss cone on an epoxy skin sandwich.

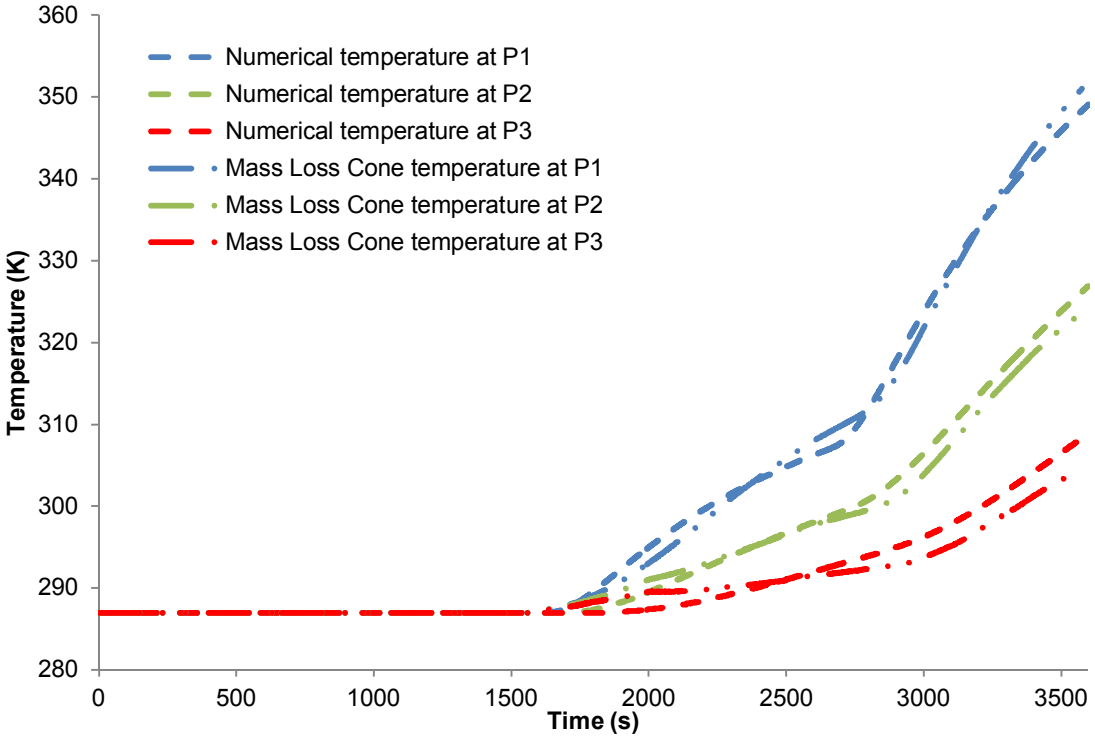

Figure 35: Equivalent heat flux as input, to reproduce the heating process of an epoxy skin sandwich by an oven with the ISO 834 temperature curve.

The final step (Figure 36) is to compare three temperatures for the same case that is the heating process of a sample of epoxy skin sandwich:

- Temperature from the small scale oven ISO834
- Temperature from the numerical code (in order to obtain the equivalent radiant heat flux)
- Temperature from the mass loss cone applying the equivalent radiant heat flux.

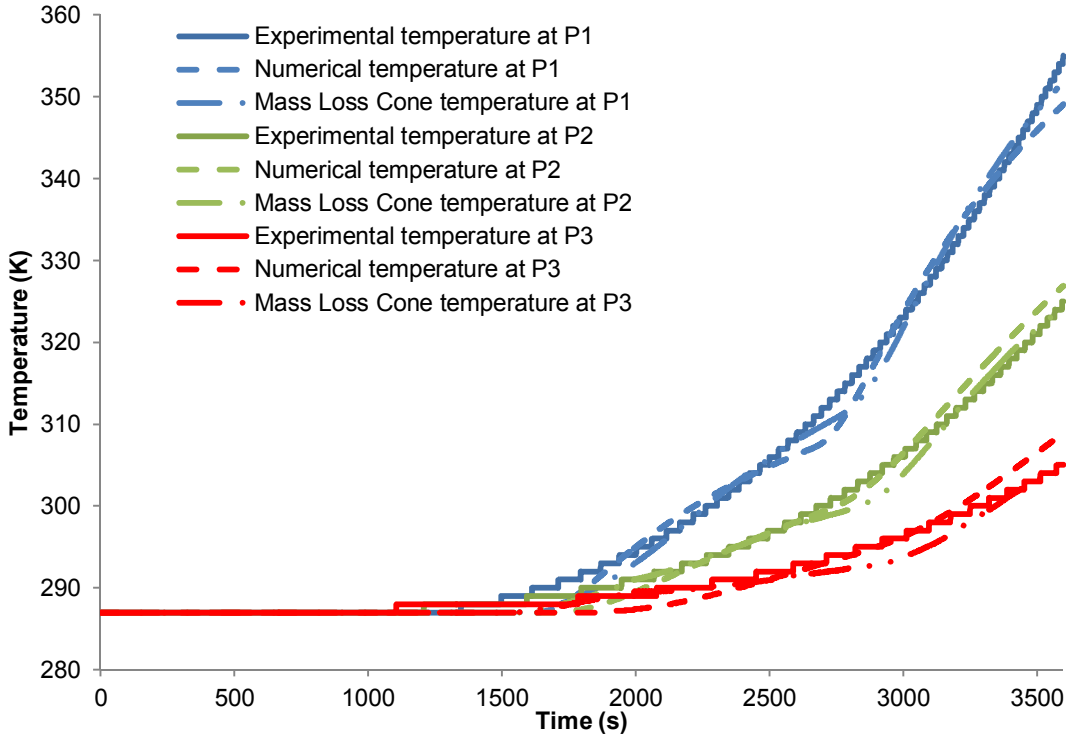

Figure 36: Comparison of temperatures for the heating process of an epoxy skin sandwich.

The Figure 36 shows that the theory and model developed for the COMPASS project gives nice results.

4. Conclusion

This report deals with the H-TRIS. This new experimental rig has been developed during the COMPASS project. The rig might be useful as a screening test rig in order to choose the best sandwich material and its thermal insulation for the construction of vessels.
In order to be able to use the H-TRIS, a theory has been developed. Indeed the H-TRIS should be able to reproduce the heating stress of an ISO 834 oven test.
From an ISO 834 oven test, the temperature gradient is reproduce by an easy one dimension numerical code that gives as output an equivalent radiant heat flux. This heat flux is the input of the H-TRIS and permits to test the studied the impact of different mechanical stress on the studied sandwich specimen without the addition of the thermal insulation. It allows performing tests with a very low radiant heat.

References

[1] Isao Kimpara, Use of advanced composite materials in marine vehicles, Marine Structures, Volume 4, Issue 2, 1991, Pages 117-127.

[2] Milton O. Critchfield, Thomas D. Judy, Alan D. Kurzweil, Low-cost design and fabrication of composite ship structures, Marine Structures, Volume 7, Issue 2, 1994, Pages 475-494.

[3] A.K. Green, W.H. Bowyer, The development of improved attachment methods for stiffening frames on large grp panels, Composites, Volume 12, Issue 1, 1981, Pages 49-55.

[4] Regulation 17, International Maritime Organization. SOLAS Consolidated Edition 2009. International Convention for the Safety of Life at Sea.

[5] F. Evegren, Preliminary study of the Øko-Ø-færge project, SP report 2012:03.

[6] J. Gutierez et al., "Fire safety engineering applied to the evaluation of the safety level of marine composite structure", 13th conf. Fire and Mat. 2013.

[7] International Code for Application of Fire Test Procedures, FTP 2010, International Maritime Organization.

[8] C. Maluk, PhD Thesis, "Development and application of a novel test method for studying the fire behavior of CFRP pre stressed concrete structural elements." The University of Edinburgh, 2014.

[9] C. Maluk et al., "novel fire testing methodology: Why, how and what now?", 1st Inter. Conf. on Performance Based land Life Cycle Struct. Eng., 5-5 December 2012, p. 448-458.

[10] ISO 834 Fire-resistance tests — Elements of building construction.

[11] Y. Bai et al., "Experimental investigations on temperature-dependent thermo-physical and mechanical properties of pultruded GFRP composites", Thermochimica Acta, 2008, 469, 1-2: 28–35.

[12] Y. Bai et al., "Modeling of thermophysical properties for FRP composites under elevated and high temperatures", Comp. Sci. Techn., 2007, 67, 15-16:3098–3109.

[13] E. Kandare et al., Thermo-mechanical Responses of Fiber-reinforced Epoxy Composites Exposed to High Temperature Environments. Part I: Experimental Data Acquisition, J. of Comp. Mat., 2010, 44, 26: 3093-3114.

[14] A. Grenier, PhD Thesis, "Fire characteristics of cored composite materials for marine use" Worcester Polytechnic Institute, 1996.

[15] H. Halverson et al., "Simulation of response of composite structures under fire exposure", Sc. and Eng. of Comp. Mat., 2005, 12, 1-2: 3–101.

[16] ISO 5660-1:2002, Reaction-to-fire tests -- Heat release, smoke production and mass loss rate -- Part 1: Heat release rate (cone calorimeter method)

[17] H. Zhang , T. L. Hu & J. Ch. Zhang (2009) Surface emissivity of fabric in the 8–14 μ m waveband, The Journal of The Textile Institute, 100:1, 90-94.

[18] M. Bordival, F.M. Schmidt, Maoult Y.L., Velay V. (2009), Optimization of preform temperature distribution for the stretch-blow molding of PET bottles: Infrared heating and blowing modeling. Polym Eng Sci, 49: 783–793.

[19] J. Vlachopoulos, D. Strutt, Plastics Technician's Toolbox, Chapter 1, Volume 2,

Pages 21-33, SPE 2002.

Appendix A: Frame of the mechanical part of the H-TRIS

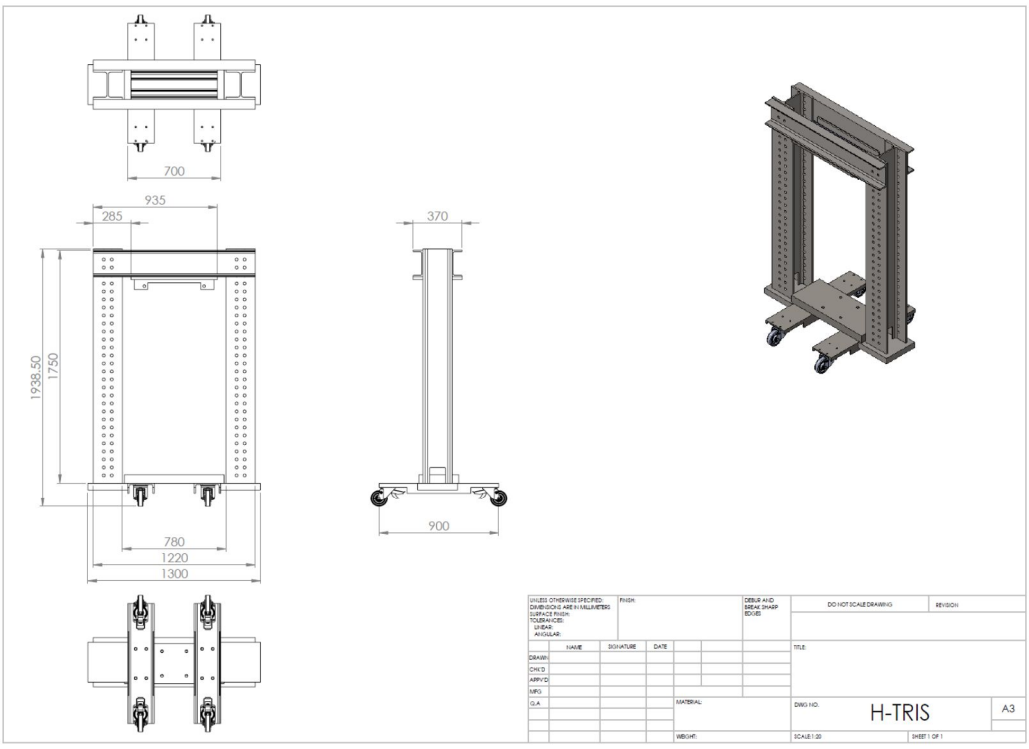

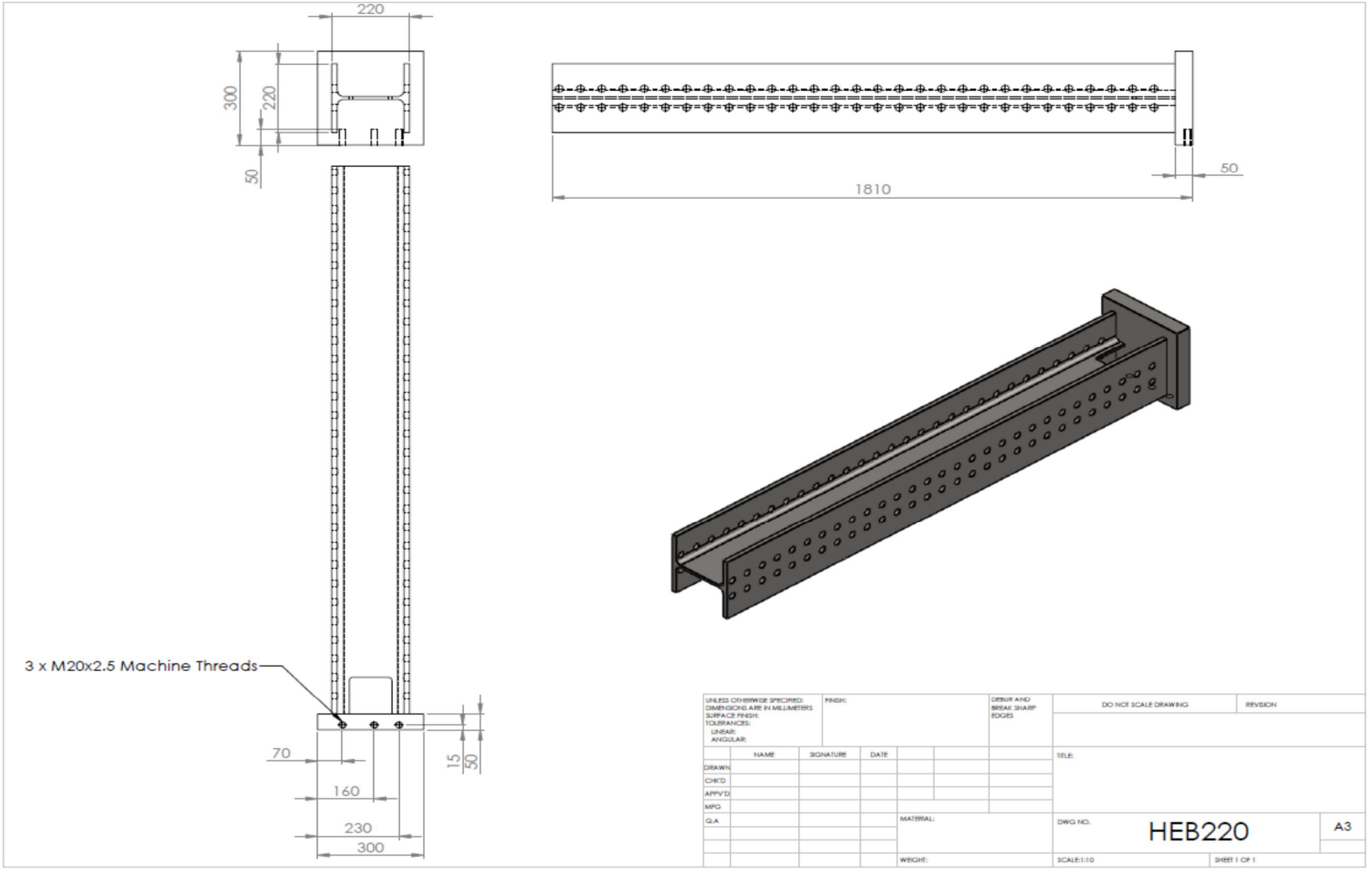
220
300
220
50
1810
50
3 x M20x2.5 Machine Threads
70
160
230
300
15
50
UNLESS OTHERWISE SPECIFIED:
DIMENSIONS ARE IN MILLIMETERS
SURFACE FINISH:
TOLERANCES:
LINEAR:
ANGULAR:
FINISH:
DEBUR AND BREAK SHARP EDGES
DO NOT SCALE DRAWING
REVISION
NAME
SIGNATURE
DATE
DRAWN
CHK'D
APPV'D
MFG
Q.A
MATERIAL:
WEIGHT:
TITLE:
DWG NO.
HEB220
A3
SCALE:1:10
SHEET 1 OF 1

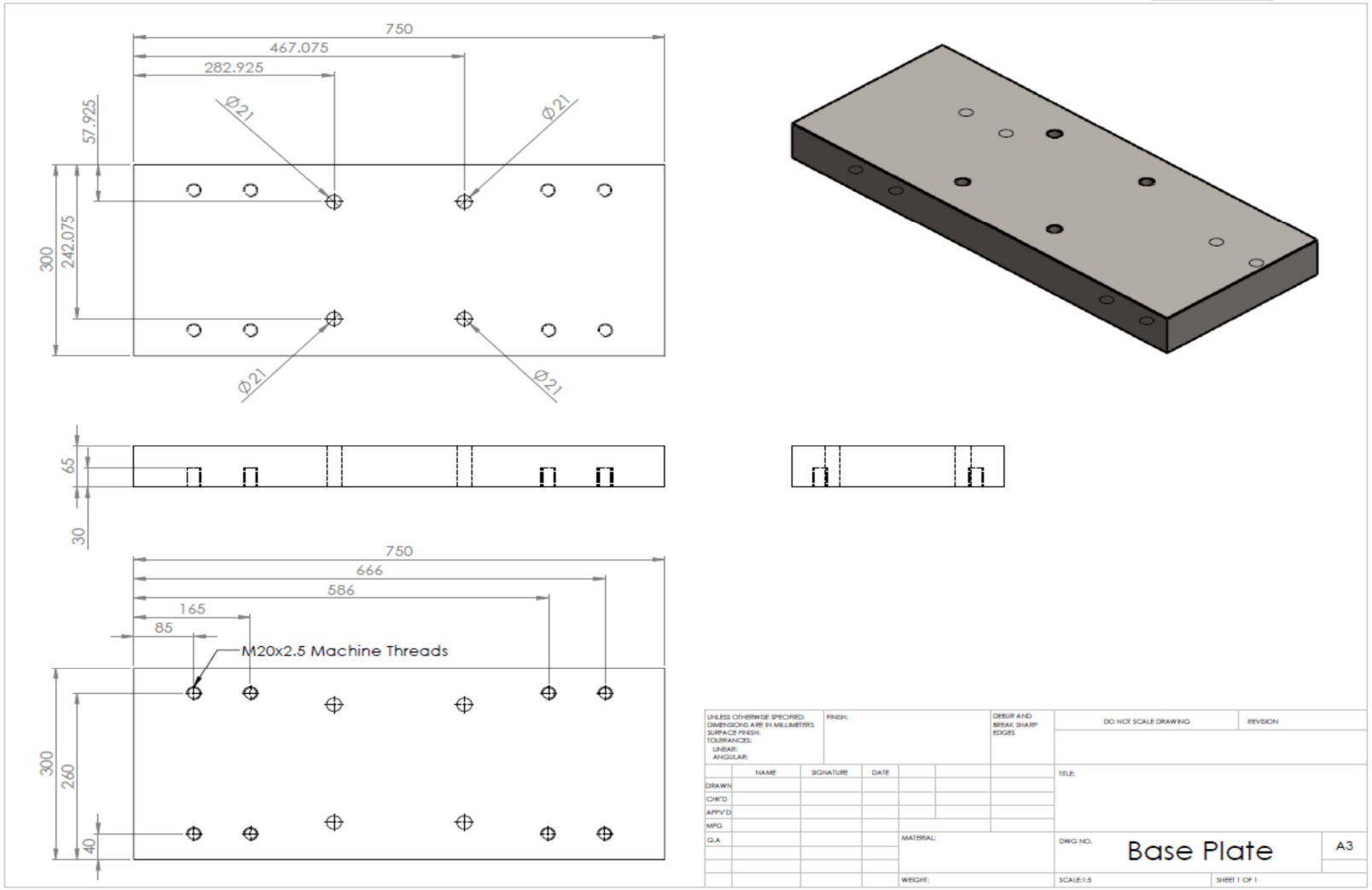
750
467.075
282.925
Ø21
Ø21
57.925
300
242.075
Ø21
Ø21
65
30
750
666
586
165
85
M20x2.5 Machine Threads
300
260
40
UNLESS OTHERWISE SPECIFIED:
DIMENSIONS ARE IN MILLIMETERS
SURFACE FINISH:
TOLERANCES:
LINEAR:
ANGULAR:
FINISH:
DEBUR AND BREAK SHARP EDGES
DO NOT SCALE DRAWING
REVISION
NAME
SIGNATURE
DATE
DRAWN
CHK'D
APP'V'D
MFG
Q.A
MATERIAL:
WEIGHT:
TITLE:
DWG NO.
Base Plate
A3
SCALE:1:5
SHEET 1 OF 1

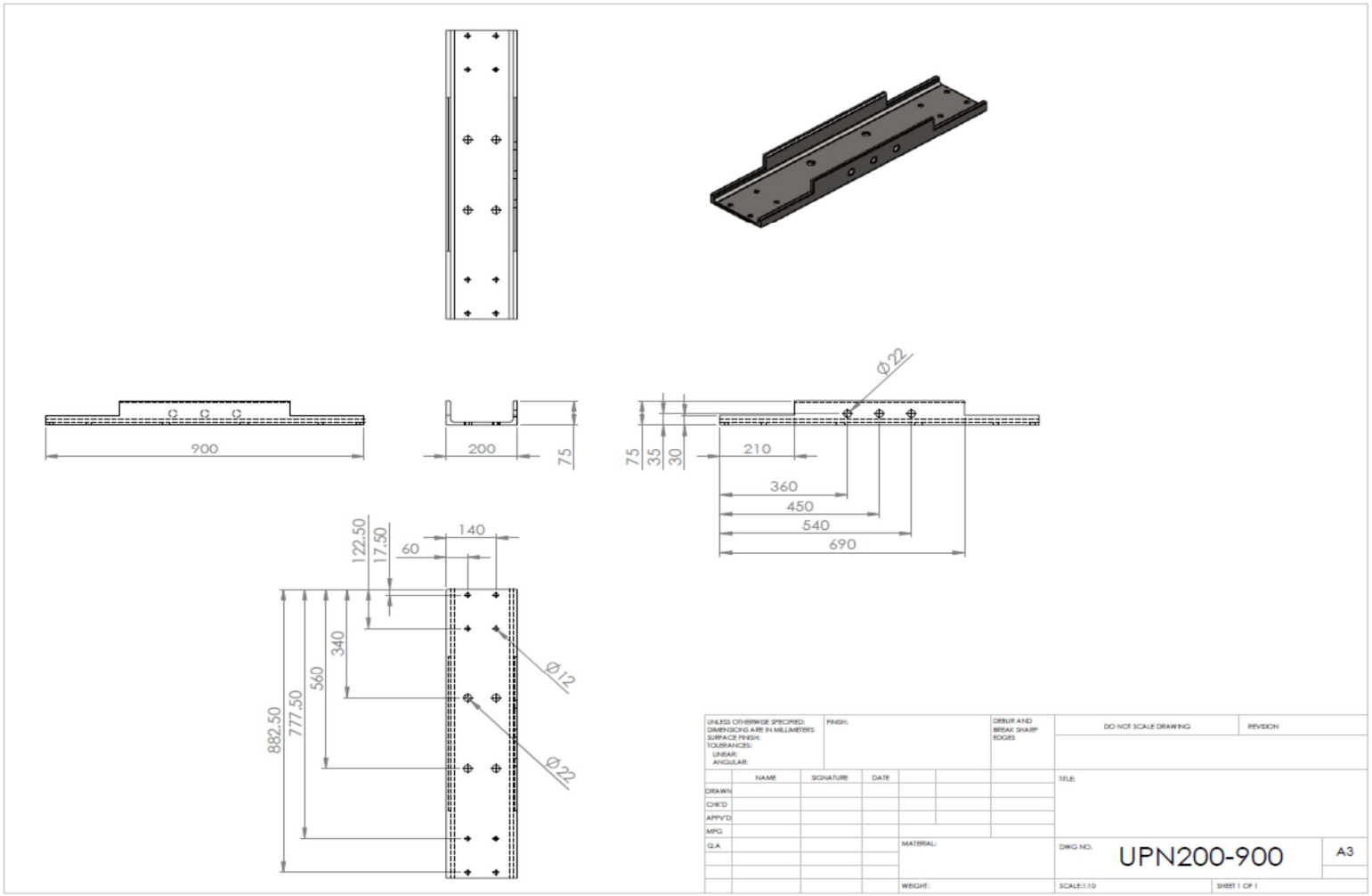
900
200
75
Ø22
75
35
30
210
360
450
540
690
140
122.50
17.50
60
340
560
777.50
882.50
Ø12
Ø22
UNLESS OTHERWISE SPECIFIED:
DIMENSIONS ARE IN MILLIMETERS
SURFACE FINISH:
TOLERANCES:
LINEAR:
ANGULAR:
FINISH:
DEBUR AND BREAK SHARP EDGES
DO NOT SCALE DRAWING
REVISION
NAME
SIGNATURE
DATE
DRAWN
CHK'D
APPV'D
MFG
Q.A
MATERIAL:
WEIGHT:
TITLE:
DWG NO.
UPN200-900
A3
SCALE:1:10
SHEET 1 OF 1

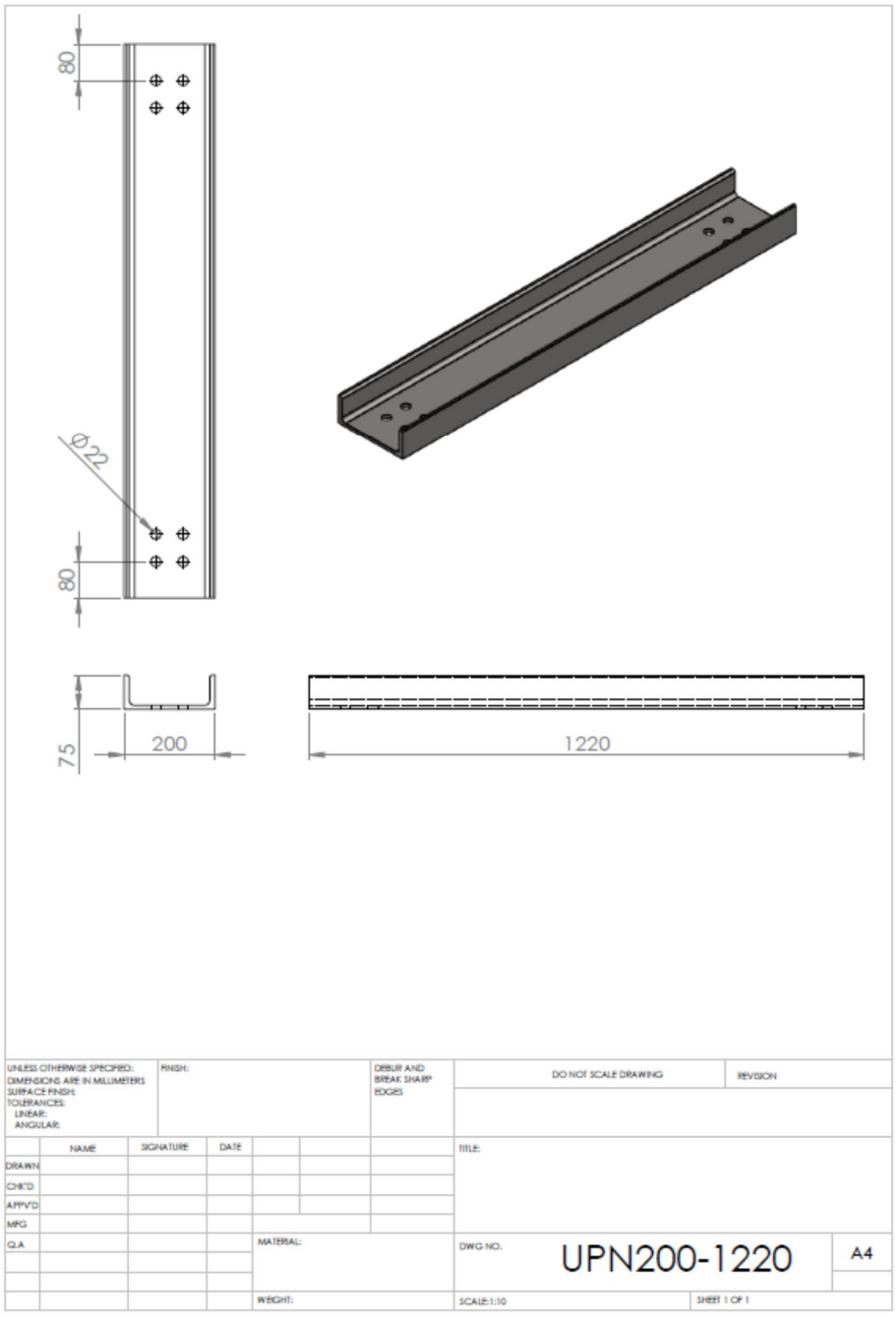
80
Ø22
80
75
200
1220
UNLESS OTHERWISE SPECIFIED:
DIMENSIONS ARE IN MILLIMETERS
SURFACE FINISH:
TOLERANCES:
LINEAR:
ANGULAR:
FINISH:
DEBUR AND BREAK SHARP EDGES
DO NOT SCALE DRAWING
REVISION
NAME
SIGNATURE
DATE
DRAWN
CHK'D
APPV'D
MFG
Q.A
MATERIAL:
WEIGHT:
TITLE:
DWG NO.
UPN200-1220
A4
SCALE:1:10
SHEET 1 OF 1

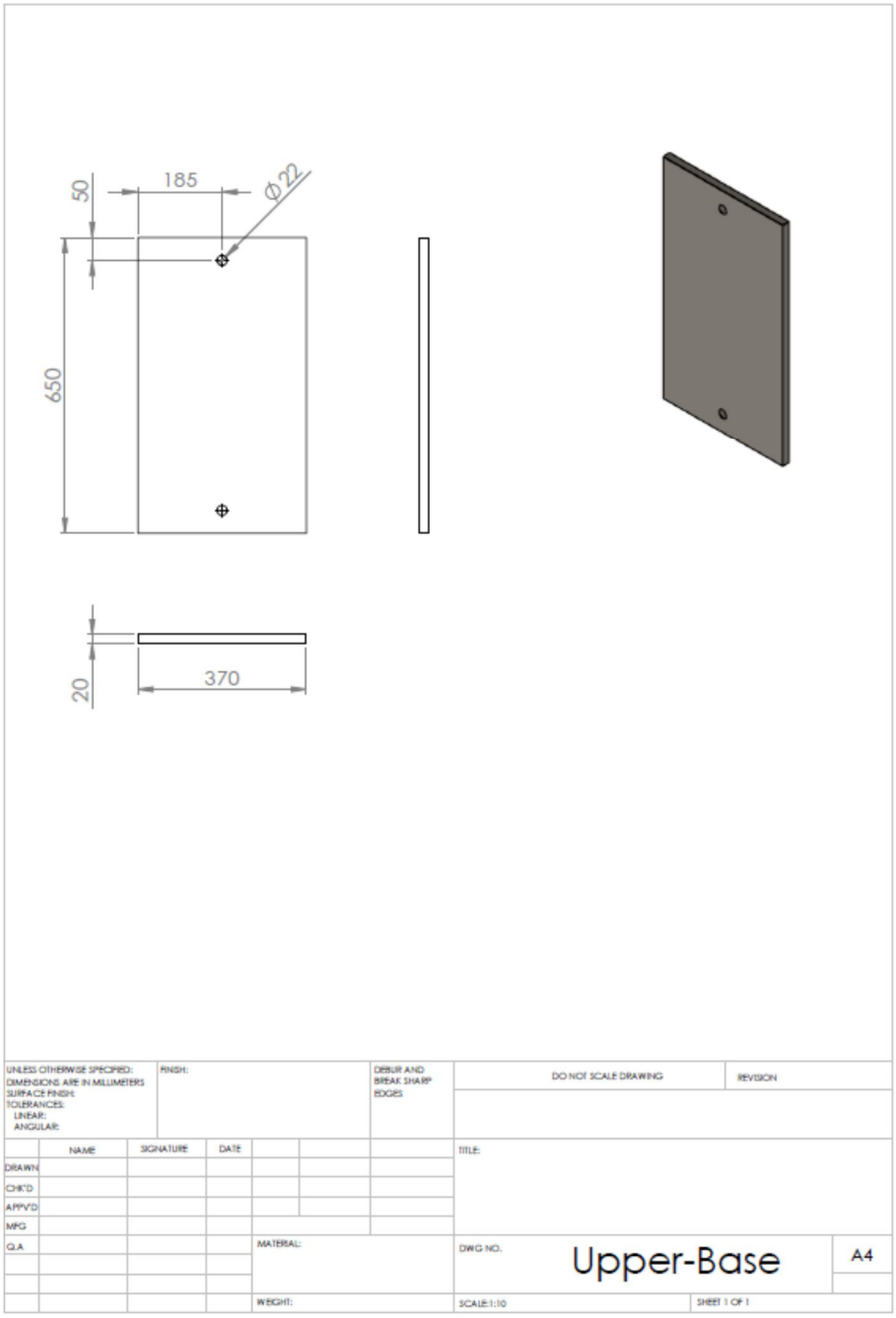
185
Ø22
50
650
370
20
UNLESS OTHERWISE SPECIFIED:
DIMENSIONS ARE IN MILLIMETERS
SURFACE FINISH:
TOLERANCES:
LINEAR:
ANGULAR:
FINISH:
DEBUR AND BREAK SHARP EDGES
DO NOT SCALE DRAWING
REVISION
NAME
SIGNATURE
DATE
DRAWN
CHK'D
APPV'D
MFG
Q.A
MATERIAL:
WEIGHT:
TITLE:
DWG NO.
Upper-Base
A4
SCALE:1:10
SHEET 1 OF 1

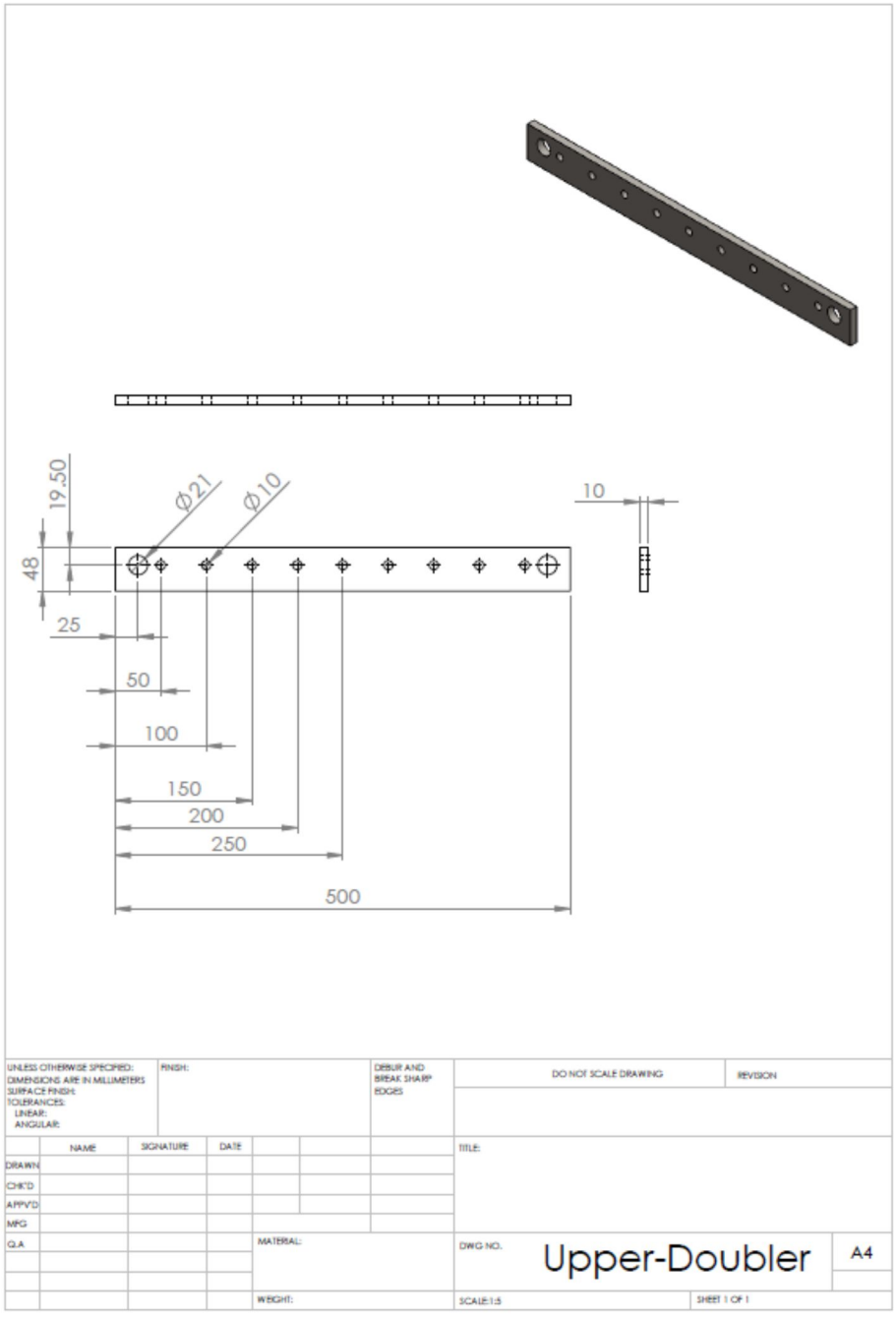
19,50
Ø21
Ø10
10
48
25
50
100
150
200
250
500
UNLESS OTHERWISE SPECIFIED:
DIMENSIONS ARE IN MILLIMETERS
SURFACE FINISH:
TOLERANCES:
LINEAR:
ANGULAR:
FINISH:
DEBUR AND BREAK SHARP EDGES
DO NOT SCALE DRAWING
REVISION
NAME
SIGNATURE
DATE
DRAWN
CHK'D
APPV'D
MFG
Q.A
TITLE:
MATERIAL:
DWG NO.
Upper-Doubler
A4
WEIGHT:
SCALE:1:5
SHEET 1 OF 1

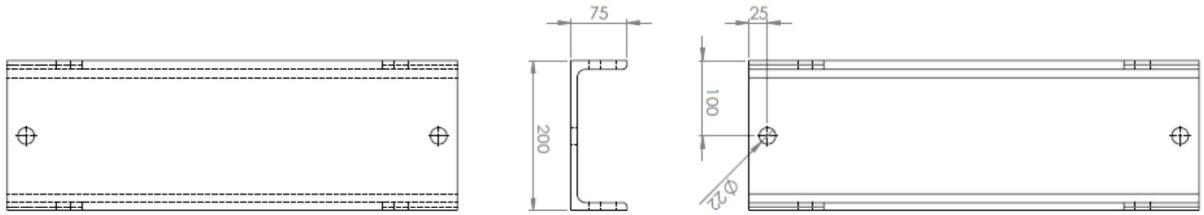

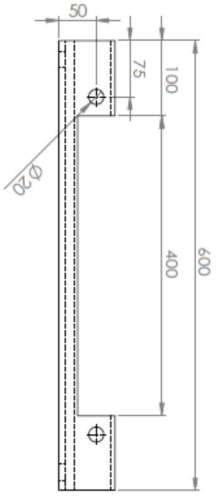

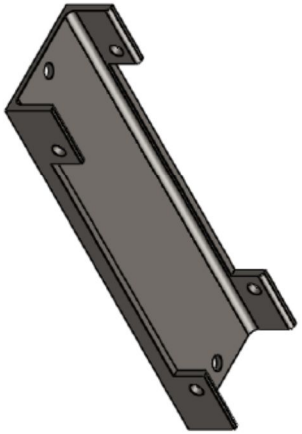

UNLESS OTHERWISE SPECIFIED: DIMENSIONS ARE IN MILLIMETERS SURFACE FINISH: TOLERANCES: LINEAR: ANGULAR:			FINISH:			DEBUR AND BREAK SHARP EDGES	DO NOT SCALE DRAWING
	NAME	SIGNATURE	DATE				TITLE:
DRAWN							
CHK'D							
APP'D							
MFG							
QA				MATERIAL:			DWG NO. UPN200-600
							A3
				WEIGHT:			SCALE:1:5 SHEET 1 OF 1

ANNEX H: Mid-scale tests of composites under combined thermal and mechanical loading

DTU Mechanical Engineering
Department of Mechanical Engineering

DTU Civil Engineering
Department of Civil Engineering

Date : August 2016
Project name : COMPASS – COMposite superstructures for large PASsenger Ships

Author : Vasileios Karatzas

Contents

1 Introduction

1.1 Background

Composites are increasingly being implemented in a variety of industrial applications in which metallic materials were considered as the sole viable solution. This is attributed to the outstanding physical, thermal, chemical and mechanical properties that composites materials exhibit. Key advantages of composites over many metal alloys include low density, high specific stiffness and specific strength, good fatigue endurance, excellent corrosion resistance, outstanding thermal insulation and low thermal expansion. However, there are certain disadvantages with composites that have been hindering their growth in some markets. Possibly the major disadvantage of the majority of composite materials is poor performance in fire. When composites are exposed to high temperatures (typically above 300-400^{o}C) the organic matrix decomposes releasing heat, smoke, soot and toxic volatiles. In addition, if the fibres used to reinforce composites are organic, such as aramid and polyethylene, they will also decompose and contribute to the generation of heat, smoke and fumes. More importantly when composites are heated to moderate temperature (typically at the range of 100-200^{o}C), they soften, creep and distort which in turn can result in buckling and failure of load-bearing composite structures [1].

As such, the behaviour of polymer composite materials in fire has been a major concern and much effort has been devoted to assessing and reducing their fire hazard in the last decades. Understanding the structural performance in fire is a critical safety issue because the loss in stiffness, strength and creep resistance can cause composite structures to distort and collapse. Structural properties of composites in fire are therefore arguably as important to safety as the fire reaction properties that have generally been more widely studied.

The advantages of composites constitute them very appealing for naval applications and therefore the majority of high speed light craft vessels are made of composite materials. However, their implementation in SOLAS ships has been hindered by their poor performance in fire. Contrarily to SOLAS ships, some applications of composites are present in military naval ships and submarines, these applications are listed in [2]. According to this review, composites were mostly implemented in relatively small ships or in non-structural/non-critical components on large ships and submarines such as superstructures and masts.

An excellent state of the art on along with a critical review of research progress in modelling the structural response of polymer matrix composites exposed to fire is presented in [3]. Models for analysing the thermal, chemical, physical, and failure processes that control the structural responses of laminates and sandwich composite materials in fire are reviewed. Models for calculating the residual structural properties of composites following fire are also described. Progress towards validation of the models by experimental characterisation of the structural properties of composites during and following fire is assessed. In conclusion, deficiencies in the fire structural models are identified, which provide the focus for future research in the field.

In this section a brief overview of the ongoing research in the structural behaviour of composites under elevated temperatures is presented. The majority of the presented studies concentrate on the testing of single skin FRP and sandwich materials under combined axial mechanical loading and one sided thermal loading, imposed via a burner or a small climate chamber. Scope of these studies is to propose suitable design tools for the correct dimensioning of composite structures to avoid premature collapse in case of fire.

Several researches have been focused on the behaviour of FRP laminates under combined thermomechanical loading. These studies enabled the better understanding of the different failure mechanisms on FRP elements and represented a necessary preliminary step before sandwich structures were studied. Dao et al [4] performed experiments on single skin vinylester glass composites with insulation and compared the results with the ones from similar tests on aluminium plates. Based on semi-empirical material degradation laws and models of the temperature profile across the thickness of the laminate, they proposed a macroscopic collapse model accounting for buckling like collapse modes but not for kinking wrinkling and delaminations that may occur at the composite. Gu and Asaro performed a series of experiments [5] and subsequently [6] used the aforementioned approach to obtain an analytical expression for the buckling load from the theory of functionally graded materials and later compared experimental results of single skin and sandwich specimens to the predictions of the model, showing overall good agreement. Their work was later on expanded to include different failure modes such as bending due to buckling shift of neutral axis, thermal distortion under thermal gradients without mechanical loads and skin wrinkling in sandwich materials [7] [8] [9].

In a similar work Gibson et al [10] used a thermal model in conjunction with laminate analysis to model a loaded composite plate under one-sided heat flux. The authors subsequently verified the proposed model with experimental results of polyester glass laminates exposed to one side heat under tension and compression. In a subsequent publication the authors demonstrated the modelling of thermal and decomposition behaviour during combined thermomechanical testing of thermosetting and thermoplastic single skin panels. The model has been subsequently extended to include mechanical response and failure behaviour. Results showed that it is possible to achieve reasonable agreement between model predictions and data from small-scale tests on composites under load in fire. Based on this model, they suggested a design methodology for naval architects [11].

Other similar works include those of Feih et al [12][13][14][15] who modelled the skin failure of sandwich composites in fire under tension and compression and tested a variety of single skin and composite materials. Boyd et al [16] presented a framework for the modelling of the response of structural composites subjected to combined mechanical loading and fire emphasizing on the response of composites at temperatures below the decomposition temperature, where the viscoelastic response of the composite material becomes important. Hörold et al [17] developed a test set-up for structural integrity investigations under fire for intermediate scale testing and proceeded to test medium sized sandwich panels.

Summarizing, different models have been proposed for the prediction of the behaviour of single skin and sandwich composite materials. These models take into account different modes of failure such as global buckling, skin wrinkling, skin crushing to name a few. For their implementation it is necessary to measure the material properties under elevated temperatures of the FRP and the core, in the case of sandwich materials. The majority of the studies focuses on intermediate scale testing and assumes that the nature of the failure mechanisms will not change with increasing scale. However, in the papers reviewed here the effects of delamination and debonding between the core and the face have not been taken into account.

1.2 Scope

In this work, medium sized sandwich panels were tested under combined thermal and mechanical loading. The experiments were performed employing a burner whose position and intensity could account for different Heat flux scenarios, in combination with a custom hydraulic compression testing rig which was developed to operate at high temperatures. The setup resembles the H-TRIS testing rig developed by Maluke et al [18]. Constant compressive loading of different magnitudes were applied for each test series while simultaneously one face of the specimens were exposed at a constant heat flux. One scenario has been also taken into consideration with a non-constant heat flux during testing. The change in the heat flux was calculated so as to reproduce the same temperature profile as for the insulated specimen exposed to the ISO834 temperature curve tested at the down-sized version of the large fire resistance furnaces (referred to as the "Model furnace") at DBI's facilities.

Unlike the previous studies, an attempt to find a simplified way to account for the delamination and debonding phenomena under combined thermal and mechanical loading was made.

2 Experimental Testing

2.1 Testing Apparatus (H-TRIS)

For the conduction of the experiments a special custom made rig has been designed and constructed. The rig allowed for the one sided heating of the specimen with the use of a burner while simultaneously the specimen was loaded at a constant load with the use of a MTS hydraulic actuator with a capacity of 100 kN. Testing took place at DTU BYG's Fire lab premises. Pictures of the setup are presented in Figures 1 and 2. The testing rig is versatile with the burner and the mechanical loading rig being independent of one another and movable. The setup was positioned underneath a hood to account for the possible decomposition of the specimens which would produce volatile emissions. The loading rig was insulated to avoid, first and foremost, the exposure of the load cell and the actuator to high temperatures, and additionally to prevent the emission of heat from the metallic frame of the mechanical part to the specimen which would interfere with the selected testing conditions.

Figure 1: Burner (left) and insulated loading rig (right)

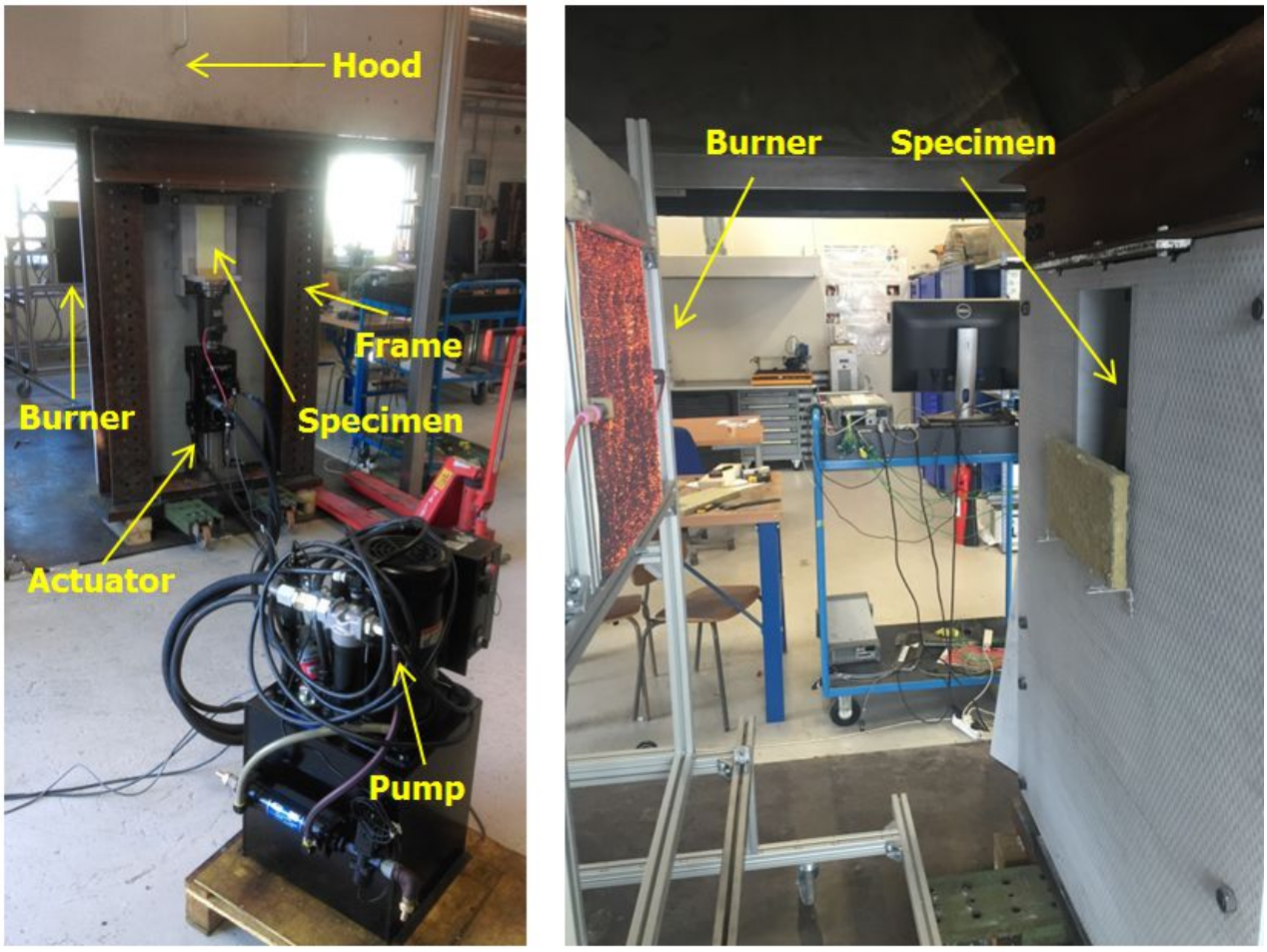

Figure 2: Combined assembly unexposed side (left) and side exposed to burner (right)

2.2 Specimen Description

In total 26 sandwich specimens were tested, not taking into account trial tests. The materials were the same as the ones used for the material characterization tests and the large scale tests. In particular, layers of GBX450L-1250 E-glass Stitched fabric impregnated in epoxy resin were used for the skin of the sandwich panels. The core material was Divinycell P100 provided by DIAB. The details regarding the materials and the manufacturing procedure are given below.

2.2.1 Materials

Fibres: GBX450L-1250 E-glass Stitched fabric
Resin: Epoxy (Prime 20 LV or similar), curing for 16 hours at 50 °C
Fibre volume fraction: 50%
Core: Divinycell P100
Nominal ply thickness for volume fraction of 50%: 0.37 mm
Production method: Vacuum infusion
Hardwood: Birch plywood

The material orientation is given below:

Specimen layer sequence:
2 x GBX450 g/m2 @ 0/90°
2 x GBX450 g/m2 @ 0/90°
1 x 40mm Divinycell P100
2 x GBX450 g/m2 @ 90/0°
2 x GBX450 g/m2 @ 90/0°

2.2.2 Geometry of Specimens

The specimens were cut from larger panels and had a nominal width of 100 mm. The panel dimensions and fibre orientation is given in Figure 3. Note that the orientation angles indicate the fibre orientation and not necessarily the roll orientation. The wood insert was positioned to ensure the proper load transfer to the specimens during the compression tests. These areas were positioned inside the grips of the testing machine. The length of the specimen outside the gripping area was equal to 300 mm. The thickness of the specimens was the same as for the full scale tests with a total nominal thickness equal to 43 mm.

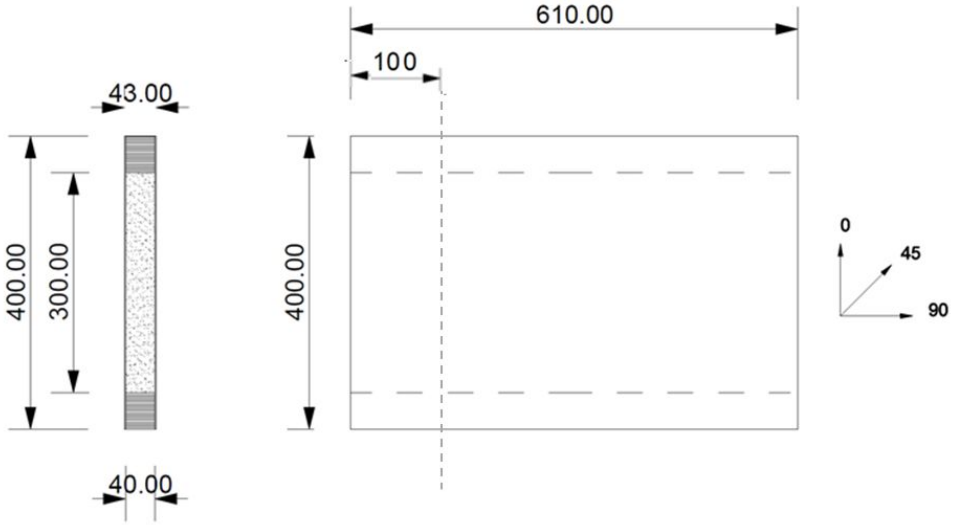

Figure 3: Specimen Geometry

2.2.3 Heat Flux calibration

Prior to the performance of the experiments, tests were performed to investigate whether the target level of 3.6 kW/m^2 could be achieved. In addition it was necessary to quantify how much time was required for the burner to produce a steady heat flux output. To this end a water cooled heat flux gauge (Hukseflux SBG01-005) was positioned exactly at the same location as where the exposed face of the specimen would be during the tests and the burner was set in operation. The burner was positioned in the suitable distance from the specimen to produce 3.6 kW/m^2. Figure 4 depicts the heat flux measurements as a function of time. Results indicate that the heat flux exhibits a rather oscillatory behaviour with the difference between the minimum and maximum recorded values being 0.8 kW/m^2 once the heat flux has been stabilized. For the latter to occur, the burner should be in operation for about 7 minutes. The slight increase of the average impacting heat flux at the vicinity of 17 minutes is caused due to the slight change in the position of the burner during the test.

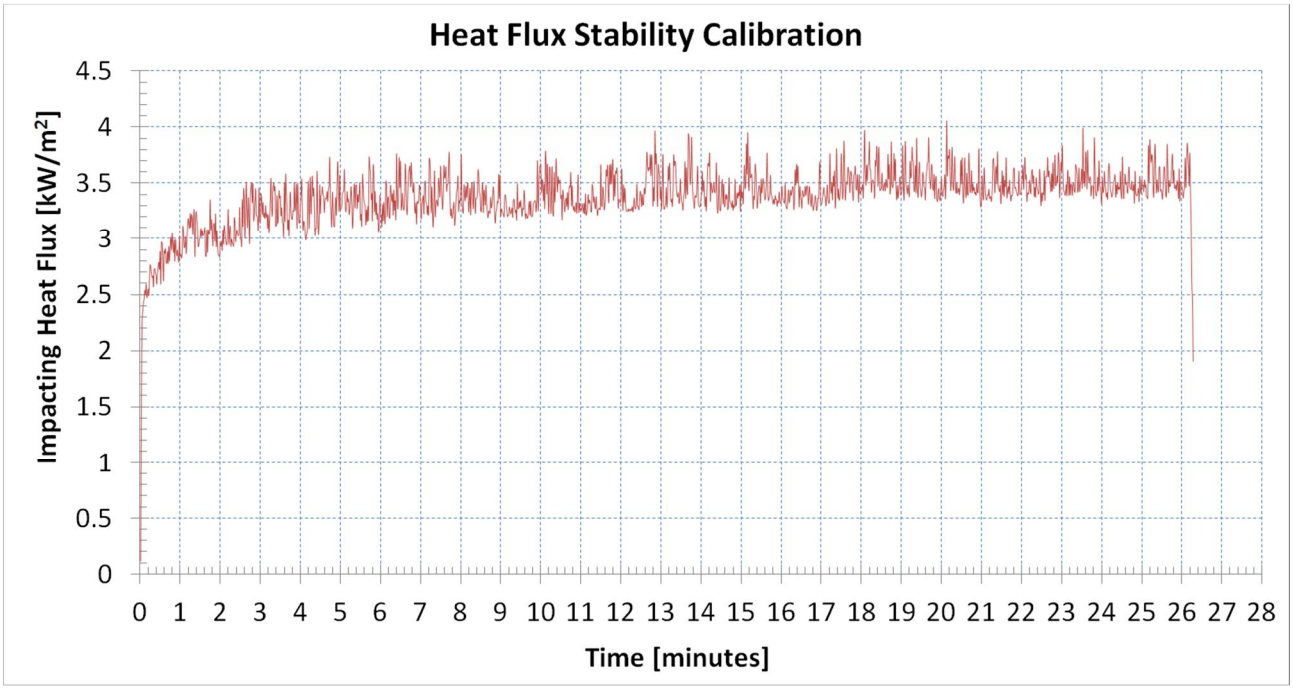

Figure 4: Heat flux stability

To investigate whether the impacting heat flux was uniformly distributed on the specimen's surface, a specimen was positioned and tested without applying any mechanical loading. A total of 5 thermocouples were placed exactly on the exposed surface. Holes were drilled throughout the thickness of the specimen for the correct positioning of the thermocouples. The thermocouples were placed in a cross shaped pattern as shown in Figure 5. Thermocouple TC-3 was located at the centre of the specimen. The temperature measured from the thermocouples is presented as a function of time in Figure 6. Results indicate that the heat flux is uniform across the exposed surface of the specimen.

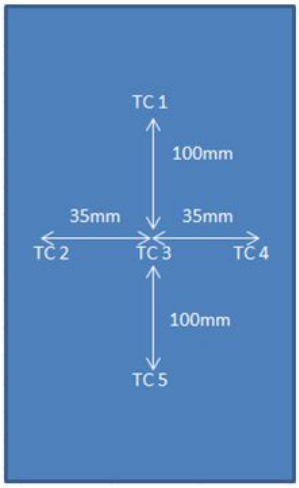

Figure 5: Thermocouple position for the investigation of the heat flux uniformity

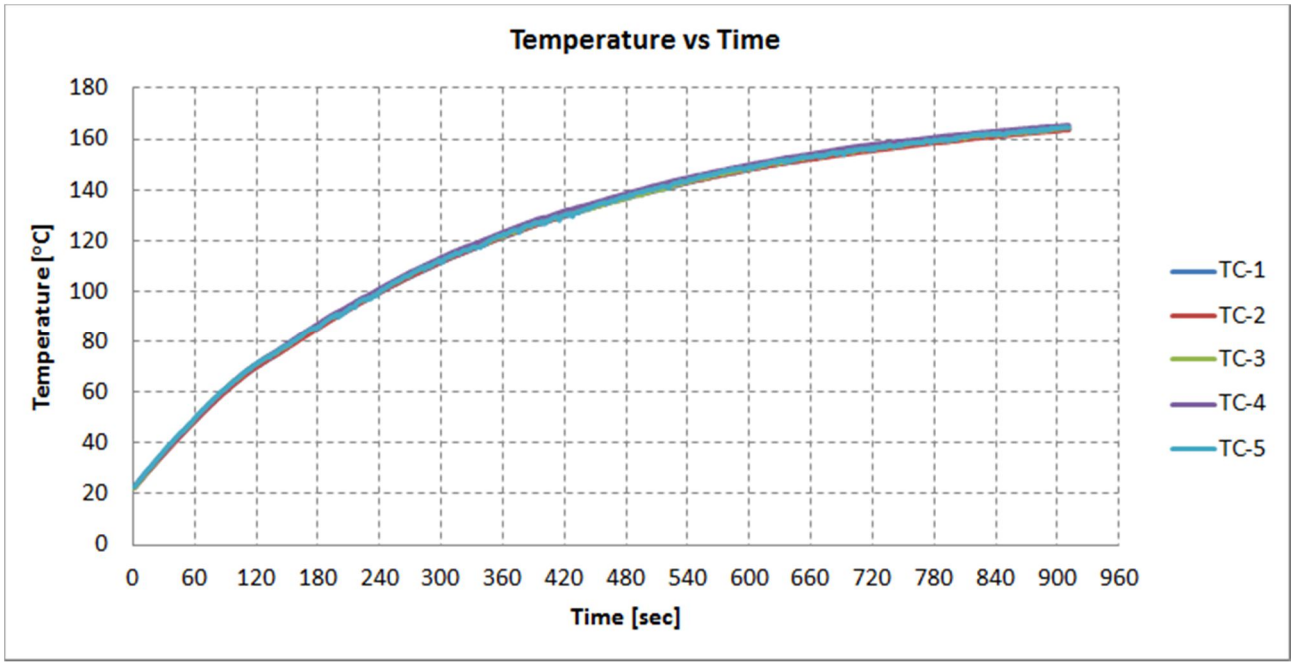

Figure 6: Temperature as a function of time

2.3 Specimen Instrumentation

Apart from the imposed force and the axial displacement of the actuator, a digital image correlation (DIC) system was stationed at the unexposed side of the specimen in order to investigate the out of plane deflection of the specimens during testing. The software used for processing is Aramis from GOM. The system uses two 4 megapixel digital cameras to determine the movement in the specimen by processing the deformation of a black and white speckle pattern which was created using spray paints. The DIC system could not be used on the exposed heated side as the spray speckle pattern required for the DIC measurements, being flammable, could jeopardize the integrity of the measured data and interfere with the conduction of the experiment. Regarding the thermal loading, 5 thermocouples (Omega M8-CAXL-IM050G-1m-50mm-SMPW-M) were placed at different positions along the thickness to measure the temperature distribution during testing using an Agilent 34972A LXI data acquisition system. In detail, one thermocouple was positioned exactly at the specimen surface that was exposed to the heat, the second one at the interface between the skin that was exposed to the surface and the core. The other three thermocouples were located at 10mm 20mm and 30mm away from the aforementioned interface towards the unexposed face. The thermocouples were mounted by drilling holes at the specimen from the unexposed side. The instrumentation is depicted in Figure 7 while the positions of the thermocouples are presented in Figures 8 and 9. The data acquisition frequency for the thermocouples was set equal to 1 Hz.

A camera was recording the test procedure, focused on the exposed side of the specimen to correlate the evolution of damage on the exposed face with the measured out of plane displacement on the back side.

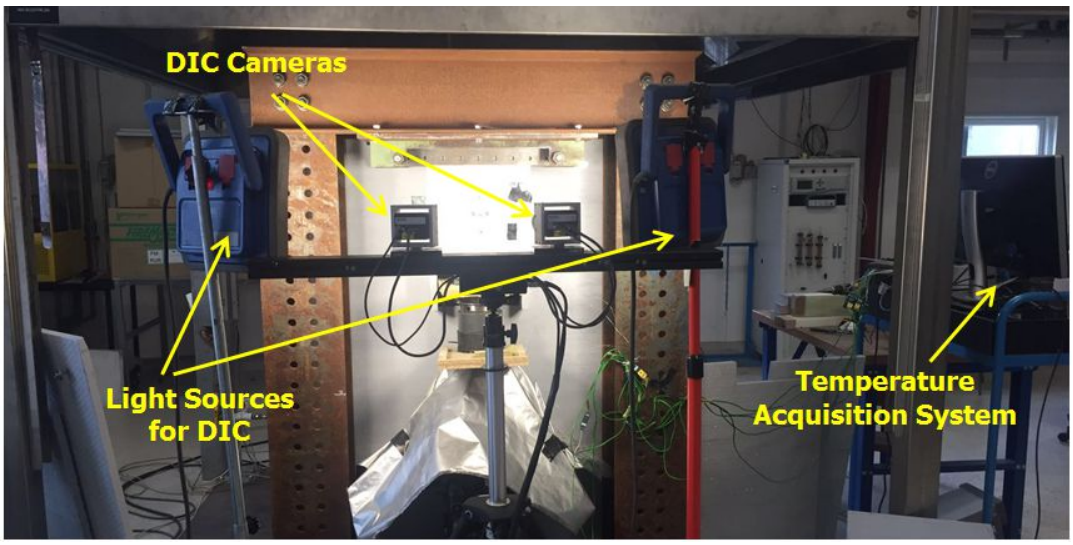

Figure 7: Instrumentation

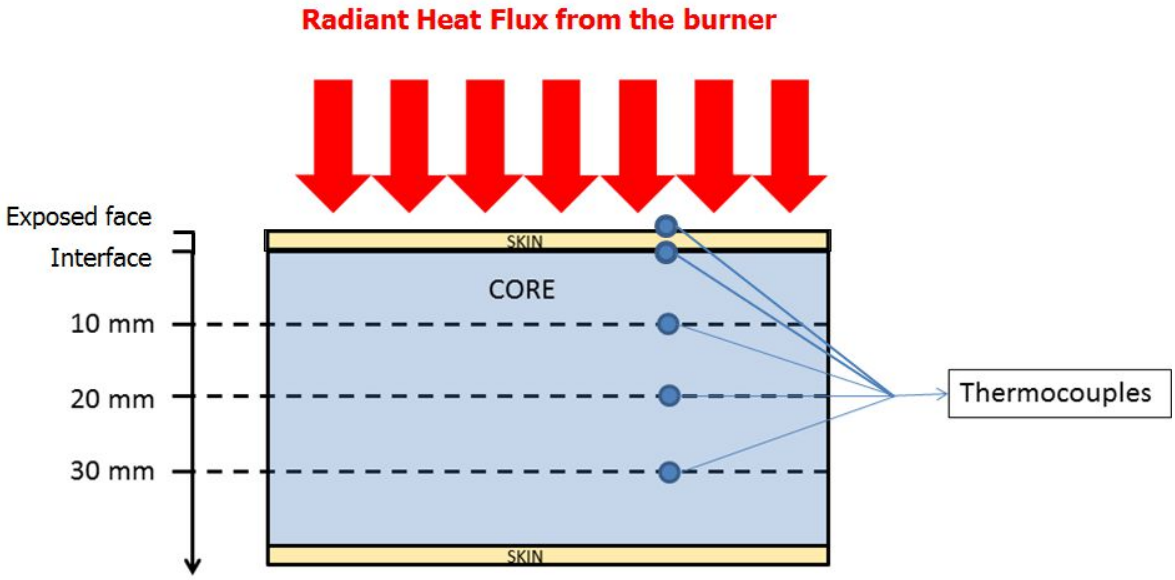

Figure 8: Positioning of thermocouples through the thickness of the specimen

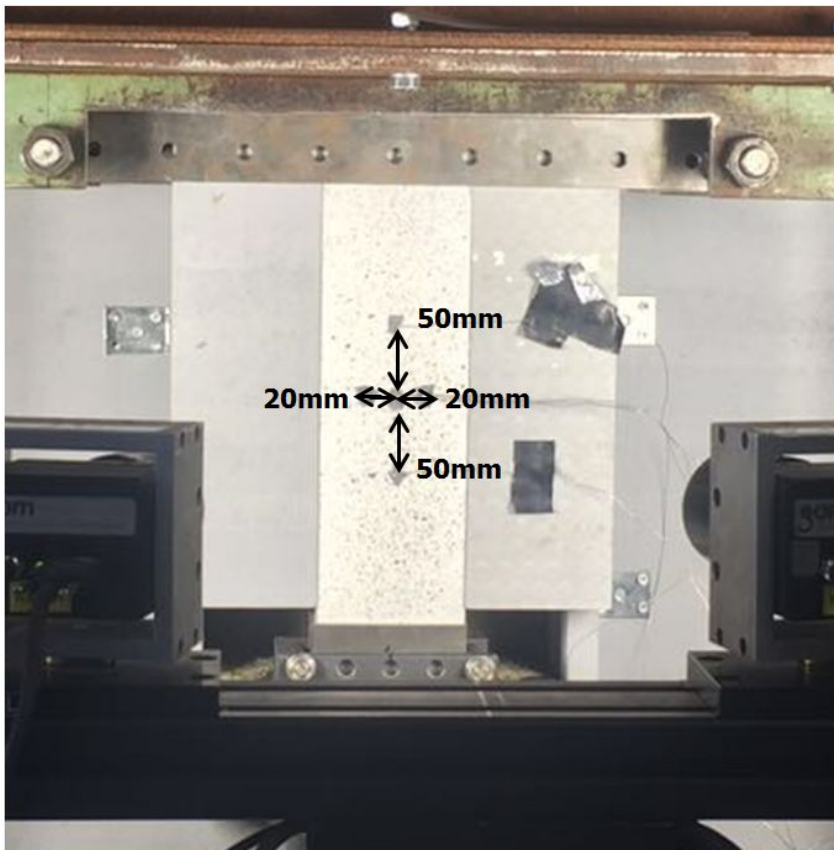

Figure 9: Thermocouples position with respect to the centre of the specimen

2.4 Definition of Test Series

The specimens were tested following different combinations of radiant heat fluxes and applied compressive loading. In most cases the heat flux was kept constant and equal to 3.6 kW/m^2. This heat flux intensity was selected based on preceding analyses which are presented at Annexes F and G. In addition to the constant heat flux tests, one test series in which the heat flux was changed during testing was selected. The heat flux change was chosen so as to simulate the temperature distribution across the specimen thickness as measured by the thermocouples in the model furnace tests at DBI (for more information on the subject are available at Annexes F and G). Prior to defining the magnitude of the compressive loading, specimens were tested until their ultimate failure to measure their load bearing capacity at room temperature. Based on the ultimate load of these specimens the compressive loading of the remaining tests series were defined (Table 1).

The specimens were clamped using two steel plates that act as friction grips at the upper part of the specimen. The length of the specimen that was clamped from each side was 50 mm (equal to the length of the wooden insert). At the bottom part of the specimen once again two double plates were positioned and gripped with the use of two L profile bars. The bottom fixture was positioned to ensure that no damage would initiate from the wooden insert at the bottom. This fixture was resting on a spherical joint and did not constraint the out of plane displacement nor the rotation of the bottom part of the specimen. The spherical joint, being free to rotate prohibited the transmission of bending moments and shear forces to the actuator. The gripping setup is depicted in Figure 10. Bending moments are expected to be developed during these tests as the change in the material properties of the specimens due to the one sided exposure to heat will cause a shift of the neutral axis of the specimen.

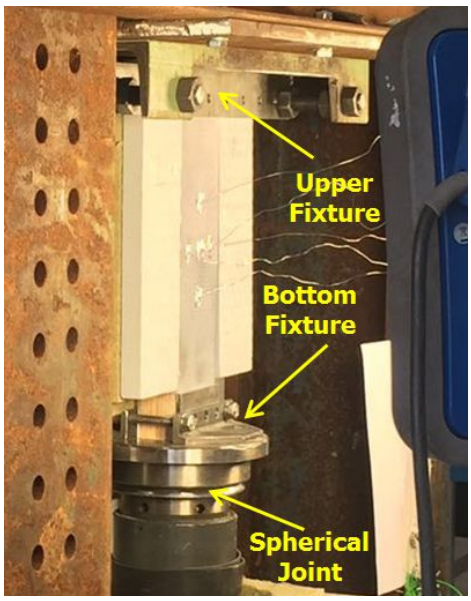

Figure 10: Fixtures

Table 1: Test Series

	Heat Flux	**Mechanical Loading**
Reference experiments	-	Up to ultimate failure (reference)
Constant Heat Flux experiments	3.6 kW/m^2	10 % of the ultimate load of the reference
	3.6 kW/m^2	20 % of the ultimate load of the reference
	3.6 kW/m^2	40 % of the ultimate load of the reference
	3.6 kW/m^2	60 % of the ultimate load of the reference
	3.6 kW/m^2	70 % of the ultimate load of the reference
ISOcurve experiments	a) 1.3 kW/m^2 for 1039 sec followed by: b) 3.6 kW/m^2 for 400 sec	15 % of the ultimate load of the reference

2.5 Testing and Results

2.5.1 Reference Tests

Three specimens were tested at room temperature to measure what is the ultimate load bearing capacity of the specimens. These specimens were tested using displacement control with a rate of 3 mm/min until the ultimate failure. No thermocouples were employed for these tests. The results are concentrated in Table 2 along with the standard deviation and the coefficient of variance. Figure 11 depicts the force displacement curves of the specimens. The initial slightly non linear behaviour that is exhibited up to 5 kN is attributed to the minimization of tolerances between the specimen and the fixtures and the self-alignment of the specimen thanks to the spherical joint.

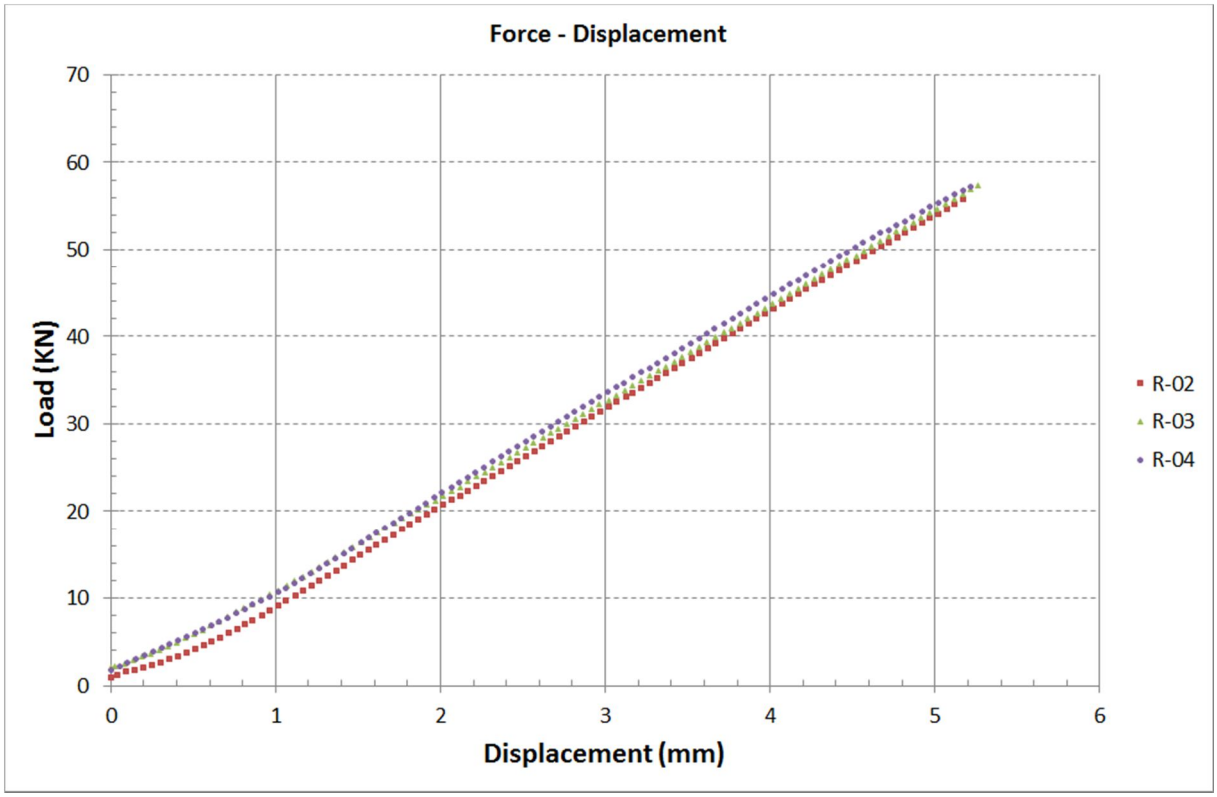

Figure 11: Force – displacement curves of the reference specimens

Table 2: Ultimate load of the reference specimens

Specimen Nomenclature	Ultimate failure load [kN]
R-2	55.756
R-3	57.368
R-4	57.232
AVERAGE	56.79
Standard deviation	0.894
CoV	1.57%

Results indicate excellent repeatability. The average failure load of the reference specimens was 56.79 kN. This load corresponds to a compressive stress of 189.3 MPa which is significantly lower than 323 MPa which is the ultimate compressive stress as measured during the material characterization tests (see Annex E for more details). The difference between the two is attributed to the different type of failure exhibited, as in the material characterization tests the ultimate load referred to the compressive failure of the skin, while the reference specimens of the mid scale tests failed due to what could be described as buckling driven delamination between the sandwich faces and the core. The failure mode is depicted in Figure 12 and was identical for all the reference specimens.

Figure 12: Typical failure mode of the reference specimens

Having measured the failure load of the reference specimens Table 1 can be rewritten as shown in Table 3

Table 3: Test series

	Heat Flux	**Mechanical Loading**
Constant Heat Flux experiments	3.6 kW/m^2	5.68 kN
	3.6 kW/m^2	11.36 kN
	3.6 kW/m^2	22.72 kN
	3.6 kW/m^2	34.07 kN
	3.6 kW/m^2	39.75 kN
ISOcurve experiments	a) 1.3 kW/m^2 for 1039 sec followed by: b) 3.6 kW/m^2 for 400 sec	7.5 kN

2.6 Constant heat Flux experiments

In the case of the constant heat flux tests series, after the positioning of the specimen and the selected instrumentation, testing was performed following the steps below:

a) The specimen was preloaded using displacement control until the reaction force reached about to 2 kN to minimize initial tolerances and check the alignment of the specimen.
b) The specimen was loaded using force control up to the desired force level. Performance of the first set of measurements using the digital image correlation technique.
c) Protection of the exposed surface of the burner by positioning a wide and thick fire insulation panel between the burner and the mechanical loading rig.
d) Proper positioning of the burner at the desired distance and ignition of the burner.
e) Countdown to 10 minutes in order for the heat flux to stabilize.
f) Removal of the insulation panel that was positioned between the burner and the loading rig at step c). Simultaneously the data acquisition from the thermocouples and the digital image correlation setup was initiated.
g) Testing
h) Failure of specimen
i) End of test

A total of 4 specimens were tested for the majority of the defined test series.

2.6.1 Results

2.6.1.1 Time to Failure

Due to the bulk of generated data indicative representative results are presented in this report to describe the response of the specimens. Naturally, the discussion and analysis of results will be performed taking into account the results of all tests. Table 4 presents the required time to failure for each test series when exposed to 3.6 kW/m^2 heat flux. The specimens marked with red (i.e. specimen 5.68-1 and 22.71-4) were not considered for the analysis of the results as, due to errors during the temperature acquisition, data were not recorded. The times-to-failure of these specimens are referenced for reasons of completeness. As expected, the time needed for failure decreases with the increase of the applied mechanical loading. Additionally the repeatability of the results appears to decrease for the experiments with lower mechanical loading.

Table 4: Time to failure for the 3.6 kW/m^2 experiments

	Specimen Nomenclature	Time to Ultimate Failure	Time to Ultimate Failure
		sec	min
5.68 kN Series	5.68-1	2940	49.00
	5.68-2	4219	70.32
	5.68-3	2512	41.87
	5.68-4	3369	56.15
	5.68-5	2539	42.32
	AVERAGE	3159.75	52.66
	Standard deviation	708.76	11.81
	CoV	22.43%	22.43%
	Specimen Nomenclature	Time to Ultimate Failure	Time to Ultimate Failure
		sec	min
11.36 kN Series	11.36-3	184	3.07
	11.36-5	215	3.58
	11.36-6	185	3.08
	AVERAGE	194.67	3.24
	Standard deviation	17.62	0.29
	CoV	9.05%	9.05%
	Specimen Nomenclature	Time to Ultimate Failure	Time to Ultimate Failure
		sec	min
22.71 kN Series	22.71-1	142	2.37
	22.71-2	122	2.03
	22.71-3	142	2.37
	22.71-4	125	2.08
	AVERAGE	135.33	2.26
	Standard deviation	10.75	0.18
	CoV	7.94%	7.94%
	Specimen Nomenclature	Time to Ultimate Failure	Time to Ultimate Failure
		sec	min
34.07 kN Series	34.07-1	99	1.65
	34.07-2	107	1.78
	34.07-3	100	1.67
	34.07-4	93	1.55
	AVERAGE	99.75	1.66
	Standard deviation	5.74	0.10
	CoV	5.75%	5.75%
	Specimen Nomenclature	Time to Ultimate Failure	Time to Ultimate Failure
		sec	min
39.75 kN Series	39.75-1	93	1.55
	39.75-2	92	1.53
	39.75-3	93	1.55
	39.75-4	94	1.57
	AVERAGE	93.00	1.55
	Standard deviation	0.82	0.01
	CoV	0.88%	0.88%

2.6.1.2 Force displacement curves

The force – time and force – displacement curves of specimen 39.75-3 are presented in Figures 13 and 14 respectively. The force – time curve depicts the gradual ramping of the load up to the desired load of 39.75 kN. Subsequently, the load is held steady (load control) during experimental testing until the failure of the specimen. The force displacement curve is initially non-linear up to almost 5 kN for the same reasons mentioned for the reference specimens. The specimen's response then is linear until the target load of 39.75 kN is reached. Once the specimen is exposed to the heat source it expands leading to the slight reduction of the displacement from 3.48 mm to 3.46 mm until the point where the material properties have degraded making the specimen more compliant and therefore leading to the increase of displacement until the point of ultimate failure.

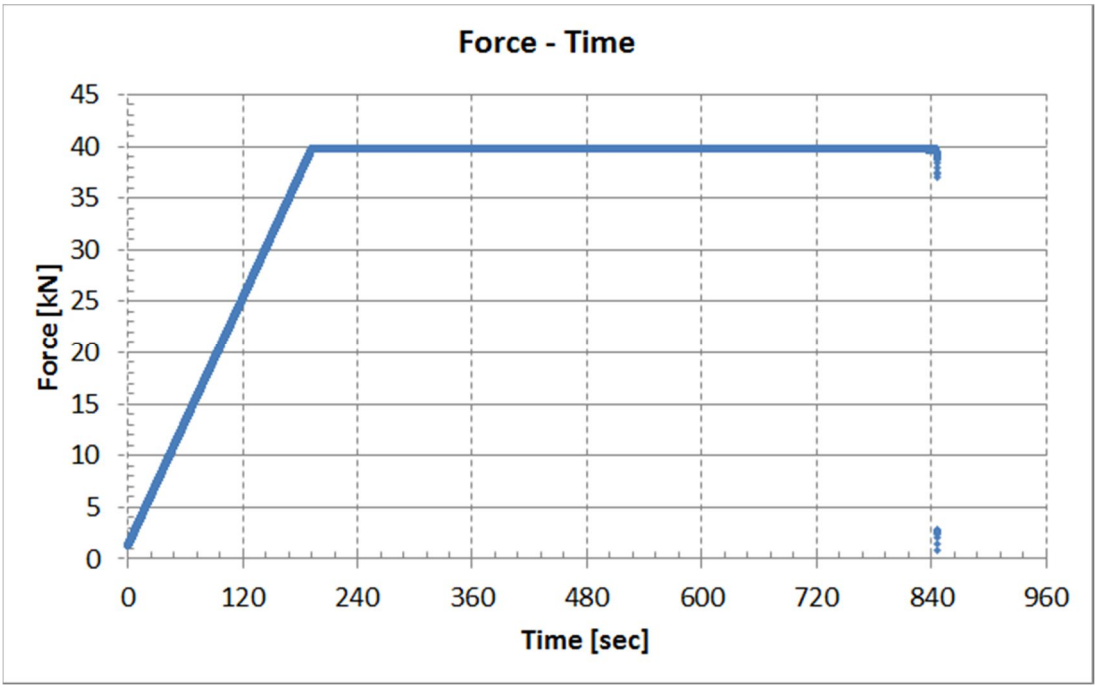

Figure 13: Force – Time curve

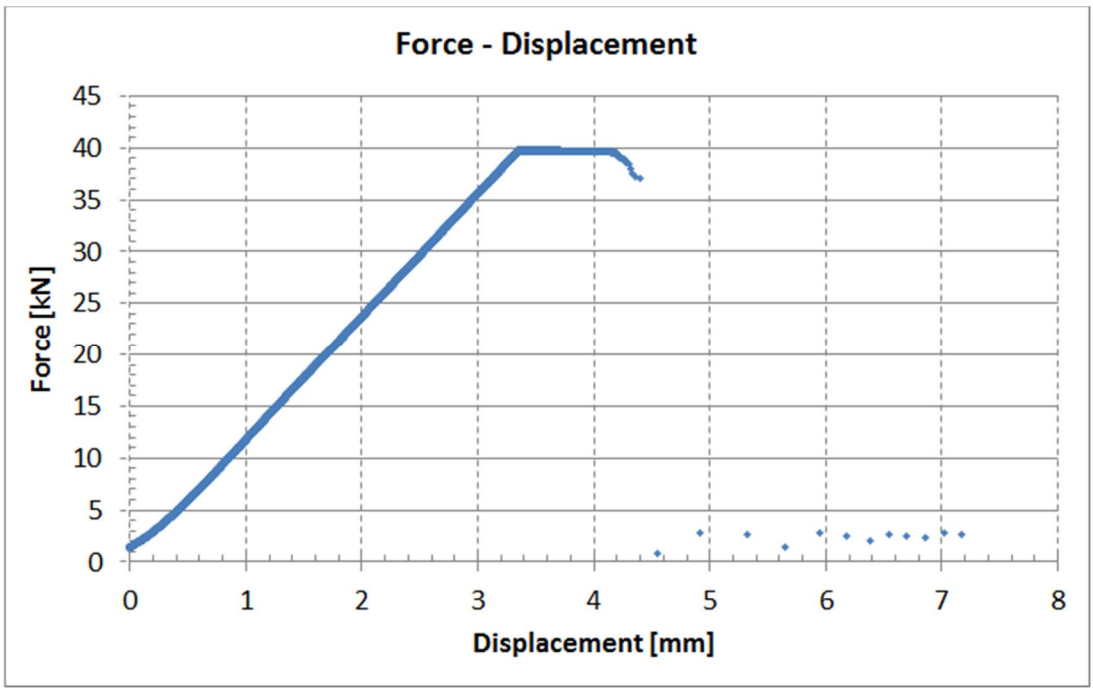

Figure 14: Force – Displacement curve

Concerning the failure mode, all specimens failed in a similar manner regardless the magnitude of the applied mechanical loading. The failure pattern was similar to the one noted for the reference specimens, i.e. debonding between the exposed skin and the core of the sandwich. Indicative images of specimens after failure are depicted in figures 15 to 19.

Figure 15: Representative failure of the specimens tested at 39.75 kN and 3.6 kW/m^2

Figure 16: Representative failure of the specimens tested at 34.07 kN and 3.6 kW/m^2

Figure 17: Representative failure of the specimens tested at 22.71 kN and 3.6 kW/m^2

Figure 18: Representative failure of the specimens tested at 11.36 kN and 3.6 kW/m^2

Figure 19: Representative failure of the specimens tested at 5.68 kN and 3.6 kW

Observing the failed specimens the following remarks can be made. Firstly, unlike the reference specimens, due to the application of thermal loading, localized debonding between the plies of the laminate preceded the skin-core debonding. This local failure is located close to the tab area and is more pronounced in specimens that underwent longer exposure to heat. The location of the localized failure is associated to the bending of the specimen due to the non-symmetrical heating in combination with the applied mechanical loading. As the temperature increases at the exposed side the neutral axis of the specimen is shifted from the middle of the specimen towards the unexposed side. This gives rise to secondary bending, deflecting the area of the specimen between the tabs away from the burner consequently reducing the magnitude of the impacting heat flux at that area. This phenomenon is more visible at the 5.68 kN specimens (Figure 19) as they were exposed to the heat for a substantially longer time compared to the rest of the specimens. The darkened resin indicates higher developed temperatures.

2.6.1.3 DIC Measurements

Once again due to the bulk of the generated results representative measurements will be listed in this section. The results obtained during testing of specimen 5.68-2 are described as the 5.68 kN specimens were exposed for longer times to the heat source and demonstrate more clearly the evolution of damage. Figure 20 correlates the back face of the specimen to the generated facets using the Aramis software. The gaps in the facets figure area around the centre of the specimens are caused due to the application of tape to firmly hold the thermocouples in place during testing. The tape covered the speckle pattern and therefore there are no data available at these regions.

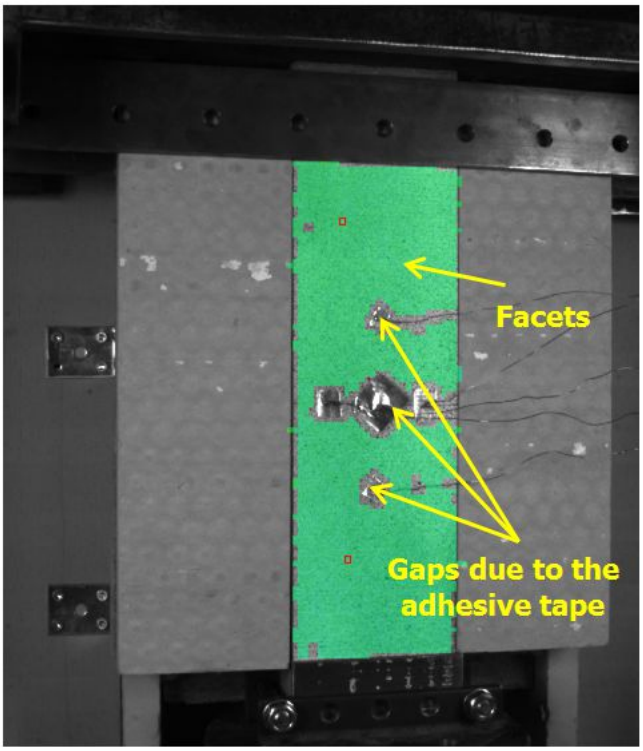

Figure 20: DIC facets

The out of plane deflection of the specimen at four selected locations are depicted in Figure 21. The locations are lying in the longitudinal axis of symmetry and are symmetric with respect to the transverse axis of symmetry. In Figure 21 the out of plane deflections (Y axis) are positive when facing away from the exposed side, the X axis presents the stages which in other words are the picture number taken by the DIC cameras.

The stage frequency was varied between tests series in order to obtain a reasonable amount of data for processing. At the 5.68 kN series the DIC cameras captures a picture every 30 sec. The specimen is exposed to the burner at stage 27 (Figure 21). Stages 0 to 27 correspond to the increase of the mechanical loading until the target value of 5.68 kN was reached and present little interest. The stages needed for the stabilization of the heat flux have been filtered out to make the presentation of results more tangible.

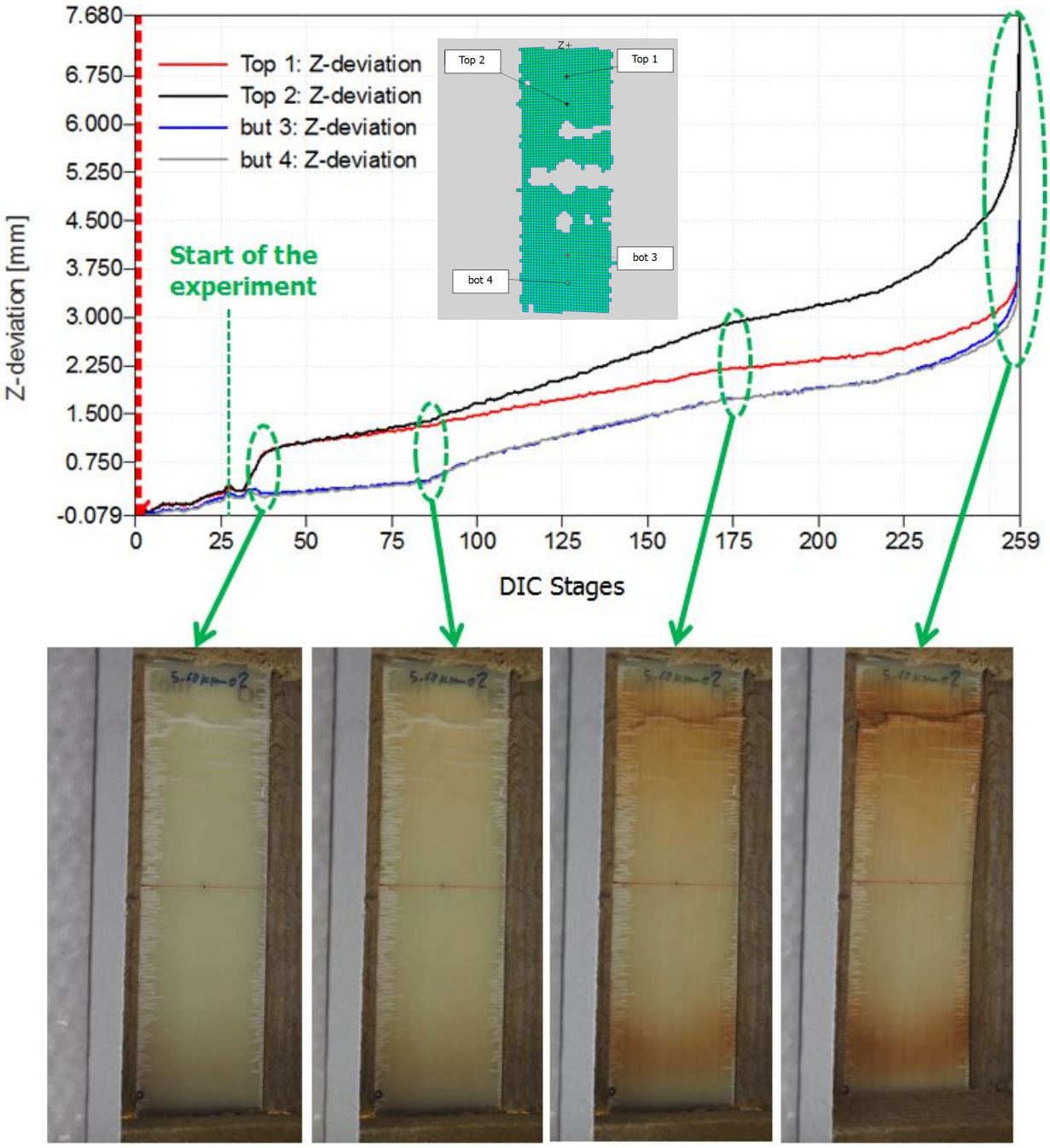

Figure 21: Out of plane deflection of specimen 5.68-2

Figure 21 allows for some very interesting observations. At the first stages after the test was initiated (i.e. after stage 27) a decrease of the out of plane deflection is noted. This is caused by the thermal expansion of the exposed skin which causes the specimen to bend towards the burner. Subsequently as the temperature continues to rise the deflection starts to increase again due to the bending caused by the softening of the skin. However this increase is not uniform to the top and the bottom points. This can be explained when the pictures from the exposed face are taken into consideration. As the photos indicate, local failure has initiated at the top of the exposed face which locally increases the bending compliance of the specimen. Subsequently, as time progresses, the material properties at the bottom part of the specimen at the exposed side start degrading as well which is indicated by the slight discoloration at that area. The damage continues to evolve at the specimen which increases the out of plane deflection until the point that the specimen loses its load bearing capacity and fails.

2.6.1.4 Temperature measurements

Figures 22 to 26 present representative graphs of the recorded temperature as a function of time. The starting point for the time is the exposure of the specimen to the heat source.

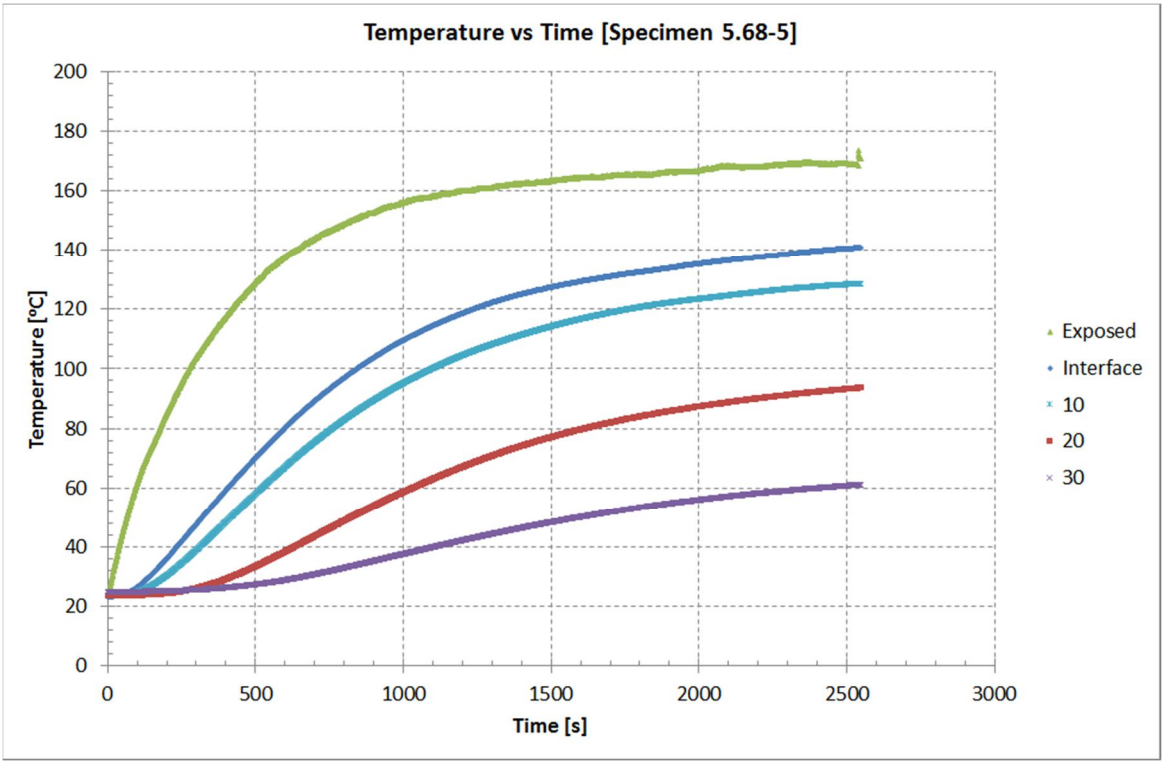

Figure 22: Temperature measurements for Specimen 5.68-5

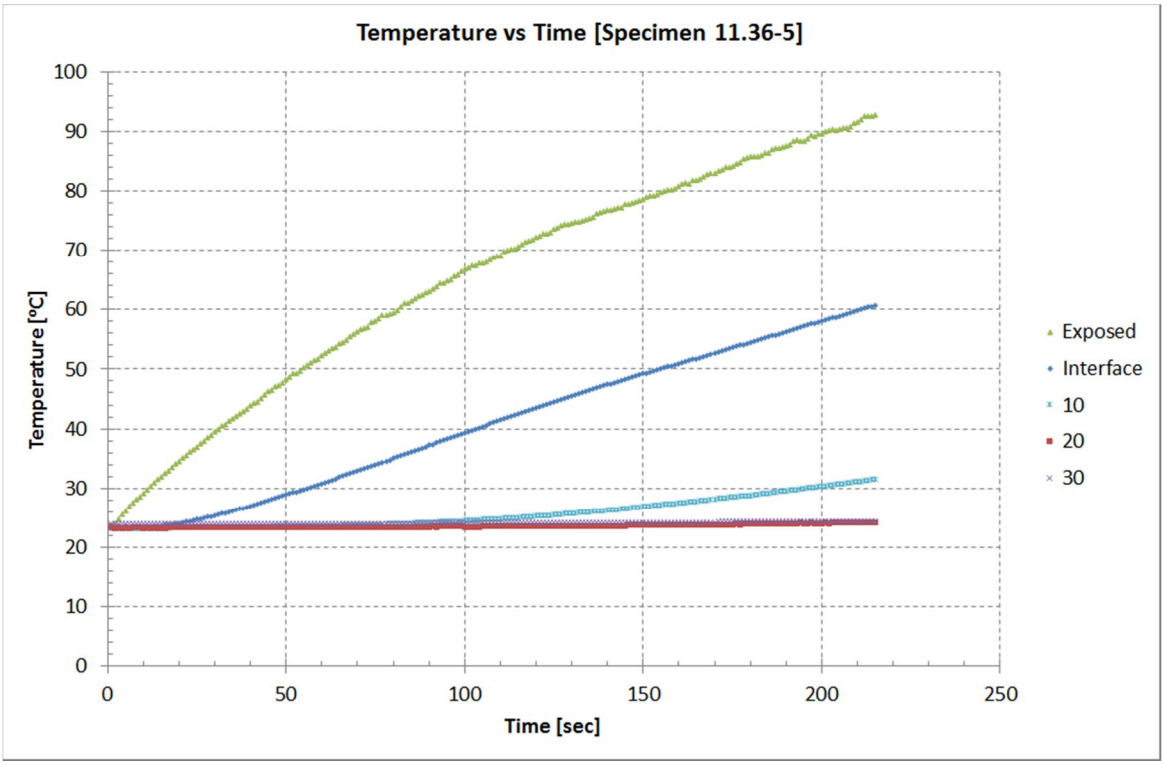

Figure 23: Temperature measurements for Specimen 11.36-5

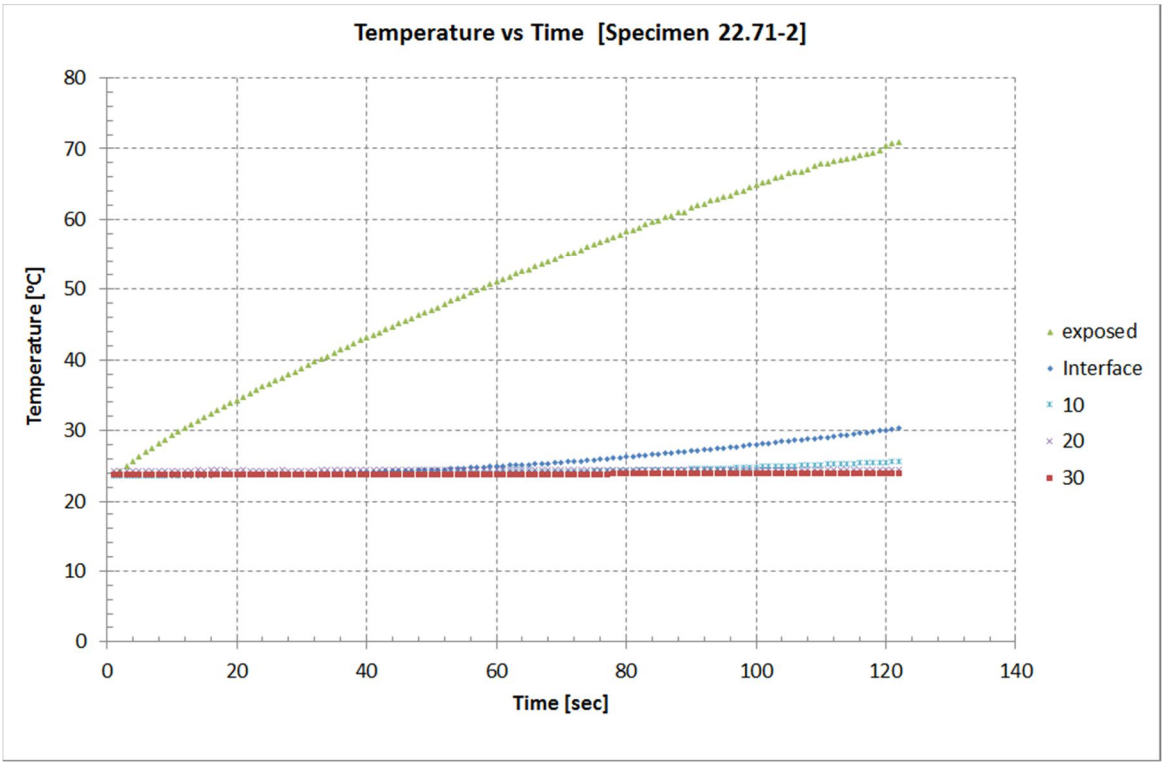

Figure 24: Temperature measurements for Specimen 22.71-2

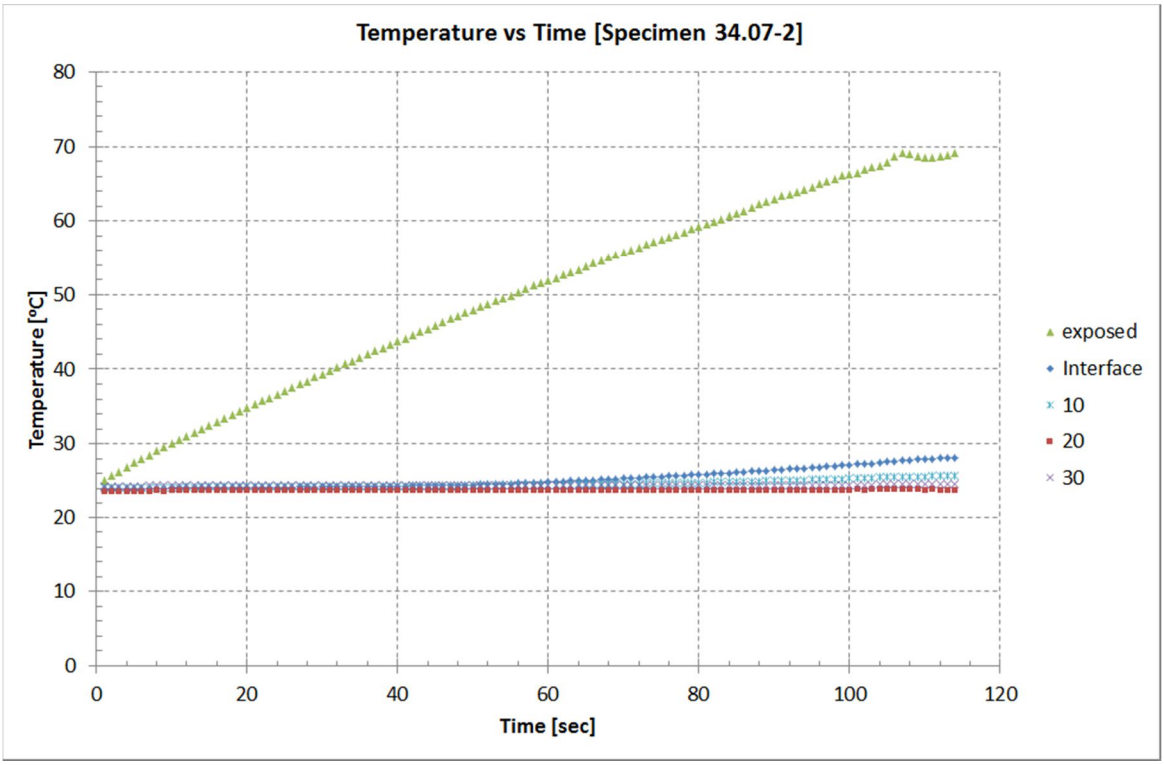

Figure 25: Temperature measurements for Specimen 34.07-2

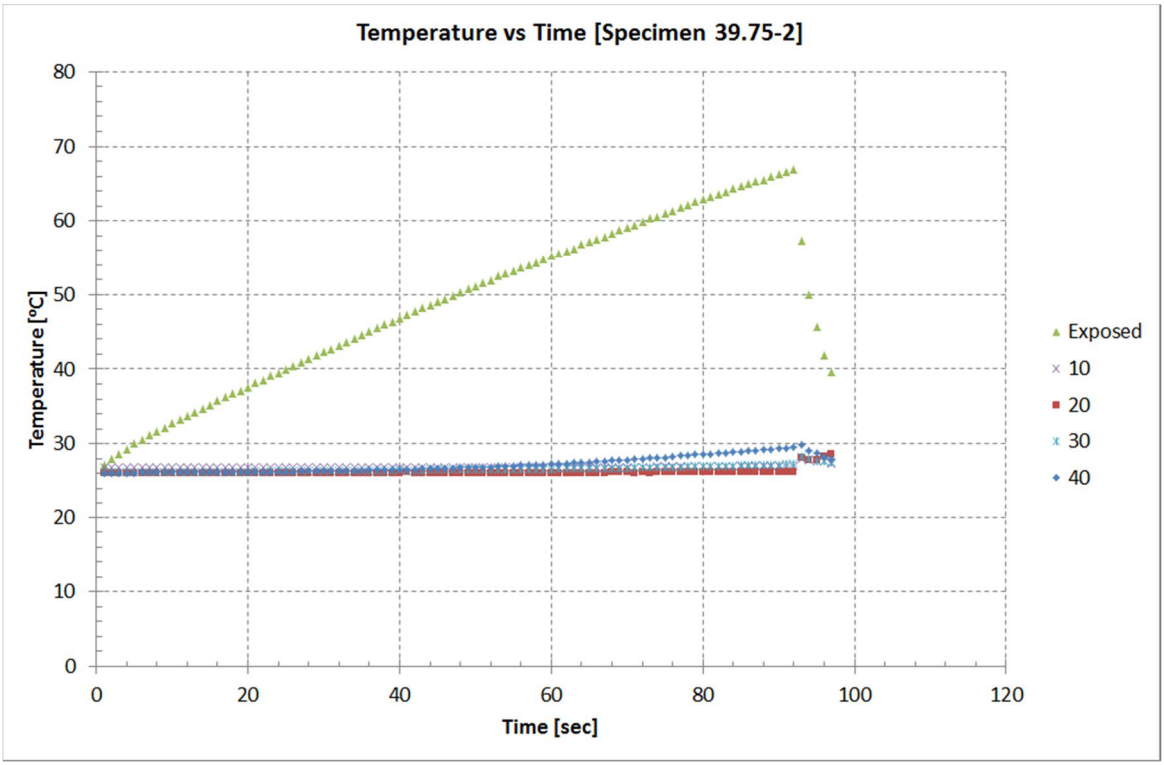

Figure 26: Temperature measurements for Specimen 39.75-2

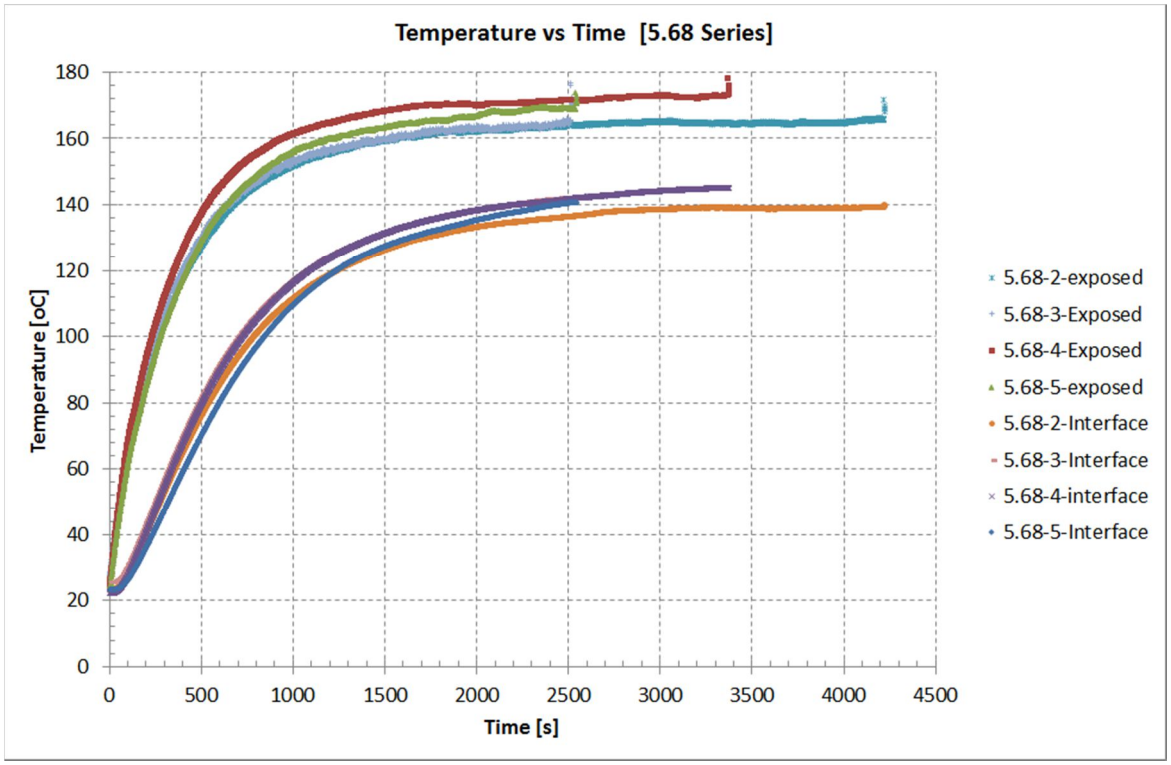

Figure 27: Temperature measurements at the exposed side and at the interface for the 5.68 series

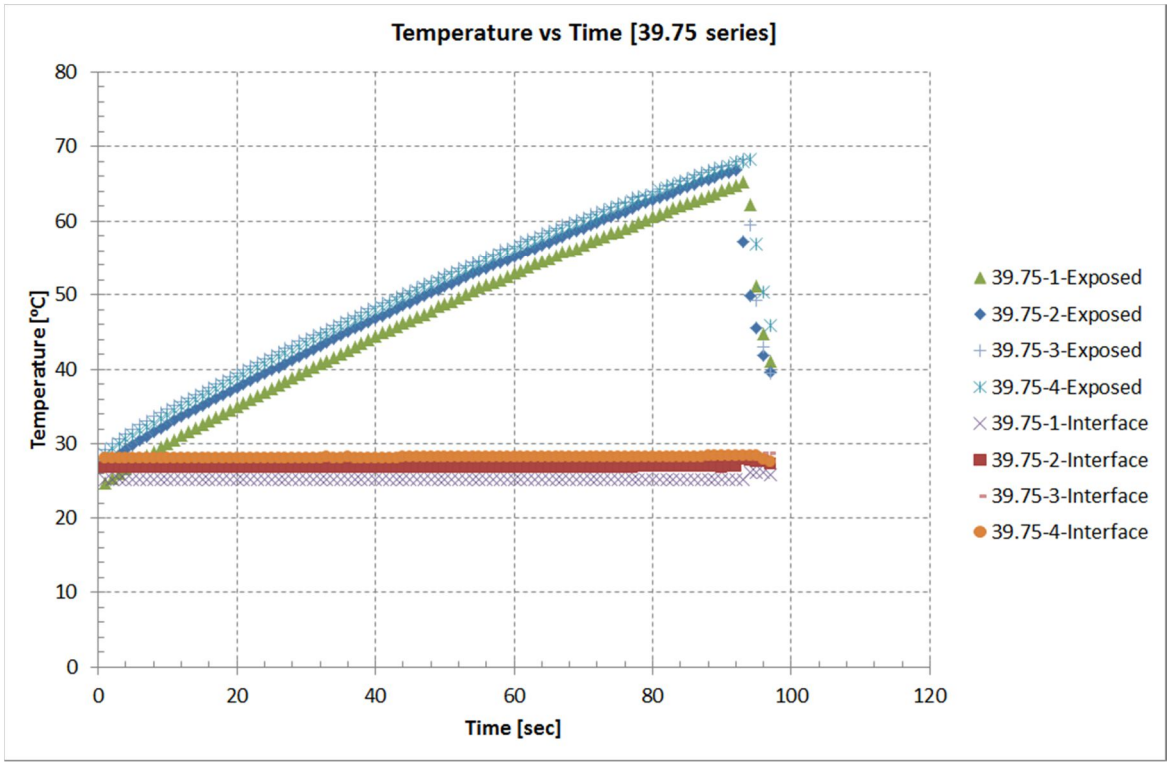

Figure 28: Temperature measurements at the exposed side and at the interface for the 39.75 series

As anticipated the temperature is higher at the positions of the thermocouples closer to the burner. In all test series, with the exception of the 5.68 kN specimens, the thermocouples located 20 mm and 30 mm away from the interface did not record any rise in temperature. Likewise for the same test series the thermocouple positioned 10mm away from the interface recorded a very small rise in temperature below the order of 7°C. In all the test series, save for the 5.68 kN, the temperature at the exposed face rises in a rather linear fashion commencing with the start of the test. The temperature at the interface rises in a linear fashion as well but with a delay of about 60 seconds in most specimens as heat is being conducted from the exposed side to the interface.

The results of the 5.68 kN provide more insight on the temperature distribution through the thickness of the specimen. Up until about 200 sec the behaviour of the curves is identical to the ones of the other series, with the temperatures rising along with the testing time. However, gradually, the rate of temperature increase starts changing eventually reaching a plateau for most thermocouples.

Indicative graphs comparing the measurements at the exposed side and the interface between the specimens for two test series are depicted in Figures 27 and 28. The curves indicate satisfactory repeatability. Combining the observed failure mode with the results of the thermocouples, it is obvious that the temperatures at the exposed face and at the interface greatly affect the load bearing capacity of the specimen. This argument is further consolidated by expanding Table 4 to additionally account for the temperature at these locations at the time of failure of each specimen. The results are listed in Table 5. The temperature measurements reveal excellent repeatability between the results with a standard deviation below 5 °C for all test series.

To investigate what is the dependency between the applied mechanical load and the developed temperature, the force versus temperature at the exposed side and the force versus temperature at the interface were plotted (Figures 29 and 30 respectively). As far as the load bearing capacity as a function of the temperature at the exposed surface is concerned, the degradation seems to follow the same *tanh* trend as the one observed at the material characterization tests (Annex E, [1]). However, due to the lack of data for the temperature range from 25°C to 65°C this is only a speculation and additional testing is required. Expressing the load bearing capacity as a function of the temperature at the interface between the skin and the core data a clear power law relation between the two emerges. In particular the power law curve presented in Figure 31 yields a good fit between the data points.

Table 5: Concentrative results for the 3.6 kW/m^2 experiments

	Specimen Nomenclature	Time to Ultimate Failure	Time to Ultimate Failure	Temperature @ Exposed	Temperature @ Interface
		sec	min	°C	°C
5.68 kN Series	5.68-1	2940	49.00	-	-
	5.68-2	4219	70.32	165.98	139.24
	5.68-3	2512	41.87	165.18	142.29
	5.68-4	3369	56.15	173.15	145.18
	5.68-5	2539	42.32	168.62	140.77
	AVERAGE	3159.75	52.66	168.23	141.87
	Standard deviation	708.76	11.81	3.59	2.53
	CoV	22.43%	22.43%	2.13%	1.78%
	Specimen Nomenclature	Time to Ultimate Failure	Time to Ultimate Failure	Temperature @ Exposed	Temperature @ Interface
		sec	min	°C	°C
11.36 kN Series	11.36-3	184	3.07	89.95	61.24
	11.36-5	215	3.58	92.75	60.70
	11.36-6	185	3.08	90.83	57.07
	AVERAGE	194.67	3.24	91.18	59.67
	Standard deviation	17.62	0.29	1.43	2.27
	CoV	9.05%	9.05%	1.57%	3.80%
	Specimen Nomenclature	Time to Ultimate Failure	Time to Ultimate Failure	Temperature @ Exposed	Temperature @ Interface
		sec	min	°C	°C
22.71 kN Series	22.71-1	142	2.37	73.19	38.68
	22.71-2	122	2.03	70.88	30.31
	22.71-3	142	2.37	72.59	33.18
	22.712-4	125	2.08	N/A	N/A
	AVERAGE	135.33	2.26	72.22	34.05
	Standard deviation	10.75	0.18	1.20	4.25
	CoV	7.94%	7.94%	1.66%	12.50%
	Specimen Nomenclature	Time to Ultimate Failure	Time to Ultimate Failure	Temperature @ Exposed	Temperature @ Interface
		sec	min	°C	°C
34.07 kN Series	34.07-1	99	1.65	61.86	25.22
	34.07-2	107	1.78	69.12	27.73
	34.07-3	100	1.67	67.97	29.17
	34.07-4	93	1.55	60.98	26.70
	AVERAGE	99.75	1.66	64.98	27.20
	Standard deviation	5.74	0.10	4.16	1.67
	CoV	5.75%	5.75%	6.40%	6.12%
	Specimen Nomenclature	Time to Ultimate Failure	Time to Ultimate Failure	Temperature @ Exposed	Temperature @ Interface
		sec	min	°C	°C
39.75 kN Series	39.75-1	93	1.55	65.26	27.19
	39.75-2	92	1.53	66.87	29.51
	39.75-3	93	1.55	68.31	31.05
	39.75-4	94	1.57	68.27	31.09
	AVERAGE	93.00	1.55	67.18	29.71
	Standard deviation	0.82	0.01	1.44	1.83
	CoV	0.88%	0.88%	2.15%	6.17%

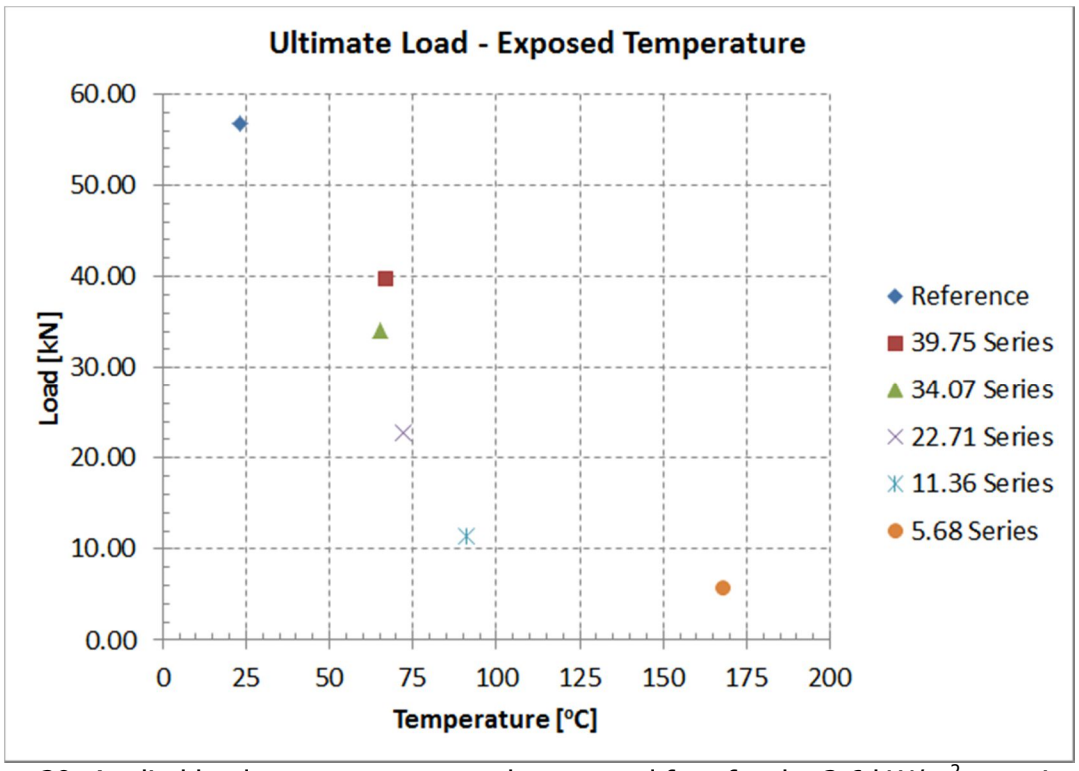

Figure 29: Applied load vs temperature at the exposed face for the 3.6 kW/m^2 experiments

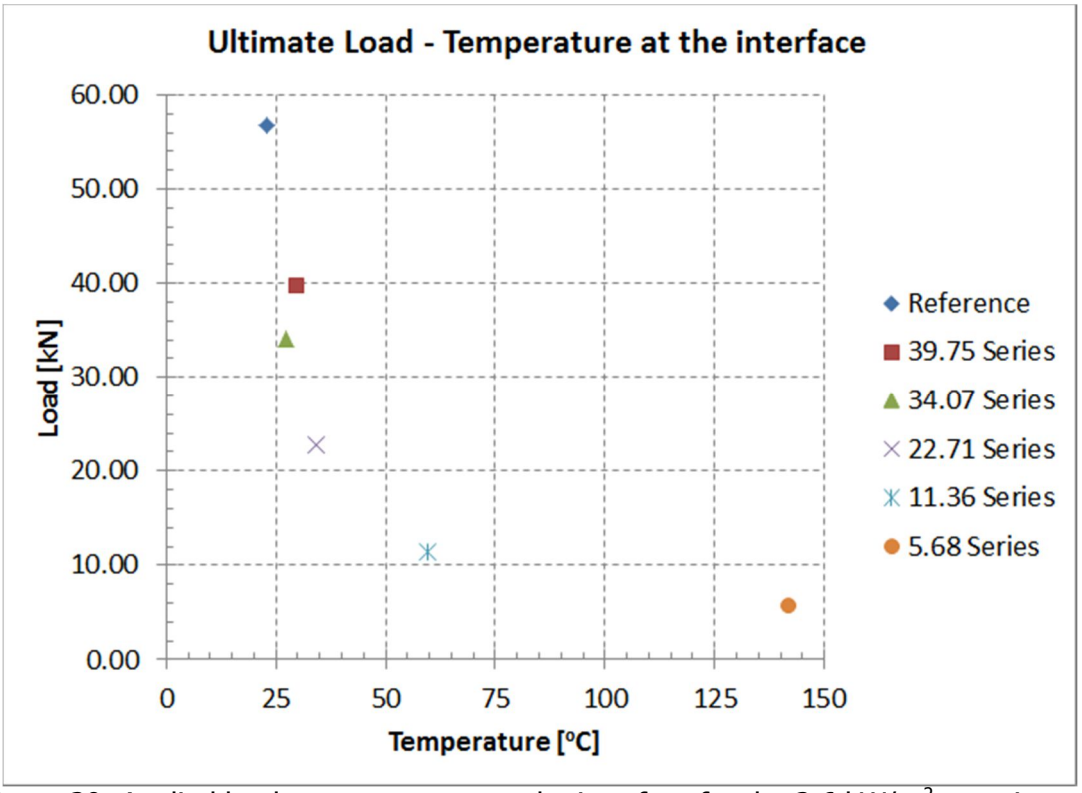

Figure 30: Applied load vs temperature at the interface for the 3.6 kW/m^2 experiments

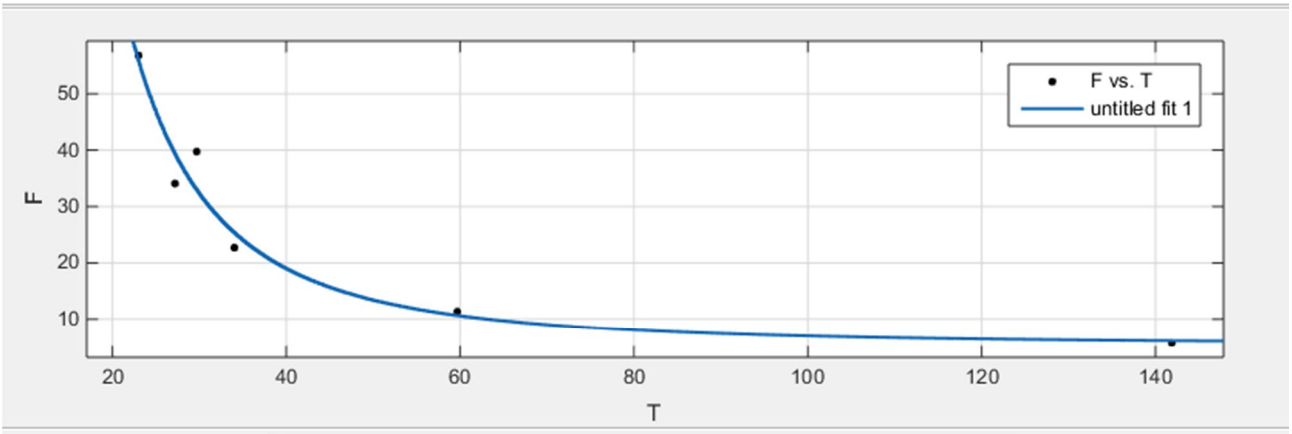

Results

General model Power2:
f(x) = a*x^b+c
Coefficients (with 95% confidence bounds):
a = 8.456e+04 (-5.424e+05, 7.115e+05)
b = -2.367 (-4.748, 0.01435)
c = 5.371 (-11.35, 22.09)

Goodness of fit:
SSE: 82.5
R-square: 0.9543
Adjusted R-square: 0.9239
RMSE: 5.244

Figure 31: Power law fitting curve for the applied load vs temperature at the exposed face

2.7 Iso Curve Experiments

In this test series the impacting heat flux was varied during testing in order to reproduce the same temperature distribution through the thickness of the specimens as the one measured during the ISO834 model furnace experiments (refer to Annex F and Annex G for more information). By employing numerical tools the following heat flux scenario was identified to yield the same temperature distribution (Table 6). The testing time of the proposed steps sums up to about 1440 sec. This time is significantly less than the 3600 sec which correspond to the duration of the furnace ISO curve tests presented in the corresponding Annex. In order for the results of the different approaches to be directly comparable the idle time of 1560 time should be added before the two steps presented in Table 6. This time is referred to as idle, given that during the first 1560 sec of testing in the model furnace no temperature increase is noted in the positions inside the core due to the existence of fire insulation in these tests.

Table 6: Heat flux equivalent

	Heat Flux
ISOcurve experiments	a) 1.3 kW/m^2 for 1039 sec followed by: b) 3.6 kW/m^2 for 400 sec

2.7.1 Results

The force displacement and force time curves do not differ from the ones explained for the constant heat flux series and therefore do not present any additional interest for them to be presented. The time to failure and the recorded temperature on the exposed surface and at the interface are presented in Table 7. Unlike the constant heat flux experiments presented earlier the repeatability of the temperature at failure is not good with the coefficient of variance being as high as 35% at the interface. The temperature distribution as a function of time is however identical (Figure 32) which signifies that there were no deviations on the impacting heat flux between these experiments. The applied loading was the same and equal to 7.5 kN and kept steady during testing for each test. Moreover the specimens were produced from the same batch as the constant heat flux specimens which exhibited excellent repeatability therefore any deviations at the specimen quality seem unlikely. Inspection of the DIC measurements at the stage where the constant load of 7.5 kN was reached revealed no substantial differences between the out of plane deflections which could serve as an indication of improper positioning of the specimens at the fixtures.

These observation show that further testing is necessary. Unfortunately, as there were no remaining specimens, additional experiments could not be performed to find out the reasons for this significant deviation.

To verify that the imposed heat flux scenario can reproduce the desired temperature distribution at the specimen, the temperature measurements at the thermocouples inside the core from the Heat flux approach (Figure 33) were compared to the ones obtained from the mass cone calorimeter the model furnace tests and the numerical code (Figure 34) (refer to Annexes F and G for more information about the latter three). The 1560 seconds have also been taken into account and the temperature expressed in Kelvin in Figure 33 to facilitate the comparison between the curves.

Results exhibit the same trend albeit for a parallel shift between the measurements of the two methods. The difference between the Isocurve specimens and the Heat flux approach is about 10 degrees with the results of the heat flux approach being higher than the ones obtained with the cone calorimeter and the small furnace tests. This is due to the fact that the latter experiments were conducted during winter while the former during summer hence the ambient condition was different leading to this shift.

The results from the non-constant heat flux series have been encompassed in the load bearing capacity vs temperature graphs (Figures 35 and 36) which were originally produced for the constant heat flux experiments. The standard deviation has also been plotted in the form of error bars. The large scatter does not allow for a safe interpretation of the results and further investigation is needed before any conclusions can be drawn as to whether these tests follow the same trend as the constant heat flux ones.

Table 7: Concentrative results for the ISOcurve experiments

	Experiments with varying heat flux				
	Specimen Nomenclature	Time to Ultimate Failure sec	Time to Ultimate Failure min	Temperature @ Exposed °C	Temperature @ Interface °C
7.5 kN Isocurve	ISO-1	2078	34.63	162.37	123.34
	ISO-2	1117	18.62	99.21	62.88
	ISO-3	1391	23.18	133.90	80.04
	AVERAGE	1528.67	25.48	131.82	88.75
	Standard deviation	495.07	8.25	31.63	31.16
	CoV	32.39%	32.39%	24.00%	35.10%

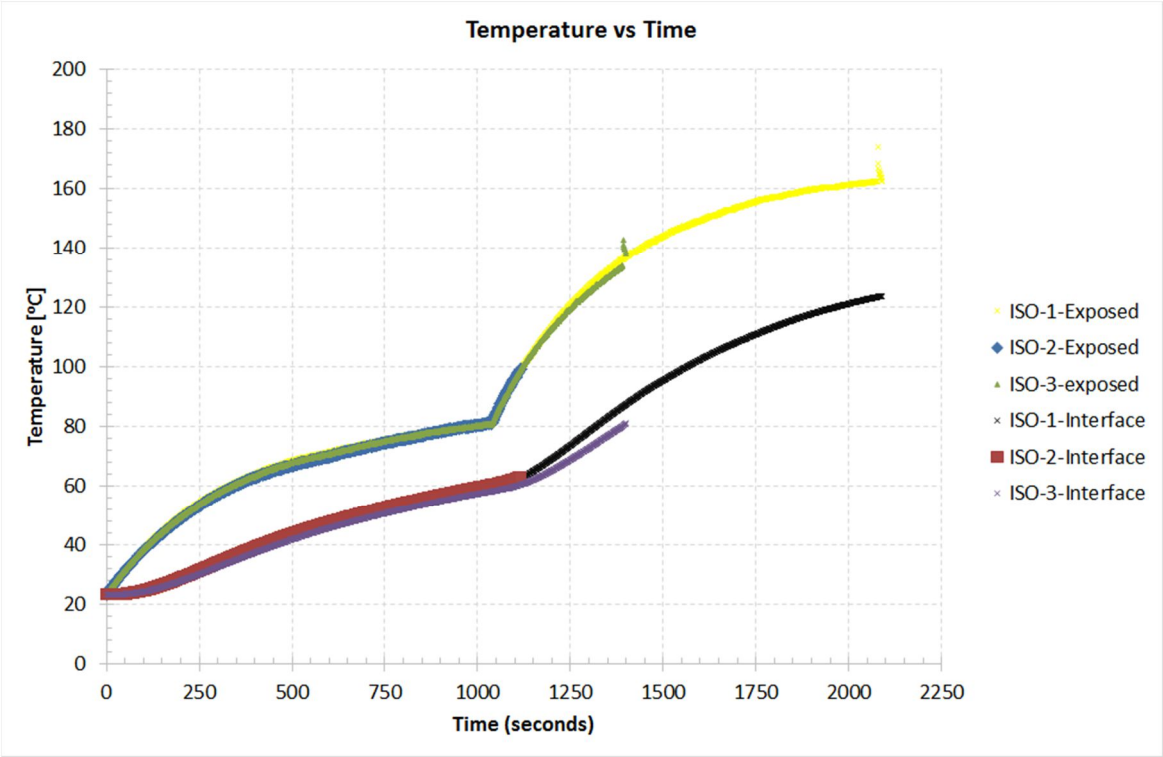

Figure 32: Temperature distribution at the exposed face and the interface for the ISOcurve series

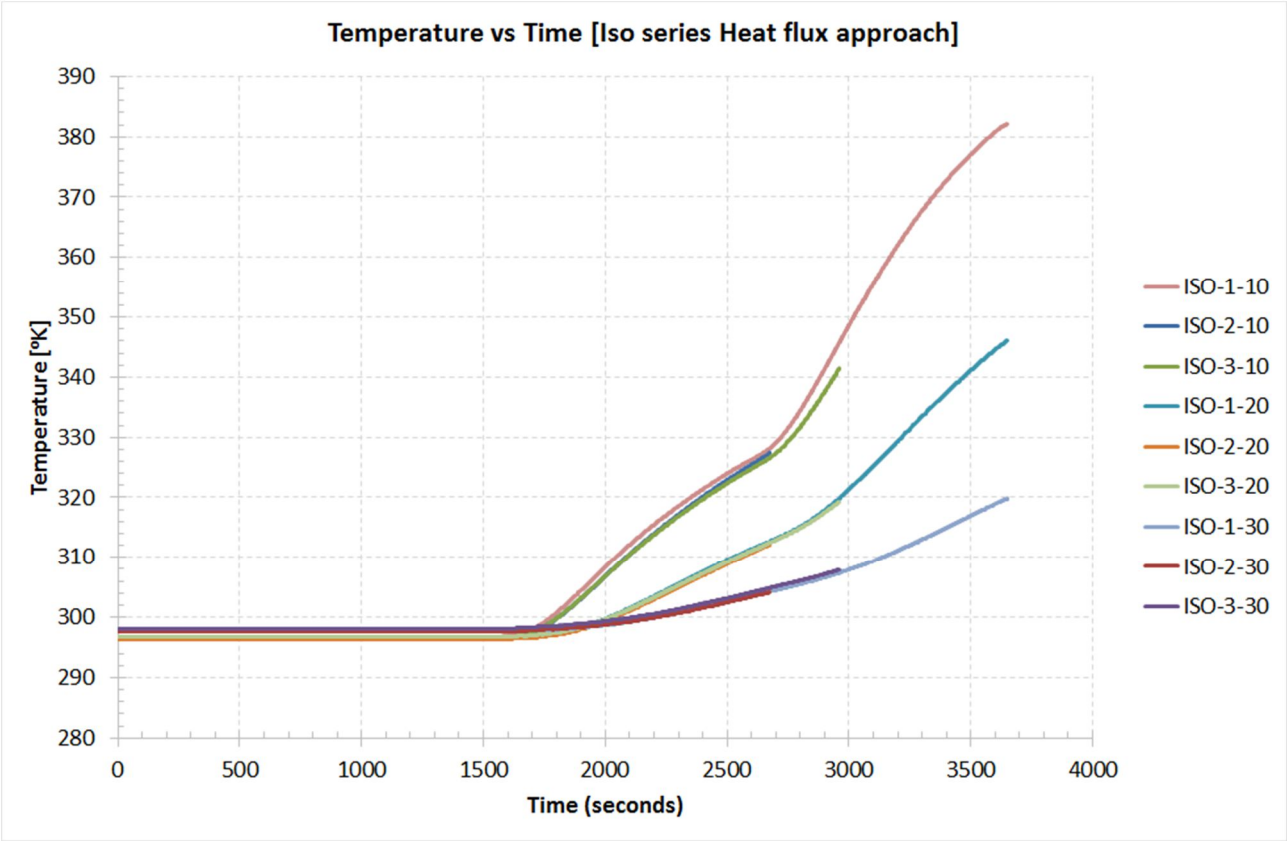

Figure 33:Temperature versus time inside the core for the Isocurve series test using the heat flux equivalent

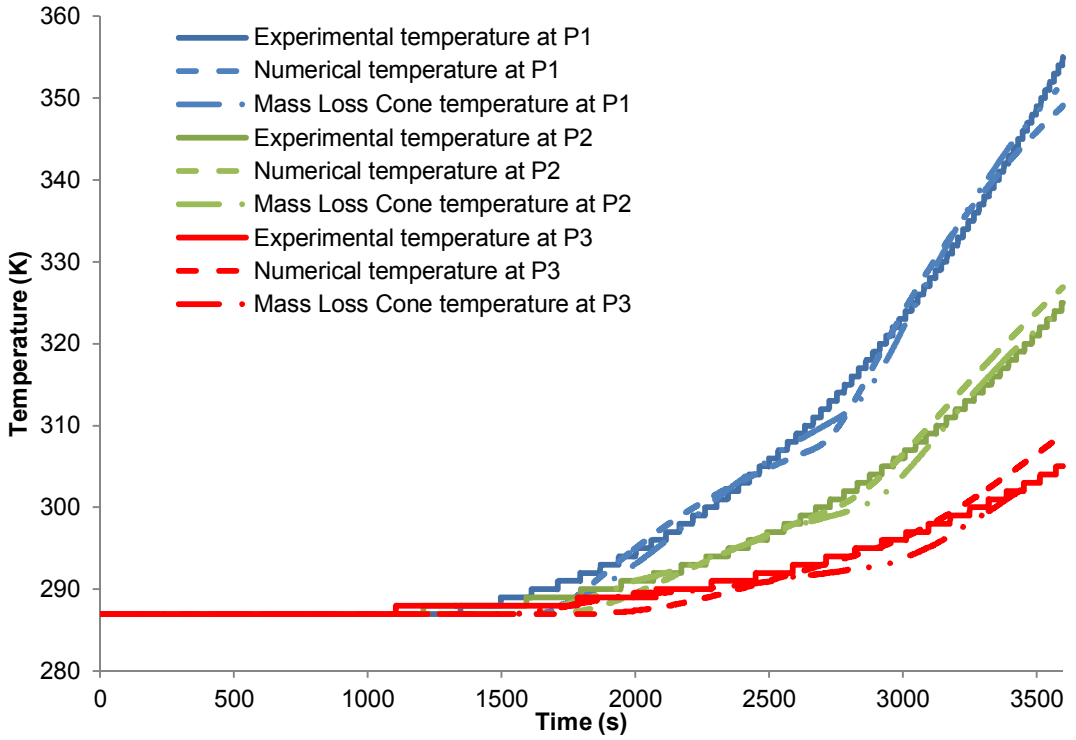

Figure 34: Obtained results inside the core from the mass loss cone calorimeter, model furnace tests and numerical simulations

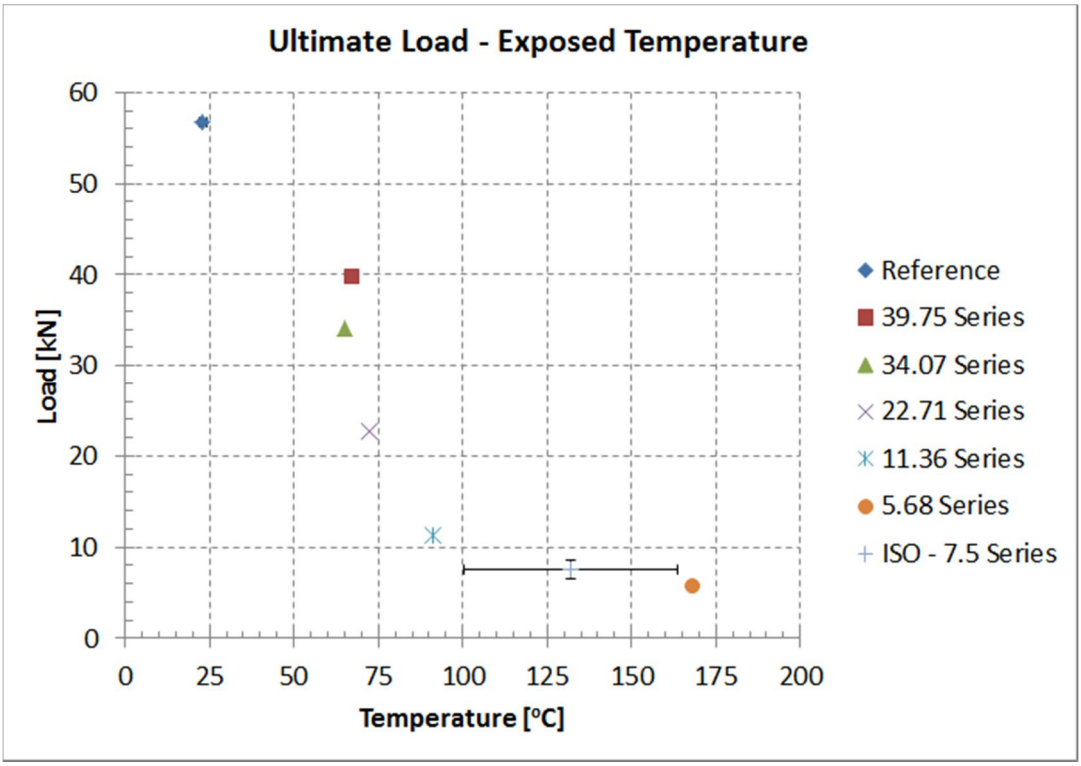

Figure 35: Applied load vs temperature at the exposed face for all test series

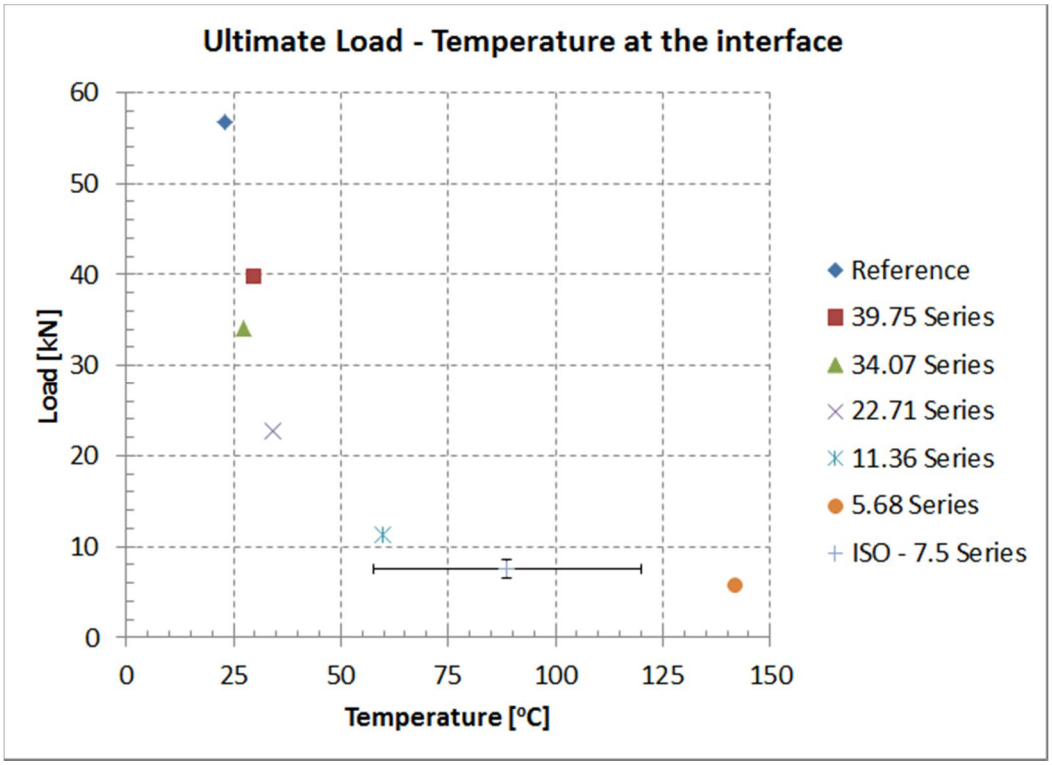

Figure 36: Applied load vs temperature at the interface for the all test series

3 Conclusions

A large number of experiments has been conducted with varying combinations of applied mechanical loading and radiant heat fluxes. The results of all the test series indicate that the failure mode is caused by the debonding of the skin to the core which was also noted in the case of the large scale tests. In addition, the well-known dependency between the applied mechanical loading and the developed temperature was validated.

The failure mechanism sequence on the other hand is rather complicated, and dependents on multiple mechanisms which are also interdependent. The most important of which being the degradation of the exposed skin and the interface properties due to the increasing temperature. Furthermore with the rise of temperature the change in the material properties of the skin leads to the generation of a bending moment due to the relocation of the neutral axis of the specimen. The magnitude of this moment is a function of the applied loading and the relocation of the neutral axis. This potentially leads to significantly different loading conditions in the specimens with varying ratios of bending moment to axial loads. This obscures the effect of each loading component to the load bearing capacity of the specimens.

Nevertheless, the results of the specimens that were subjected to constant heat flux presented very good repeatability and exhibited a clear trend between the applied loading and the developed temperature. Regarding the ISO curve tests the results presented significant scatter and therefore no conclusions can be drawn for these.

Additional testing is required to allow the connection of these mid scale test series to larger scales. A very interesting subject for future studies would be to perform dedicated fracture mechanics experiments at elevated temperature and for different loadings to study the effect of temperature at the fracture energy of the interface at different phase angles.

Despite the fact that the conducted mid-scale experiments do not allow for the measurement of the fracture properties of the interface, significant insight has been gained on the evolution of damage, the failure mechanisms and the governing parameters for the load bearing capacity of sandwich structures subjected to combined thermomechanical loading.

4 Literature

[1] A. G. Gibson, A.P. Mouritz, *Fire Properties of Polymer Composite materials*. 2006.
[2] A. P. Mouritz, E. Gellert, P. Burchill, and K. Challis, "Review of advanced composite structures for naval ships and submarines," vol. 53, 2001.
[3] A. P. Mouritz, S. Feih, E. Kandare, Z. Mathys, a. G. Gibson, P. E. Des Jardin, S. W. Case, and B. Y. Lattimer, "Review of fire structural modelling of polymer composites," *Compos. Part A Appl. Sci. Manuf.*, vol. 40, no. 12, pp. 1800–1814, Dec. 2009.
[4] M. Dao and R. J. Asaro, "A study on failure prediction and design criteria for fibre composites under fire degradation," *Compos. Part A Appl. Sci. Manuf.*, vol. 30, pp. 123–131, 1999.
[5] R. J. Asaro, B. Lattimer, and W. Ramroth, "Structural response of FRP composites during fire," *Compos. Struct.*, vol. 87, no. 4, pp. 382–393, Feb. 2009.
[6] P. Gu and R. J. Asaro, "Structural buckling of polymer matrix composites due to reduced stiffness from fire damage," *Compos. Struct.*, vol. 69, pp. 65–75, 2005.
[7] P. Gu and R. J. Asaro, "Designing polymer matrix composite panels for structural integrity in fire," *Compos. Struct.*, vol. 88, no. 3, pp. 461–467, 2009.
[8] P. Gu and R. J. Asaro, "Designing sandwich polymer matrix composite panels for structural integrity in fire," *Compos. Struct.*, vol. 88, no. 3, pp. 461–467, 2009.
[9] P. Gu, M. Dao, and R. J. Asaro, "Structural stability of polymer matrix composite panels in fire," *Mar. Struct.*, vol. 22, no. 3, pp. 354–372, 2009.
[10] A. G. Gibson, Y.-S. Wu, J. T. Evans, and A. P. Mouritz, "Laminate Theory Analysis of Composites under Load in Fire," *J. Compos. Mater.*, vol. 40, no. 7, pp. 639–658, 2006.
[11] A. P. Mouritz, S. Feih, Z. Mathys, and a. G. Gibson, "Mechanical Property Degradation of Naval Composite Materials," *Fire Technol.*, vol. 47, no. 4, pp. 913–939, Dec. 2011.
[12] S. Feih, Z. Mathys, a. G. Gibson, and a. P. Mouritz, "Modelling the compression strength of polymer laminates in fire," *Compos. Part A Appl. Sci. Manuf.*, vol. 38, no. 11, pp. 2354–2365, Nov. 2007.
[13] S. Feih, Z. Mathys, a. G. Gibson, and a. P. Mouritz, "Modeling Compressive Skin Failure of Sandwich Composites in Fire," *J. Sandw. Struct. Mater.*, vol. 10, no. 3, pp. 217–245, May 2008.
[14] S. Feih, Z. Mathys, a. G. G. Gibson, and a. P. P. Mouritz, "Modelling the tension and compression strengths of polymer laminates in fire," *Compos. Sci. Technol.*, vol. 67, no. 3–4, pp. 551–564, Mar. 2007.
[15] S. Feih and a. P. Mouritz, "Tensile properties of carbon fibres and carbon fibre-polymer composites in fire," *Compos. Part A Appl. Sci. Manuf.*, vol. 43, no. 5, pp. 765–772, May 2012.
[16] S. E. Boyd, J. V. Bausano, S. W. Case, and J. J. Lesko, "Mechanistic Approach to Structural Fire Modeling of Composites," *Fire Technol.*, vol. 47, pp. 941–983, 2011.
[17] A. Horold, B. Schartel, V. Trappe, M. Korzen and M. Naumann, "Structural Integrity of Sandwich Structures in Fire: An Intermediate-Scale Approach", *Composite Interfaces* : 741–759, 2013
[18] C. Maluk, PhD Thesis, "Development and application of a novel test method for studying the fire behavior of CFRP pre stressed concrete structural elements." The University of Edinburgh, 2014